DISSERTATION

The Nuclear Excitation of Thorium-229 in the CaF_2 Environment

Development of a Crystalline Nuclear Clock

Ausgeführt zum Zwecke der Erlangung des akademischen Grades
eines Doktors der Naturwissenschaften

Von:
Kjeld BEEKS
Matrikelnummer: 11731409

Unter der Leitung von:
Thorsten SCHUMM
Atominstitut (E141)

eingereicht an der Technischen Universität Wien

Fakultät für Physik

Vienna

April 2022

K. Beeks

Abstract

The ^{229}Th nucleus has the lowest known first nuclear excited state out of all isotopes. The transition energy from ground to first excited state was measured to be between 7.88 eV and 8.47 eV (1σ), or between 146.4 nm and 157.3 nm. The lifetime of this state depends heavily on the chemical environment due to the two competing nuclear decay processes: Radiative photon emission and internal conversion. In internal conversion the energy of the excited nucleus is transferred to a bound electron of the atom which is promoted to the continuum. Due to the nuclear structure and selection rules of ^{229}Th, photon emission is strongly suppressed while internal conversion is preferred if energetically allowed. The low energy of the first nuclear excited state is too low for internal conversion to take place if the charge state of the atom is higher than 1+. Above 1+, this first nuclear excited state is long lived with an estimated lifetime of around 5000 seconds. This metastable nuclear states is commonly referred to as isomer and is denoted as $^{229\mathrm{m}}$Th.

The low energy of $^{229\mathrm{m}}$Th has sparked many ideas for application over the years. Out of all isotopes, ^{229}Th seems to have the only nuclear excited state accessible by lasers and frequency combs. This allows to probe the nuclear level structure with a precision unprecedented in nuclear physics. The most sought after application for this unique state is currently to build an optical clock. The low energy nuclear excited state even allows to build a solid state optical clock by doping the ^{229}Th in a large bandgap material, such as CaF_2. The CaF_2 single crystal is transparent up to 122.5 nm, hence transparent to the predicted emission wavelength of the isomer. Doping ^{229}Th into CaF_2 thus allows optical excitation and detection of the nucleus. The ^{229}Th will substitutionally replace the Ca in the crystal lattice, which ensures a 4+ oxidation state and a long lifetime. Although the nucleus couples to its environment, it allows for a high precision clock to be built even in a solid state environment due to the high number of nuclei ($>10^{16}$) in the doped crystal. Such a clock would be a highly sensitive probe to new physics due to the unique nature of the nuclear excitation.

In this thesis, the doping and nuclear excitation of ^{229}Th into CaF_2 is investigated. The crystal environment is characterized through crystal growing and vacuum ultraviolet (VUV) optical techniques. The nuclear excitation is investigated through viability calculations using experimental characterizations of three distinctly different nuclear excitation methods: Resonant VUV photon irradiation, nuclear decay and x-ray irradiation.

A detailed description is given on how cylindrical ^{229}Th doped CaF_2 single crystals were grown (3.2 mm diameter, 1 cm length). The size of crystals was reduced by a factor of 200 compared to previous work to increase doping concentrations of the scarcely available ^{229}Th. Doping concentrations reached were: $2.6{\cdot}10^{20}$ cm^{-3} for ^{232}Th with 5 % transmission at 150 nm and $1.2{\cdot}10^{18}$ cm^{-3} for ^{229}Th with 10 % transmission at 150 nm. Radioactivity amplified fluoride loss in CaF_2 during growth, which decreased the resulting VUV transparency and stopped the further increase of ^{229}Th concentration. Adding fluoride to these crystals increased their transparency. It was suggested that the charge state changes due to fluoride loss from Th^{4+} to Th^{3+}. In the ^{229}Th doped CaF_2, radioactively induced VUV luminescence was detected at 170 nm. It was conjectured to be due to Th^{3+}. Possibly, the absorption of a charge transfer state was detected at 124 nm in ^{232}Th doped CaF_2, where it is inferred that the charge state of Th is 4+.

Using resonant VUV photons to excite ^{229}Th was studied. VUV irradiation damages ^{232}Th doped CaF_2 which increases the VUV absorption strongly. When the crystals are cooled to 80 K, no damage was detected after VUV irradiation. VUV induced luminescence of ^{229}Th doped CaF_2 was characterized. A luminescence at 168 nm was detected, indicating the presence of Th^{3+}. It was calculated that a signal-to-noise ratio (SNR) of 1000 to measure ^{229m}Th photon emission for a 1 s integration time can be reached by using resonant VUV photon excitation, assuming no internal conversion.

Using nuclear decay to produce ^{229m}Th was studied. It was found that using the current ^{233}U doped into CaF_2 crystals would not result in detection of the nuclear photon emission. Another method was proposed where ^{228}Ra would be doped into CaF_2 and activated through neutron capture. The transmission loss and VUV luminescence in undoped CaF_2 by neutron irradiation was characterized. It was found that this method would be able to measure a ^{229m}Th photon emission with a SNR of at least 17, assuming no internal conversion, over a wide range of lifetimes (minutes to hours).

Using x-ray irradiation to excite the ^{229}Th nucleus was studied. It was found that x-ray irradiation induced VUV luminescence in both ^{232}Th and ^{229}Th doped crystals of 170 nm or lower (conjectured to be due to Th^{3+}). Damage due to x-ray irradiation was characterized and was found to decrease due to Th doping as compared to undoped crystals. It was calculated that using this method to observe ^{229m}Th photon emission results in a SNR of at least 20 for a 1 s integration time, assuming no internal conversion. No signal was however observed in experiments, indicating that internal conversion plays a significant role.

In this thesis it is shown that growing VUV transparent ^{229}Th doped into CaF_2 is possible, and several nuclear excitation methods are shown to be viable. More characterization of the microscopic doping structure is needed, but the nuclear clock is closer then ever.

Zusammenfassung

Der ^{229}Th-Kern hat von allen Isotopen den niederenergetischten bekannten Kernübergang. Die Übergangsenergie vom Grundzustand zum ersten angeregten Zustand wurde zwischen 7,88 eV und 8,47 eV (1σ) oder zwischen 146,4 nm und 157,3 nm gemessen. Die Lebensdauer dieses Zustands hängt stark von der chemischen Umgebung ab, aufgrund der beiden konkurrierenden nuklearen Zerfallsprozesse: strahlende Photonenemission und interne Umwandlung. Bei der interne Umwandlung wird die Energie des angeregten Kerns auf ein gebundenes Elektron des Atoms übertragen, das ins Kontinuum befördert wird. Aufgrund der Kernstruktur und der Auswahlregeln von ^{229}Th wird die Photonenemission stark unterdrückt, während die interne Umwandlung bevorzugt wird, wenn dies energetisch möglich ist. Die niedrige Energie des ersten angeregten Kernzustands ist zu niedrig für eine interne Umwandlung, wenn der Ladungszustand des Atoms höher als 1+ ist. Oberhalb von 1+ hat dieser erste angeregte Kernzustand eine lange Lebensdauer mit einer geschätzten Lebensdauer von etwa 5000 Sekunden. Metastabile Kernzustände werden allgemein Isomere genennt und mit $^{229\mathrm{m}}$Th bezeichnet.

Die geringe Energie von $^{229\mathrm{m}}$Th hat im Laufe der Jahre viele Ideen für Anwendungen hervorgebracht. Von allen Isotopen scheint ^{229}Th den einzigen angeregten Kernzustand zu haben, der für Laser und Frequenzkämme zugänglich ist. Dies ermöglicht es, die nukleare Ebenenstruktur mit einer in der Kernphysik bisher unerreichten Präzision zu untersuchen. Die begehrteste Anwendung für $^{229\mathrm{m}}$Th ist derzeit der Bau einer optischen Uhr. Der niederenergetische angeregte Kernzustand ermöglicht sogar den Bau einer Festkörperuhr durch Dotierung des ^{229}Th in einem Material mit großer Bandlücke, z.B. $\mathrm{CaF_2}$. Der $\mathrm{CaF_2}$-Einkristall ist bis 122,5 nm transparent, also transparent für die vorhergesagte Emissionswellenlänge des Isomers. Die Dotierung von ^{229}Th in $\mathrm{CaF_2}$ ermöglicht somit eine optische Anregung und Detektion des Kernzustands. Das ^{229}Th wird das Ca im Kristallgitter ersetzen, was eine Oxidationsstufe von 4+ und eine lange Lebensdauer sicherstellt. Obwohl der Kern an seine Umgebung koppelt, ermöglicht er aufgrund der hohen Anzahl von Kernen ($> 10^{16}$) im dotierten Kristall den Bau einer hochpräzisen Uhr sogar in einer Festkörperumgebung. Eine solche Uhr wäre aufgrund der einzigartigen Natur der Kernanregung eine hochempfindliche Sonde für neue Physik.

In dieser Arbeit wird die Dotierung und nukleare Anregung von ^{229}Th in $\mathrm{CaF_2}$ untersucht. Die Kristallumgebung wird durch Kristallzüchtung und optische Techniken im Vakuum-Ultraviolett (VUV) charakterisiert. Die Kernanregung wird durch Realisierbarkeitsberechnungen unter Verwendung experimenteller Charakterisierungen von drei deutlich unterschiedlichen Kernanregungsmethoden untersucht: Resonante VUV-Photonenbestrahlung, Kernzerfall und Röntgenbestrahlung.

Es wird detailliert beschrieben, wie zylindrische ^{229}Th-dotierte CaF_2-Einkristalle (3,2 mm Durchmesser, 1 cm Länge) gezüchtet wurden. Die Größe der Kristalle wurde im Vergleich zu früheren Arbeiten um den Faktor 200 reduziert, um die Dotierungskonzentrationen des kaum verfügbaren ^{229}Th zu erhöhen. Erreichte Dotierungskonzentrationen waren: $2{,}6 \cdot 10^{20}$ cm^{-3} für ^{232}Th mit 5 % Transmission bei 150 nm und $1{,}2 \cdot 10^{18}$ cm^{-3} für ^{229}Th mit 10 % Transmission bei 150 nm. Radioaktivität verstärkte den Fluoridverlust in CaF_2 während des Wachstums, was die resultierende VUV-Transparenz verringerte und den weiteren Anstieg der ^{229}Th-Konzentration stoppte. Die Zugabe von Fluorid zu diesen Kristallen erhöhte ihre Transparenz. Es wurde vermutet, dass sich der Ladungszustand aufgrund des Fluoridverlusts von Th^{4+} zu Th^{3+} ändert. In ^{229}Th-dotiertem CaF_2 wurde radioaktiv induzierte VUV-Lumineszenz bei 170 nm nachgewiesen. Es wurde vermutet, dass es auf Th^{3+} zurückzuführen ist. Möglicherweise wurde die Absorption eines Ladungstransferzustands bei 124 nm in ^{232}Th-dotiertem CaF_2 nachgewiesen, woraus geschlossen wird, dass der Ladungszustand von Th 4+ ist.

Untersucht wurde die Verwendung von resonanten VUV-Photonen zur Anregung von ^{229}Th. VUV-Bestrahlung schädigt ^{232}Th-dotiertes CaF_2, was die VUV-Absorption stark erhöht. Beim Abkühlen der Kristalle auf 80 K wurde nach der VUV-Bestrahlung keine Beschädigung festgestellt. VUV-induzierte Lumineszenz von ^{229}Th-dotiertem CaF_2 wurde charakterisiert. Eine Lumineszenz bei 168 nm wurde detektiert, was auf das Vorhandensein von Th^{3+} hinweist. Es wurde berechnet, dass ein Signal-Rausch-Verhältnis (SNR) von 1000 zur Messung der ^{229m}Th-Photonenemission für eine Integrationszeit von 1 s erreicht werden kann, indem eine resonante VUV-Photonenanregung verwendet wird, vorausgesetzt, dass keine interne Umwandlung erfolgt.

Untersucht wurde die Verwendung von Kernzerfall zur Erzeugung von ^{229m}Th. Es wurde festgestellt, dass die Verwendung des Aktuelles 233U dotiert in CaF_2-Kristalle nicht zum Nachweis der nuklearen Photonenemission führen würde. Eine andere Methode wurde vorgeschlagen, bei der ^{228}Ra dotiert in CaF_2 durch Neutroneneinfang aktiviert wird. Der Transmissionsverlust und die VUV-Lumineszenz in undotiertem CaF_2 durch Neutronenbestrahlung wurden charakterisiert. Es wurde festgestellt dass diese Methode in der Lage wäre eine ^{229m}Th-Photonenemission mit einem SNR von mindestens 17 zu messen über einen weiten Bereich von Lebensdauern (Minuten bis Stunden), vorausgesetzt, dass keine interne Umwandlung erfolgt.

Es wurde die Verwendung von Röntgenstrahlung zur Anregung des ^{229}Th-Kerns untersucht. Es wurde festgestellt, dass Röntgenbestrahlung VUV-Lumineszenz von 170 nm oder niedriger sowohl in mit ^{232}Th als auch mit ^{229}Th dotierten Kristallen induzierte (vermutlich von Th^{3+}). Schäden aufgrund die Röntgenbestrahlung wurden charakterisiert und es wurde festgestellt, dass sie aufgrund von Th-Dotierung im Vergleich zu

undotierten Kristallen abnahmen. Es wurde berechnet, dass die Verwendung dieser Methode zur Beobachtung der $^{229\mathrm{m}}$Th-Photonenemission zu einem SNR von mindestens 20 für eine Integrationszeit von 1 s führt, wenn keine interne Umwandlung angenommen wird. In Experimenten wurde jedoch kein Signal beobachtet, was darauf hindeutet, dass die interne Umwandlung eine signifikante Rolle spielt.

In dieser Arbeit wird gezeigt, dass das Züchten von VUV-transparentem ^{229}Th dotiert in CaF_2 möglich ist, und es wird gezeigt dass mehrere nukleare Anregungsmethoden Realisirbar sind. Eine weitere Charakterisierung der mikroskopischen Dotierungsstruktur ist erforderlich, aber die Kernuhr ist näher als je zuvor.

Acknowledgements

Vienna saw me grow scientifically, but also mature as a person. I am for ever grateful to the scientists around me who challenged my often overconfidence, and the friends around me who have made my time unforgettable. I hope I have provided some happiness, motivation and challenge in return. Pivotal to my time as a PhD-student was the Atominstitut and the people inhabiting it over the years. This is a magical place, and the world should know.

First of all I want to thank Professor Thorsten Schumm with all my heart. He took me in after I doubted a bit to come to Vienna from the Netherlands. He always made sure that I could focus on research and enjoying life, while he put in tremendous work behind the scenes. The times we spent chatting in the courtyard of ATI, in a bar in Heidelberg (home) or on the airport are unforgettable to me. Growing crystals, working with radioactive material, optics, vacuum systems wouldn't have been possible without him. I want to thank him for introducing me to the wonderful world of Thorium, the Atominstitut, Vienna and research. I want to thank him for his help, quick responses and being a great officemate. Your scientific and life advice will stay with me, and I sincerely hope that we will often see each other in the future! One could not wish for a better supervisor.

Both the referees, Professors Lino da Costa Pereira and Iain Moore, I want to thank for reviewing my thesis. If you read this before starting the review process, I hope this gives you the strength to get through the 200+ pages. I'm sorry for making it so long, but a lot happened in my time as a PhD. I want to thank Iain for the time we spent together during conferences such as Heidelberg or Sofia, for making the conferences "young" and I'm very happy that you could be there for the end of my thesis. I want to thank Lino for his enthusiasm in the Thorium topic and I hope we get to work together more in the future. I'm very interested in the solid state characterization of our crystals and hope to hear more from that soon. Although we haven't met in person yet, I am happy to have you as a reviewer!

I want to thank the CoQuS/VCQ program for giving me the opportunity to organize many events over the years and to broaden my scientific horizon by interaction with many physicists across Vienna and trips abroad. The people in CoQuS, from the secretaries to the PhDs to the professors, have significantly contributed to my personal and scientific development. I will never forget the dinners with speakers and professors, the trips to Barcelona, Obertraun and Shanghai, the CoQuS barbecues and the summer schools. Especially Christiane, Susi and later Nadine deserve praise for letting it run as smoothly as was possible alongside PhD students. I want to thank the Quantum Physics Professors in Vienna to have set up such a program, which I was happy to be part of.

I sincerely want to thank Professor Koji Yoshimura for inviting me to Japan, and making sure my time was well spent there. I want to thank him for his kind words, the lunches we had, the scientific discussions, the shabu-shabu restaurant and all the help in getting to Japan! I fell in love with southern Japan and hope to return soon. Sadly the virus made it impossible to come to Japan in the later years of my PhD, although I tried, but I hope we can compensate for that in the future. I still remember how we first met in Heidelberg over lunch, maybe it was a coincidence we sat next to each other or maybe not. I hope the crystals we produced will produce results soon, SPring-8 is an amazing facility and I'm honored to have been allowed to work there with you. Cycling around the synchrotron and having the same lunch every day is etched into my memory. I hope we meet again soon!

Everyone in the Thorium research community has been an amazing contribution to my time in the field. I want to specifically thank Peter Thirolf for late night discussions in Sofia, Ekkehard Peik for his enthusiasm in and starting the experimental search for the isomer in Europe,, Lars and Benedict for hosting me in Munich, Masuda-san and Yoshimi-san for my time in Japan, Piet van Duppen and his team for inviting me to CERN, Simon and Arno for the dutch night shift at ISOLDE, and many more times I am probably forgetting. I hope to see you all soon again!

Everyone in the Schumm group, more specifically the Thorium part, receives high praise. I want to thank Simon for his short time with me where he juggled being a dad and a postdoc successfully. I learned a lot about vacuum systems, optics and general physics from him. I thank him for showing me around the group the first time I visited Vienna, and all the good times afterwards. The next postdoc, Tomas, has changed me as a person tremendously. His "can do" attitude, strong sense of experimental practicality and infinite energy to do research have made my time as a PhD incredible. I had so much fun growing crystals, tightening vacuum systems, working with radioactive material and interesting never ending discussions about the physics. You showed me that research can easily be applied to life, for example characterizing your bodies' alcohol processing speed. Thank you so much for taking me on all these skiing trips (sorry for the accident), where the tradition of hot tea with a kick will stick with me forever! Also the introduction to Slovakian wines I must mention, every time a new box showed up at the porter meant a new interesting experience! I hope we will stay in touch even after I leave Vienna, you are a great postdoc and a tremendous friend. My office mate for a long time, Georgy, was always there to discuss some physics or to pass a chocolate or two.

Veronika, sadly and luckily now in London, did an amazing job as our in-group chemist. She provided us with the necessary know-how and fearless handling of radioactive material. Also many thanks to Martin who took over from her and has continued to provide us with many insights, hard work and kindness. I enjoyed the cloud chamber you two built together, a great way to visualize our crystals! The other physics PhD students: Fabian, Niyusha, David and Thomas made our group a whole lot bigger and diverse. I want to thank you for all the time you have given me to write my thesis, helped me in the lab, and I hope you will have a great time in the group just as I did, and I am looking forward to many more drinks, movies and trips together! Also the Cesium Crew I want to thank for the lunch trains when I was the only PhD on the Thorium side. I enjoyed our lunches and our crazy discussions and ideas during lunch! I want to specifically thank Benedikt for making time for me in his busy schedule. He introduced me to his friends, and I hope to keep the tradition of St. Patty's day drinking together! I enjoyed our insane going out in Barcelona, crazy Shanghai nights, drinking in Vienna, organisation of events and everything else! Max I want to specifically thank for taking me to clubs, hotdog stands, soundsystems, illegal parties and dancing under the Ubahn bridge.

Not only the Schumm group, but the entire Atominstitut deserves high praise. The friends I made and the people I worked with will leave a mark on me. I want to thank the mechanical workshop that produced all the parts I needed quickly and in high quality, the porters for always being there for a chat and all the other staff for making the labs run smoothly and with no hassle. I want to thank the radiation safety, Dieter and Monika, for helping us work with our material and teaching us sternly how to behave. Johannes Sterba and Jan Welch also deserves praise for that, and for the help with the activation experiments. Jan deserves extra praise for tolerating my crazy ideas over lunch, thank you for all that you (have) taught me about chemistry! I want to thank the entire Schmiedmayer group for letting me use their coffee machine and bothering its people with my banter, the same for the Rauschenbeutel group. Here I made more friends for life in no particular order: Jakob, Martin, Sam, Jan, Mattia, Pradyumna, Filippo, Stephan (+Sina), João, Amin, Arno, Camille, Frederik, Fritz, Andrew, Thomas, Wenzel and many more! I will never forget karaoke in Café Concerto, drinking in the courtyard, Mattia's birthday in Italy, Frederiks christmas spirit, DND, barbecues, chai, star gazing, hanging out at the Danube, days of hard working, days of hardly working, oktober fest, the beer fund, trips, climbing, football and much more.

I also want to thank all the students I've had over the years, since they had their hands in the work that is gathered in this thesis: Marion, Andreas, Florian, Peter, Lukas, Felix, Florian, Felix and Sam. Special praise goes out to Marion who tolerated being in the group the longest and became a lifetime friend. Thank you for accompanying me to Munich to do some cool physics! I wouldn't have made as much progress in my research and teaching skills if it wasn't for these students constantly pestering me with what they could do and breaking the experiments. Mostly though, they provided me with good conversations in and outside of the lab which made me love working in academia.

A big thank you also goes out to my entire family, who has tolerated my departure from the Netherlands, shortcomings in having regular calls. They have supported me tremendously throughout my thesis and visited me in Vienna often. Every time I returned to the Netherlands I was immediately relieved of PhD stress by their care and support. They always supplied me with enough cheese, worstenbroodjes and beer for the trip back to survive until the next time. I want to thank all my friends in the Netherlands and abroad who have visited me and helped me explore Vienna. Especially Just, Louis, Rogier, Luuk, Danny, Demi, Gert-Jan, Peet, Mark and Jelle. Some of you even visited me multiple times and I hope that in the future we would keep this up! I also want to thank the Dutch community in Vienna for giving me a piece of home abroad! I want to also mention my gaming buddy Paul, who has helped me out with some frustration through super smash bros and has become a true friend over the course of many years that I was here.

Vienna has changed me for the better, I am eternally grateful for everything and everyone who has made my time here unforgettable!

Contents

Chapter 1

The Road To a Nuclear Clock

1.1 Discovery and Characterization of the Unique Nuclear State Thorium-229m

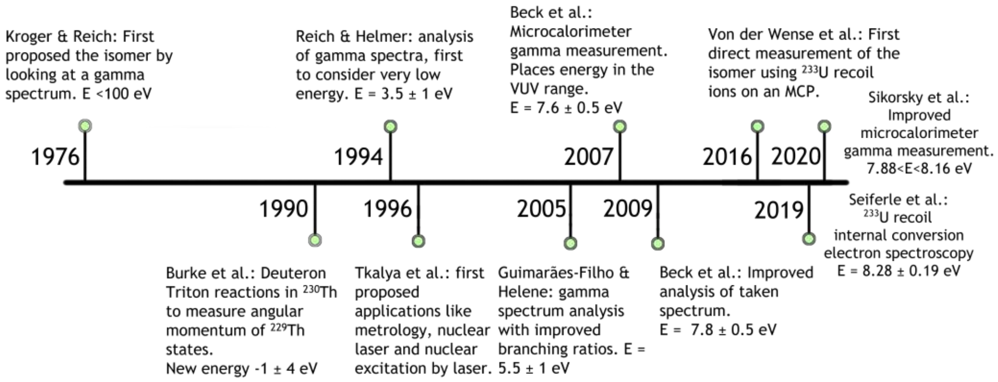

FIGURE 1.1: Timeline from the discovery of the unusual first nuclear excited state of thorium-229 to the first direct measurement following the determination of its energy. [1–10]

Thorium-229 (^{229}Th) is an artificial radioactive element with a half-life of 7825±87 (two σ) years [11], it decays 100 % via an α-decay of 5.167 MeV (Q_α) to radium-224. For the full decay chain, see figure 2.15. This short half-life means this isotope cannot be primordial and is thus artificially produced. Because ^{229}Th is artificially produced, very little ($\approx$ g) is available worldwide which complicates experimental progress [12]. Chemically, thorium is part of the actinides, but behaves more like hafnium or zirconium due to the two unpaired electrons in the outer d shell. The electron configuration of Th is [Rn]6d^{2}7s^2, of Th$^+$ is [Rn]6d^{2}7s or [Rn](6d 7s)^3 of Th^{2+} is [Rn]5f6d [13] and of Th^{3+} is [Rn]5f.

The ^{229}Th nucleus has a unique nuclear level structure, which is known from gamma ray spectra of the decay of the mother isotope uranium-233. The excitation energy from ground to first excited state of this nucleus (E_{is}) was measured in [9, 10] to be $7.88 < E_{is} < 8.47\,\text{eV}$ (1σ). By comparison, most nuclear excited states are in the MeV range. The next known lowest nuclear excited state is uranium-235 with 76 eV [14]. The low energy first nuclear excited state of ^{229}Th has sparked many ideas for application over the years and fueled research towards understanding of this isotope. Out of all isotopes ^{229}Th seems to have the only excited state accessible by lasers and frequency combs, which allows to probe the excited state with a precision unprecedented in nuclear physics.

One of the applications of the first excited state of ^{229}Th proposed, is to build an optical clock using this unique isotope [4]. The low energy nuclear excited state even allows to build a solid state optical clock by doping the ^{229}Th in a large bandgap material [15], because of the weak coupling between the nucleus and its environment. Due to the nuclear structure of ^{229}Th this first excited state is long lived ($\approx$5000 s) [16]. The nuclear selection rules prevent this state from emitting a photon, but due to coupling to the environment it is possible with this long lifetime. This long lived nuclear state is commonly denoted as isomer which is frequently written as thorium-229m or $^{229\text{m}}$Th, where "m" is for metastable. The discovery of the unique isomer is rooted in its radioactivity, scattering experiments and knowledge of nuclear band structure.

The discovery of radioactivity by the Curies and Becquerel provided the field with experimental tools to study nuclear structure and subatomic particles. Quickly after the discovery of radioactivity the electron, proton, neutron and isotopes were discovered while α-decay, β-decay, and γ-decay were realized to be respectively helium cores, electrons, and photons. These discoveries sparked the early nuclear models and lead to our understanding of electron and nuclear shell structure today. In these early days, Rutherford and Andrade [17] performed the first γ spectroscopy of radium B (^{214}Pb) using a rock salt crystal as a diffraction crystal.

The characterization of isotopes through γ spectra continued, while tools to measure γ rays of higher energies with more precision were developed. The spectra of γ rays emitted through the radioactive decay of isotopes is an excellent tool to study nuclear structure. Each measured γ ray represents the decay of one nuclear excited state to another and when all rays are measured, the nuclear structure can be reconstructed when combined with other measurements. These type of measurements were instrumental in gaining understanding of the unique nuclear structure of ^{229}Th.

In 1971, through informal communication, the existence of a very low first nuclear excited state of ^{229}Th was first proposed, which was noted in the 1972 nuclear data sheet publication [18]. In this publication, an attempt was made to make a structured study of the characteristics of nuclei around ^{229}Th because they were known to be highly deformed and thus had unique properties. Through a combination of deuterium/tritium scattering experiments on ^{230}Th(d,t)^{229}Th and ^{232}Th(d,t)^{231}Th plus γ ray spectra of the ^{233}U α-decay the isomer state was inferred. A more complete publication with more dedicated measurements to constrict its energy and arguments for its existence were published in 1976 by Kroger and Reich [1].

A theoretical understanding of highly deformed nuclei was developed by Nilsson in 1955 and thus preceded the experimental characterization. To understand the unique properties of deformed nuclei we follow the Nilsson model [19], which also describes the nuclear excited states of ^{229}Th. In this model the Hamiltonian is solved for a single particle (proton or neutron) in an effective nuclear mean field potential which is non-isotropic: the nucleus is assumed to have an ellipsoidal shape or a non-isotropic harmonic potential. This choice was made because rotational bands were observed in gamma spectra of nuclear decay, indicating the nucleus rotated as a whole. Nuclear states in a single rotational band are characterized by having the same single particle state, but different nuclear angular momenta. These rotational bands are only possible for asymmetrical particles, therefore an asymmetric model was applied.

The result of this model is single particle states from the above rotational bands characterized by the Nilsson quantum numbers $K^{\pi}[Nn_z\Lambda]$. Here π = (-1)^N is the parity, K the projection of the total nuclear angular momentum onto the symmetry axis of the system, N the total energy of the single particle state, n_z the energy of the single particle state projected onto the symmetry axis of the system and Λ the orbital angular momentum of the single particle state projected onto the symmetry axis of the nucleus.

The ground and first excited states of the ^{229}Th nucleus are characterized by $5/2^+[633]$ and $3/2^+[631]$, respectively. From these quantum numbers we can see that these two state only differ in Λ and K, thus having different single particle states and different total nuclear angular momenta. Every higher excited state of a rotational band doesn't change the single particle state, just the rotational energy of the nucleus. Therefore only the K value changes for state in the same band.

The long photonic lifetime of the isomeric state originates from above characteristics: Due to selection rules only magnetic dipole (M1) radiation and electric quadrupole (E2) radiation are allowed for the isomer's de-excitation. A photon emission is electric dipole radiation (E1) and is thus not favored, which creates a long lived state. The higher lying excited states also have a low probability to emit photons due to the same selection rules. Still, due to the inverse scaling of lifetime with energy, their lifetime is relatively short. Internal conversion is the preferred mode of decay between same parity nuclear states.

Internal conversion is the process where the nucleus de-excites by emitting one of the electrons bound to the nucleus. The energy needed for this process is thus at least the electron binding energy, the rest will be kinetic energy. The internal conversion leads to a much shorter lifetime and dominates the deformed nuclei de-excitation. The lifetime of their nuclear excited states would be extended if the internal conversion decay mode can be blocked (e.g ionization of the atom).

We now follow the timeline in figure 1.1. In the publication by Kroger and Reich it was stated that the energy of the first excited state of ^{229}Th had to be lower than 100 eV, a unique property in nuclear structure. The scattering experiments were never published and interest was long lost, until the scattering experiments were repeated in 1990 which again confirmed the existence of this odd state [2]. This sparked another more precise measurement of the γ ray spectrum of ^{233}U decay to ^{229}Th which resulted in a first published value for this low nuclear excited state, 3.5 ± 1 eV [3].

The newly determined energy would produce photons in the optical region, around 350 nm. Because of this, techniques from atomic systems which resonate in the optical region could now be applied to this one isotope. In 1996, twenty years after the 1976 discovery of the unique properties of ^{229}Th, the idea to make an optical clock not based on an atomic transition but a nuclear transition was born [4]. More applications for this unique isotope were proposed in this paper, such as a gamma laser and probing the chemical environment with a nuclear state.

The predicted value for the first nuclear excited state of ^{229}Th of 3.5 eV started a decade of experiments aimed at measuring an isomer photon emission at 350 nm. It was thought that the photon produced by the nucleus was indeed observed, but this was later debunked as radioactivity-induced fluorescence of nitrogen in 1999 [20]. After this decade the community matured to be more sceptical in their measurements of this elusive first excited state of ^{229}Th. The failed experiments initiated again more precise γ ray measurements and a new analysis of them. First a new analysis increased the energy to 5.5 eV in 2005 [5], then a new measurement with a very precise microcalorimeter further increased the energy to 7.6 eV in 2007 [6] with a last increase to 7.8 eV through an improved analysis in 2009 [7].

The new energy of 7.8 eV placed the photon wavelength at ≈160 nm, in the vacuum ultraviolet (VUV) region. This region is characterized by the fact that photons below ≈200 nm are absorbed in air, and thus need to travel through vacuum or another transparent medium to be detected. These new requirements meant that new experiments needed to be designed in order to measure the low-energy isomer photon emitted from the first nuclear excited state of ^{229}Th. After the first mention of the unique properties of ^{229}Th in 1976 it took twenty years to realize its potential in 1996. After another twenty years, in 2016, for the first time the first nuclear excited state of ^{229}Th was directly measured and unequivocally proven to actually exist [8]. If this trend continues, the first practical application will be realized in 2036.

The first direct measurement of the isomer state was performed by measuring the internal conversion of the first excited state on a micro channel plate (MCP). Usually the internal conversion electrons are emitted at high energies due to the normally high energies of nuclear excited states (≈10-1000 keV). In the case of $^{229\mathrm{m}}$Th there is only enough energy in the nucleus to overcome the first ionization energy by ejecting the outermost electron with some kinetic energy. This also means that if the Th is ionized, internal conversion is forbidden.

Due to the internal conversion of the isomer state in neutral Th, many initial experiments failed to measure a photon. In neutral Th, every decay from the first excited state will go through internal conversion rather than for radiative nuclear decay: The decay rate of internal conversion is 10^8 times higher. Any measurement aimed at measuring an photon emission coming from neutral $^{229\mathrm{m}}$Th thus failed. The experiments of [8] succeeded because an ion beam was created which contained $^{229\mathrm{m}}$Th$^{2+,3+}$. In this beam, no internal conversion would happen and only very little photon decay. The beam quickly transported newly created $^{229\mathrm{m}}$Th from ^{233}U α-decay to an MCP where the Th ions could neutralize on the surface. After neutralization, internal conversion takes place which ejects an electron. This energetic electron ejection then caused an electron avalanche in the MCP where the $^{229\mathrm{m}}$Th$^{2+,3+}$ was implanted. This experiment produced the first measurable signal of the nuclear decay of $^{229\mathrm{m}}$Th.

The direct measurement of the isomer state through internal conversion enabled an isomer energy determination different from analyzing γ spectra. In this experiment, the ion beam described above was shot at a graphene foil instead of an MCP. The ions have enough kinetic energy to pass through the graphene foil, where they are neutralized by the electrons in the foil. The now atoms continue and the isomer atoms will undergo internal conversion ≈ μs later, thus ejecting an electron. An electron spectrometer then accurately measured the kinetic energy of the ejected electron, which together with its binding energy was used to determine the energy of the isomer [9]. Simultaneously, another more precise ^{233}U decay γ ray spectrum measurement was taken [10] which together established the new value for the first nuclear excited state of ^{229}Th to be 8.15 ± 0.45 eV[1]. The new value increased the energy even more, to photons with a wavelength of 150 nm. This time, experiments only needed to be adjusted slightly which still costs a tremendous amount of work. Luckily, this wavelength still allows for building an optical clock with the isomer state.

---

[1] average of all reported values with 68 % confidence interval error propagation

Interestingly, after 20 years of attempting to measure a photon being emitted by the ^{229}Th nucleus, the isomer state was measured by an alternative process. Recently more methods have been proposed to probe the nuclear state without measuring the photon de-excitation: Through non-destructive state monitoring. This is independent of the decay rate of the nuclear state, and it can be performed in other frequency ranges. For example: The nuclear magnetic moment changes upon excitation, which changes for example the hyperfine splitting of the electronic excited states [21]. By monitoring the hyperfine splitting of a single ^{229}Th nucleus it can thus be determined if it is excited. This method is much more reliable because an electronic excited state can be chosen for which intense narrow lasers have been developed with which such a spectroscopy is trivial. Another example is that in a crystal, the nuclear magnetic properties of ^{229}Th interact with electric field gradients which together create a quadrupole structure depending on the excitation state of the nucleus [22]. Developing new excitation and detection methods of the isomer will be crucial to build an optical clock, as suggested in 1996.

1.2 Building A Nuclear Clock

Atomic optical clocks have been an essential part of our lives in both technological applications and fundamental research [23] and are a very mature technology [24]. Their precision makes them probes which are sensitive to electromagnetic forces and gravitational shifts. Looking for changes in fundamental constants with clocks could provide us a glimpse of new physics. In GPS satellites clocks have proven to be essential to technological advances. In the future clocks might even predict earthquakes [25]. In which areas would a nuclear clock be beneficial?

To understand why a nuclear clock is a worthwhile endeavor, one needs to understand how a clock works and subsequently how an atomic clock works. Clocks were developed following the need to tell time more precisely than natural phenomena, such as the sun's motion, will provide. A clock can be built out of widely different components, but the basic components are the same. First of all a clock uses something as an oscillator, a device that repeats the same process over and over again with a constant time interval for its repetition. This oscillation will inevitably lose energy to its environment so a controller is attached to replenish the lost energy. A counter will count each oscillation and store this information. This information in the counter is converted by an indicator to a convenient unit such as the second. For a classic pendulum clock the oscillator would be the pendulum, the controller would be a weight on a string or a wound up spring, the counter would be an escapement which takes as little energy from the pendulum as possibly to count the number of swings and through gears this counting of the swings would be converted to an hours/minutes/seconds time on a clock face.

For an atomic clock the components can be arranged in similar categories. The oscillator is an atomic transition, an energy difference between two orbitals of an electron which has the same energy for any atom as long as the same orbitals are probed for the same isotope. This energy difference can be driven using a laser which produces a continuous stream of photons which is a very well defined electromagnetic oscillation. Due to the nature of photons, the wavelength λ, frequency ν and energy E are all related through $\mathrm{E} = \mathrm{h}\nu = \mathrm{h}\frac{\mathrm{c}}{\lambda}$ (in vacuum). Thus any energy of an atomic transition can be directly converted to a frequency of an oscillation and thus a time. The atomic transition is modeled as an harmonic oscillator, which responds very strongly when the driving oscillation frequency is close to the resonant frequency. The atom will absorb and scatter the laser light more when the laser is in perfect resonance with the atomic transition. By measuring for example the scattered light one can precisely tune and feedback-stabilize the electromagnetic oscillation of the laser to the atomic energy. The laser now emits one single energy, or wavelength, or frequency. The spectrum of this continuous wave is a single peak at a single frequency. For this it is important that the laser itself has an extremely narrow spectrum, or single peak linewidth, as this will limit the precision to which the exact frequency of the excitation can be measured.

Now that the oscillator is driven, and the laser or controller has been tuned to the same oscillation frequency, the laser frequency can be measured by a counter. The counter is now a frequency comb, a femtosecond laser that sends out pulses in an extremely regular time interval and has a fixed phase relation between its pulses. From Fourier analysis one can calculate that the frequency spectrum of such a pulsed laser is a comb spectrum. The mathematically perfect pulse train is called a Dirac comb, which is its own Fourier transform. The name frequency comb comes from the apparent ”teeth” that characterize the spectrum. When the oscillation of a frequency comb is overlapped and ”beaten” with the CW spectroscopy laser the wave amplitudes are simply superimposed. In the frequency domain the comb spectrum will interact with the single peak of the laser. This will create so called beat notes which can be easily inferred from trigonometry. When we add two CW lasers with frequencies ν_1 and ν_2 the resulting wave will show the sum and difference frequency components

$$\cos 2\pi\nu_1 t + \cos 2\pi\nu_1 t = \cos 2\pi\frac{\nu_1+\nu_2}{2}t + \cos 2\pi\frac{\nu_1-\nu_2}{2}t. \tag{1.1}$$

This also holds for a CW spectroscopy laser and a frequency comb. If one of the comb teeth is close to the single peak of the CW spectroscopy laser, this will create a much lower difference frequency. The frequency comb is thus tuned such that the difference frequency is several orders of magnitude lower than the laser frequency. This complicated procedure is needed to down-convert the extremely high frequencies of lasers (hundreds to thousands of THz) to frequencies that electronics can handle (GHz and lower). The electronic counter will in the end use the known frequency of the frequency comb plus the frequency difference to the CW spectroscopy laser to output a highly precise electronic time signal that can be used as a clock.

This exact same process of building an optical clock using an electronic excitation should also be applicable to a nuclear excitation, provided that there are spectroscopy lasers that can drive the excitation with the correct energy and frequency combs in the VUV that can down-convert the frequency of the laser.

The first nuclear excited state of ^{229}Th is the only nuclear state with which an optical clock can be built with contemporary technology. To date, no narrow continuous wave laser has been developed for this wavelength which will limit the current precision of a nuclear clock. Frequency combs with a linewidth less than a MHz [26] can be used to excite the nucleus, if intense enough. The same laser can also be used to provide the frequency down-conversion to produce the electronic clock signal.

As stated above, a clock can be made by looking at the sun, or by performing spectroscopy on an atom. A sun-dial is less precise and accurate then an atomic optical clock. To quantify the difference between these oscillators, they are modeled as harmonic oscillators. The Q factor, which has two definitions which are almost equal, is then a measure for the strength and narrowness of an oscillator assuming a small damping constant (Γ):

$$Q = \frac{\omega_0}{\Delta\omega}, \tag{1.2}$$

$$Q = 2\pi\frac{\text{Energy in the system}}{\text{Energy lost every cycle}}. \tag{1.3}$$

Where ω_0 is the resonance frequency of the system and $\Delta\omega$ the FWHM of the resonance. For convenience, usually the first Q factor is considered since the second definition requires a more rigorous mathematical approach different for each type of oscillator. By comparing Q factors between oscillators their difference can be quantified, a higher Q factor resulting in a less damped system which results in a more stable frequency standard.

For atomic transitions then, the resonance is least perturbed by the driving laser if $\Gamma << 1$, which results in a very narrow resonance $\Delta\omega << 1$. The peak response of the system has a simple solution if Q is large, which is $E_0\frac{Q}{\omega_0^2}$, where E_0 is the amplitude of the driving laser. Thus the least damped system will produce a strong narrow resonance and will thus have a very large Q factor. In terms of an atomic transition, the lifetime is $\frac{1}{\Gamma}$, a long lived state is thus a very good resonator.

For example, the Q factor of a tuning fork is approximately 10^3, a quartz wristwatch 10^4, a cesium fountain clock 10^{10} and a mercury ion optical clock 10^{14} [27]. The Q factor of the $^{229\mathrm{m}}$Th state can be calculated using the currently known values to be $Q = \frac{8.15\ \mathrm{eV}}{1/5000\ \mathrm{s}} \approx 10^{19}$, a very good resonator thus. The total Q factor of any oscillator will be changed by external effects: A pendulum feels the air resistance, a spring has inelastic deformation and an atomic transition can be broadened. This can be collisions (collisional broadening), kinetic energy (Doppler broadening), interaction with the laser (power broadening), or coupling to the environment, which is the case in a crystal. These factors will reduce the Q factor for an atomic system, and also for the ^{229}Th nuclear excitation, and thus the ultimate clock performance.

The Q factor is not the only important parameter considered when building a clock. As discussed, the clock is operated by measuring the frequency of a laser feedback-stabilized (”locked”) to an atomic or nuclear excitation. How well one can lock this laser to this excitation also depends on the response of the excitation, the integration τ_{av} and interrogation time T_{int}. The more particles N one has, the stronger the response. In a perfect system this approaches the standard quantum limit $Q \approx \omega_0 \cdot \sqrt{NT_{int}\tau_{av}}$ [28]. So to build a good clock one needs a high-frequency resonance, many particles, a long lived state and a long averaging times.

Through the previously mentioned internal conversion the isomer state decays faster than through photon emission, and thus will be a much worse clock. However, the short lifetime did enable us to first directly measure the isomer state, as opposed to indirectly reconstructing the nuclear excited level structure through gamma spectroscopy of the radioactive decay of ^{233}U. In the end a long-lived state is needed with a sharp resonance, meaning we want to suppress the internal conversion. This is done when the isomeric thorium is ionized and does not have enough energy to ionize itself further. In an ion trap or in an ionic crystal, this state can be created. The internal conversion however can possibly be used to quench the excited state for improved clock operation [29]. Considering these aspects, we can establish four main arguments to build a nuclear clock:

Firstly, due to the smaller nuclear magnetic moment of the nucleus the systematic shifts in frequency due to external electromagnetic fields of a nuclear clock should be smaller than for an atomic clock. A decrease in the size, and thus the error in these shifts, will reduce the overall error budget of this clock which will increase its accuracy. One can compare the Bohr magneton $\mu_B = \frac{e\hbar}{2m_e}$ to the nuclear magneton $\mu_N = \frac{e\hbar}{2m_p}$ which results in $\frac{\mu_B}{\mu_N} = \frac{m_p}{m_e} \approx 10^3$, the ratio between the electron mass and proton mass. This shows that nuclear excitations are less sensitive to external fields than electron excitations. The nuclear magnetic moments of the ground state is $0.360(7)\mu_N$ and of excited state $-0.37(6)\mu_N$ [22]. These differ due to the different configuration of proton and neutron spins between ground and isomer state. Also, just as the electron states show hyperfine splitting due to the nuclear magnetic moment, the nuclear state will be split due to hyperfine interaction with the electrons. Due to this splitting the frequency can be shifted as well, but the effect can be mitigated to be again smaller than for electrons [15].

Secondly, due to the weak coupling of ^{229}Th to the environment, it can be doped in a crystal and still function as a good clock [30]. In the crystal lattice, the spectroscopy of Th nuclei benefit from being in the Lamb-Dicke regime. The recoil produced by the isomer decay is much smaller than the energy needed to create a phonon, reducing shifts. In a crystal, the nuclear excitation will be shifted due to electric field gradients in the crystal and broadened due to coupling to other surrounding nuclear spins. These shifts will be larger than for ^{229}Th in an ion trap but, due to the small nuclear magnetic moment, they probably remain manageable to build a high precision solid state nuclear clock [31]. The number of oscillators in this clock ($\approx 10^{16}$) is many orders of magnitude higher than what is used in an ion trap (tens) or in cold gasses (millions). As can be seen from the Q factor described previously, having a large number of oscillators will greatly increase clock performance by increasing the signal to noise ratio. The increase in clock performance only holds if the crystal environment can be controlled well and every nucleus is influenced similarly by its environment. Practically, in any crystal there will be inhomogeneous broadening of the nuclear resonance due to the surrounding ions.

Thirdly, the nuclear clock would be much more sensitive to fine structure constant changes and dark matter or energy for example, owing to the nearly degenerate ground state of ^{229}Th. The small energy difference between ground and isomer state is a result of the deformed nucleus. It is deformed just enough such that these two states are only eVs apart. One can compare this energy to the average binding energy per nucleon ($\approx$MeV) which is the average energy needed to remove the nucleon from the nucleus. The neutron that is excited between ground and isomer state of the ^{229}Th nucleus is bound by these energies. When an external effect produces a tiny change in these MeV energies that determine the binding energy (nuclear force or coulomb repulsion), it would still mean a relatively significant change of energy in the $\approx 8\,$eV state of a nuclear clock [32]. The nuclear optical clock would thus be highly sensitive to perturbations involving the electromagnetic force and even sensitive to perturbations involving the strong force.

Lastly, building this clock grants the opportunity to study the interaction of the nuclear with the atomic, which no other system in the world grants. Through experiments it is observed that the interaction of the nucleus with its electrons is present, but is a relatively unknown effect. Effects such as quenching of the nucleus through crystal defect states, electron bridge excitation through its own electrons or defect states and nuclear hyperfine splitting can be studied [15, 29]. Possibly even a solid state nuclear laser can be built [33].

To build this clock, internal conversion needs to be blocked to ensure a long lifetime and thus a large Q factor. To block internal conversion and ensure optical decay, ^{229}Th can be ionized [34–36] or doped in a large bandgap crystal [37, 38]. These approaches ensure that the nucleus has no available electron states to communicate its energy for internal conversion. This also ensures that the environment transmits VUV photons for detection. If one dopes a large bandgap crystal with the ^{229}Th nucleus and is able to address the isomeric state, a new platform is created: A next generation clock that is able to study new physics and atomic-nuclear interactions.

1.3 A Solid State Nuclear Clock

In 2003 the idea was first coined that the nuclear state should be relatively independent of its surroundings and would be addressable in a solid state environment [15]. Doping ^{229}Th in a crystal as opposed to trapping the ion affects the clock performance of the ^{229}Th nucleus, as accurately described in [30]. In the crystal lattice, the atoms are in the Lamb-Dicke regime: The recoil energy from the isomer decay $E_{recoil} = E^2/(2Mc^2) = 1.5{\cdot}10^{-11}$ eV is much smaller than the energy needed to create a phonon in CaF_2 ($\approx$ 2.5 meV). A first order Doppler shift is thus excluded. The second order Doppler shift will broaden and shift the transition by several hundreds of Hz. Aside from Doppler shifts, the temperature dependent electron densities, surrounding nuclear magnetic moments, electric field gradients and structural changes in the surroundings will shift the isomer transition and cause inhomogeneous broadening decreasing the ultimate clock performance. The clock performance is still competitive with current optical atomic clocks [30], especially because of the large number of nuclei and thus worth the pursuit.

Our approach is to use CaF_2 crystals as host matrix. CaF_2 has a direct bandgap of approximately 11.8 eV [39]. The optical profile however is dominated by an indirect exciton excitation at 11.2 eV [40] which reduces the optical transmission window to about 9.8 eV at room temperature. The bandgap is higher in energy than the ^{229m}Th excitation thus will be transparent to a nuclear photon emission and will prohibit internal conversion. Doping Th into CaF_2 will create defect states that reduce transparency [41]. However, these can possibly be used to interact with the nucleus through electron bridge processes [42]. As described above, the surrounding atoms will broaden the linewidth of the isomer excitation which will decrease clock performance. The extra broadening however will increase the excitation bandwidth and will increase the nuclear photon emission decay rate. Higher decay rates and broader linewidths will help to excite and detect the first photon emission of the ^{229}Th nucleus in the crystal environment. Currently, excitation of the ^{229}Th nucleus in a crystal is attempted through X-ray irradiation [43], VUV irradiation [37, 44], defect states [29], and nuclear decay: in particular uranium-233 decay [45] and actinium-229 decay [46]. These excitation methods of the ^{229}Th nucleus doped into CaF_2 crystals bring with it significant challenges:

Only x-ray irradiation and nuclear decay from uranium-233 have proven to produce excited nuclei, and these methods require large facilities and access to radioactive isotopes. Other methods described above have not proven effective yet. The coupling of the nucleus to VUV photons is weak because it is inversely proportional to the lifetime and the frequency of the excitation cubed. When using the Uranium-233 decay as an excitation source of the isomer in the crystal, the local alpha damage that it creates might reduce the optical transmission. Another challenge is that ^{229}Th is an artificial isotope, and very little of it is available [12]. Growing macroscopic crystals with significant doping needs milligrams of the isotope which aside from availability issues will also have an activity of several MBq.

Due to the inherent radioactivity and the high energy of the excitation radiation all methods mentioned above will damage the crystal [47, 48] and cause self reduction of the ion [49]. In self reduction the oxidation state of the dopant is changed through capturing of conduction band electrons generated by the radioactivity of the dopant. Self reduction might promote internal conversion, especially if the ion is neutralized. The self reduction and crystal damage, will reduce nuclear photon detection probability and increase the probability of internal conversion. Relaxation of defects and radioactivity will produce a photon background which will make any signal harder to measure. Lastly, internal conversion may inherently be the dominant decay path of the nuclear isomer. Cooling the crystals might reduce non-radiative relaxation as is seen in atomic fluorescence in crystals [50, 51].

The three nuclear excitation approaches; nuclear reaction, x-ray excitation and VUV photon excitation, are complimentary as the excitation radiation is in three energy ranges (respectively MeV, keV and eV). These different energies will allow different processes to take place in both the nucleus and the host crystal. The timescales and intensities of irradiation of the crystal will affect the viability of the approaches as well: They damage the crystal. We take this multi-path approach to excite the nucleus in

CaF_2 to increase the chances of a successful experiment. We can summarize the above mentioned challenges into four points:

1. Growing highly doped CaF_2 crystals and creating a large number of excited ^{229}Th nuclei in them. For the doping enough dopant material needs to be obtained, all of the isotopes used are scarce. Growing macroscopic crystals with significant doping needs milligrams of an isotope which usually are highly active (MBq).
2. Prohibiting internal conversion as decay process. Measuring electrons in a crystal is much harder than photons. Internal conversion may inherently be the dominant decay path of the nuclear isomer, cooling the crystals might reduce non-radiative decay as is seen in atomic fluorescence in crystals [50, 51].
3. Preventing damage to the crystal due to high energy irradiation [47, 48], which reduces any signal to noise ratio and increases the probability of internal conversion.
4. Characterize the luminescence of the crystal which is produced through relaxation of defects and radioactivity. The produced background will make a nuclear photon emission signal harder to measure.

These challenges and more will be addressed in this thesis. The challenge of growing crystals will be tackled in its own chapters: Literature studies, experimental crystal growing and crystal characterization (2, 3 & 4). The thesis is structured such that challenges 2-4 are discussed in one chapter per approach, for which literature search and characterization experiments were performed (5, 6 & 7). Every one of these chapters ends with a viability study using the experimental characterizations. The experiments performed in this thesis are very diverse and are thus bunched to avoid confusion. A summarizing conclusion will connect the results of the experiments together and look at the challenges named above, while an outlook is given with suggestions for future experiments.

Chapter 2 will detail the current state of knowledge on CaF_2, doping of Th in CaF_2 and how radiation affects the crystal. By studying the crystal theoretically it can be assessed if the growth of Th:CaF_2 is worthwhile. Firstly, it covers the calculated effect of Th on the bandgap of the crystal, the known defects in undoped CaF_2 and the defects the Th doping creates. Secondly, the effects of irradiation (α, β and photons) on (doped) CaF_2 is studied: Crystal damaging processes and Cherenkov radiation more specifically. Lastly the luminescence processes known in (doped) CaF_2 are detailed.

Chapter 3 focuses on the crystal growing. It begins with a study on the methods employed in growing large (doped) single CaF_2 crystals: approaches, phase diagram and health considerations. Afterwards it continues to show the chemistry to produce the thorium powder and the devices used in this thesis to grow, cut, and polish the ^{229}Th:CaF$_2$. The final result is a table with all the produced crystals.

Chapter 4 describes all the built and used experimental setups for crystal characterization. This involves the VUV spectroscopy instruments used, the transmission/absorption setups and the luminescence detection setups. This chapter contains many experimental calibrations, possibly useful to the reader. Also many designs and design flaws are presented. The setups are also provided with their theoretical efficiencies, and where possible, experimental efficiencies. The results of the crystal characterization are presented here: Absorption measurements, luminescence measurements and some AFM, electron microscope and NAA measurements. Also in this chapter, first results of a possible charge transfer defect state in Th:CaF$_2$ are presented and the effects of fluoride (F$^-$) deficiency/enrichment.

Chapter 5 covers the experiments carried out to learn more about directly exciting the ^{229}Th nucleus in CaF$_2$ with VUV photons. First the viability from a theoretical standpoint is evaluated, after which the unknowns in this viability analysis are characterized. The setups built for this purpose are detailed and their results presented. The effect of VUV irradiation damage is quantified together with schemes to mitigate this damage. The VUV irradiation luminescence background is characterized and a possible defect state of Th:CaF$_2$ is presented here.

Chapter 6 studies exciting the ^{229}Th nucleus using nuclear decay processes. The isomer can be excited through decay of ^{233}U and by neutron capture of ^{228}Ra both doped in CaF$_2$. Viability studies on both methods to measure the photon emission of ^{229m}Th are presented. To characterize the unknown parameters in the neutron capture method, undoped CaF$_2$ crystals were activated in the Atominstitut nuclear reactor to study the damage done to the crystals and the VUV background created after neutron capture. The setups and results of this study show that this approach is very likely to succeed.

Chapter 7 shows the performed experiments to excite the ^{229}Th nucleus using x-rays through nuclear resonant scattering in the SPring-8 synchrotron. First, a viability study of this method is presented. Afterwards the experimental setups used to measure the isomeric photonic decay are described. The damaging effects of x-rays are studied together with the x-ray induced background. This chapter ends with a discussion on the viability of the experiment while looking at the knowledge gained during many beam times.

Lastly Chapter 8 summarizes the work, addresses the above challenges and makes suggestions for new experiments and research directions. I hope the reader enjoys this thesis, and hope that it provides her or him with useful information.

Chapter 2

Theoretical Investigation of (^{229}Th:)CaF_2 Crystals

Growth of Th doped CaF_2, or Th:CaF_2, is usually of little interest as scintillator or laser crystal because the 4+ oxidation state of Th makes it optically inactive (radon configuration). This is precisely why it is the perfect oxidation state for nuclear optical clock operation: no other absorption around the isomer energy should be present in the ion, which could decrease clock performance. Although of little optical interest, Th doped CaF_2 has been grown for electrical relaxation and electron beam damage research [52–54]. In nature, thorium is actually an often seen dopant of CaF_2 due to its natural occurrence, albeit in low concentrations [55].

Before any crystal is grown, it is important to study the incorporation of the dopant in the lattice and the effect of the dopant on the electronic band structure 2.1. When doping a crystal, there is a possibility it expels the dopant rather than incorporating it. By studying the ionic radii of the involved ions one can estimate if the dopant is incorporated. Aside from incorporation, if the bandgap of the crystal reduces heavily due to doping, the nuclear state cannot be addressed by VUV photons and an optical clock cannot function. The probability of internal conversion of the nucleus will also be reduced when the bandgap is large. Doping CaF_2 with Th, regardless of isotope, will thus affect the electronic band structure and will produce new defect states. A defect state is an imperfection in the crystal, a displacement or variation of an ion in the perfect CaF_2 fluorite lattice. All known and calculated defects in (Th:)CaF_2 are detailed in the following. If the bandgap is not significantly affected, growth can be attempted.

After the crystal is grown, the radioactivity and thorium doping affect the crystal differently. Radioactivity induces fluorescence inherent to the CaF_2 crystal and Cherenkov radiation. The violent α-decays will produce many defect centers, therefore all known created defects in pure and doped CaF$_2$ are detailed in the following.

Information on the effects of a radioactive agent doped into a crystal is scarce, and will be tackled in this thesis both in literature search and characterization experiments. The daughters of the radioactive decay will over time increase, and will contaminate the crystal possibly reducing transmission or showing up in crystal luminescence. Many contaminants can also enter the crystal before, during and after the growth through chemical processes. A table is provided with known fluorescence of pure CaF$_2$ and of contaminants in the CaF$_2$ crystal. This can be useful to distinguish a possible nuclear signal from others spectral features in future experiments.

2.1 Effect of Th Doping on the Electronic Band Structure

The theoretical effect of doping thorium into CaF$_2$ was explored theoretically to see if developing the growth process would be worthwhile. Undoped CaF$_2$ crystals have a direct excitation bandgap of 11.8 eV [39]. The absorption of this material close to the bandgap is however dominated by a broad indirect exciton (electron hole pair) excitation at 11.2 eV [40] which reduces the VUV transmission to $\approx$ 9.8 eV.

The high energy absorption of CaF$_2$ is higher in energy than the $\approx$8 eV nuclear excitation of ^{229}Th and thus non-radiative quenching of the nuclear excitation to a crystal excitation should be heavily suppressed. The larger density of states in the solid as opposed to vacuum will however decrease the lifetime of the nuclear excitation by the refractive index cubed, resulting in an approximately four times reduction in lifetime ($n_{\mathrm{CaF_2}}(150\,\mathrm{nm})^3 \approx 4$) [4, 56].

The effects of thorium doping into CaF$_2$ are first analyzed in section 2.1.1 based on the chemistry and ionic radius of thorium to identify possible configurations of thorium in CaF$_2$. In section 2.1.2 doping Th in CaF$_2$ has been numerically evaluated by using density functional theory (DFT) using the configurations evaluated in the previous section using the results in [57].

2.1.1 Thorium Configuration in CaF$_2$

The undoped CaF$_2$ has a cubic crystal structure called the fluorite structure. Effectively, it is a BCC lattice with a Ca^{2+} ion in the center of every other cube. A schematic representation can be seen in figure 2.1 or 2.6.

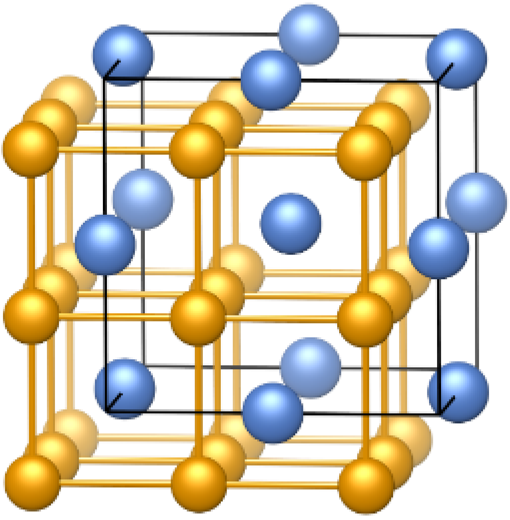

FIGURE 2.1: Schematic representation of the CaF_2 lattice. The yellow spheres are F^- and the blue spheres are Ca^{2+}. Taken from [57].

The Ca^{2+} cation has a coordination number of 8, surrounded by 8 F^-. The F^- anion has a coordination number of 4, surrounded by 4 Ca^{2+}. The coordination number in a crystal is the amount of nearest neighbors. When thorium is doped into this crystal, it will locally distort the lattice but should ideally not change the electronic properties. Changes in electron excited states could open up states that can quench the nuclear excited state.

Due to the high electropositivity of thorium of 1.3 Pauling it is expected that it will take its most common oxidation state of 4+ when doped into CaF_2. It is most probable that thorium substitutes the calcium in the crystal since both are positively charged. The excess charge of the Th^{4+} ion will be compensated for in the crystal, so called charge compensation. To determine the position and oxidation state of thorium in CaF_2, and the charge compensation mechanism, one can numerically calculate the most favorable positions of atoms by using DFT calculations for each conceivable dopant location and charge compensation. DFT calculations are discussed in section 2.1. To not calculate every location and charge compensation mechanism, a selection can be made by looking at ionic radii.

In 1969 Shannon [58] collected and categorized data on interatomic distances in oxide and fluoride crystals. It was shown that this data can be used to calculate an "effective" ionic radius, independent of crystal structure, for an element. This ionic radius shows clear trends depending on oxidation state and coordination number and can thus be used to predict the interatomic distance for new compounds and the possibility of mixing compounds.

This categorized data is valuable for synthesis, but also for doping. The effective ionic radius allows to model the crystal as a collection of hard spheres. This means that if one wants to dope an element into a crystal, if the sphere fits, the probability is high this new configuration will work. The size of the sphere depends mainly on oxidation state and coordination number, but electronic spin, covalency, repulsive forces, and polyhedral distortion needs to be taken into account as well to a lesser degree.

To apply this theory to thorium doping into CaF$_2$, we need to consider the possible oxidation states and corresponding charge compensation which gives its coordination number. Charge compensation is the process of inducing defects to compensate for the charge difference of cation (Ca^{2+}) and dopant (Th^{4+}). Here we assume that Th^{4+} will substitute Ca^{2+} in the lattice, which is more likely than substituting F^{-}. The charge compensation happens naturally because it is the energetically most favorable state. We will consider the most common oxidation state of thorium as 4+, but will also look at a less common oxidation state 3+, as this oxidation state is sometimes observed in anion (fluoride or F^{-}) deficient crystals [59].

Substitutional Th^{4+} will need two extra compensation negative charges surrounding it in the lattice due to its higher charge as compared to Ca^{2+}. The two negative charges can be provided in numerous ways such as: two extra fluoride interstitials, a calcium vacancy, an oxygen interstitial, two oxygen substitutes for fluoride, two sodium substitutes for calcium or two free electron interstitials. The different charge compensations will lead to different coordination numbers of the thorium, respectively: 10, 9, 8, 8, 8, 8. The ionic radius of Th^{4+} with a coordination number of 10 is 1.13 Å, 9 is 1.09 Å and 8 is 1.05 Å. The ionic radius of Ca^{2+} with a coordination number of 8 is 1.12 Å [60]. The ionic radius that most matches that of Ca^{2+} will be the most likely charge compensation mechanism.

From the above numbers it is expected that two interstitial fluorides is the most likely charge compensation and the thorium will be well incorporated. An oxygen interstitial seems a strong possibility as well. These charge compensations were theoretically evaluated in [57] and the most likely compensation was found to be two fluoride interstitials under a 90° orientation or a calcium vacancy next to the thorium dopant if no contaminants are present. Sodium substitutions or oxygen substitutions might be just as likely if present in the crystal growth.

Substitutional Th^{3+} will need one extra compensation negative charge surrounding it in the lattice due to its higher charge as compared to Ca^{2+}. The possibilities for this are: one fluoride interstitial, one oxygen substitution for fluoride, one sodium substitute or one electron interstitial. The corresponding coordination numbers for thorium are: 9, 8, 8, 8. The ionic radius of Th^{3+} has not been measured thus we need to infer it from the relation to other species.

From [61] we can find the ionic radius of Th^{3+} with coordination number 6 to be 1.042 Å. Using the figures in [60] and comparing thorium to cerium, a chemically equivalent element, we can derive an ionic radius of 1.10 Å for coordination number 7, of 1.17 Å for coordination number 8 and 1.20 Å for coordination number 9. From this it is most likely that the Th^{3+} will have a low coordination number, 7 or 8. Most ideal would be a calcium plus a fluoride vacancy which would create a coordination number of 7. Less ideal is an oxygen substitution or sodium substitution. In a fluoride deficient crystal removing CaF seems likely such that the the overall fluoride deficiency decreases in the CaF$_2$ crystal.

2.1.2 DFT Calculation

The electronic properties of CaF$_2$ doped with thorium can be calculated using Density Functional Theory (DFT). DFT came out of the theory of [62] and was further developed by [63]. A more intuitive explanation can be found in [64] which draws parallels to statistical physics to explain DFT which we follow:

In statistical physics, one can set up the grand canonical potential of N particles in a volume V with temperature T and chemical potential μ to be $\Omega[\mu, T, V]$. From the grand canonical potential we can derive the characteristics of the system. To apply this technique to an electron gas with N electrons in a solid-state system we have to make some modifications. The system is now not contained in a volume V but an external potential $v(\mathbf{r})$. The temperature in DFT calculations is assumed to be 0 K, so not taken into account. Since the potential $v(\mathbf{r})$ is measured from an arbitrary origin we can redefine it such that we set the chemical potential as the origin, effectively setting $\mu = 0$ or redefining the potential as $v(\mathbf{r}) - \mu$. We are now left with the grand potential only dependent on the externally applied potential.

We now define a new free energy F which is explicitly dependent on the electron density $n(\mathbf{r})$. This free energy is a functional Legendre transform of the grand potential. By minimizing this free energy, the ideal electron density is found, and with it the correct potential $v(\mathbf{r})$

$$F[n(\mathbf{r})] = \Omega[v(\mathbf{r})] - \int n(\mathbf{r})v(\mathbf{r})d\mathbf{r}, \tag{2.1}$$

which is called the Hohenberg-Kohn free energy. Equation 2.1 is basically the total energy minus the potential or internal energy of the electron system. The free energy has the unique property that when it is minimized for $n(\mathbf{r})$ at constant $v(\mathbf{r})$ the relation

$$\frac{dF}{dn(\mathbf{r})} = -v(\mathbf{r}), \tag{2.2}$$

holds. The fact that a free energy as a function of $n(\mathbf{r})$ exists with this property which is similar to the properties of the grand potential is central to DFT and one of the theorems in [62]. For electrons this free energy, which is the total energy minus the potential energy, is defined as

$$F[n(\mathbf{r})] = F_{ni}[n(\mathbf{r})] + E_{es}[n(\mathbf{r})] + E_{xc}[n(\mathbf{r})]. \tag{2.3}$$

Here $F_{ni}[n(\mathbf{r})]$ is the non-interacting kinetic energy of the electrons,

$$E_{es}[n(\mathbf{r})] = \frac{e^2}{2} \int \frac{dr dr'}{|r - r'|} n(r) n(r'), \tag{2.4}$$

the electrostatic energy, e the fundamental charge and $E_{xc}[n(\mathbf{r})]$ the exchange correlation energy, basically the remaining undefined terms. The big step forward for numerical computation was done by Kohn and Shamm [63]. They introduced the effective potential v_{eff}. The effective potential for non-interacting particles can be constructed from equations 2.2 and 2.3. When the free energy is evaluated at its minimum for constant v($\mathbf{r}$) and the derivative with respect to particle density is taken we can construct

$$v_{eff}(\boldsymbol{r}) = v(\boldsymbol{r}) - e\phi(\boldsymbol{r}) + v_{xc}(\boldsymbol{r}). \tag{2.5}$$

by rearranging the terms. Where $v_{xc}(\boldsymbol{r})$ is the potential due to exchange correlations and is defined as

$$v_{xc}(\boldsymbol{r}) = \frac{\delta E}{\delta n(\boldsymbol{r})}. \tag{2.6}$$

and

$$\phi(\boldsymbol{r}) = -e \int \frac{n(\boldsymbol{r}')}{|\boldsymbol{r} - \boldsymbol{r}'|} d\boldsymbol{r}'. \tag{2.7}$$

The effective potential can now be used to evaluate the Schrödinger equation for non-interaction particles

$$\left[-\frac{\hbar^2}{2m}\nabla^2 + v_{eff}(\boldsymbol{r})\right]\psi_i(\boldsymbol{r}) = \epsilon_i\psi_i(\boldsymbol{r}) \tag{2.8}$$

and the resulting wave functions of the electrons $\psi_i(\mathbf{r})$ with corresponding energies ϵ_i can be used to compute the electron density

$$n(\boldsymbol{r}) = \sum_{i=1}^{N} |\psi_i(\boldsymbol{r})|^2. \tag{2.9}$$

Now the the system is solved self consistently for $v_{eff}(\mathbf{r})$ and $n(\mathbf{r})$. Once the electron density is computed it can be used again to find the effective potential (only dependent on ion positions and electron density), which can then be used to solve the Schrödinger equation to again find the electron density. Every step the total energy can computed in order to validate it is minimized. Once convergent, the resulting states and their energies can be used to compute the density of states (DOS) and from that the bandgap of the CaF$_2$ doped with thorium (figure 2.3).

The choice of exchange correlation potential influences the outcome of these calculations greatly and is adapted for each system DFT is used on. This thus goes into the finer details of using DFT. Examples are atoms, nuclei, molecules, crystals and much more. Choices of exchange correlation potential for our system were varied and can be found in [57]. For more reading: a general introduction [64] and more in-depth discussions [65, 66].

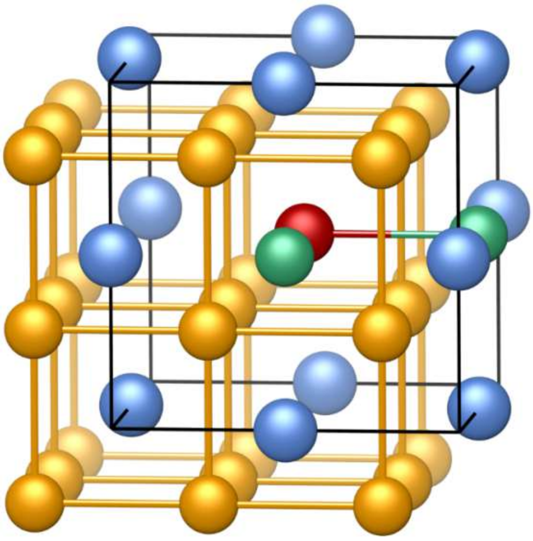

FIGURE 2.2: Schematic representation of the most favorable charge compensation mechanism of the CaF$_2$ lattice doped with Th. The yellow spheres are lattice F$^-$, the green spheres are interstitial F$^-$, the blue spheres are Ca^{2+} and the red sphere is Th^{4+}. Taken from [57].

In [57] all probable configurations of thorium doping were considered and it was found that charge compensation with two interstitial fluorides under an angle of 90° is the ground state of CaF$_2$ doped with thorium (see figure 2.2). In reality, all compensation configurations will exist. There will be enough thermal energy, Boltzmann distributed, to accordingly produce a certain population of each compensation mechanism. Different oxidation states of thorium can in this case also exist alongside the ground state compensation configuration. The two fluoride compensation agrees well with the ionic radius argument where the most ideal situation is Th^{4+} with a coordination number of 10.

When looking at the density of states (DOS) (figure 2.3) of this compensation mechanism one can see that there are some defect states near the bandgap edge around 8.5 eV caused by the doping. This defect state or Charge Transfer State (CTS) is an excitation that moves an electron bound to a fluoride atom into an excited state that is more localized on the thorium atom. This excitation thus is high in energy and in momentum due to the large displacement. This CTS is spatially close to the thorium atom. This opens up possibilities to quench or excite the nucleus if their energies are close enough. Possibly this defect center can be used to excite the isomer, as discussed in the section 2.3.1.

The conclusion is that thorium will most likely be incorporated in the CaF$_2$ crystal lattice as a substitution of Ca^{2+}, and will have two interstitial fluorides as compensation for its excess charge. This will not affect the bandgap of the crystal significantly which will thus remain transparent to VUV photons. A color center will be created by doping thorium which needs further investigation.

2.2 Defects in Undoped CaF$_2$

Although thorium doping will affect the crystal structure and possibly create new defects, the doping concentrations studied in this thesis are only up to 1 %. Since 99 % of the crystal is still CaF$_2$ an accurate study of the defects in undoped CaF$_2$ are invaluable to understand the dynamics inside the crystal.

Studies on defects of crystals with fluorite structure and thus CaF$_2$ are numerous [67–69]. Due to this, much is known about CaF$_2$ defect structures. However many topics still are not well understood. For example: cluster forming of interstitial and vacancies, surface effects, colloid bands and anion excess/deficiency are open topics. The basis of point defects, larger structures and other known effects in CaF$_2$ will be shortly described here for undoped CaF$_2$ which follows the description by Hayes [67, 69].

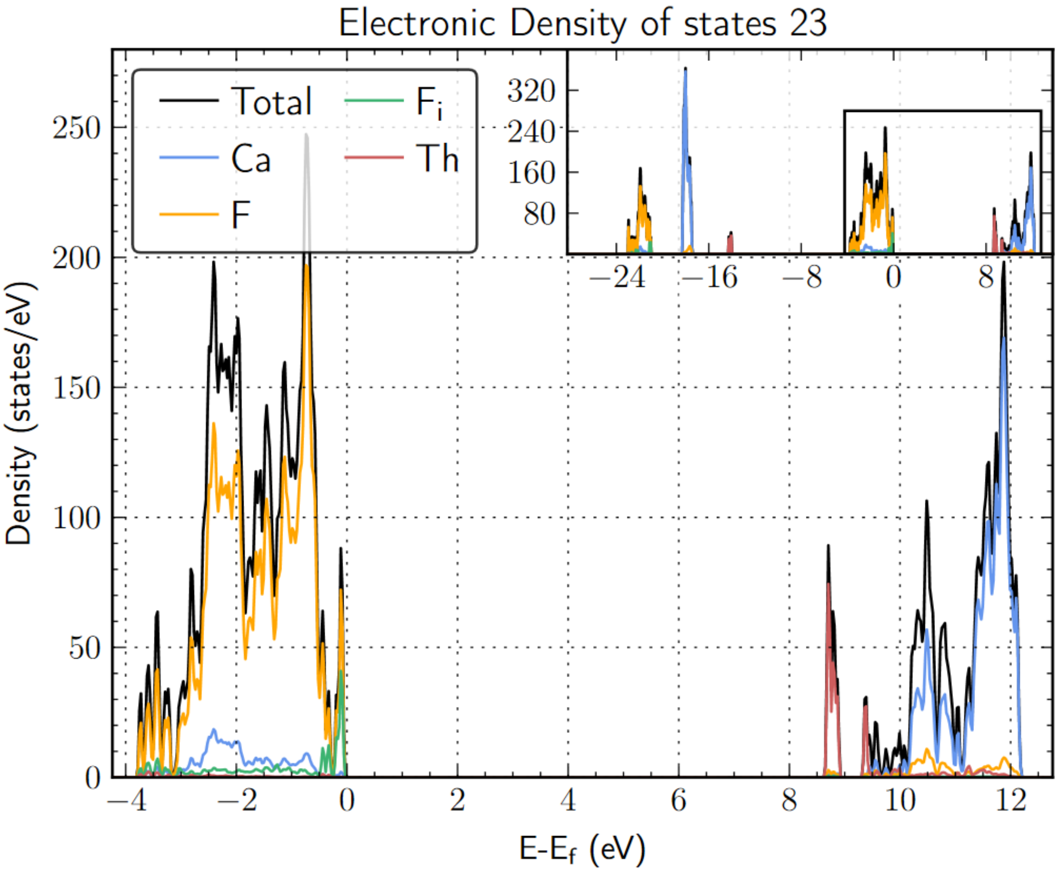

FIGURE 2.3: Density of states versus energy of the state. We can see that the interstitial fluorides and the thorium do not significantly affect the size of the bandgap which for undoped CaF$_2$ calculated by the same method was 8.6 eV.

2.2.1 Frenkel Defect System

In general, there are two types of point defect systems: Frenkel and Schottky defect systems. A point defect is a imperfection in the crystal lattice the size of one atom. In the Schottky defect system, the crystal lattice is very densely packed. Because of this, no interstitials can exist and only vacancies occur in the crystal as defects. Other types of defects can exist though on surfaces and at impurity sites. In Schottky ionic crystals charge compensation of a defect happens by having equal amounts of vacancies of either the cations or anions. In crystals of neutral species no charge compensation is needed for a vacancy.

Frenkel defect systems have both vacancies and interstitials of the same species. In CaF$_2$ the defect mechanics are dominated by negatively charged F$^-$ interstitials and positively charged F$^-$ vacancies, thus is a Frenkel type system. The CaF$_2$ defect system is dominated by fluoride movement because the fluoride ions can move through the crystal expending much less energy (0.6-1.5 eV) than the calcium ions. Also, the energy needed to form a anion Frenkel pair (F$^-$ interstitial and vacancy) is only 2.7 eV, but to form a cation Frenkel pair is more than 6 eV.

The energy required to form a Schottky pair in CaF$_2$ (F and Ca vacancy) is 5 eV. This indicates that in almost all normal circumstances producing anion defects is preferred, and the cation defects are of very minor importance. We now go more into detail of the anion defects in CaF$_2$.

2.2.2 F Center

The F center is one of the most studied defects in ionic crystals. The name comes from the German "Farbezentrum" meaning color center. Essentially, the F center is an electron trapped in an anion vacancy, in the case of CaF$_2$ a missing fluoride. This "electron in a box potential" has excited states quite isolated from the crystal and can be optically active, hence the name. There is no relation between the term "F" center and the resulting "F" vacancy in CaF$_2$, only confusion.

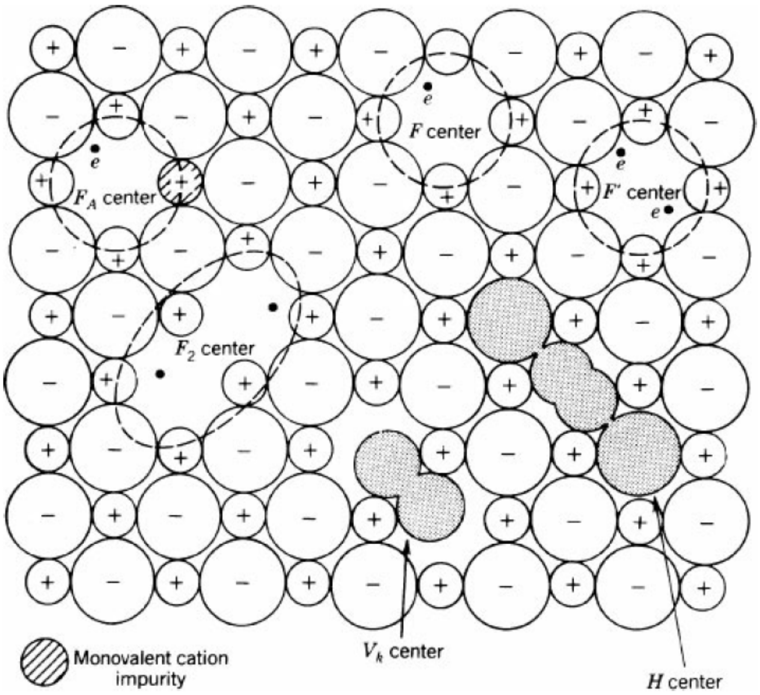

Figure 2.4: Common defects in an ionic crystal (F, F$_A$, F$_2$, F', V$_k$ and H center), the cubic lattice of for example NaCl was taken here. The F$_2$ center is not an F$_2$ molecule. The V$_k$ and H center however are akin to a F$_2^-$ molecule. Taken from [69]

In figure 2.4 the F center is schematically drawn. It is effectively an electron in a 3D box potential, similar to a hydrogen atom. The three dimensional potential well or box is created due to the surrounding charges: A F$^-$ used to occupy this space so the crystal dictates that a negative charge is most ideal there. Due to this similarity, the orbitals of this trapped electron can be labeled similarly [67].

When this electron gets excited from the 1s to the 2p state it will be according to the Franck-Condon principle without movement of the surrounding ions. The electron can respond much faster. After that the lattice will relax and adapt to this new situation bringing the F center in a state 2p*. This state will then decay to the ground state, usually with a Stokes shift (energy difference) such that the decay is of lower energy then the excitation due to the relaxation of the lattice. The F center is usually spectrally broad, about 0.2 eV FWHM due to the surroundings and relaxation of the lattice. It can very much be affected by electronic and magnetic fields.

Due to its broad excitation and similarity to hydrogen states it has several bands: The F, K, and L bands. The absorption of the K and L bands is weaker (usually 10 % and 1 % of the F band) and increases the photoconductivity of the sample. The K and L bands absorption promotes electrons to the conduction band or similarly, ionizes the F center electron to the continuum (conduction band). The lifetime of the excited states is usually $\approx \mu s$ due to mixing of $2p*$ and $2s*$ states after relaxation. The mixing increases lifetime as compared to a more hydrogen like state. The F band of the F center in CaF$_2$, absorbs at 378 nm (3.28 eV) central wavelength [70]. Emission of the F center has been observed at 585 nm (2.12 eV) in undoped CaF$_2$ and 775 nm (1.6 eV) in Na doped CaF$_2$ [71].

The probability of an F center moving, or its mobility, is described by an energy barrier ΔE_F and the thermal energy distribution of the crystal. The energy barrier has been calculated to be between 0.9 eV and 1.5 eV [47] depending on the relaxation of the lattice. The rate of F centers moving ν_F can then be approximated by

$$\nu_F(T) = \nu_0(T) e^{-\frac{\Delta E_F}{k_B T}}, \tag{2.10}$$

where $\nu_0 = \frac{k_b T(RT)}{h} \approx 5 \cdot 10^{12}$ Hz is the frequency of lattice vibrations, k_B the Boltzmann constant and T ($T(RT)$) the temperature (Room Temperature). Now one can calculate that $\nu_F(300K) \approx 1$ mHz and $\nu_F(1273K) \approx 3$ GHz, showing that F center mobility is low at room temperature, and fast at high temperatures which is the basis of crystal annealing. For example: A CaF$_2$ crystal has an equal high density (10^{16} cm^{-3}) of F and H defects (see section 2.2.5). For now it is sufficient to know that these point defects annihilate if they come in contact (see figure 2.4). If equally spaced, the distance of one F center to one H center is approximately $(10^{22}/10^{16})^{-1/3} = 100$ lattice sites. At 300 K it would take them a minimum of 50000 seconds or 14 hours to reach one another, compared to 16 ns at 1300 K. In reality, the random motion of the defects will increase the time until the defects pair and annihilate. To remove all defects, room temperature annealing might take months. Annealing CaF$_2$ crystals to at least 500 °C can completely return it to its original state [47, 72, 73].

There are also several variations of F centers. The F$_A$ center is an F center adjacent to an impurity (see figure 2.4). No characterization of F$_A$ centers of Th:CaF$_2$ could be found. Cerium doped CaF$_2$, electronically similar to Thorium doping, has an F$_A$ absorption around 400 nm (3.1 eV) which can be seen in [74]. In for example U^{3+} doped CaF$_2$ the absorption band shifts to 406 nm (3.05 eV) [75]. Another variation is the F' center, which contains two electrons instead of one. At low temperatures (<100 K) the F' center is stable. It often has a broad absorption band lower in energy than the F center, extending into the visible range [69]. An F center that is ionized, or lost its electron, is called an α center. This is then a pure fluoride vacancy. The absorption of the α center usually lies lower in energy than the F center absorption. Since there is nothing in the defect that can be excited it is still unclear what is excited. It is assumed that this absorption is caused by the creation of a perturbed electron hole pair, an exciton.

It is common that two or more F centers are next to one another, called M (2), R (3) and N (4) centers. The M center has absorption bands at 520 nm (2.4 eV) and 365 nm (3.4 eV), it emits at 600 nm (2.0 eV) [76]. The R center has an absorption band at 665 nm (1.86 eV) [67]. This 600 nm orange emission is what colors CaF$_2$ crystals orange (see for example figure 3.21 or 6.14). The M/R/N centers are stable in CaF$_2$ because the metallic Ca lattice has approximately the same spacing/lattice constant as CaF$_2$, which is the case for many alkali earth fluorides. When even more F centers agglomerate, metallic colloidal particles can be formed which have very different properties. The M and R centers can show extremely narrow spectral absorption lines at 20 K. At these low temperatures absorption of these centers can happen without interacting with phonons, which narrows the line. These so called Zero Phonon Lines (ZPL) are analogues to the Mössbauer effect of nuclei: recoil free emission and absorption of photons.

Combinations of these centers with different impurities in both anion and cation position can make it extremely difficult to assign absorption bands and to predict defect behavior in CaF$_2$. For example due to annealing, F$_A$ centers will form more stable M$_A$ centers in Na:CaF$_2$ crystals [77]. This same process can also change the oxidation state of the involved impurity as happens in U:CaF$_2$ [78]. The interaction with F centers can also change the oxidation state when different concentrations of F centers are produced as a consequence of the growing process [79]. These are only the dynamics involving F centers which are studied the most intensively. In the end more defect centers are involved but the complexity of the interactions makes the study of the complete process increasingly difficult.

2.2.3 Ca Colloid

When enough F centers agglomerate, one can go beyond N centers and form larger clusters. These centers are highly stable [47] and usually form when the crystal is irradiated with high energy radiation or when F center rich crystals are annealed. In these clusters, the electrons in the F vacancies are taken up by the Ca ions and neutral metallic colloids are formed $2e^- + Ca^{2+} \rightarrow Ca$. The formation of colloids is present in many ionic crystals and has been extensively studied [80].

The growth of the colloids can be described by the General Nucleation Theory (GNT) describing the F centers as gas particles and the colloids as precipitates. The process is extremely slow at low temperatures, but at high temperatures F centers hop lattice sites more and two F centers can agglomerate to the lower energy state of an M center. This nucleus can attract more F centers due to its stability, and can grow to an R center, then N center and eventually a colloid. The sizes of these colloids can be up to $10\,\mu$m. They preferentially nucleate on dislocation lines, defects and grain boundaries which probably increases stability of the intermediate states between F center and colloid.

The colloids not only absorb but also scatter the light. By using Mie theory [81] the absorption and scattering of these particles can be calculated [47]. Important are the radius R of the particles, the plasma frequency ω_p of the particle, the pressure on the particle and the complex index of refraction n_0 of the surrounding material. The assumptions in Mie theory do not hold for particles larger than 10 nm or non-spherical particles. For very small particles ($R << 1$ nm, practically $5\,\text{nm} < R < 10\,\text{nm}$) a simple formula can be derived for the absorption maximum λ_m that does not take into account the pressure on the particle and assumes spherical particles:

$$\lambda_m = \frac{2\pi c}{\omega_p}(\epsilon_0 + 2n_0^2)^{1/2} \tag{2.11}$$

where ϵ_0 is the vacuum permittivity. We can now use this equation to see what effect doping thorium has on the absorption wavelength of Ca metal colloids. Naturally, doping thorium will change the refractive index of the material. Since ThF$_4$ has a higher refractive index (1.55 at 300 nm [82]) than CaF$_2$ (1.45 at 300 nm [56]), most likely doping thorium will increase the refractive index [83]. This will increase λ_m of the colloids. If any of the dopant ends up in the metal nanoparticles however, it will most likely increase the electron density (Th donates 4 electrons) and will increase ω_p thus decrease λ_m.

These two effects are competing thus it is hard to predict how the center absorption wavelength of Ca metal colloids will shift due to doping.

In figure 2.5 the absorption and scattering of Ca metal colloid particles is numerically calculated taking into account the full Mie equations for different particle sizes. The particles are assumed spherical, although there is evidence that they are not [84]. As is common for colloids, a higher order peak is visible. The main absorption center is around 550 nm (2.25 eV) and for the smaller higher order peak around 200 nm (6.0 eV). This has been experimentally verified [84]; it was observed that the size distribution very much shapes the absorption. The two spectral absorptions now vary from 550 nm to 960 nm and from 200 nm to 160 nm.

If the particles become very large, they are also not spherical anymore and thus the theoretical model used in [47] is not valid anymore. As a rule of thumb, the large peak tends to decrease in strength and moves towards higher wavelengths for larger particles, moving all the way into the infrared [84, 85]. The higher order peak seems to move towards lower wavelengths for larger particle sizes. The absorption of Ca metal colloids is what colors CaF$_2$ purple (see for example figure 7.14 or 4.55), the colloids absorb all the green colors out of the visible spectrum such that only deep blues and reds remain.

2.2.4 V$_\mathrm{k}$ Center

The V$_\mathrm{k}$ center is essentially a self trapped hole, which is drawn in figure 2.4 for alkali halides and in figure 2.6 for CaF$_2$. This self trapped hole binds together two anions into a molecule-in-a-crystal. In the case of CaF$_2$ this produces an F$_2^-$ molecule in a crystal. Spectroscopic observations show that the molecule-in-a-crystal model describes the defect well [69]. The absorption bands of the V$_\mathrm{k}$ center lie at 320 nm (3.87 eV) and 750 nm (1.65 eV) [86]. The defect is preferentially aligned along the (100) axis, but the axis can be changed by excitation with polarized light [67]. The activation energy for a 180° lattice site hop of a V$_\mathrm{k}$ center is 0.19 eV at 90 K and 0.31 eV at 120 K.

2.2.5 H Center

The H center is a hole trapped in between an interstitial anion and a lattice anion, see figure 2.4 for general and figure 2.6 for CaF$_2$ configuration. Since this defect is also similar to an F$_2^-$ molecule, it has very similar spectroscopic behavior as the V$_\mathrm{k}$ center, with a measured absorption band at 310 nm (4.00 eV) slightly shifted from the V$_\mathrm{k}$ center. It is however aligned along the (110) axis. The orientation of this center cannot be changed by excitation with polarized light. In CaF$_2$ when the crystal is

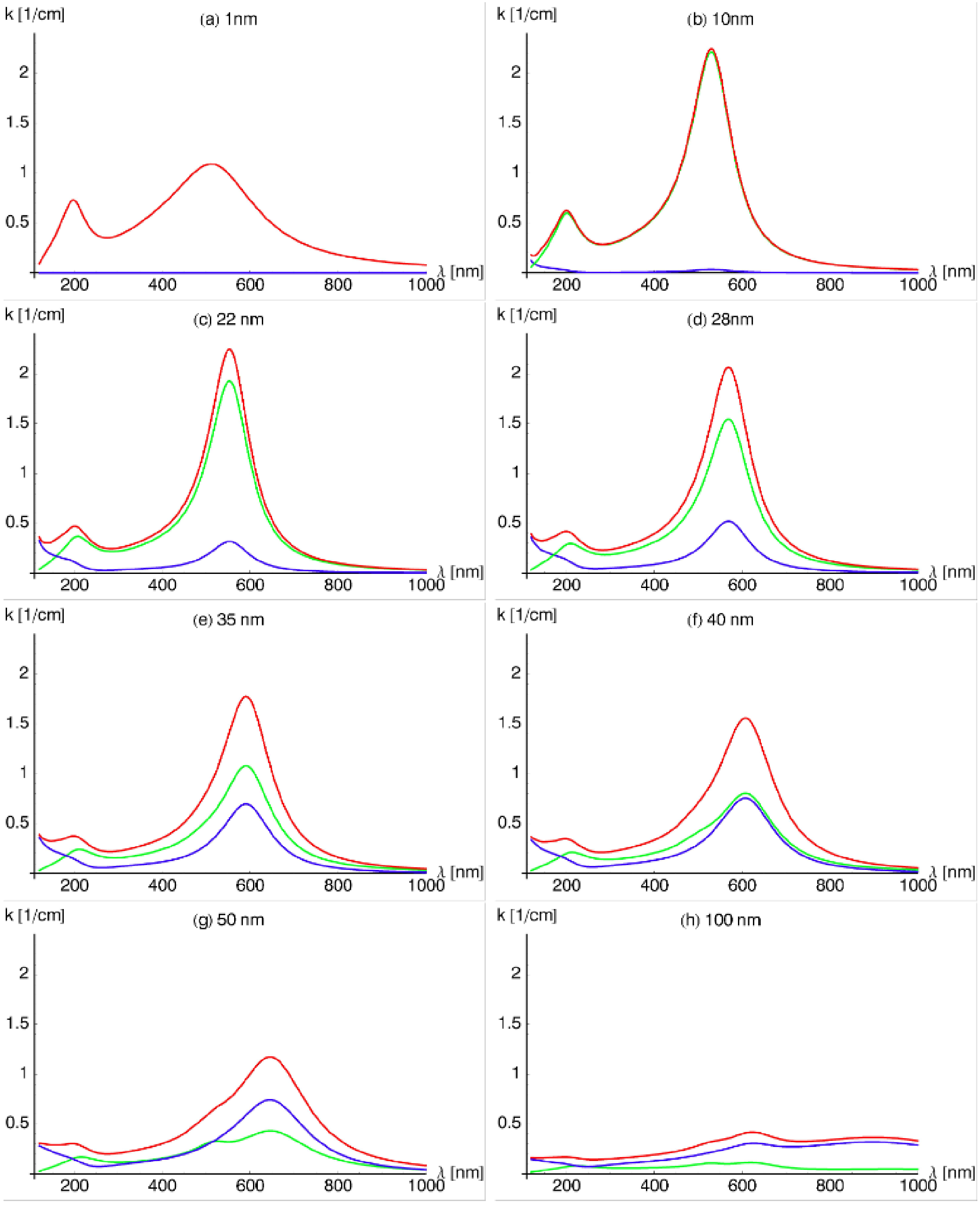

Figure 2.5: Extinction (red), absorption (green), and scattering (blue) of Ca colloids in CaF$_2$ calculated from Mie-theory for different colloid radii. For small colloids the extinction is dominated by absorption, larger colloids show stronger scattering and the total extinction decreases. Taken from [47].

annealed V_k centers produced are often partially healed and partially converted to H centers. The H center activation energy for a lattice hop is estimated to be 0.25 eV, similar to the V_k center.

2.2.6 Self Trapped Exciton

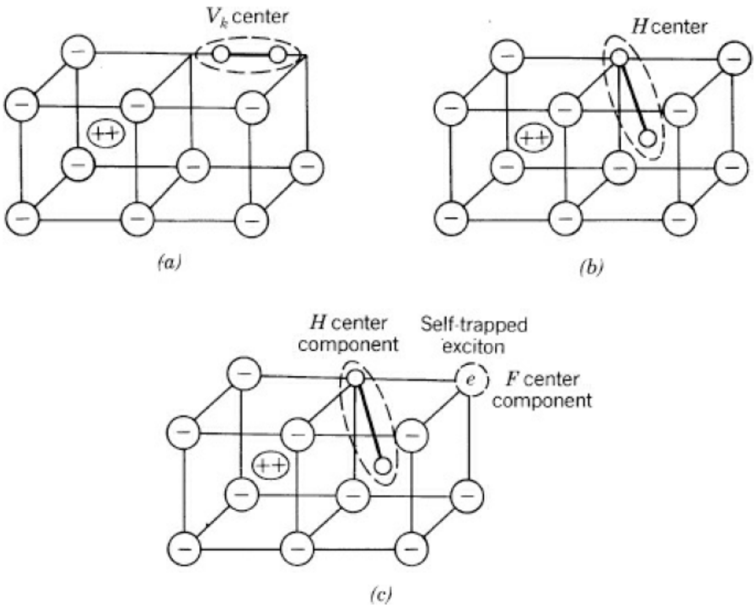

FIGURE 2.6: Schematic representation of (a) the self-trapped hole (V$_k$ center), (b) the H center, and (c) the self-trapped exciton in the fluorite structure. The STE is represented as a close F-H center pair. Taken from [69].

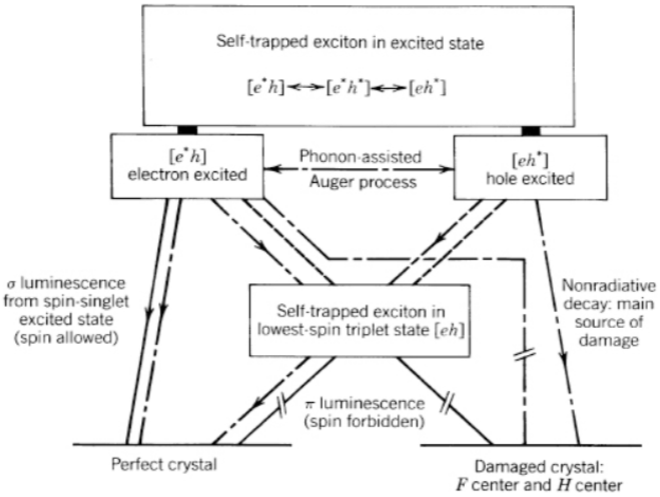

FIGURE 2.7: Different radiative and non-radiative decay paths of several different configurations of STEs. The solid lines are strong optical transitions, broken lines weak transitions, semi-broken/semi-solid are non-radiative decays and lines with a break are semi-forbidden or long-lived states. Taken from [69].

The self trapped exciton (STE) is a very well studied phenomenon [87]. The STE is essentially a bound state of a trapped hole and a bound electron, a [$V_k^+e^-$] or [h^+e^-]. Note that h indicates a hole, and not an H center. This defect can be in three distinct states, where one or both constituents are excited ([$h^{+*}e^-$],[h^+e^{-*}] and [$h^{+*}e^{-*}$]). This defect can effectively be described as a hydrogen atom with a different effective mass.

Also equivalent to an atom, the STE has many excited states that for example fluoresce in CaF$_2$ under VUV irradiation from 200 nm up until 500 nm [88].

In CaF$_2$ the formation energy of this defect is 11.18 eV, very close to the exciton formation energy at 12.2 eV. Upon formation, it is a V$_k$ center with a captured electron. It then quickly decays into a close proximity F-H pair [89]. The V$_k$ center, the H center and the close F-H pair are schematically drawn in figure 2.6. This close F-H pair has several different possible orientations within the lattice and several different decay paths, illustrated in figure 2.7.

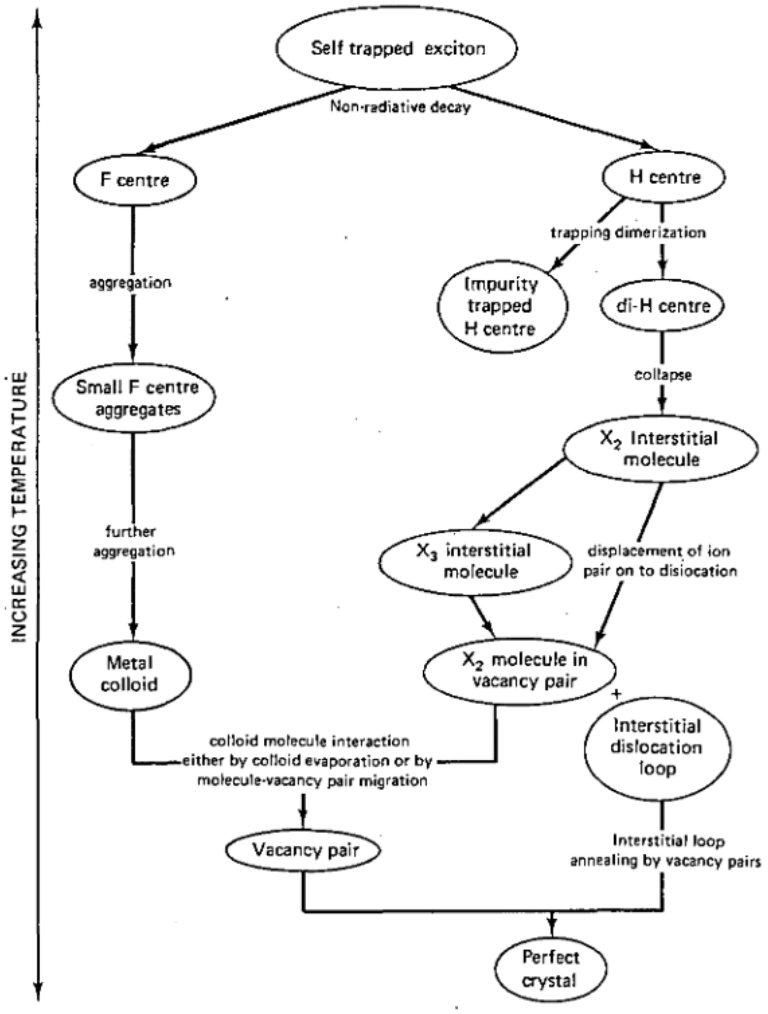

FIGURE 2.8: Steps in the process from STE to perfect crystal. The lower in the diagram the higher the temperature is needed to initiate the process. For example, at low temperatures only F and H centers are produced. At higher temperatures metal colloids and dislocation loops can be produced. Taken from [90].

The STE can swap between excited hole or excited electron by an Auger process. In this configuration the spin of the hole and electron is in a singlet configuration. These configurations will decay into one of three states: Firstly is return to perfect crystal under the emission of a σ polarized photon (polarization parallel to the H center orientation) or through a non-radiative process. The lifetime of this state is nanoseconds. Secondly, decay to the lowest triplet state (spin of hole and electron aligned) through a non-radiative process or weakly through photon emission. This state is long-lived, because all its options for decay are weak or semi-forbidden, the lifetime is μs. This state can decay to the perfect crystal under emission of a π polarized photon (polarization perpendicular to H center orientation) and through non-radiative decay. It can also decay under emission of a photon to a damage center, an F and H center pair. Third and last, the STE can decay non-radiatively to a damage center, an F and H center pair. The process of the creation of an STE via crystal damage to perfect crystal is schematically shown in figure 2.8

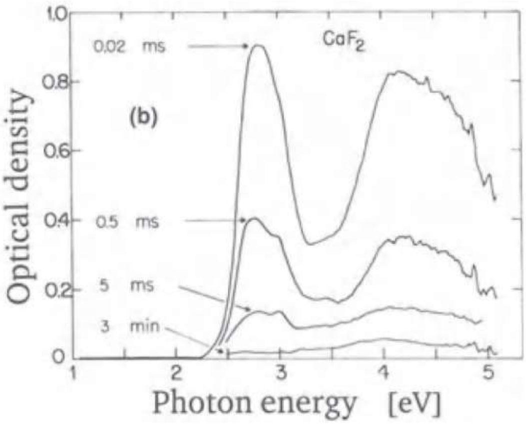

FIGURE 2.9: Optical absorption spectrum for CaF$_2$ shown for the indicated delays after irradiation by an electron pulse at T = 10 K. Taken from [87].

In this process, the F center and H center are split and no longer form a pair (and thus an STE). The split F and H can only heal by finding one another and annihilating again, a process which can be sped up under heating (annealing). The excited self trapped exciton can always decay non-radiatively, a process stimulated by the presence of phonons (higher temperatures) as can be seen in figure 2.7 and governed by the empirical equation [51] for the quantum efficiency (number of emitted photons per number of incident photons):

$$q(T) = \frac{1}{1 + Ce^{-\frac{E_q}{k_b T}}}, \tag{2.12}$$

where C is an empirical constant, E_q the quenching energy of the optically active center, k_B the Boltzmann constant and T the temperature. At high enough temperatures all STEs can decay non-radiatively. The quenching energy is the excited energy at which the STE state can spontaneously decay completely non-radiatively. The absorption spectrum of STEs in CaF$_2$ after an electron pulse to create them can be seen in figure 2.9.

2.2.7 Surface Defects

Aside from the bulk, the surface of CaF_2 can be host to many defects, which can affect absorption in a variety of ways. In [91] for the first time, bulk and surface absorption of undoped CaF_2 were separated. The defects on the surface enable absorption which is not seen in the bulk. F centers on the surface seem to attract oxides, hydroxides, and H_2O which can create intermediate states that increase absorption. The lower wavelengths are more sensitive to defects on the surface, even having a nonzero two-photon surface absorption. For all VUV wavelengths, the surface absorption dominates over bulk for crystals up to 6 mm in thickness [91].

In [91] an exponential relationship was discovered between polishing quality and surface absorption. A surface roughness of 0.2 nm reduces surface absorption to a minimum. This effect can be explained; the roughness increases the amount of kink and edge dislocations which have higher binding energies [92]. The absorption of these surface defects leads to surface luminescence for bad surface quality at 4.4 eV (STE) and 2.55 eV (surface oxygen center) [93].

It is shown that freshly cleaved CaF_2 has the least absorption and luminescence. After some aging, both increase. CaF_2 left in air with 100 % humidity forms a 30 to 40 Å film of water after an hour [94]. After polishing a cleaved surface, the absorption seemingly increases in [93] but possibly a better surface quality after polishing would exponentially decrease, as suggested by [91]. A special heat treatment can be employed to completely remove these surface effects due to aging [72]. Annealing CaF_2 in a dry atmosphere at 500 °C for as long as possible should guarantee best results, at 600 °C if done for no more than 15 minutes. At higher temperatures the CaF_2 will start reacting with the oxygen in the air. Other liquids than water can also readily be adsorbed into the surface and create absorption [95].

It has been suggested that CaF_2 has a surface dead layer, where the surface luminescence is inefficient. This means that the electron-hole pair can be excited at lower energies, but will most likely decay non-radiatively. It was further investigated that any optical finish will create a rough top surface and a subsurface with damage due to the mechanical handling [97]. By decreasing the stress normal to the surface and a smooth material removal rate the subsurface damage can be reduced. Under high energy irradiation the surface of CaF_2 can lose fluoride [98–100]. It was also shown in [97] that adding a protective SiO layer can prevent fluoride from escaping and protect the surface from damage 10000 times longer than without protective layer. High power laser damage causes fractures in the surface rather than local melting [96]. This fractured surface

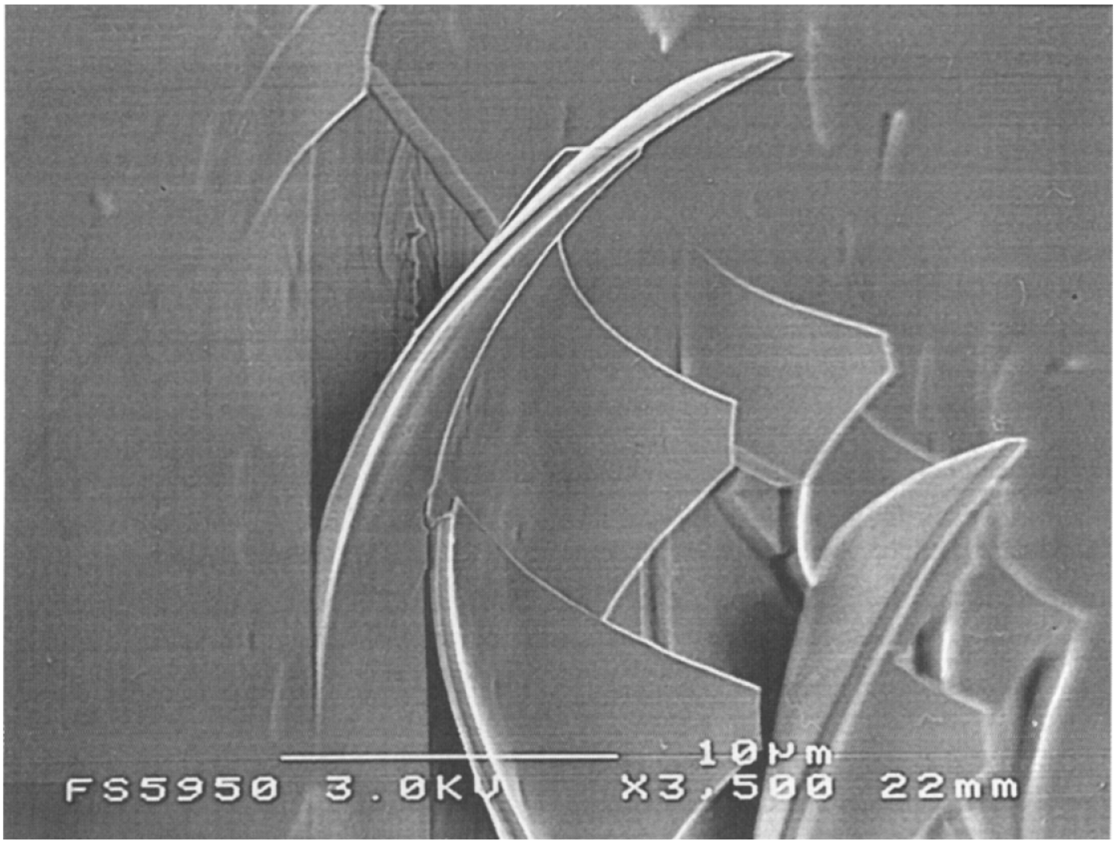

FIGURE 2.10: SEM micrograph of CaF$_2$ (111) surface irradiated by one laser pulse of 10 J/cm^2 at 532 nm. Despite the longer wavelength damage morphology is comparable to that of 248 nm. The crystal was tilted 77° with respect to the incident electron beam thus allowing measurement of the fragment thickness. Taken from [96]

then proceeds to peel off, see figure 2.10, which seems to support the surface dead layer theory. Luminescence is inefficient in this region so local heating might be much higher.

2.3 Defects in Thorium Doped CaF$_2$

Little research has been done on thorium doped CaF$_2$. Few doping related defects have been discovered as opposed to for example Yb:CaF$_2$, which is a laser material. One example could be found in [54] where undoped, uranium doped, and thorium doped CaF$_2$ were exposed to electron beams. It was shown that the electron beam first creates dislocation loops, and after heavier irradiation Ca colloids by producing F centers that cluster together. This seems to indicate that first the F centers order in a line, and afterwards cluster spherically.

In undoped and uranium doped crystals, these colloids formed a regular structure after heavy irradiation. The regular structure did not form in Th:CaF$_2$. The thorium blocks the motion of the F centers, which usually move along the (100) direction. This effect

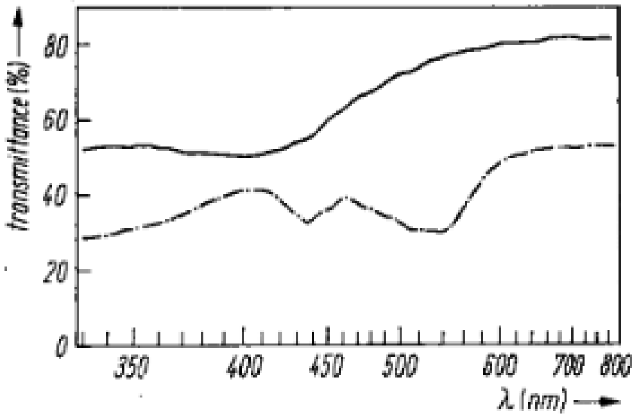

FIGURE 2.11: Optical transmission spectrum of Th:CaF$_2$ (solid line) and U:CaF$_2$ (broken line) at room temperature. Taken from [54].

was observed at 0.1 weight % of doping concentration. The blocking only allows much smaller colloid clusters to form, possibly not allowing them to move to a regular lattice. In [54] one optical absorption spectrum was measured of Th:CaF$_2$, seen in figure 2.11. The 400 nm absorption was attributed to doped Th^{4+}, because a similar absorption band was observed in doped U^{6+} which is isoelectronic to the Th^{4+}. More likely is that this is due to a type of F center (F,F$_A$, R, M, N, etc.), which have broad absorption around 400 nm and are present in every CaF$_2$ crystal. No absorption measurements at these wavelengths have been taken in this thesis.

Doping with thorium will create a anion-excess fluorite structure. These are common, and known to exist for many dopants with higher oxidation states than the Ca^{2+}. To a first approximation, these additional F$^-$ ions that compensate for the higher oxidation state can just be regarded as interstitials that occupy the empty cubes of the fluorite structures. If this is the case, the 90° orientation shown in section 2.1 is the most probable compensation orientation. Possibly, higher order defect structures are more favorable such as ordered/disordered defect clusters or lattice modulation. Examples of defect clusters are the 2:2:2 defect structure of UO$_2$, transformation of the normal fluorite cube into an square antiprism (4 lattice fluorides become (110) interstitials) or larger Ca$_6$F$_{36}$ clusters which create 4 extra fluorides at the empty cube in the center position (see figure 2.12).

A last possibility for compensation for the thorium doping is a lattice modulation, which is a large scale modulation of anion or cation density. Because thorium defects seem to stop the motion of F centers locally, large scale modulation seems improbable.

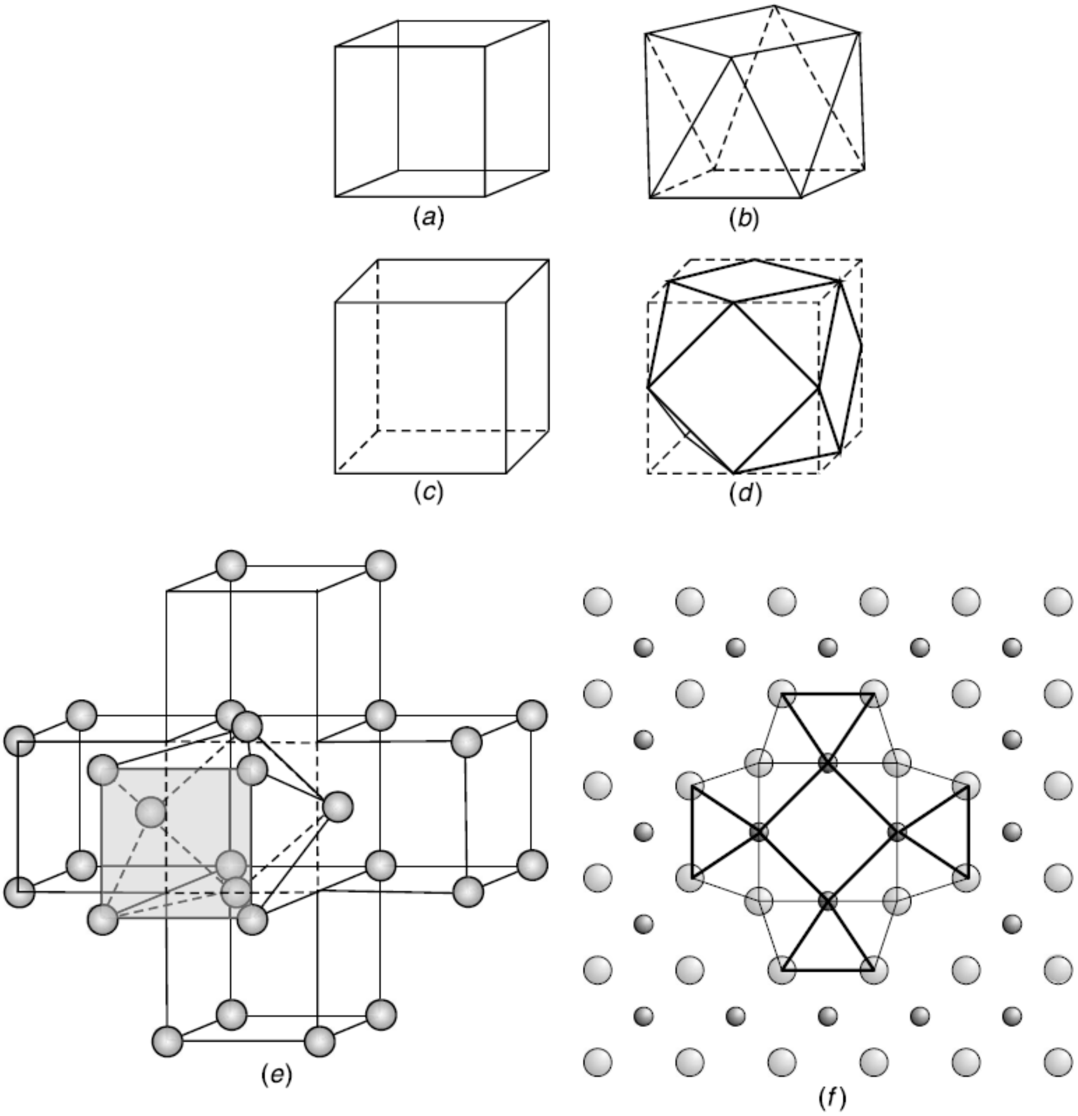

FIGURE 2.12: Large scale defect structures and transformations of the fluorite structure. In (a,b) the transformation of a square antiprism is shown, in (c,d) the transformation into a cuboctahedron. In (e) a square antiprism is shown in a larger structure, which creates 4 (110) F$^-$ interstitials. In (f) four square antiprisms create one cuboctahedron in the center which locally means 4 extra fluorides. Here smaller spheres are Ca and larger ones are F. Taken from [68].

2.3.1 Charge Transfer State

As mentioned in section 2.1, doping thorium into CaF$_2$ creates electronic states close to the bandgap edge for a 90° orientated two F interstitials compensation. In [57] this was first seen. It was then suggested that these localized thorium defects, if they exist, could be used to transfer energy to the thorium nucleus which was further explored in [42]. After closer inspection, it was found that this defect state is a charge transfer state (CTS). This CTS is effectively the electron on the fluoride interstitial moving to the thorium after absorbing a photon, changing the oxidation state of thorium to 3+ and

		$A^{sp}(d \to o)$ (s^{-1})		
	E_d (eV)	$E1$	$M1$	$E2$
$\lvert d_1\rangle$	9.90	7.84×10^4	5.04×10^2	9.26×10^1
$\lvert d_2\rangle$	10.43	4.35×10^0	2.51×10^1	2.57×10^0
$\lvert d_3\rangle$	10.50	1.99×10^6	7.09×10^1	5.95×10^1
$\lvert d_4\rangle$	10.51	6.16×10^1	4.81×10^1	5.69×10^0
$\lvert d_5\rangle$	10.59	7.27×10^6	6.64×10^1	3.03×10^1
$\lvert d_6\rangle$	10.63	1.12×10^5	2.20×10^1	1.82×10^0
$\lvert d_7\rangle$	10.68	1.19×10^7	1.24×10^1	1.56×10^1
$\lvert d_8\rangle$	11.01	2.16×10^5	2.18×10^1	2.74×10^2

FIGURE 2.13: Energies of the 8 defect states as calculated by DFT using the VASP package. On the right are the transition rates for different multipolarities for their respective defects. Taken from [29].

neutralizing the fluoride. Depending on the electronic state of thorium that it enters, this CTS has a different energy. Eight different CTS are possible, a summary is given in table 2.13.

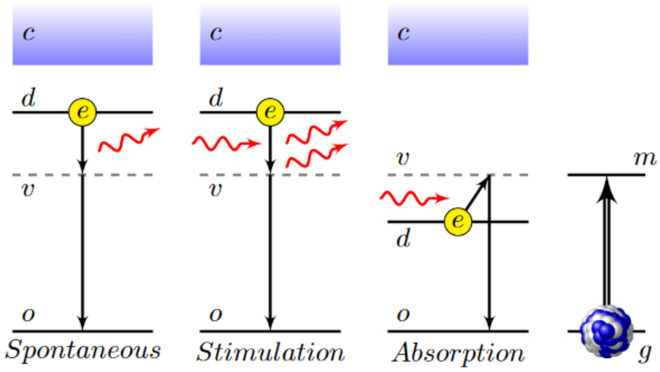

FIGURE 2.14: Different excitation processes involving the defect states and the nuclear excitation to the isomer state. From left to right: (1) If the defect state has a higher energy than the isomer, spontaneous decay is possible via an intermediate virtual state: Under the emission of a lower energy photon the nucleus can be excited. (2) If a photon with the right energy is present, stimulated emission can take place under excitation of the nucleus and de-excitation of the defect state via the virtual state. (3) Under absorption of an appropriate photon and the defect state energy the nucleus can be excited through a virtual state. Taken from [42]

In [42] it was investigated whether this CTS could be used to transfer energy to the nucleus, a new way to excite the isomer, either via stimulated absorption or stimulated emission. The process is schematically drawn in figure 2.14. In this work the wavefunction of the defect states was calculated using DFT, more specifically the software package VASP developed in Vienna [101]. The overlap of these wavefunctions with the nuclear ones was used to calculate the probability of using this CTS to excite the nucleus. The result was that using this type of excitation can be two orders of magnitude more efficient than a direct excitation of the nucleus with a VUV lamp. The main reason for this is that in the VUV region, no high power tuneable lasers are easily available.

The broad CTS can be more easily excited by a broadband high power source such as a lamp, and a narrow high power optical laser can then be used to drive the excitation from CTS to nuclear isomer excitation. The energies of the CTS were calculated to be around 120 nm (table 2.13 in [29]). Theoretical estimates using DFT can be rather inaccurate because VASP calculates ground state properties. Once an electron is excited the assumptions of VASP do not hold and the prediction of 120 nm is thus not precise.

In private communication [102], quantum mechanical calculations were used using multiconfigurational wave functions specifically designed to describe CTS to calculate the energy of the thorium CTS. These resulted in broad 10 nm wide absorptions between 120-130 nm for CTS from lattice fluoride and 275-300 nm for CTS from the charge compensation interstitial fluorides of the Th center. These calculations assume that the electron moves from the fluoride $2p$ ground state to either the thorium $5f$ state with a probability of 97 %, or to the thorium $6f$ state with a probability of 3 %.

One can compare these to other charge transfer states observed in large bandgap crystals. In [103], Yb was doped in several large bandgap crystals. For example, the CTS from F$^-$ to Yb^{3+} in ScPO$_4$ was observed absorbing at 195 nm, and emitting at 270 nm. In Eu:CaF$_2$ the CTS from F$^-$ to Eu^{3+} was observed [104].

2.4 Radioactivity, Damage, and Self Excitation

Thorium-229 has a half-life of about 8000 years. The exact determination of this value is hard due to the little material available. Recent experiments put it more exactly at 7917±48 (two σ) years [105] or 7825±87 (two σ) years [11]. ^{229}Th decays 100 % via an α-decay of 5.167 MeV (Q_α). In its decay chain (figure 2.15) only short lived elements appear until bismuth-209, creating a secular equilibrium with the activity of the ^{229}Th. Per Th decay, 5 α particles are emitted with energies higher than 5 MeV.

When doping the CaF$_2$ with this active (we use >100 kBq) material an average of approximately $2.5 \cdot 10^6\,\mathrm{eV\,s^{-1}}$ or picowatts will be deposited. This will not cause any significant heating, but it will make any type of excitation energetically possibly within the crystal. For example creation of defects [69], surface self sputtering [106] or oxidation state change through self irradiation [107, 108]. The 3 α-decays is what makes the ^{229}Th decay chain interesting for medical applications where the short lived daughter ^{225}Ac is used for targeted α treatment [109].

In this section we describe the production of defects and photons, theoretical and experimental, through irradiation of any kind. These defects or imperfections in the crystal

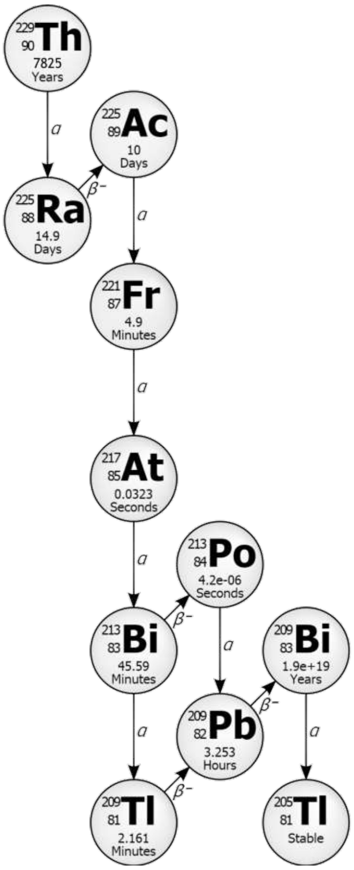

FIGURE 2.15: Decay chain of ^{229}Th. All daughters have a lifetime below 15 days aside from ^{209}Bi. The quick triple α-decay after ^{225}Ac is used for medical applications.

can end up to be absorptive in the VUV region, which is defined as damage to the crystal. We will focus on irradiation by radioactive decay products, but also VUV and x-ray irradiation. The light produced by these processes are mainly Cherenkov radiation and crystal STE luminescence.

2.4.1 Irradiation Induced Defects

Different types of irradiation produce different defects and have different effects on the crystal. By doping crystals with ^{229}Th and trying to excite the nucleus we submit the crystal to many types of irradiation: α, recoiling nuclei, β^-, γ, x-ray, neutron and VUV photon. Generally all of them have high energies aside from VUV photons, thus they need to be treated differently.

Using ionizing radiation it is possible to excite electrons from deeper core levels, such as the K shell, of atoms to the conduction band of the crystal. In this process the normal valence band of the solid state system is skipped. This will produce several effects: x-rays from recombination into the deep holes, photons, electron emissions, phonons, lattice displacements and defects. In [69] and [51] a good overview is given.

Soft x-rays on average need 3 times the bandgap energy (≈36 eV for CaF$_2$) to be efficiently absorbed and are very inefficient at displacing atoms, mainly creating excitons. VUV photons are inefficient at displacing atoms and mainly create excitons. Both behave similarly and mainly produce damage through STE decay as shown in figure 2.7 and 2.8 where produced F and H centers are separated and form larger agglomerates. These imperfections in the crystal will then become absorption centers and reduce transmission.

Under VUV irradiation the CaF$_2$ lattice will mainly produce point defects [47], defects the size of a single atom such as vacancies or interstitials. For example, F and H centers will be produced until the rate of formation is in equilibrium with the recombination-annihilation rate. Damage is produced because the two centers diffuse through the crystal and do not always recombine as seen in figure 2.8. The rate of diffusion is characterized by the diffusion energy, which is the barrier needed to overcome to hop lattice sites. The diffusion energy of H centers is lower than for F centers at room temperature thus H centers will diffuse more. This results in agglomerations of F centers in the irradiated area and H centers moving out of the irradiated area.

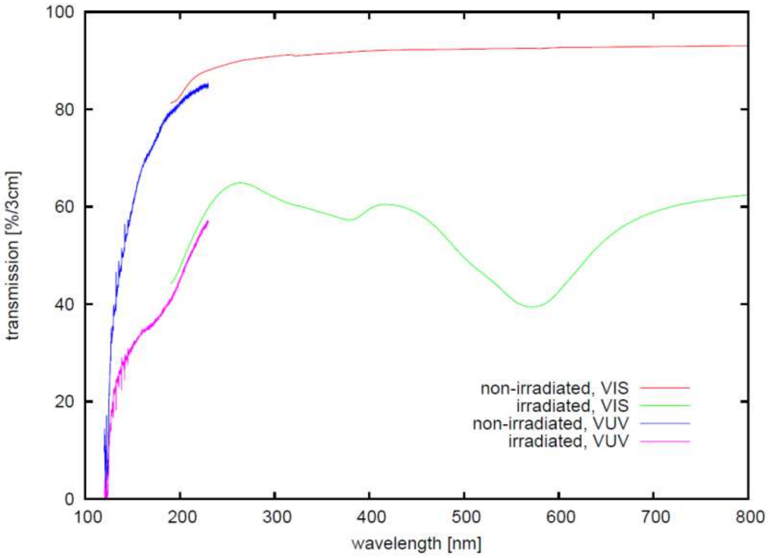

Figure 2.16: VUV transmission of an undoped CaF$_2$ before and after irradiation by a 193 nm excimer laser with 10^4 pulses and a fluence of 50 mJ/cm^2. Absorption around 150 and 550 nm is due to metallic colloids, absorption between 300 and 400 nm due to F centers and larger agglomerates. Figure taken from [47].

The agglomerations of F centers will first produce the more stable M or R centers and eventually the F centers will conglomerate to metallic calcium colloids (2.2.3). The colloids absorb and scatter light in the VUV, reducing the effective transmission of the crystal in the VUV. As the lattice constant of metallic Calcium and CaF$_2$ is nearly identical, the formation of colloids is very stable. As long as F centers are available, these colloids grow. The absorption of the produced centers by VUV irradiation is experimentally measured and shown in figure 2.16. As explained in section 2.3, by doping CaF$_2$ with Th, the F centers will be pinned by the Th, preventing formation of larger colloids.

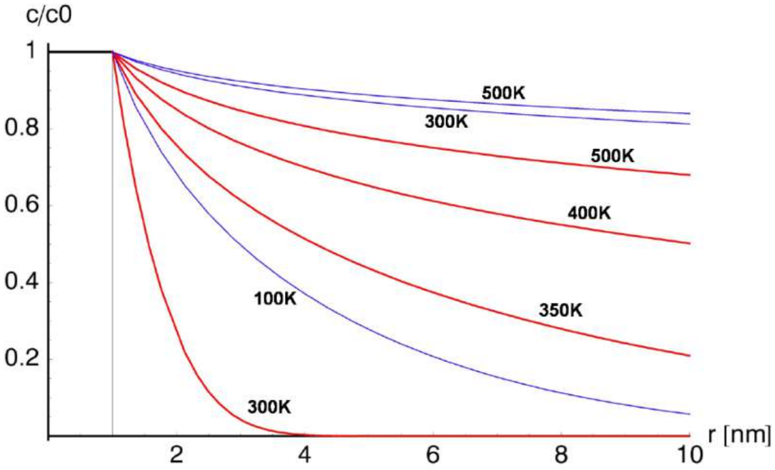

FIGURE 2.17: Calculated temperature dependent concentration of F (red) and H (blue) centers after a diffusion time of 1 month in undoped CaF$_2$. It can be seen that small changes around room temperature heavily affect the mobility of F centers but not much of H centers. Taken from [47].

The above process can be reversed, by increasing the mobility of F centers by heating such that all F and H pairs recombine and annihilate. Heating however will also provide the energy to form defects, so the right temperature is needed where the least amount of defects is formed but the F and H centers can freely recombine. As shown in figure 2.17, heating the crystal greatly affects the F center mobility but almost not the H center mobility. This is due to the lower diffusion energy of an H center. If the crystal is fluoride deficient, annealing can not be used to regain the perfect crystal structure. If for example fluorine (F$_2$) is lost due to the VUV irradiation or any other process, annealing cannot heal the defects because there are more F centers (F$^-$ vacancies) than H centers (F$_{2^-\text{ molecule}}$.

Heating a CaF$_2$ crystal as to anneal it, will go through several phases. Around 150 ℃ the diffusion rate increase of F centers will only make the colloids grow, as F centers can now move more freely in their local area but do not find the far away H centers yet. Around 250 ℃ the colloids start to become smaller. Only at 400 ℃ the VUV transmission returns completely to normal, as described in [47]. In [72] a temperature of 500 ℃ was suggested to dissolve even the smallest colloids.

For describing damage by particles with mass, mainly classical collision dynamics is used. This means that the maximum energy transfer (E_{max}) is determined by the masses of incident and target particle (M_I and M_T) and initial energy E_I

$$E_{max} = E_I \frac{4M_I M_T}{(M_I + M_T)^2}. \tag{2.13}$$

Thus electrons can transfer only very little of their energy per collision (0.007 % for a Cu atom), protons and neutrons a reasonable amount (6.1 % for a Cu atom) and larger atoms almost everything (100 % for equal mass collisions). The cross section for larger and neutral particles and thus the transferred energy is higher than for small charged particles. Hard sphere scattering describes scattering of neutrons and slow large particles. Rutherford scattering describes scattering of electrons, protons and α particles.

If the first particle in a solid lattice is hit under a shallow angle, the angle under which it moves away is smaller than the incoming angle due to conservation of momentum. The next particle it then hits will again have a smaller angle of motion respective to the lattice axis than the previous one. This means that in a long chain of particles in a lattice, the small angle deviation from the lattice axis will become smaller with each collision. This effect is called focusing, effectively transporting collisional energy from one site to the other. This effect makes it possible to create interstitials and vacancies with some distance from one another, basically creating damage. The principle for channeling, in which a particle moves through the empty axis of a crystal (for example the middle of a cube in a cubic structure), is the same. The collisional angle will decrease with each collision until the particle moves exactly along the empty axis of a crystal.

A simplification of the collision model is the displacement energy (E$_\mathrm{D}$). This is the minimum energy needed to displace a lattice atom from its lattice position. For CaF$_2$ theoretical studies predict 23 eV for the Ca ion and 10 eV for the F ion. In this same study it was shown that it is first of all more likely to produce damage in the fluoride lattice, and that, if this lattice is hit with a high energy particle, the damage will be limited to the fluoride lattice [110].

Taking into account the displacement energy and the masses of the incoming particles a general picture can be sketched for the damage done by incoming high energy particles. This is sketched in figure 2.18 for electrons, light ions and heavy ions. Electrons, because their mass is so small, will maximally transfer 0.01 % of their maximum energy: Thus a 100 keV electron is needed to displace one fluoride in the very unlikely case of a head on collision. Rutherford scattering decreases collisional energy transfer efficiency significantly from the maximum, causing many grazing incidence collisions. In practice, this means that a 2.5 MeV electron is needed to displace one fluoride. Only the thallium-209 in the thorium-229 decay chain has a Q$_\beta$ = 3.9 MeV and is thus able to produce electrons with these energies. The probability however is low: the Q$_\beta$ value is the total energy emitted during decay, which is distributed over recoil nucleus, neutrino and β^- so it is unlikely the electron has these high energies. The amount of thallium-209 that is produced in the thorium-229 decay is also low, bismuth-213 is more likely to decay to polonium-213 (97.80 %).

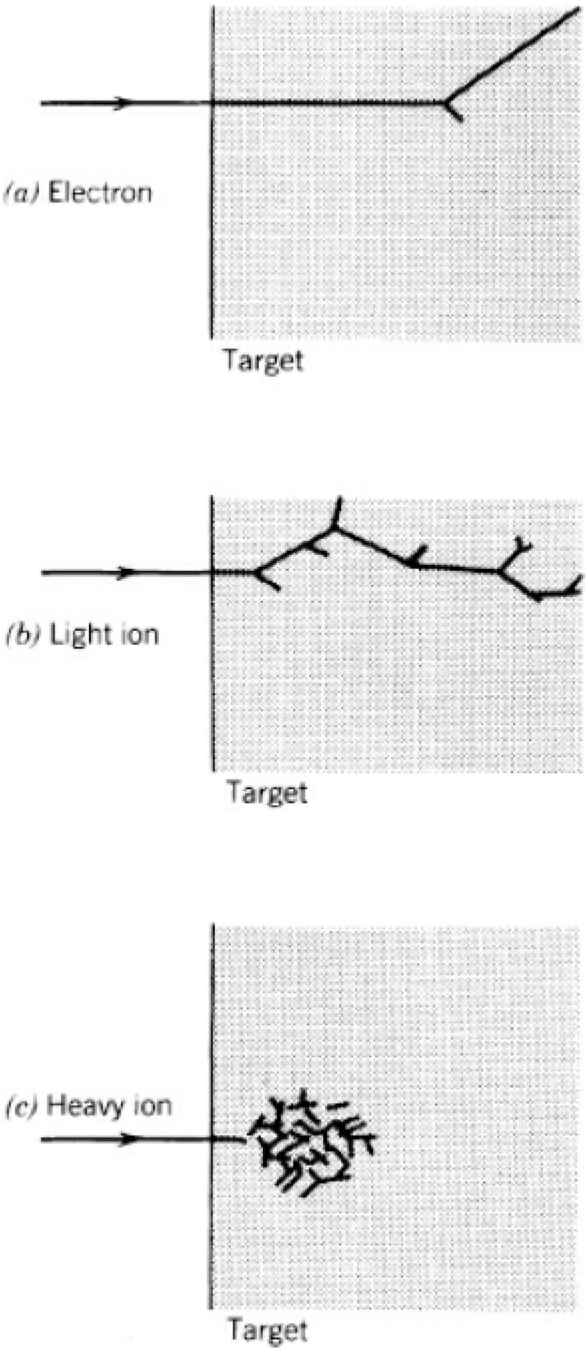

FIGURE 2.18: Damage distributions created through irradiation by a) electrons, b) light ions and c) heavy ions. Taken from [69].

The grazing angle collisions, which have low maximum energy transfer efficiency, make light particles cause defects which are well separated and almost never with secondary collisions (see image (a) in figure 2.18). Protons and α particles can maximally transfer 4.8 % and 57 % of their energy. That means a 200 eV proton or 20 eV α is enough to displace a fluoride. Again, due to Rutherford scattering, the collisional energy transfer efficiency will be decreased. In the end this creates a damage profile of still well separated defects with some secondary collisions (see image (b) in figure 2.18). In practice, 2 keV protons and 200 eV α particles are needed for one fluoride displacement. Neutrons, although the maximum energy transfer is the same as protons, will cause a lot of damage because they are not limited by Rutherford scattering, increasing energy transfer efficiency per collision. Larger ions are also not limited by Rutherford scattering due to their size, and will deposit all their energy in a very localized region with many secondaries (see image (c) in figure 2.18).

2.4.2 Experimental Investigations in Literature

Single crystal undoped CaF_2 has been experimentally studied under heavy ion (200 MeV Xe^{14+}) irradiation [111]. With increasing dose, the CaF_2 becomes purple. This effect is also seen in nature with natural polycrystalline CaF_2 which has spent extended time in close proximity to natural uranium [73]. The purple coloring is due to large Ca metallic colloids forming. Normally, high doses can amorphize a crystal as was seen with YAG in [111]. CaF_2 with its metallic colloid with almost the same lattice constant seems to saturate damage at a certain dose. This means that further irradiation both evaporates the colloids as it creates more F centers that precipitate into colloids. In the end, an equilibrium is reached such that the total damage does not increase. The crystal is spared from amorphization and no evidence is found that it deviates much from its original single crystal structure, albeit with a high very concentration of F centers and larger agglomerations of these.

If fluoride is ejected from the crystal and the stoichiometric ratio changes then damage can still increase. The stoichiometric ratio is the ratio between reagents to produce this crystal, in this case calcium and fluorine. Any number other than 1 means an excess or deficiency of one of the reagents. Excess or deficiency of fluoride means a permanently higher concentration of F or H centers, which increases absorption.

CaF_2 doped with low concentrations is more resistant to radiation damage, especially with Sr [112]. Radiation induced processes can also oxidize and reduce dopant, especially the trivalent rare earths [67, 113–115].

2.4.3 Cherenkov Radiation and Radioluminescence

Aside from damage, the radioactivity produces photons: radioluminescence and Cherenkov radiation. CaF$_2$ has been used as a scintillator extensively to measure charged particles, x-rays, γ-rays and has even been used to detect possible WIMPs (Weakly Interacting Massive Particles, hypothetical particles proposed as candidate for dark matter) [116–118]. The yield has been established to be roughly 19000 photons/MeV deposited in the material. In radioluminescence defects are created in the material due to the high energy deposition as detailed above. These defects annihilate and produce mainly STE luminescence.

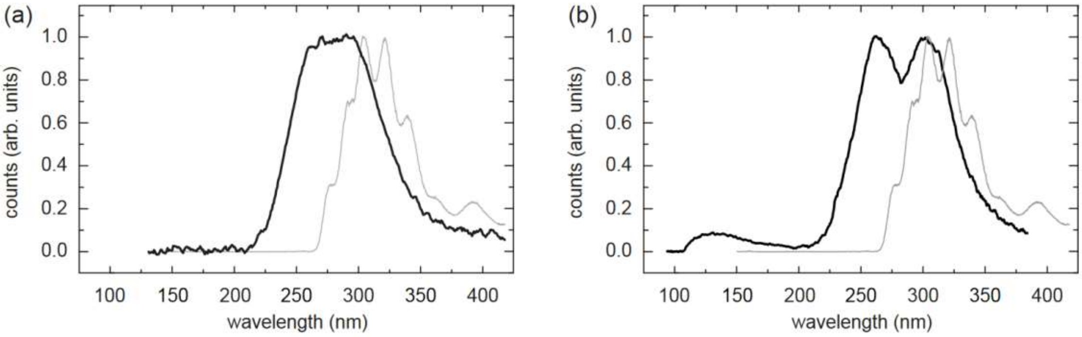

FIGURE 2.19: a) Radioluminescence from 5 kBq ^{229}Th:CaF$_2$ (bold) compared to a D$_2$ lamp excited photoluminescence of CaF$_2$ (gray) at 15 nm resolution. b) undoped CaF$_2$ in contact with 7.5 MBq ^{233}U radioluminescence spectrum at 4 nm resolution. Taken from [119].

Radioluminescence of undoped CaF$_2$ in contact with a ^{233}U source and of ^{229}Th doped CaF$_2$ was characterized for our experiments [119]. In figure 2.19 the results are shown where the dominant difference is the Cherenkov radiation that can be seen below 200 nm. Both isotopes are pure α emitters, but the more active ^{233}U source is older and has more daughters grown in, which emit high energy β^- particles that produce Cherenkov radiation. The daughters of the ^{229}Th should also produce Cherenkov radiation in the crystal, but the intensity was too low to be measured in these experiments.

Cherenkov radiation is well known as the blue light emitted by nuclear reactors. This light is produced by charged particles that travel faster than the phase velocity of light (v_n) in a dielectric. In the case of a nuclear reactor it's β^- particles in water. This effect is not the interaction of the electron with individual atoms or radiative scattering off of nuclei, it is rather the production of polarization in a material which upon depolarization emits radiation.

The change from polarized to non-polarized driven by the high energy electron emits radiation and will thus have a wavefront following the electron. If the particle speed v (or $\beta = v/c$), is too slow, there are no interference effects of these wavefronts to consider. If the particle is travelling faster than that light can travel in this dielectric ($v_n = \frac{c}{n(\lambda)}$), the wavefronts will constructively interfere and coherently build up into the typical conical wavefront of Cherenkov radiation. The emission angle of this coherent wavefront can be derived to be $\cos\theta = \frac{1}{n(\lambda)\beta}$ [120]. The minimum kinetic energy E_k that a singly charged particle with mass m needs to produce Cherenkov radiation ($v > v_n$) can be derived to be

$$E_e > mc^2 \left(\frac{1}{\sqrt{1 - \frac{1}{n(\lambda)}^2}} - 1 \right), \tag{2.14}$$

which for a β^- particle in CaF$_2$ comes down to $E_{e,min} = 149$ keV for 150 nm at 25 °C. The number of photons N_{ph} per length traveled x in the material per wavelength λ of β^- particles with this energy is given by the Frank-Tamm equation [120]

$$\frac{dN_{ph}}{dx d\lambda} = \frac{2\pi\alpha}{\lambda^2} \left(1 - \left(\frac{c}{vn(\lambda)} \right)^2 \right) \tag{2.15}$$

where α is the fine-structure constant ($\approx \frac{1}{137}$). As can be seen from the equation, the number of photons is only mildly dependent on the speed but is inversely proportional to the wavelength. Because the speed of light in a material is wavelength-dependent, the approach of Frank and Tamm [120] assumes that $n(\lambda)$ is a function that continually varies slowly with wavelength. This is the case for CaF$_2$, aside approaching the bandgap. This approach is thus not valid there.

To calculate the spectrum of a β^--decay in CaF$_2$ we will use the continuously slowing down approximation (CSDA). This approximation assumes that the energy lost per distance $\frac{dE_e}{dx}$ is always equal to the stopping power and no fluctuations apply. We use the ESTAR data to approximate the CaF$_2$ stopping power [121]. Using this approximation we can calculate [45]

$$\frac{dN_{ph}}{d\lambda}(E_{e,0}) = \int_{E_{e,min}}^{E_{e,0}} \frac{dN_{ph}}{dx d\lambda}(E_e) \left| \frac{dx}{dE_e} \right| dE_e, \tag{2.16}$$

where $E_{e,0}$ is the initial energy of the β^-. Using these equations one can calculate the Cherenkov spectrum produced by ^{229}Th, which is in equilibrium with its daughters, in CaF$_2$ as seen in figure 2.20. In these calculations the spectrum has been multiplied by its transmission spectrum. This is done because the Frank-Tamm equation does not hold close to the transmission edge due to the sharp increase in the refractive index (and thus the sharp decrease of the speed of light in this material). Multiplying it with

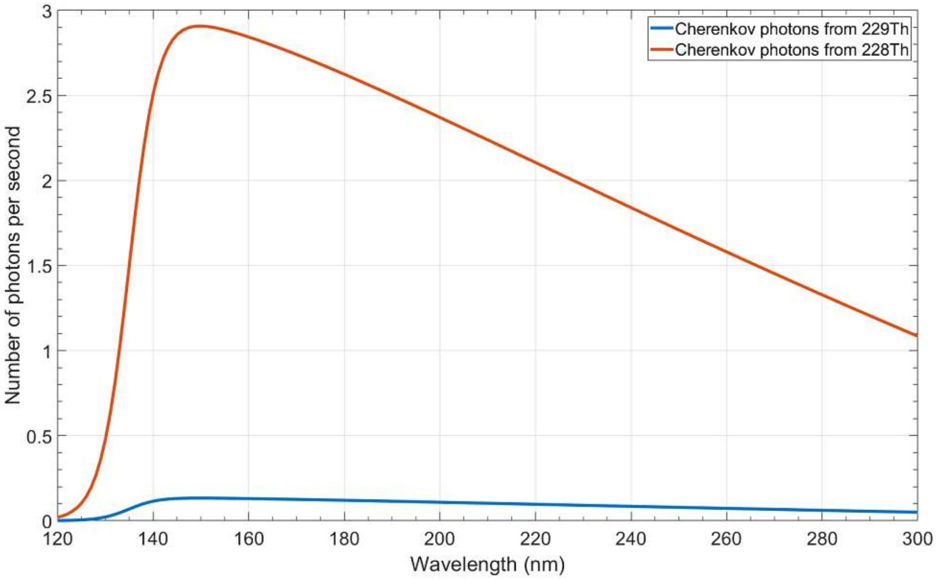

FIGURE 2.20: Number of emitted Cherenkov photons per wavelength for a crystal doped with 1 Bq of ^{229}Th. This was calculated by using above equations and approximations, and by multiplying it with the CaF$_2$ crystal transmission. The 1 Bq of ^{229}Th corresponds to the amount produced by a 11422 Bq ^{233}U crystal with a ingrowth time of three years. Also displayed is the Cherenkov radiation produced if that ^{233}U crystal has a 1 ppm contamination of the much shorter lived ^{232}U and the subsequent Cherenkov produced by its daughter ^{228}Th. Due to the shorter lifetimes the Cherenkov intensity is higher. The 1 ppm contamination produces 10^7 times more Cherenkov light. This can be easily shown because the β^--decays have approximately the same energy and the ^{232}U lives 10^3 times shorter than the ^{233}U and ^{228}Th lives 10^4 times shorter than the ^{229}Th

the crystal transmission spectrum approximates the experimentally observed Cherenkov emission by a CaF$_2$ crystal.

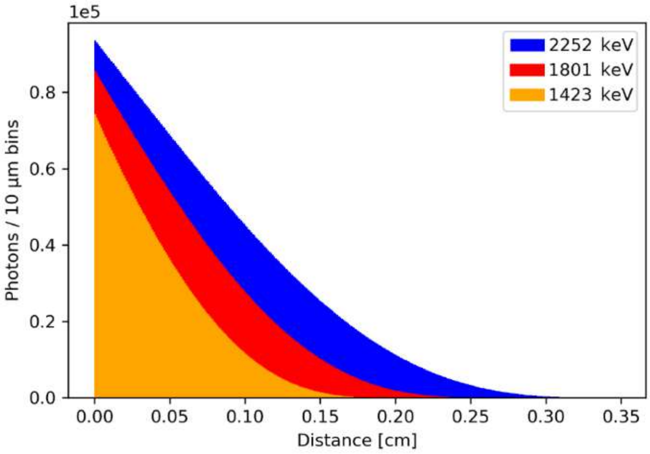

FIGURE 2.21: Number of emitted Cherenkov photons per distance traveled for β^--decay in CaF$_2$ for three different energies. In the first 0.15 cm over 95 % of all photons are emitted.

Since many of the crystals have a physical size on the order of the distance traveled by the electrons (≈mm) in the crystal it is important to take the size into account. In figure 2.21 the photons emitted per distance traveled is calculated using above equations. Here we can see that reducing the thickness of a crystal can significantly reduce the amount of Cherenkov radiation produced. This also means that if a high concentration of ^{229}Th is doped in a small crystal the signal to background ratio around 150 nm will increase. This figure does not take into account the angular and spectral distribution of this process, which could be interesting to study to find an optimal thickness for high SNR ratio.

2.5 Luminescence in CaF$_2$

The luminescence of CaF$_2$ is an important background in the experiments. Absorbed energy will mainly be emitted by STEs and some by other defects if present. Some characteristics of CaF$_2$ are important to note here:

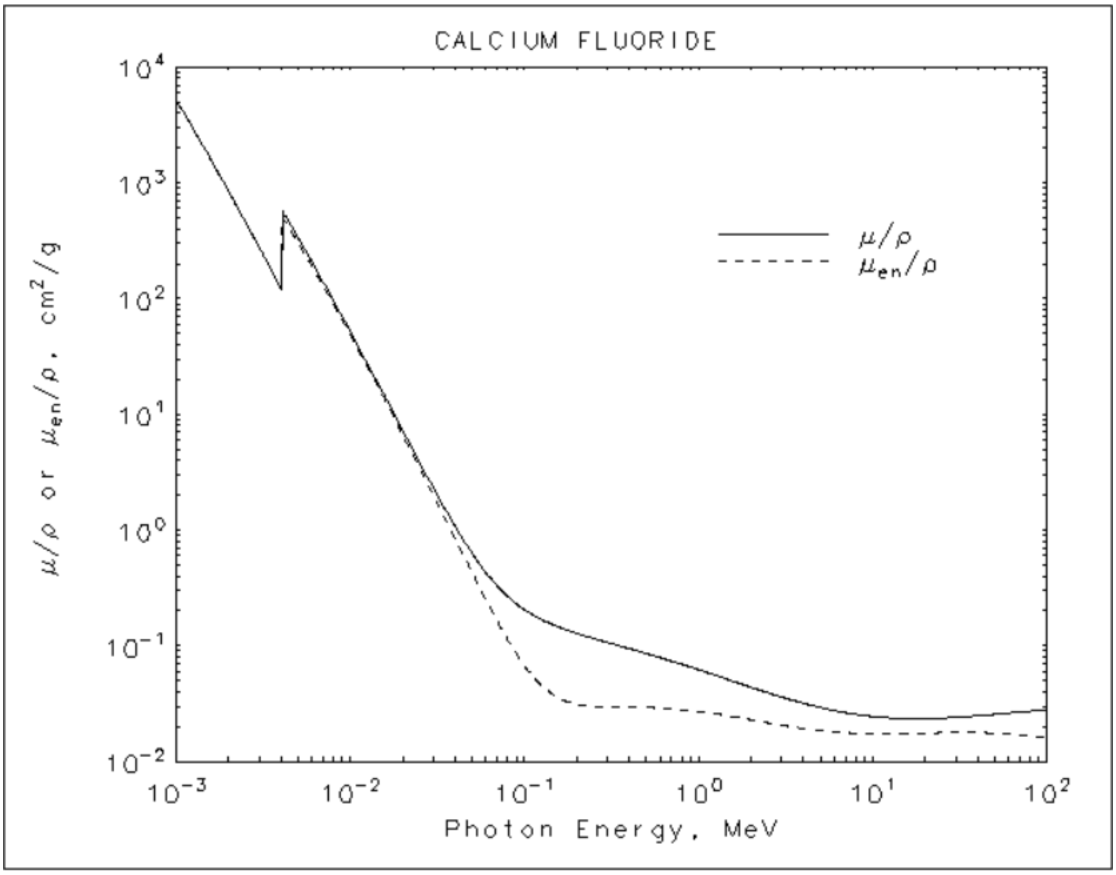

FIGURE 2.22: Mass attenuation coefficient μ/ρ and mass energy absorption coefficient μ_{en}/ρ of CaF$_2$ for different x-ray energies. Taken from NIST [122]

- Optical properties: Undoped CaF$_2$ is transparent from 122.5 nm upwards, below this wavelength no luminescence can be expected.

- Radiation hardness: Radiation damage in CaF$_2$ saturates after a dose of 10^{14} collisions/cm^2 for 200 MeV Xe^{14+}. Large colloids are formed that have a broad absorption shoulder up until 180 nm and a broad absorption centered around 550 nm.
- Density/stopping power: Because CaF$_2$ is only comprised of light elements, high energy photon absorption is reduced which reduces luminescence through this excitation. For details see figure 2.22.

2.5.1 STE Luminescence

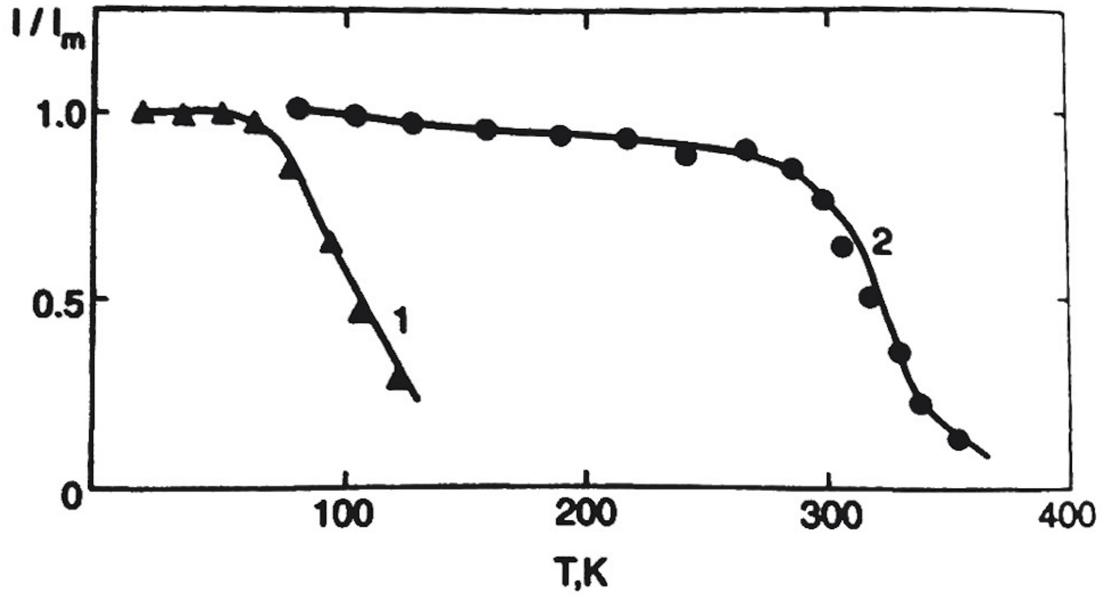

FIGURE 2.23: Thermoluminescence curve of the fast 275 nm singlet (1) and slow 305 nm triplet (2) emission in CaF$_2$. These curves are measured by damaging a 30 K CaF$_2$ crystal with x-rays and slowly heating the crystal afterwards. This causes the x-ray induced defects to gain mobility and annihilate. Above a 100 K the singlet mainly decays non-radiatively, above 320 K the triplet mainly decays non-radiatively. During x-ray irradiation at 300 K it is observed that both singlet and triplet luminesce, indicating that such a large number of STEs is created that enough still decay radiatively. figure taken from [51].

The luminescence due to STE luminescence (see figure 2.19), or F center/H center recombination, has a couple of general characteristics that are important to summarize [51, 88]:

- Conversion efficiency: 3 % of incoming energy is emitted.
- Decay time: ≈ 50 μs for triplet STE and ≈ 10 ns for singlet STE and most other defects.

- Level of afterglow: There are 2 fast exponential decay constants, 450 ms and 23 s. After that the afterglow decays via a power law over 20 hours. The afterglow is so long-lived due to the low mobility of F centers at room temperature (1 mHz).

- Temperature stability: The singlet and triplet photon emission of the STE are quite temperature independent until a critical temperature where non-radiative decay takes over, see figure 2.23

- Emission wavelength: The STE emission ranges from 200 nm to 500 nm, with peaks mainly at 275 nm (singlet) and 305 nm (triplet). Longer wavelength or lower energy emissions are due to excited states of the STEs which decay through more phonons and at lower energy photon emission.

2.5.2 Selected Dopants

A good overview of known optical dopant luminescence for CaF$_2$ was compiled by [123], here repeated and translated to English for completeness with added VUV luminescence in table 2.5.3. The lanthanides are detailed because of their similarity to the actinides, which are studied less due to their radioactivity. The experiments performed with thorium and uranium and possibly in the future with actinium, protactinium and neptunium can benefit from knowledge of their possible spectral characteristics. It should be noted here that the spectral line assignment of the actinides to the oxidation state is tentative. Normally, the oxidation state of an impurity can be readily changed in CaF$_2$ by γ irradiation, electrolytic reduction and baking in Ca vapor. The self irradiation of the radioactive actinides changes their oxidation state over time. In this case neptunium, plutonium and curium oxidize from 3+ to 4+ and americium and einsteinium reduce from 3+ to 2+. [49].

2.5.3 Table of Absorption and Emission of Dopants and Defects in CaF$_2$

Impurity absorption and emission in CaF$_2$

Impurity	Absorption (nm)	Emission (nm)	Reference
STE	282 and 428 nm (exciton creation at 110 nm)	200-400 nm, peak at 280 and 305 nm	[51, 87]
M-center	365 and 520 nm	600 nm	[76]
Pb^{2+}	128, 151, 165 and 205 nm	176 and 219 nm	[124]
Bi^{3+}	135, 151, 158 and 219 nm	175 and 225 nm	[125]
Ce^{3+}	Two groups with peaks at 243 and 305 nm, and 187, 194, 203 and 216 nm	318 and 342 nm	[126, 127]
Pr^{3+}	Broad bands beneath 200 nm	400 nm intense peak, weak bands at 220-280 nm and 450 nm and higher	[128, 129]
Nd^{3+}	Strong 160 nm, weak 201, 207, 247, 257, 288 and 296 nm	Strong 170-200, 300, 860 and 1064 nm, weak 354, 382 and 414 nm	[130, 131]
Sm^{2+}	Bands 147, 240, 256, 288, 307, 425, 445, line at 495, 507, 535, 632 nm	Broad band at 170-200 and at 750 nm	[132–134]
Sm^{3+}	230 and 400 nm	lines at 567.5, 571, 572.2, 605.5, 616.7, 617.6, 621.9, 651.6, 660, 661.5, 675, 710, 715, 735 nm	[123, 135, 136]
Eu^{2+}	Bands from 200-250 nm and 325-400 nm	Bands from 400-475 nm	[132]

Eu^{3+}	148 and 313 nm	528, 573, 580, 605, 616, 630, 638, 640 nm	[137, 138] [135, 139]
Gd^{3+}	124.7, 248 and 335 nm	129 and 312 nm	[50]
Tb^{3+}	210 and 250-260 nm	380.2, 414.9, 436.7, 460.8, 487.8, 546.4, 588.2 and 621.1 nm	[140, 141]
Dy^{2+}	Bands from 230-490, 580, 720 and 910 nm	Multiple lines from 2.3-2.6 μm	[142]
Dy^{3+}	337.1, 458.0, 465.8, 472.7 and 476.5 nm	Many lines from 469 to 864.2 nm	[143]
Ho^{2+}	Bands at 512, 680 and 897 nm	Some lines between 1.8 and 3 μm	[144]
Ho^{3+}	between 150-160 nm, lines around 640 nm	bands at 158, 170, 185 nm and line groups at 220-320, 540 and 640 nm	[134, 145–147]
Er^{2+}	Bands at 344, 400, 485, 610, 910 nm	Some lines between 1.9 and 2.4 μm	[144]
Er^{3+}	130, 150, 145 and 155 nm	310-320, 397-403, 466-471, 514-531, 613-621, 756-780 nm	[148, 149]
Tm^{2+}	Broad bands from 200-700 nm	1067-1247 nm	[150]
Tm^{3+}	115-160, 172-175 nm	150-190, 295, 344, 360, 450, 470, 510, 1350-2000 nm	[134, 151–154]
Yb^{2+}	214, 227, 260, 271, 315 and 360 nm	540, 565 nm	[155]
Yb^{3+}	900-1150 nm	940-1100 nm	[155]
Lu^{3+}	120.5, 160 nm	125.5 nm	[50, 156]
U^{3+}	550		[49]
U^{4+}	Bands between 1500-1650 nm		[49]
Np^{3+}	580 and 1050 nm		[49, 157]

Np^{4+}	Lines between 725-735, 967-995 and 1663-1729 nm		[49, 107, 157]
Pu^{3+}	Lines around 500, 625, and 658 nm	480 and 580 nm	[49, 158]
Pu^{4+}	Lines around 380, 415, 455, 553, 580, 651, 810, 843 and 1070 nm		[49, 158]
Am^{2+}		685 and 690 nm	[107]
Cm^{3+}	390, 480-540, 790 and 1060 nm	607 and 608 nm	[49, 159]
Bk^{3+}		Lines from 663-678 nm	[159]
Es^{2+}		Lines from 587-638 nm	[159]

Chapter 3

The Growth of Highly Doped ^{229}Th:CaF$_2$

Radioactively doped materials have been studied for a variety of reasons. Trace amounts, which are either doped or produced by neutron capture, can be used as local probes [160] or to study material composition [161]. Many efforts have been undertaken on growing highly doped radioactive crystals, some of them in CaF$_2$ doped with the long-lived isotopes of uranium [75], neptunium [157, 162], and plutonium [163]. In nature, CaF$_2$ can be found doped with large amounts of uranium. Through the decay of this natural isotope the CaF$_2$ is subjected to years of radioactivity. This produces what is called ”fetid” fluorite, due to the smell it produces when it is cracked open [55]. The cause of the smell is F$_2$ trapped in the crystal that is produced by radiolysis of CaF$_2$ (dissociation into Ca and F$_2$ through radioactivity) [164].

Growing crystals with short-lived elements is challenging, due to the time it needs to grow a crystal and the higher specific activity: for a similar doping concentration one will get a more radioactive sample. Growing radioactive crystals in general is challenging: the radioactivity of the raw material (100 kBq - 1 MBq) has diverse effects on many aspects of crystal growing: The preparation, the handling, and the nuclear chemical processes during the growth. In this thesis, doping with the shorter lived ^{229}Th is only attempted because of the possible application as a solid state nuclear clock. For all other purposes, doping with the long-lived ^{232}Th should have the same electronic effect on the crystal, making doping with ^{229}Th obsolete when one is not concerned with properties of the nucleus.

As opposed to the natural isotope, ^{232}Th, the ^{229}Th isotope is artificial. All available ^{229}Th is a decay product of ^{233}U. The ^{233}U was produced first by neutron irradiation of ^{232}Th targets as part of the military and civilian nuclear program of the US. Using ^{233}U as nuclear weapons material was dismissed due to the presence of ^{232}U in the material. This isotope is a byproduct of the ^{233}U production and emits a dangerous high energy γ-ray with an energy of ≈1 MeV. Later, ^{233}U was produced in very large quantities with the idea to fuel nuclear power reactors, 1556 kg were produced at the Savannah River Site (USA) in the late 1950s [165]. One can calculate that from this 1556 kg, 45 g of ^{229}Th should have been produced since. Chemical separation of this isotope is very labor intensive and is limited due to chemical impurities, so only very small amounts are available (≈mg). The main motivation to separate ^{229}Th is its medical applications [166] but the recent nuclear clock application has also gathered attention [22].

The group of Eric Hudson at UCLA had the company AC materials grow ^{229}Th:LiSrAlF$_6$ crystals [44]. Their group explored the excitation and fluorescence of ^{232}Th doped crystals [167] (Th:NaYF, Th:YLF, Th:LiCAF, Na$_2$ThF$_6$, LiSAF) to investigate background and optical transparency. They settled on LiSrAlF because it showed the least VUV irradiation induced luminescence and highest VUV transparency. Their ongoing attempts at exciting and measuring the nuclear excitation so far failed for unreported reasons.

Our approach is to grow CaF$_2$ doped with ^{229}Th. The rare ^{229}Th isotope is purchased from commercial suppliers or research institutes as thorium nitrate (Th(NO$_3$)$_4$) dissolved in nitric acid (HNO$_3$). In 2014 two samples of ^{229}Th (2.8 and 195 kBq, or 10^{15} and $7 \cdot 10^{16}$ atoms) were bought from the company Eckert & Ziegler. Crystal V057 was grown with these batches as the final and highest doping concentration ^{229}Th:CaF$_2$ crystal with a doping concentration of 10^{16} cm^{-3}. This proved to be insufficient concentration to perform an experiment that would measure a photon produced by the nuclear decay. There was a need for higher concentration crystals thus more ^{229}Th needed to be procured and smaller crystals needed to be grown.

The Oak Ridge National Laboratories (ORNL) evolved from the Manhattan project. Due to its success, research was expanded. The research done at ORNL included: separations chemistry, work in materials and fuels, the development of neutron scattering, neutron activation analysis, C-14 tracer analysis and the development, production, and distribution of radioisotopes. ORNL has been a producer and supplier of isotopes since 1946, and is today for some isotopes still the only supplier [168]. We obtained 7.33 MBq or $2.6 \cdot 10^{18}$ atoms of ^{229}Th from ORNL in 2018.

Because of the limited availability of the ^{229}Th isotope, a growth method had to be chosen to bring dopant losses to an absolute minimum. There are three main groups of crystal growth techniques: Vapor deposition [169], Solution growth [170] and melt growth [171]. In vapor deposition one or more species are evaporated through heating (usually in vacuum) and condensate on a colder substrate. The species can chemically react on the substrate to form more complicated molecules and the crystal orientation can be controlled by using the appropriate substrate. In solution growth, one or more species are dissolved in a liquid and these solidify through chemical reaction or supersaturation. Supersaturation is when the concentration of a dissolved material goes beyond the maximum saturation. The dissolved material will then start to solidify into a small particle. Once such a small particle has been generated the energy required to solidify on this particle is lower than producing another particle, stimulating single crystal growth. In melt growth, a powder of the species is liquefied and frozen to produce a bulk crystal. If done on a single crystal substrate or single seed crystal, this can promote single crystal growth.

All 3 techniques are used to grow CaF_2 where melt growth is specifically used to produce large crystals. All techniques can be used to grow single crystals in a particular crystal axis orientation, if the substrate or seed is appropriately orientated. It was found that across methods, the slower CaF_2 is grown, the lower the dislocation density in the single crystal. Vapor deposition is not very suited for doped growth due to the differences in boiling temperature between ThF_4 and CaF_2. Using vapor growth would also induce large losses of the scarce dopant. Solution growth is an interesting low temperature alternative but can be prone to contaminants and grows mainly small poly-crystals. Melt growth was chosen to develop a solid state nuclear clock to reduce losses and grow large single crystals.

After a short summary of the melt growth methods from literature, the chapter continues to describe the Th:CaF$_2$ growing process used in Vienna. It follows on the crystal growing work done in [172]. We reduce the length and diameter of the grown crystals in order to increase the concentration by a factor of $\approx$200. The chemical aspects of producing the raw material powders for growing, the mechanical aspects of filling seed single crystals and the thermal cycle of the growth process are presented. The chapter ends with a table summarizing all the grown crystals with their characteristics.

3.1 Radioactively Doped CaF_2 Melt Growth

Melt growth of doped CaF_2 needs a crucible to contain the high temperature melt. Graphite is often the material of choice due to its high chemical stability over a wide temperature range and low cost. The main source of contamination at these high temperatures is oxygen that reacts with the CaF_2. Also in vacuum, the liquid CaF_2 will start evaporating fluorine (F_2). To counteract these two effects, PbF_2 is added as a scavenger to react with the oxygen before CaF_2 and to increase partial pressure of F_2 in the starting phases of the growth [173]. Within melt growth, four techniques are often used for CaF_2 [92].

3.1.1 Czochralski Growth

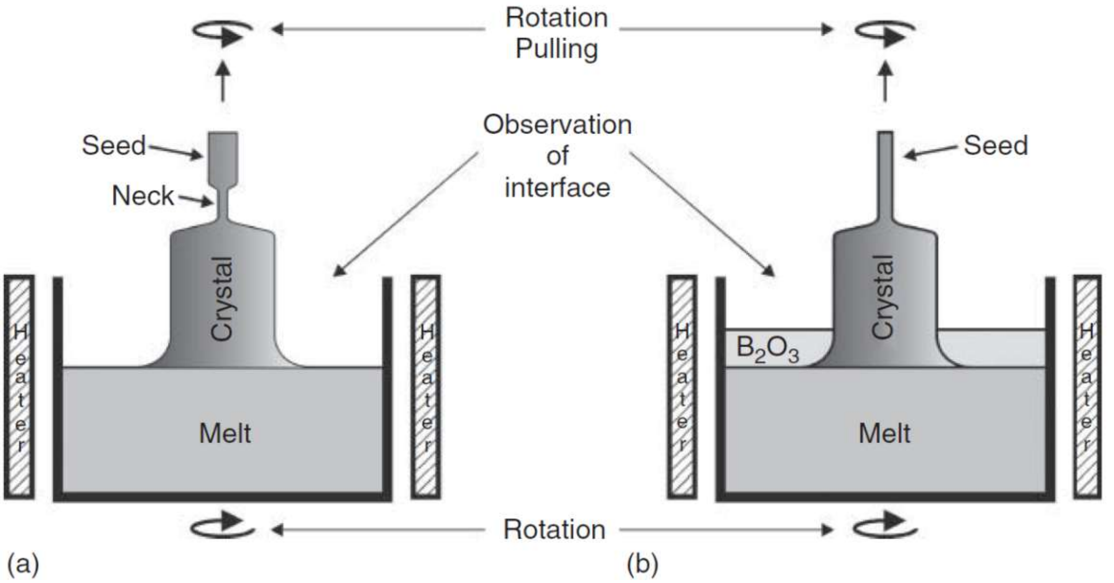

FIGURE 3.1: Czochralski growth apparatus (schematically): (a) Cz growth for Si with seed and necking structure and (b) GaAs Cz growth with B2O3 melt cover and without necking structure. Taken from [92].

Czochralski (Cz) growth, developed in 1918 [174], is one of the most technologically advanced and controllable growing methods. This is mainly because it is used to grow silicon for the semiconductor industry [175]. The method is illustrated in figure 3.1.

During Cz growth the raw material, possibly with dopants, is molten in a crucible using resistive or induction heating. This is usually done in a chamber filled with an inert gas or under vacuum. A seed single crystal is then brought close to the molten surface to bring seed and melt to the same temperature. The seed is then inserted into the liquid phase, and immediately pulled up slowly. While pulling up the crystal it moves further from the heaters thus starts to cool down. The liquid melt stays connected to the seed single crystal and also cools down slowly. The melt closest to the seed will solidify on the seed to a single crystal as well. In this process, constantly melt is solidified and new melt is pulled towards the crystal producing a large rod of single crystal. To guarantee homogeneity, usually seed and melt are rotated in opposite directions. Now the growing process is started by pulling the crystal. The diameter of the grown crystal depends on the densities of both phases and pulling speed of the seed

$$\nu_{eff} = \frac{\nu_{appl} A_{cruc}}{A_{cruc} - A_{cr}\rho_s/\rho_l}, \tag{3.1}$$

where $\nu_{eff/appl}$ is the effective or applied pulling speed, $A_{cruc/cr}$ the surface area of the crucible or crystal and $\rho_{s/l}$ the density of the solid or liquid state. The surface area of the crystal is determined by the melting temperature and the temperature gradient at the interface. Specialized techniques, such as creating a neck, are to decrease dislocation densities in silicon crystals. The minimum growing speed is limited by the diameter of crystal that one wants to obtain: The diameter will increase when using slow growing speeds. If one wants a small crystal the growing speed needs to be fast, so dislocation density will increase.

Cz growth was not chosen to produce ^{229}Th:CaF$_2$ because of the residue. In every Cz growth quite some residue is left, and the dopant preferentially stays dissolved in the melt thus the residue. Growing using this method would be wasteful to produce ^{229}Th:CaF$_2$.

3.1.2 μ-Pulling Down Growth

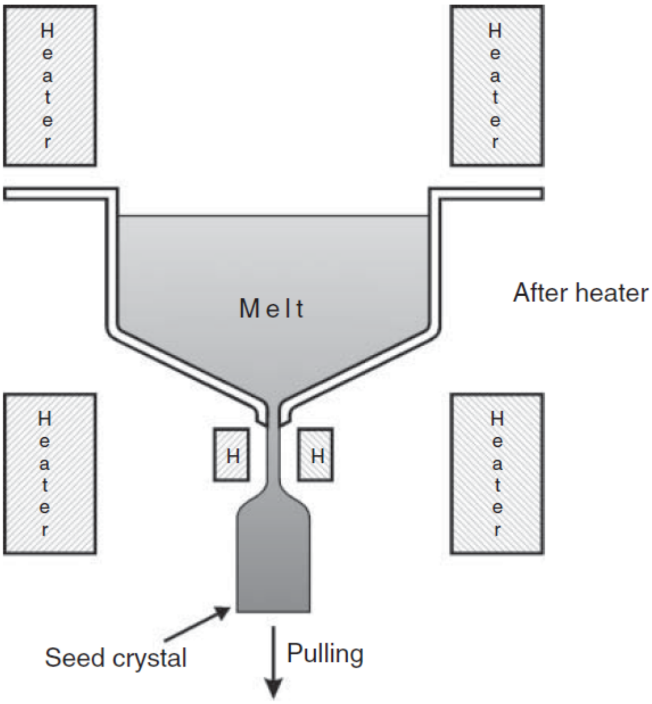

FIGURE 3.2: Schematic drawing of the μ-pulling down technique. Taken from [92]

A derivative of Cz growth, μ-pulling down resolves the issue of the residue taking up the dopant. The method is illustrated in figure 3.2. In this method, a melt is created in a crucible with a micro nozzle at the bottom out of which the melt will flow. A seed crystal is brought into contact with the melt and then pulls it downward out of the crucible. The size of the nozzle at the bottom prevents the melt to escape, owing to capillary forces due to the wetting angle with carbon and the high viscosity of CaF$_2$. Small crystals of micrometers to millimeters diameter are grown using this method. The surface area of the crucible in equation 3.1 is now the area of the micro nozzle. This method is active research [176]. It can possibly be used to grow fibers and crystals of any desired shape. Not all combinations of crucible and crystal work, depending on the adhesion of the liquid to the crucible the liquid material will slowly come out of the nozzle.

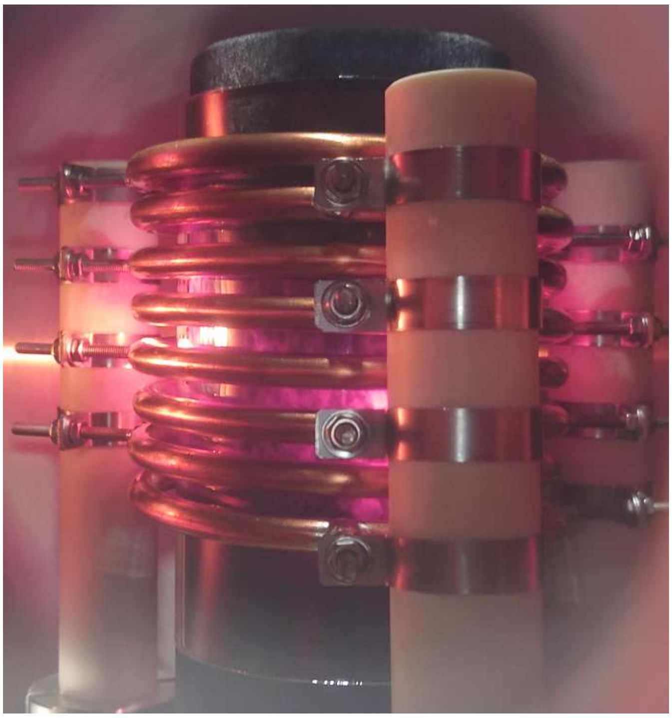

FIGURE 3.3: Graphite crucible and induction heating coils of the μ-pulling down growing chamber recently installed in Vienna. The chamber can be evacuated or filled with a gas during growth. Using a higher ambient pressure in the growing chamber will possible reduce fluoride evaporation and VUV characteristics will improve if for example CF$_4$ or NF$_3$ gas is used to increase F$_2$ pressure in the chamber [177].

This technique will be used in Vienna in the future, the device is being characterized at the moment and first induction heating tests are performed (see figure 3.3). Using μ-pulling down for growing single crystal doped CaF$_2$ has been demonstrated [178], but the VUV characteristics of these crystals has not been evaluated. Using this method, crystals shaped for use as optical elements can be produced, reducing losses of cutting and polishing even further. Possibly, even fibers of ^{229}Th:CaF$_2$ can be grown.

3.1.3 Bridgman Stockbarger Growth

The Bridgman Stockbarger growth, first described in [179], works on the principle of producing a steep temperature gradient around the melting temperature of the chosen material. The general setup is schematically drawn in figure 3.4. In the middle of the heaters is a crucible containing powder of the chosen material which can be moved up and down. The crucible has thermocouples attached to it as to monitor the progression

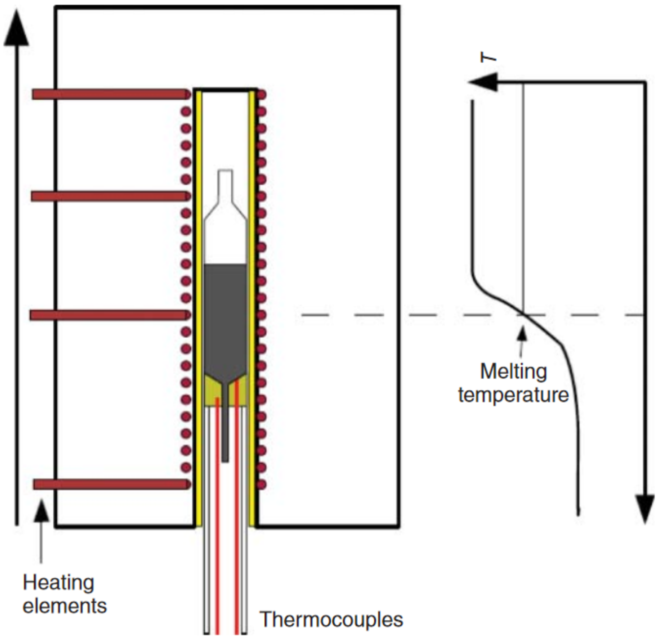

FIGURE 3.4: Schematic drawing of a Bridgman Stockbarger or Vertical Gradient freeze setup. Taken from [92]

through the temperature gradient. The material is first fully molten. The crucible as a whole is then slowly moved through the produced temperature gradient. The material that passes the gradient to the colder side will start freezing or crystallizing. Once the crystal has fully passed the steep temperature gradient it is fully crystallized. Heaters around the crucible keep an essentially constant temperature and maintain the steep temperature gradient.

The crucible is shaped such that the bottom is a capillary. In this method, the molten raw material first passes the gradient in a capillary. The capillary restricts the nucleation of the melt and will ensure that a single grain or crystal orientation emerges. On this capillary the main bulk crystal will be grown, which will then be a single crystal of uncontrolled orientation.

Due to the nature of this method, either the temperature gradient needs to move upward by changing the power of the heaters, or the crystal needs to be moved downwards mechanically. The entire procedure can also be performed horizontally.

If a single crystal seed is used, the crystal orientation can be ensured and the capillary is not needed. For this method to work, the seed crystal must not melt entirely. The temperature of a part of the seed crystal thus needs to be below melting point during the entire growing process. The shape of the solid/liquid interface has an effect on the defect densities of crystals grown by this method. The dislocation density can be greatly reduced if the interface shape is convex.

This method works if the temperature gradient is strong enough, otherwise nucleation can possibly happen at various different positions along the direction of temperature gradient. As an estimate for the temperature gradient of two heaters at temperatures T_1 and T_2 that are right next to one another for a material with melting temperature T_m we can use that $T_m > 0.5(T_1 + T_2)$.

An advantage of this method is that no residue is left, and thus all used dopant that did not evaporate is incorporated in the crystal. The biggest advantage of this method over Czochralski growth or μ-pulling down is that the crystal can be grown at any speed (<0.5 mm/h, reducing formed defects) without changing the diameter of the crystal. In Czochralski growth and μ-pulling down the diameter of the grown crystals are set from the start by the pulling speed, surface area of the crystal/nozzle and density of the material (see equation 3.1). In Bridgman, the crystal volume can be arbitrarily chosen by producing the appropriate crucible. A small crystal volume can be chosen to ensure high (10^{18} cm^{-3}) ^{229}Th doping concentrations with low losses of the extremely rare isotope. Downside is the moving parts that need to be at very high temperature (1691.00 K [180]) to grow CaF$_2$, which puts heavy restrictions on the materials used.

3.1.4 Vertical Gradient Freeze Growth

The vertical gradient freeze method or VGF, first developed in 1924 by Stöber [181] was inspired on the Bridgman method. The main difference is that Bridgman uses mechanical motion of a component to move the temperature gradient and VGF changes the heater temperatures to achieve this. The seeding procedure using the capillary or a seed crystal in the Bridgman method remains the same. The capillary of a stationary crucible is filled with raw material or a single crystal seed is put in the crucible with raw material on top. This method was chosen and thus developed in our group in cooperation with the Fraunhofer IISB to grow CaF$_2$ crystals with minimal dopant losses [172]. As for Bridgman, The biggest advantage of this method is that the crystal can be grown at any speed without changing the crystal diameter and thus size.

The Vienna approach is to place a single crystal seed in a graphite crucible with a powder on top. During growth, the gradient is adjusted such that the raw material on top of the seed crystal is molten together with a small part of the seed. This ensures that the seed does not completely melt, but the raw material does. The freezing barrier is then slowly moved upward so that the melt can crystallize on top of the seed crystal and thus grow a single crystal, following the orientation of the seed.

In the past, crystals of 17 mm diameter were grown [172]. This has been reduced to 3.2 mm diameter during this thesis by careful calibration and use of smaller seed crystals.

The main parameter to consider during melt growth of crystals is the Reynolds number. The Reynolds number helps to predict if turbulent or laminar flow will take place in a material. If turbulent flow is created in the crystal, more dislocations, vortexes and polycrystals are produced. The Reynolds number decreases for smaller crystals ($\propto$ L) which indicates more laminar flow and more controlled crystal growth in the liquid phase. Letting the melt reach higher temperatures increases the Reynolds number and thus produces more turbulent flow. When the crystal is cooled down to fast for solidification, crystals with more defects and chance of polycrystallinity will be produced.

Due to the higher thermal expansion coefficient of CaF$_2$ ($\approx 18.85 \cdot 10^{-6}\,°\mathrm{C}^{-1}$ at 300 K) than graphite ($\approx 4.2 \cdot 10^{-6}\,°\mathrm{C}^{-1}$ at 300 K) it is likely that dislocation densities will be high after growth due to crucible induced stress [92]. To compensate for this, a long annealing needs to be performed. In the end, the melt will take the shape of the crucible. The crystal will thus be 1.5 % smaller than the crucible when cooled down due to the high expansion coefficient difference. In vacuum the crystals shrink more due to sublimation of CaF$_2$

3.1.5 Phase Diagram of the CaF$_2$-ThF$_4$ System

When mixing two species, the melting temperature T_m will decrease due to melting point depression. To investigate the relation between T_m and the dopant concentration, the binary phase diagram needs to be studied. In [182] the phase diagram of the CaF$_2$-ThF$_4$ system was calculated and verified by measurements of the melting temperature for different mixtures of CaF$_2$ and ThF$_4$. Their results can be seen in figure 3.5. Because of the limited availability of ^{229}Th we don't expect to exceed molar fractions of 0.01 %, meaning the melting temperature of the powder mixture is not changed. Also supersaturation or supercooling effects[1] should be negligible due to the low concentrations involved.

Before CaF$_2$ melts there is a phase transition which can be seen on the top right of figure 3.5. This phase is called the superionic state and is seen in many ionic crystals [183]. In this state the anions (F$^-$) are highly mobile such that the crystal becomes an electrical conductor but the cations (Ca^{2+}) are immobile [184].

---

[1] Supercooling is when the temperature of a liquid goes below the melting temperature without solidifying, supersaturation when a higher dissolved concentration is reached than the critical concentration for solidification.

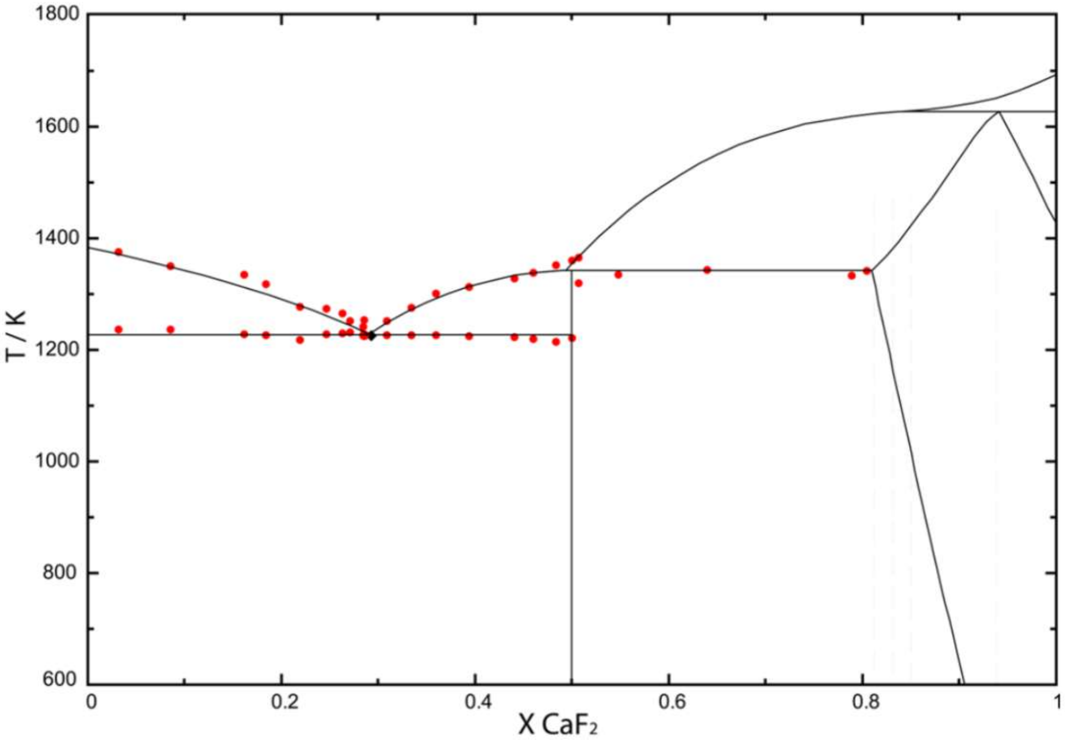

Figure 3.5: The binary phase diagram of the CaF$_2$ ThF$_4$ system. On the horizontal axis the molar fraction of CaF$_2$ is indicated, the vertical axis the temperature in Kelvin. The red dots are measurement points. Three distinct solid phases can be distinguished, Th:CaF$_2$, Ca:ThF$_4$ and ThCaF$_6$. The eutectic point can be found at 1224±6 K. At 0.91 CaF$_2$ molar fraction there is a solid to solid phase transition from CaF$_2$ to ThCaF$_6$. Taken from [182]

3.1.6 Health and Safety Considerations

Working with radioactive substances is accompanied by risks. During growth, some of the material will evaporate and contaminate the growth chamber. It will deposit on the carbon crucibles and possibly disperse as dust upon opening the growth chamber. While cutting and polishing grown crystals, again, dust may contaminate the air. Thorium-229 is the third most mortal and morbid common radioactive substance upon inhalation, after Curium-250 and Protactinium-231 [185]. The morbidity and mortality is mainly due to the three α-decays in fast succession in the ^{229}Th decay chain. The triple α-decay is the main characteristic which makes it attractive for targeted cancer irradiation in medical applications [186]. To protect against exposure to radioactivity, gas masks and protective clothing will be worn during the process.

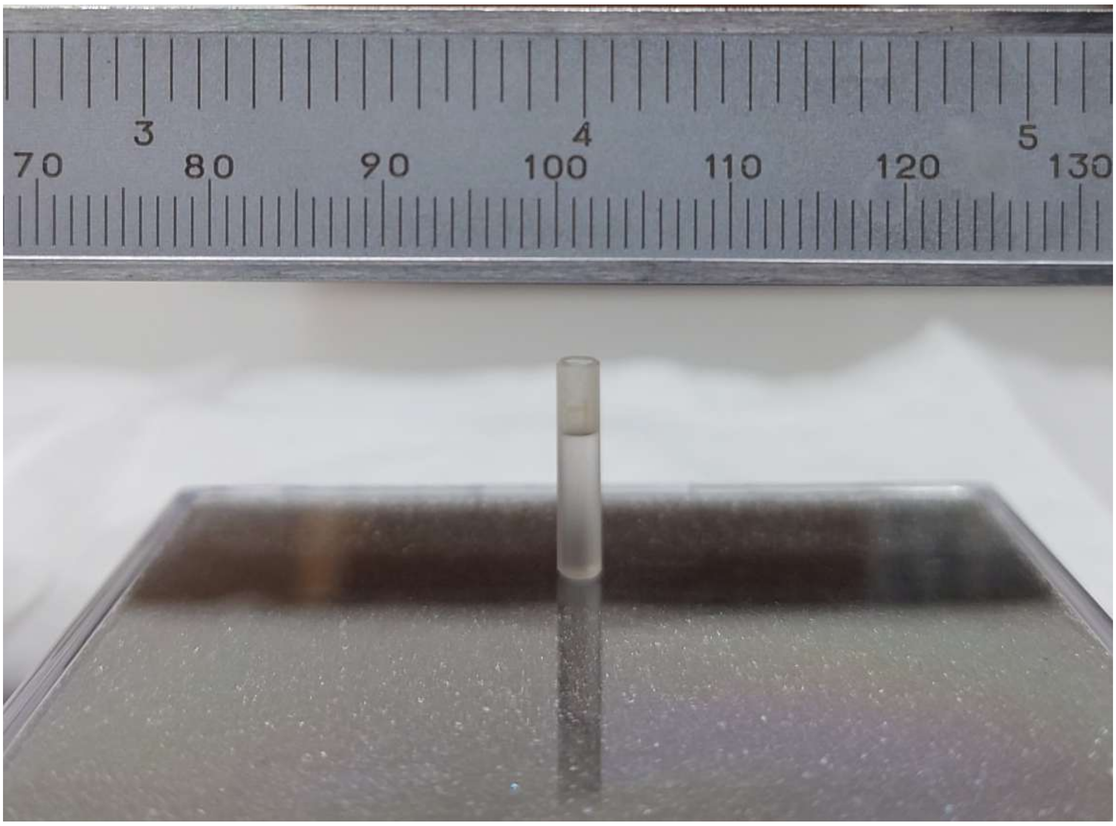

FIGURE 3.6: Seed crystals with 3.2 mm diameter, 12 mm length and 2 mm diameter, 5 mm depth pocket used for growing highly doped ^{229}Th:CaF$_2$. This pocket is filled by using a small aluminum funnel (see figure 3.10) that fits perfectly in the graphite crucible and matches the pocket diameter. This small funnel is filled using the aluminum container and large funnel (see figure 3.9).

3.2 Crystal Growing Devices, Growing Process and Optical Finishing

The initial goal at the beginning of this thesis was to increase the doping concentration of ^{229}Th in single crystal CaF$_2$ using the VGF method. The previously designed VUV excitation setup (chapter 5) and x-ray excitation setup (chapter 7) would be unable to measure a nuclear VUV signal unless the concentration would be increased. Due to the low availability of ^{229}Th, the only method to increase the doping concentration was to reduce the volume of the crystals, so the diameter was decreased from 17 mm to 3.2 mm, and the length from 40 mm to 5 mm. The main difficulty was finding a supplier for small seed crystals. In the end the smallest seed crystals to be found were 5 mm diameter, available from the companies: Korth, Mateck and Alkor. Afterwards Hyperion optics was employed to mill these crystals down to only 3.2 mm diameter and drill a small pocket in the top, see figure 3.6.

To grow CaF$_2$ crystals, a high temperature crystal growing device is needed that can contain a non-oxidizing atmosphere. Temperatures above 1500 °C are needed, and the CaF_2 needs to be protected from O_2 to prevent oxidation. In this work it was chosen to grow the crystals under vacuum to prevent oxidation. Aside from growing in a vacuum, so called oxygen scavengers are used to remove trace amounts of oxygen to prevent oxidation.

Before growth, preparing a CaF_2 powder containing scavenger and dopant requires a well controlled chemical procedure. During growth, a well tailored temperature cycle was designed in [172] to remove water from the initial powder and reduce defect production in the crystal during the growing process. This cycle consisted of: Drying, oxygen scavenging, melting/growing, annealing and slow cooling down.

A large improvement as to the crystals grown previously is using RAMAN/Excimer grade seeds and extra pure CaF_2 powder with reduced metal contamination. The RAMAN/Excimer grade seeds are grown using chemically purified CaF_2 powder. Both names (RAMAN/Excimer) are used by companies because they supply two markets: Low contamination to reduce background in Raman spectroscopy and robustness to damage from VUV light for excimer laser related experiments (157 and 193 nm). In the past [172], infrared grade CaF_2 was used which undergoes little chemical purification. Especially yttrium contamination causes degradation of VUV properties [187].

In the end, this chapter covers the cutting and polishing done to the grown crystals to prepare them for optical measurements. Down to 1 mm^3 crystals were cut and polished for experiments.

3.2.1 Decreasing Grown Crystal Diameter from 17 mm to 3.2 mm

As described above the concentration of ^{229}Th needed to be increased in order to design viable experiments. By decreasing the diameter of the seed crystals and therefore the doped crystals by a factor of $\frac{17}{3.2} \approx 5$ the volume decreased by a factor of 25 while keeping the length equal. We also decreased the length of the crystal from 40 mm to 5 mm, decreasing volume by another factor of 8. When using the same amount of ^{229}Th, the concentration will increase by 200 times and thus in any experiment with a beam spot smaller than the diameter, the signal will increase by a factor of 200. The experimental process of decreasing crystal diameter is shown in figure 3.7.

The diameter of the inner crystal crucible (see figure 3.8) was adapted and decreased to the different available seed diameters. By fitting the crucible diameter to the seed diameter, the crystal was centered in the growing setup. The fitting diameter also promoted heat conduction and allowed us to plainly put the powder on top of the

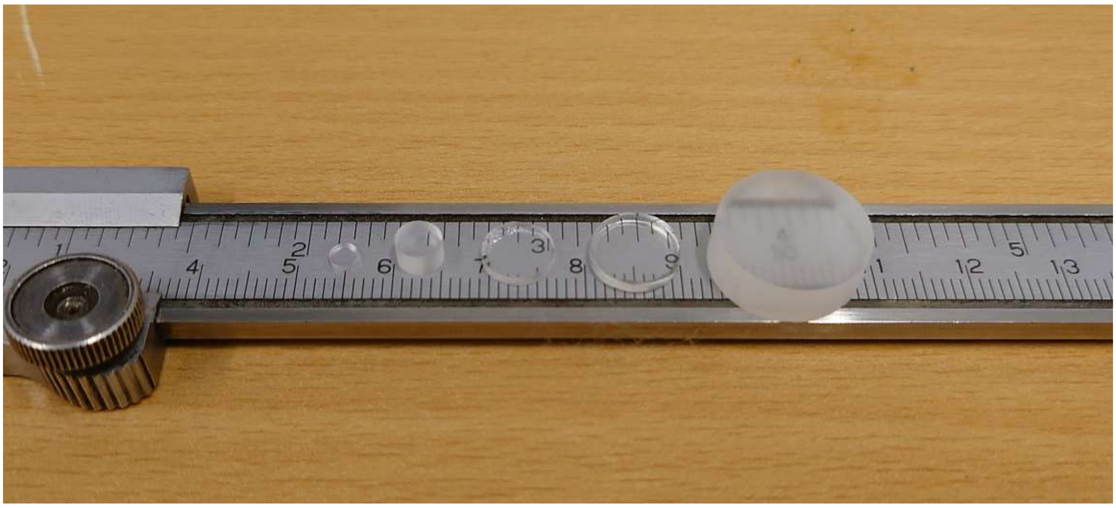

FIGURE 3.7: The experimental steps undertaken reducing the crystal diameter from 17 mm to 3.2 mm. Crystals were cut to different lengths. Diameters were limited by the diameters available for seed crystals: 17 mm, 10 mm, 8 mm and 5 mm. The last miniaturization step to 3.2 mm was done by milling down a 5 mm diameter seed by an optics company (Hyperion optics).

seed crystal. Small steps were taken in miniaturization in order to keep check on all parameters that govern the crystal growing process, for example: heat capacity of the materials, flow characteristics in the melt, absolute melting temperature and ambient pressure.

By decreasing the size of the crystals the steep temperature needed to be more precisely controlled. Small changes in temperature would more rapidly result in full melting of the crystal or no melting at all. For the larger crystals there was a larger tolerance for errors in the calibration due to higher heat capacity and usually larger length dimension. One benefit of growing smaller crystals is the reduced probability of turbulent flow caused by convection within the melt: According to the Reynolds number, problems of convection and turbulent flow should decrease with decreasing size.

The first steps in growing smaller diameter crystals were done using the same method as described in [172]: The doped CaF$_2$ powder was placed plainly on top of a seed and the growth process was started. In this phase two scavengers were tested: ZnF$_2$ and PbF$_2$. The scavenger PbF$_2$ gave the highest VUV transmission around 150 nm as was observed before [188].

The small amount of powder used in these processes was prone to fall beside the crystal, in the crevices between crystal and crucible. When a ^{229}Th crystal would be grown this would mean a doped single crystal would be grown on the side of the seed crystal, not on top. This would reduce ^{229}Th doping concentrations of the top. To counter this, a

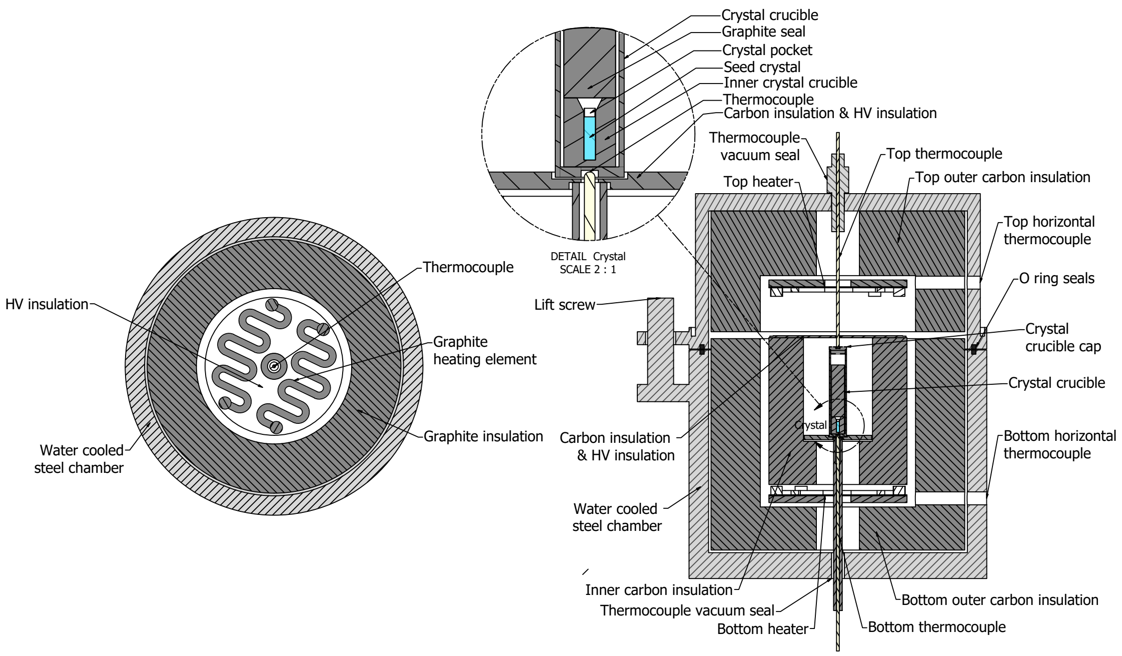

Figure 3.8: Crystal growing machine used to grow 3.2 mm diameter crystals. On the left side is a horizontal cut displaying the graphite heating element with the isolated vertical thermocouple through the center. Right image displays a vertical cut which shows all of the main components of the vertical gradient freeze growing machine and a zoom in of the crystal location. The vertical thermocouples are made of platinum/rhodium (Pt30Rh-Pt6Rh) with an alsint casing. The horizontal thermocouples are made of molybdenum. The vacuum seals for the thermocouples are made of vyton, which is able to withstand both the low pressure fluorine atmosphere and the high temperatures which still persist at the ends of the thermocouple. Water is run through the steel vacuum chamber to provide cooling.

2 mm hole was drilled in the center of the 3.2 mm diameter crystals (3.6). This pocket would contain the dopant powder without losses to the sides.

3.2.2 Preparation of ^{229}ThF$_4$:PbF$_2$:CaF$_2$ Powder

The following describes the preparation of 45 mg of ^{229}ThF$_4$:PbF$_2$:CaF$_2$ powder for growing crystals with 3.2 mm diameter and 10 mm length. Here values are reported of the process since only a limited amount of ^{229}Th was available. The powder for crystals grown with ^{232}Th used the same process and ratios as the one described below, producing 15 mg of powder for every crystal. Only the highly ^{232}Th doped crystals used a different method of powder preparation, described below (3.2.3). The ThF$_4$ and PbF$_2$ were coprecipitated. This way the small amounts of ^{229}ThF$_4$ ($\approx$15 μg to 1 mg) were incorporated in a larger quantity (>1 mg) for practical handling in the crystal growing.

^{229}Th (7.9 MBq, Oak Ridge National Laboratory, in dried nitrate form) was dissolved in 0.1 M HNO$_3$ Suprapure grade (Sigma Aldrich) prior to use. All reagents CaF$_2$ (Alfa Aesar), Pb(NO$_3$)$_2$ (Sigma Aldrich), PbF$_2$ (Alfa Aesar), 40 % HF (Sigma Aldrich) were purchased from commercial suppliers in trace metal grade and were used as received. Using higher quality CaF$_2$ powder increased the VUV transmission of the grown crystals. Water was purified in-house by triple distillation.

In a centrifugation vial a solution of ^{229}Th in 0.1 M HNO$_3$ (9 mL, 5.5 MBq) was mixed with lead(II) nitrate (2.9 mg) and precipitated as ^{229}ThF$_4$:PbF$_2$ by subsequent addition of hydrofluoric acid (40 %, 1 mL). A white precipitate appeared immediately and was allowed to rest over night. The supernatant was carefully removed using a pipette after centrifugation and the precipitate was washed with triple distilled water (2 mL, 6 times). After the fourth washing step, the supernatant was tested for remaining free fluoride ions by adding a small portion of an aqueous solution of CaCl$_2$. No appearance of any white material confirmed the absence of free fluoride ions, and two additional washing steps were performed.

The ^{229}ThF$_4$:PbF$_2$ was then poured into an aluminium container (No. 1, figure 3.9) with a small portion of water and allowed to dry in an oven at 80 °C until weight was constant (4 days). Then CaF$_2$ (28.3 mg) was added to the ^{229}ThF$_4$:PbF$_2$, mixed thoroughly and measured via γ spectroscopy. The γ spectroscopy was performed with a 151 cm^3 HPGe detector from Canberra Industries (1.8 keV resolution at the 1332 keV ^{60}Co peak; 50.1 % relative efficiency), connected to a PC-based multi-channel analyzer with preloaded filter and Loss-Free Counting (LFC) system.

The powder was then combined with a previous batch of ^{229}ThF$_4$:PbF$_2$:CaF$_2$ (15 mg, containing 0.3 MBq ^{229}Th) to give a total amount of 45 mg ^{229}ThF$_4$:PbF$_2$:CaF$_2$ with a weight ratio of 0.33:1:14 and a total activity of 5.8 MBq ^{229}Th used. The previous batch originated from a trial run of above mentioned method. The stock powder was then split in 3 parts of equal amount by weight (15 mg) to give three aluminium containers with equivalent material (No. 1, No. 2, No. 3). All vials were measured with gamma-spectroscopy in the same geometry to check the distribution of activity between the containers and stored in a desiccator until used. Due to losses during the process 4.7 MBq out of 5.8 MBq ^{229}Th were obtained as usable powder.

3.2.3 Preparation of ^{232}ThF$_4$:PbF$_2$:CaF$_2$ Powder

Two different methods for the ^{232}ThF$_4$:PbF$_2$:CaF$_2$ sample preparation were used. Method A was used to prepare ^{232}Th containing powder analogous to the ^{229}Th powder. Then conditions (ratios between components, water content, contamination, etc.) were kept constant between growing ^{232}Th:CaF$_2$ and growing ^{229}Th:CaF$_2$. Method B was used when different ratios between components should be tested. Using this method avoided the lengthy coprecipiation which allowed for quick testing. Losses of Th were not important in this method because the abundant ^{232}Th was used. The two methods were:

A: The sample was prepared analogous to the ^{229}ThF$_4$:PbF$_2$:CaF$_2$ procedure described above using ^{232}ThNO$_3$ instead of ^{229}ThNO$_3$. A small amount of ^{229}ThF$_4$:PbF$_2$:CaF$_2$ was added (1 kBq of ^{229}Th) to the ^{232}ThF$_4$:PbF$_2$:CaF$_2$ powder for tracing purposes.

B: The sample was prepared by mixing commercially available CaF$_2$, PbF$_2$ and ^{232}ThF$_4$. Then 1 kBq of ^{229}Th was also added for tracing purposes.

3.2.4 Filling the Pocket in the 3.2 mm Diameter Crystals

The final step of the powder production, drying, was done in an optically polished aluminum container (figure 3.9). A funnel where the inside is also optically polished is then connected to the top by screws. The end of the funnel fits on a second funnel (figure 3.10) which is placed in the empty space in the inner crystal crucible (figure 3.8) above the 3.2 mm crystal. This way one could flip the container directly into the second funnel which would guide the powder into the pocket of the 3.2 mm crystal. By tapping the container, second funnel, and crucible, all powder is transferred to the crystal. The amount of material left in the container was less than the minimum error of the scale (0.1 mg). Residual radioactivity measured with a proportional counter in container No. 1 was less than 100 Bq: It is unsure if this was due to daughters of ^{229}Th being implanted into the walls during radioactive decay or also ^{229}Th itself.

By polishing the container, less powder will get stuck on surface irregularities during the transfer process. The container was made out of aluminum such that the powder would not be charged by static electricity. Static charging caused the powder to get stuck on the walls in previous versions of the transfer process. The entire procedure took place in a fume hood in the radiochemistry lab and the inner crystal crucible was immediately placed carefully by inverse tweezers into the larger crucible and closed. The larger crucible was then transferred to the crystal growing device for growth.

3.2.5 Growing (doped) 3.2 mm Diameter Crystals

By using a smaller inner crystal crucible and accurate calibration of the previous 17 mm diameter setup we have been able to grow 3.2 mm diameter single crystals with a radioactive dopant using the vertical gradient freeze method (see section 3.1.4). This method was developed in our group in cooperation with the Fraunhofer IISB to grow

FIGURE 3.9: Aluminum container for ^{229}Th powder and funnel that can be mounted on top of the container. The insides of both components was polished to optical quality using diamond paste to reduce powder sticking to the walls. One milligram of powder can be barely seen on the bottom of the container.

FIGURE 3.10: Small funnel used to fill the small seed crystal (see figure 3.6). This funnel connects to the crystal and the large funnel such that powder can be filled from the large container up to the crystal with minimal losses.

17 mm diameter crystals with minimal dopant losses [172]. The biggest advantage of this method over other methods like Czochralski is that the crystal can be grown at any speed (<0.5 mm/h) without changing the diameter and the crystal volume can be kept small to ensure high ($10^{18}\,\mathrm{cm}^{-3}$) doping concentrations with the extremely rare ^{229}Th isotope. The Reynolds number decreases for smaller crystals ($\propto$ L) which indicates more laminar flow and thus easier crystal growth in the liquid phase.

We decreased the length of the crystals from 40 mm to 10 mm to further increase doping concentration. Due to this length reduction the melting front needed to be more accurately controlled such that a single crystal was grown. The 5 mm diameter seeds were

FIGURE 3.11: Tools used to fill the 1 MBq ^{229}Th powder into the 3.2 mm diameter crystals inside the fumehood of the radiochemistry lab.

bought from Korth, Mateck and Alkor and then sent to Hyperion Optics to be milled down from 5 mm to 3.2 mm diameter and to drill a 2 mm diameter hole in the top, 5 mm deep as can be seen in the zoom in of figure 3.8 and in figure 3.6. The grade of the crystals bought was RAMAN/Excimer, as detailed above. In [172] infrared grade crystals were used which contain more metal contaminants which reduces VUV transmission.

To summarize the growth method: A powder ($UF_4/ThF_4:PbF_2:CaF_2$) is put on top of a pure CaF_2 single crystal seed. In our case a pocket in a 3.2 mm diameter CaF_2 seed crystal (see figure 3.6) is filled. A steep temperature gradient is applied such that the powder melts at the top of the crystal, but not the bottom of the crystal. Then the gradient is slowly moved upward such that the melt freezes and takes the orientation of the single crystal seed.

The result of this process is a doped single crystal fused to a pure single crystal, as is visible in figure 3.12. The ^{238}U:CaF$_2$ single crystal was partly molten into the seed crystal. Uranium was used in the first attempts due to our experience with it [45], and its strong coloring effect on CaF_2 which would clearly show the melting boundary which would ensure single crystalline growth.

These crystal are grown using the same temperature recipe as the former 17 mm crystals [172]. A crucial difference is the temperature calibration procedure. The most crucial process phase is the hottest temperature, when the crystal is partly molten into the seed crystal. In this step the top heater is set to the hottest temperature and left at the same temperature for all crystals grown. This way one can produce the steepest temperature gradient over the crystal. Now only the temperature of the bottom heater

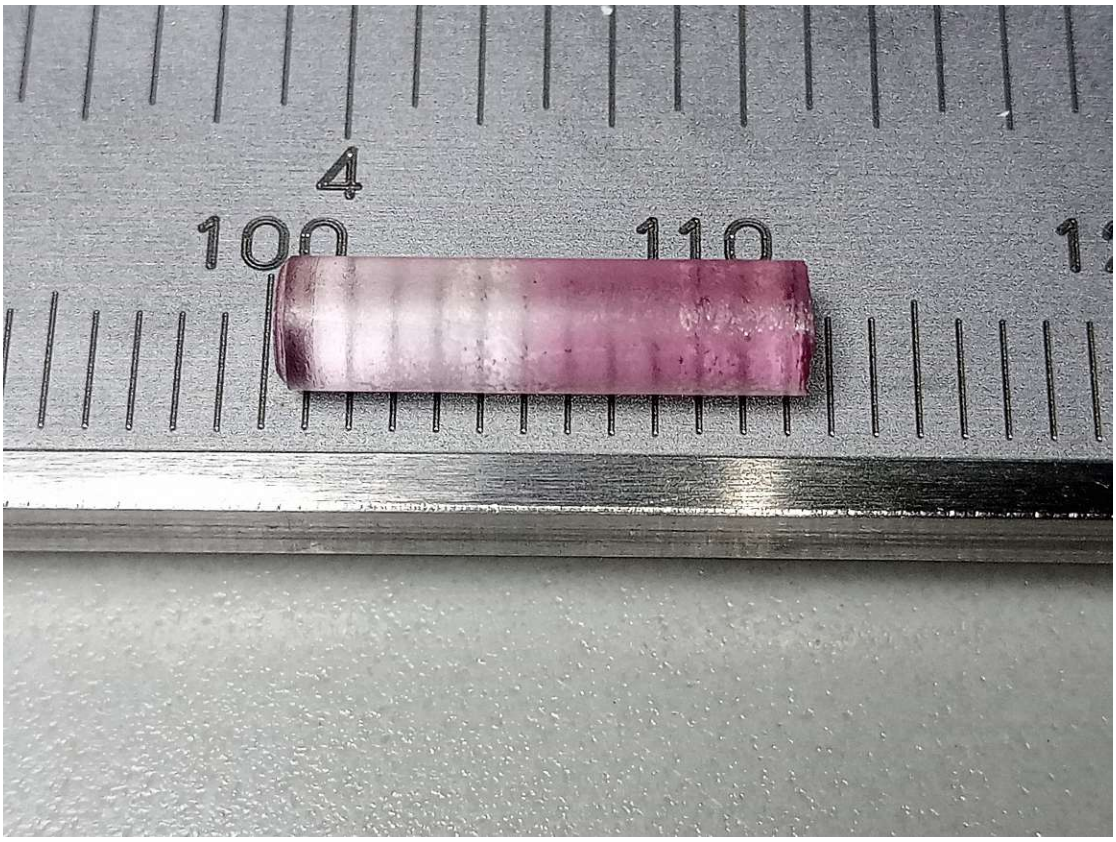

FIGURE 3.12: ^{238}U:CaF$_2$ single crystal grown as demonstration of the method. The melting boundary can be clearly seen in the color difference. The bottom (left) is slightly colored due to Uranium outgassing from the carbon crucible that accumulated there in earlier growth cycles and penetrating the upper layer of the CaF$_2$ crystal. Top of the crystal is on the right.

needs to be changed such that the melting boundary is positioned halfway into the seed crystal. The position of the temperature gradient can be identified after the growth by visual inspection for uranium doped crystals, see figure 3.12.

To calibrate at which temperature Th:CaF$_2$ needs to be grown, the more abundant ^{232}Th is used. Since thorium does not colour the CaF$_2$, the smallest possible amount of ^{229}Th is added to ^{232}Th doped crystals ($\approx$1 kBq) to identify how far the dopant penetrated into the crystal using the gamma spectrometer. A typical result can be seen in figure 3.13 for crystal C5. Once the correct growth temperature was identified ^{229}Th powder was used to grow the ^{229}Th:CaF$_2$ crystals. In the end, this was not needed for highly doped ($> 10^{18}$ cm^{-3}) ^{229}Th:CaF$_2$ as they colored orange where the ^{229}Th was doped, see figure 3.21.

One important characteristic that was identified is that the temperature calibration drifts significantly. This was due to the outside temperature changing (non-ideal lab conditions) but also the inside temperature (aging of material). The thermocouples only measure the difference between the temperature inside the oven and outside so by

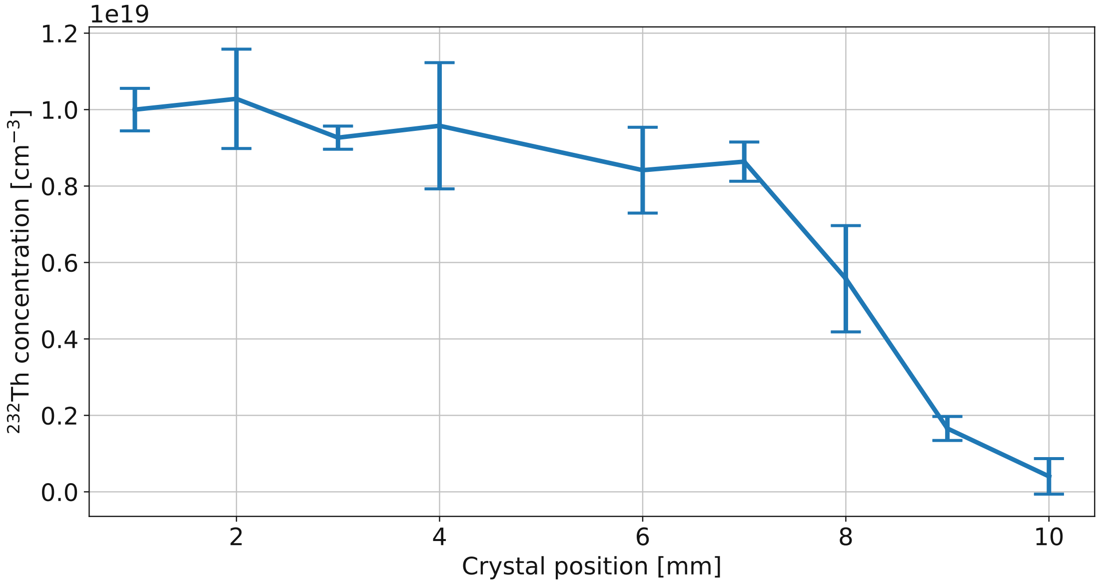

FIGURE 3.13: Concentration profile of ^{232}Th doped into CaF$_2$ by measuring a known ratio of ^{229}Th to ^{232}Th on a γ spectrometer. From top of the crystal (left) to 7 mm down into the crystal the concentration decreases slowly. This indicates that the dopant is incorporated well into the lattice with almost no freezing distillation occurring. After 7 mm a sharp drop in ^{232}Th concentration is observed, indicating the melting boundary.

measuring the outside temperature independently the drift on the inside of the system could be isolated. An independent measurement was set up to measure the outside temperature.

The set and actual temperature on the inside thus did not correspond inside the crystal growing chamber (3.8). Due to this inconsistency, shortly before reaching the melting stage of the growing process the temperatures indicated by the thermocouples was checked. By looking at the behavior of the top and bottom thermocouples, which did not age much, it could be determined if the side thermocouples were off due to aging effects. If deviations were seen the temperature was adjusted accordingly. This calibration was necessary to consistently melt partly into the seed crystal and thereby producing doped single crystals by always producing a similar temperature gradient.

3.2.6 Growth Process

To grow the 3.2 mm diameter, 1 cm long crystals, first the seed was filled with the prepared powder. The filled seed was then placed in the VGF crystal growing machine (figure 3.8). Using the VGF method (3.1.4), the seed was grown to a single crystal: By controlling the top and bottom heaters a steep temperature gradient was created. Two carbon heaters (left side of figure 3.8) are used to create the steep temperature gradient over the crystal, partially melting it. Short term temperature stability is maintained with short horizontal thermocouples close to the heaters and absolute calibration is done with long vertical thermocouples close to the crucible. Because the temperature at the crystal pocket is not the same as the one indicated by the bottom thermocouple. An iterative calibration process is needed to only melt the seed crystal midway. Important here is to carefully monitor the in and outside temperature of the thermocouples to get an accurate temperature measurement and avoid drifts in the system. The graphite and alsint cannot touch, since at high temperatures these two react which slowly degrades the casing of the thermocouples and can create vacuum leaks.

The temperature cycle of the growing process (shown in figure 3.14) is divided into five sections: 1) 18 hours of heating up the system, outgassing, and restoring pressure (see figure 3.15 2) 6 hours of scavenging oxygen through reaction with PbF$_4$ 3) 22 hours melting the top half of the crystal and slowly freeze it again 4) 18 hours annealing the crystal 5) 14 hours of cooling down. A vacuum of at least 10^{-4} mbar is obtained before growing. During growing (especially during section 1) the pressure can go up to 10^{-2} mbar. The growth typically takes 3 days.

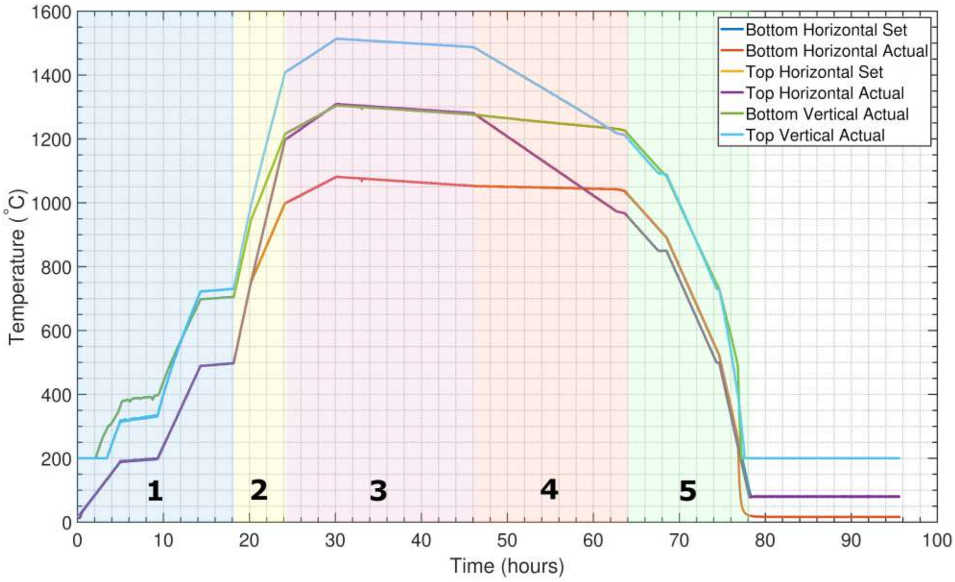

FIGURE 3.14: Temperature cycle versus time to grow 3.2 mm diameter crystals as set and measured by the thermocouples indicated in figure 3.8. The sections as described in the text are indicated as well. The entire process takes about 80 hours or approximately 3 days.

Due to the radioactive nature of the dopant, extra care has to be taken in the growth process. On the pre-pump, carbon filters are installed to absorb the evaporated dopant. The gaseous dopant also gets absorbed into the graphite insulation, which is highly active after several growth cycles. Every growth, the insulation absorbs and releases some dopant; cross-contamination of dopants was observed in a pure CaF$_2$ crystal grown after

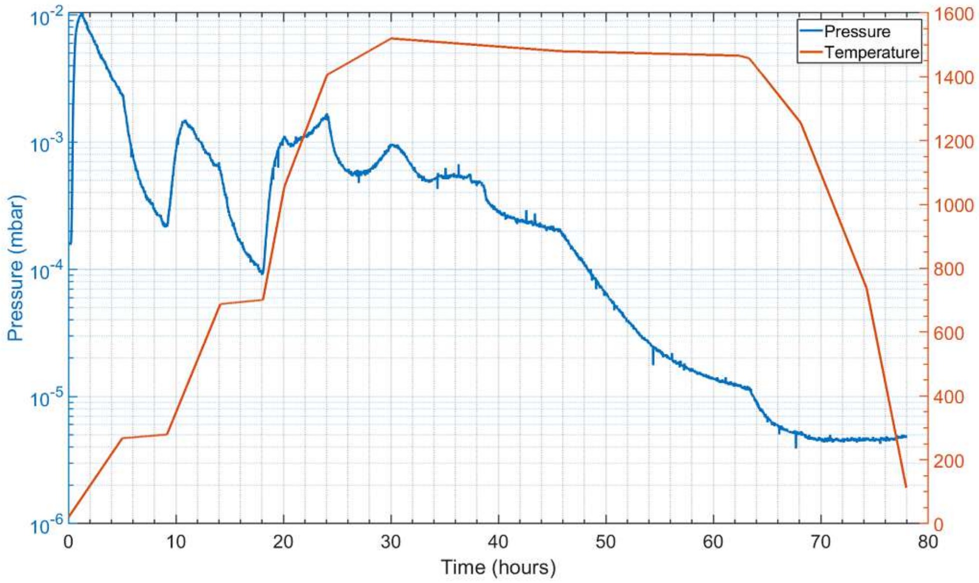

FIGURE 3.15: Pressure evolution during the temperature cycle versus time to grow 3.2 mm diameter crystals. Temperature was taken from the top vertical thermocouple. One can see that every increase in temperature increases the pressure, which after temperature stabilization decreases again. Interestingly the pressure does not significantly increase anymore at temperatures above 1000 °C.

growing a radioactively doped crystal. After every growth several tools need decontamination.

One important aspect of growing CaF$_2$ crystals is the probability of incorporating oxygen, especially at higher temperatures [188, 189]. The carbon crucible should at elevated temperatures react with any background O$_2$ in the system but will not take out the H$_2$O which is adsorbed in the crystal powder, so called crystal water. The water will oxidize the CaF$_2$ according to

$$\mathrm{CaF_2 + H_2O \rightarrow CaO + 2HF}. \tag{3.2}$$

To mitigate this, oxygen scavengers are used: Fluoride compounds that react preferentially with oxygen and water and which are successively transported away such that the oxygen is replaced by fluoride:

$$\mathrm{CaO + PbF_2 \rightarrow CaF_2 + PbO}, \tag{3.3}$$

$$\mathrm{H_2O + PbF_2 \rightarrow 2HF + PbO}. \tag{3.4}$$

The gaseous oxides will then react with the carbon in the walls where they form CO_2 and solid metal on the walls

$$2\mathrm{PbO} + \mathrm{C} \rightarrow \mathrm{Pb} + \mathrm{CO_2}. \tag{3.5}$$

PbF_2 and ZnF_2 were tested for the thorium doped crystals, as was first demonstrated in [188] to work for undoped crystals. Better VUV transmission characteristics were observed for thorium doped crystals with PbF_2 than with ZnF_2, as was demonstrated as well for undoped crystals. For all future growths only PbF_2 was used as a scavenger.

Melting a mixture of CaF_2 and ThF_4 will change the melting temperature, as investigated in [182]. Since the amount of available ^{229}Th will not allow to grow higher doping concentrations than 0.05 wt % (1 MBq) to 0.5 wt % (10 MBq) we do not expect significant changes in the melting temperature, which would affect our calibration process depending on the doping concentration, or a partial phase transition to $CaThF_6$ (at 19 wt %).

3.2.7 Cutting and Optical Polishing of Crystals

Grown crystals were cut using a diamond wire saw, see figure 3.16. The crystals were fixated on a ceramic plate using seal wax. The ceramic plate with crystal was then mounted on a rotation stage such that a 90 degree angle of the crystal axis and the cutting plane could be ensured. This cut results in a cylindrical shape which is used throughout the measurements in this thesis (figure 6.14 and 5.14). Also cubic crystals can be cut, as was done for the x-ray experiments (see figure 3.18 and 7.15).

To ensure parallel cutting surfaces, the surfaces were cut by only transversely displacing the crystal using a micrometer screw. The amount of pressure on the crystal was increased during this thesis as opposed to previous procedure [172]; this reduced vibrations of the wire making patterns on the cutting surface. Every slice of crystal would be given a number to indicate which crystal it came from and which slice it is. For example V12.1 is the top slice of V12 and Cal3.5 is the last slice of Cal3.

After cutting, the new surfaces would be polished using the polishing machine in figure 3.17. Here the crystal would be held by hand shortly on a P4000 SiC sanding paper spinning at 200 rpm with as little pressure as possible. This was done to not change the orientation of the surfaces and keep them parallel. A lubricant and cooling liquid needs to be constantly provided on the polishing paper for good results. Instead of water, isopropanol was used to lubricate and cool the crystal during polishing. As was described

FIGURE 3.16: Diamondtec wiresaw used to cut the small crystals. The diamond wire had a diameter of 0.08 mm. By using a rotation stage the crystals could be accurately cut.

in chapter 2, the isopropanol doesn't increase the VUV absorption of the crystal as much as water due to incorporation in the surface.

Using these methods, 1 mm^3 crystals were produced to be used for example in the x-ray excitation experiments, see figures 3.18 and 3.19. Other crystals were left cylindrical, producing less waste and thus lost ^{229}Th.

3.3 Produced $^{229/232}$Th:CaF$_2$ Crystals

The crystals produced during this thesis can be divided into 5 categories that were grown each with a specific purpose (see table 3.1). First the 5 mm diameter crystals were grown, named after their diameter, and characterized to see what effect miniaturization had on the optical quality. Here no seed was used which often led to vortexes in the crystal, see figure 3.20. Here it was learned that growing a single crystal was important for the VUV transparency, polycrystals had very low transmission. It was found that defects are more

FIGURE 3.17: Buehler polisher used to polish the crystals. Since the holders were not suited for the small crystals often polishing was done by hand. A P4000 SiC polishing paper was used to polish the cut crystal surfaces.

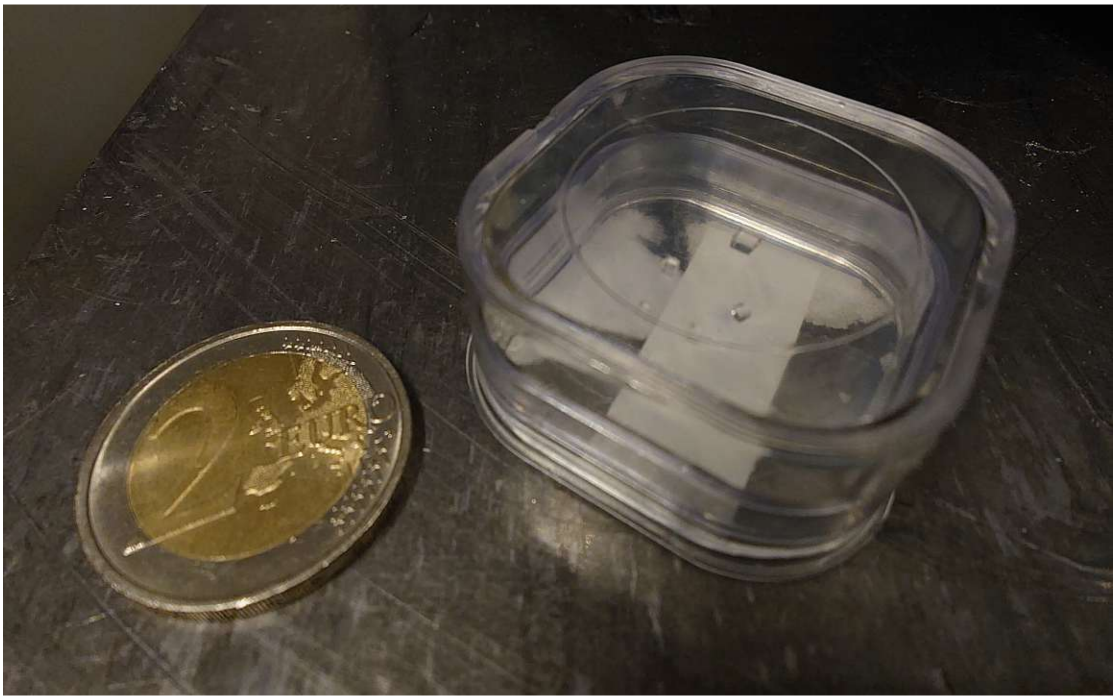

FIGURE 3.18: Four 1 mm^3 and one 4 mm^3 ^{229}Th:CaF$_2$ crystals cut and polished using above techniques.

easily created on grain boundaries and can move more easily over them. Especially VUV radiation is heavily absorbed by these boundaries and damage the crystal more easily.

FIGURE 3.19: Zoom of 1 mm^3 and 4 mm^3 crystals in figure 3.18

FIGURE 3.20: CaF$_2$ crystal grown with a vortex of bubbles. The origin of these vortexes is unknown, but radial/longitudinal temperature fluctuations and convection could be a cause. Often more and stronger vortexes were seen for crystals that were grown at very high temperatures, increasing boiling.

TABLE 3.1: Different categories of crystals and with which goal in mind they were grown.

Name	Diameter	Goal	Dopant
5mm	5 mm	Reduce crystal diameter	^{232}Th
C	3.2 mm	Grow ^{229}Th:CaF$_2$	$^{232/229}$Th
V	3.2 mm	produce high concentration of ^{232}Th	^{232}Th
Cal	3.2 mm	Recalibrate for growth of ^{229}Th:CaF$_2$	^{232}Th
X	3.2 mm	Grow high doped ^{229}Th:CaF$_2$	^{229}Th

After this the C crystals were grown, named after ”crystal”, to learn how to grow 3.2 mm diameter single crystals and in the end add ^{229}Th. Growing C crystals with ^{232}Th doping was initially successful and had good characteristics. The 6 MBq of ^{229}Th solution that was bought from ORNL was divided in 1, 2 and 3 MBq to have three attempts at growing ^{229}Th:CaF$_2$. By measuring the ^{229}Th activity in the seed crystal before and after growth in the γ spectrometer in a calibrated geometry it was found that 20 % of the ^{229}Th that was in the powder ended up in the crystal. The rest probably diffused into the graphite crucible walls, as it was highly active.

The first attempt was the successful C10, this was followed by a new calibration C11 to ensure single crystals. After which two failed attempts followed, C12 and C13. The apparent temperature to grow single crystals decreased, causing the seed to melt completely which resulted in polycrystals. Growing was stopped to plan a new course of action. In the end it was found out that only 10 % of all ^{229}Th was used, the rest remained on the walls of the container for chemical preparation. Because a lower concentration of thorium was used than expected, the melting temperature for single crystal growth changed (see figure 3.5). The remaining fraction was separated to gain another attempt at growing ^{229}Th:CaF$_2$ crystals.

To explore possible color centers in CaF$_2$ the V (for ”Version”) crystals were grown with high concentrations of ^{232}Th. After these the calibration for growing ^{229}Th:CaF$_2$ was started again. Here the Cal crystals were grown to calibrate the growing machine for ^{229}Th growth. The melting temperature for single crystal growth changed due to the concentration change.

The X crystals (named after ”Xtreme activity”) X1 and X2 were then grown as the ultimate attempt at ^{229}Th doped crystals. X1 was fully molten, and sadly a polycrystal with bad transmission. X2 was a single crystal and at first seemed perfectly clear. After 3 days the doped part became orange and thus the doping boundary became clearly visible see figure 3.21. All parts of X2 had very low VUV transmission, which meant it was not suited for experiments. With the failure of X2 the last fraction of 3 MBq was left unused.

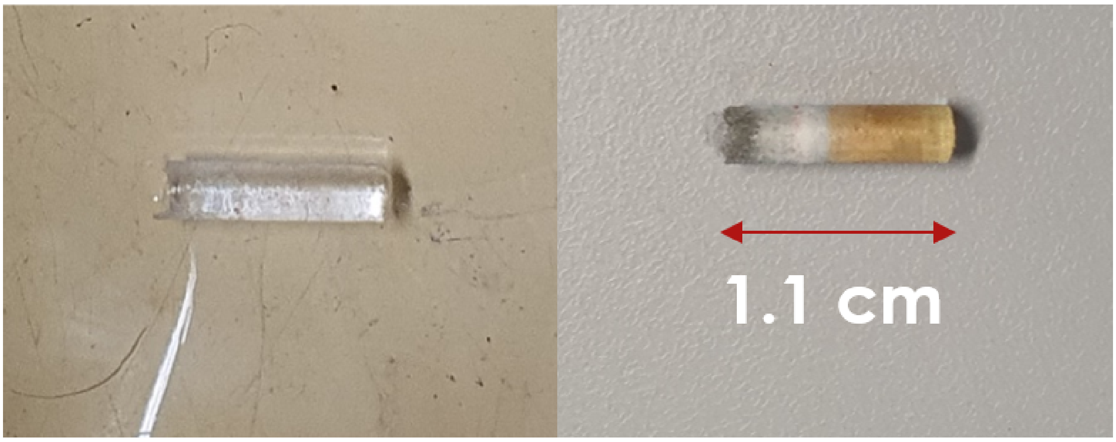

FIGURE 3.21: X2 crystal directly after growth and 3 days later. The radioactivity colored the crystal orange. By annealing the crystal it becomes clear again, but turns orange again in a similar time frame as the first time.

All grown crystals and their characteristics can be found in table 3.2. In the column with the amount of powder used the method used to prepare the powder (see sections 3.2.2 and 3.2.3), coprecipitation (coprec) or mixing (mix). The VUV transmissions were taken with the setup described in section 4.2.3 up until crystal V8, after which the setup in section 4.2.1 was used.

The best grown ^{229}Th:CaF$_2$ was the C10 crystal, with a concentration of $4 \cdot 10^{17}$ cm^{-3} and a VUV transmission of 45 % for a 2 mm thick crystal. This top 2 mm was characterized for its Cherenkov radiation and then cut into four 1 mm^3 cubes with all but one side polished, and one 2 × 2 × 1 mm slab with all sides polished (see figure 3.19).

TABLE 3.2: Produced doped CaF$_2$ crystals

Orientation	crystal	powder (mg)	$^{232/229}$Th c (cm^{-3})	Scavenger	VUV T @150 nm	Fully molten?	Other comments
no seed	5mm 1			PbF2	0	yes	
no seed	5mm 2			PbF2	0	yes	
no seed	5mm 3			ZnF2	0	yes	
no seed	5mm 4			PbF2	1.00E-04	yes	
no seed	5mm 5			PbF2	2.00E-04	yes	Thorium doped
no seed	5mm 6			PbF2	0.125	yes	
111	C0	15 (mix)		PbF2		no	Uranium doped 22 % dope efficiency
111	C1	15 (mix)	1.00E+18	PbF2 5 %	0.38	no	Uranium contamination from last growth.
111	C2	15 (mix)	1.00E+18	PbF2		no	Crystal lost
111	C3	15 (mix)	5.00E+18	ZnF2 5 %	0.08	no	Compare ZnF2 to PbF2
111	C4	15 (mix)	5.00E+18	PbF2 5 %	0.5	no	
111	C5	15 (coprec)	1.00E+19	PbF2	0.47	no	
111	C6	15 (coprec)	1.00E+19	PbF2	0.25	no	
111	C7	15 (coprec)	1.00E+19	PbF2	0.4	no	
111	C8	15 (coprec)	1.00E+19	PbF2	0.275	no	
111	C9	15 (coprec)	1.00E+19	PbF2	0.405	no	
111	C10	15 (coprec)	4.00E+17	PbF2	0.45	no	0.5 MBq ^{229}Th used for 3 crystals
111	C11	15 (coprec)	1.00E+19	PbF2	0	yes	
111	C12	15 (coprec)	8.00E+17	PbF2	0	yes	
111	C13	15 (coprec)	1.20E+18	PbF2	0.1	unknown	Vacuum leak during growth, orange crystal.
	V1	15 (coprec)	1.00E+19	PbF2	0	yes	
	V2	15 (coprec)	1.00E+19	PbF2	0	yes	
	V3	15 (coprec)	1.00E+19	PbF2	0	yes	
	V4	15 (coprec)	1.00E+19	PbF2	0	yes	
	V5	15 (coprec)	1.00E+19	PbF2		no	
	V6	15 (coprec)	1.00E+19	PbF2		no	
	V7	15 (mix)	4.00E+19	PbF2		no	Increased ^{232}Th concentration
	V8	15 (mix)	4.00E+19	PbF2	0.21	no	
	V9	15 (mix)	4.00E+19	PbF2	0.35	no	
	V10	15 (mix)	4.00E+19	PbF2	0.25	no	
	V11	15 (mix)	7.00E+19	PbF2	0.08	no	
	V12	15 (mix)	8.00E+19	PbF2	0.12	no	
111	V13	25 (mix)	2.00E+20	PbF2	0	unknown	Single crystal. Reflective flakes in the crystal.
111	V14	25 (mix)	2.60E+20	PbF2	0.05	no	V13-15 powder was pressed into pocket.
100	V15	25 (mix)	9.00E+19	PbF2	0.02	no	
111	Cal1	15 (coprec)	1.00E+19	PbF2	0	yes	
111	Cal2	15 (coprec)	1.00E+19	PbF2	0.65	no	
100	Cal3	15 (coprec)	1.00E+19	PbF2	0.7	no	
111	Cal4	15 (coprec)	1.00E+19	PbF2	0.62	no	
111	X1	15 (coprec)	1.00E+19	PbF2	0	yes	1.67 MBq of ^{229}Th used. Orange crystal
111	X2	15 (coprec)	2.00E+19	PbF2	0	no	2 MBq of ^{229}Th used. Orange crystal

Chapter 4

Experimental Characterization of ^{229}Th:CaF$_2$ Crystals

To build a solid state nuclear clock, the most important component is the crystal platform. In chapter 2, the literature knowledge and new calculations on (Th:)CaF$_2$ were presented. In chapter 3 growth methods and its implications were explained. In this chapter the VUV spectroscopy devices, setups, and methods used to characterize the optical properties of the grown crystals are detailed. Following, is the results in the form of: VUV transmission measurements, radioluminescence characterizations, Radioactively induced damage and microscopic solid state characterizations.

The basis of the excitation of the ^{229}Th nucleus in the solid state environment and later of a solid state optical clock is to understand the influence of the surrounding material. The presence of the crystal as a host matrix will be seen through all processes that happen in undoped CaF$_2$ which will affect the optical characteristics. Doping the CaF$_2$ will modulate the processes occurring as compared to undoped CaF$_2$ which calls for characterization. The doping will also create new processes for example: thorium charge transfer states (CTS), large cluster defects and pinning of F centers as discussed in section 2.3. The surrounding CaF$_2$ will affect the nuclear transition; to which degree is still unknown. The suggested CTS can be used to excite the nucleus via electron bridge processes but also might end up quenching the nucleus [29].

Growing the CaF$_2$ crystal contributes to understanding the processes in the material: one is forced to think about the water content before growth, oxygen scavenger content and possible contaminants. By seeing the relation between growing parameters and VUV transmission one can gain more understanding about the host crystal. This understanding can then be fed back into the growing process to improve the procedures. The characterizations done so, make it possible to accurately determine the viability of experiments designed to measure the isomeric photon emission in a solid. The dynamics in the growing and irradiation of the radioactive crystals is a complex system, and is therefore the focus of this thesis.

The characterization of ^{229}Th:CaF$_2$ will provide the basis to understand the processes in the grown crystals. When irradiating these crystals during excitation of the ^{229}Th nucleus, the complexity of the observations made will only increase. By understanding the basis, the more complex processes in the interaction between nucleus and crystal can be understood and eventually exploited to excite the ^{229}Th nucleus in the CaF$_2$ crystal environment.

This chapter will first cover the VUV spectroscopic devices used in the characterization of these crystals. These devices will be referred to in the following chapters as well because they are used in any setup attempting to measure the photon emission of the ^{229}Th nucleus. Many calibration curves and characterizations of these devices are given.

Afterwards two types of experimental setups are discussed: VUV transmission/absorption measurement setups that probe the transparency of the material and VUV luminescence detection setups that monitor the light output of the crystals due to their inherent radioactivity (radioluminescence). These setups are used to characterize the grown crystals directly after growth, at different temperatures, and after fluoride annealing. The damage incurred by radioactive decay is assessed and the microscopic character of the grown crystals is probed by atomic force microscopy, electron microscopy, neutron activation analysis, and electron paramagnetic resonance measurements.

4.1 VUV Spectroscopy Devices

The development of optics in the VUV wavelength region, 10 nm to 200 nm (or 124 eV to 6.2 eV), was long dominated by the need for ever smaller transistors in the lithography industry [190]. The lithography sadly skipped rather quickly from 157 nm to 13 nm. Now the industry exclusively employs 248 nm KrF excimer laser (sporadically 193 nm ArF laser) and 13 nm higher harmonic generation in Sb, avoiding the VUV region altogether. Partly due to no industrial interest, development in the VUV optics has been scarce and this concern has been mentioned in the scientific community in the past [191]. Recently, interest has been renewed due to the nuclear clock, but also due to other applications [192, 193].

Using VUV optics is a difficult due to this lack in development. There is limited availability of high reflective optics and bright light sources. The need to work in inert gasses or vacuum that is transparent to VUV increases the difficulty: many components are not compatible with operation in vacuum or non-air atmosphere. In order to manipulate the ^{229}Th nucleus with light, bright light sources are needed. In the performed experiments two VUV light sources were used: Hamamatsu D$_2$ arc discharge lamps and Excitech Elux electron beam lamps. Aside from these excimer lasers and pulsed VUV lasers will briefly be discussed and compared to the lamps, as they are important for the future of this research field. The main VUV spectroscopy tools used in this thesis are elaborated on in this section: VUV monochromators, VUV light sources and VUV detectors

4.1.1 VUV Monochromators/Spectrometers

Spectral analysis of light that has interacted with matter can say a lot about the matter. In the performed experiments, VUV transmission and fluorescence measurements are central to studying the ^{229}Th doped CaF$_2$ crystals. At the center of spectral analysis are spectrometers who separate light into its spectral components. The main component is a grating, specifically a reflective grating in the used spectrometers.

The effect of this grating is illustrated in figure 4.1. Light from a slit that falls on a reflective diffraction grating will have a normal reflection (zeroth order). Due to the wave nature of light there will also be higher order reflections: constructive interference of light will diffract different wavelengths under different angles: dispersion. If one has a spatially resolving detector, like a CCD camera, one can measure the spectrum of the light. Alternatively, if the detector is not spatially resolving, the grating can be rotated to record a spectrum.

The entrance light passes through a slit to provide a point like light source at the entrance. The design of a Seya-Namioka type spectrometer is based on the fact that the entrance light is a point source, which is focused on the exit of the device by the curved grating [194]. In this design the wavelength focused at the centre of the exit slit can be changed by rotating the grating. The entrance slit and grating together basically form a system that separates light into its spectral components. This can be used as a spectral filter when a slit is put at the exit focal point: when only allowing one wavelength to pass the exit slit the light is effectively filtered. In this setup this device is used as a monochromator where the output wavelength is chosen by rotating the grating and the bandwidth is limited by the slit size and the resolution of the grating. When a camera is put in the exit focal plane a full spectrum can be detected and the setup is used as a spectrometer. In this way the same setup can be used to serve two purposes. In this thesis, it is used as a spectrometer in combination with a CCD camera to detect a spectrum and also as a monochromator in combination with a photo multiplier tube (PMT) to detect one wavelength of light.

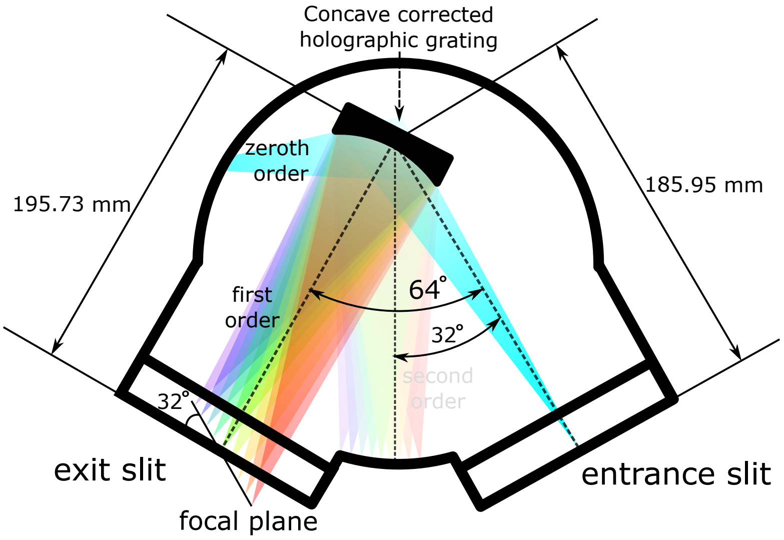

FIGURE 4.1: The optical diagram of the McPherson 234/302 monochromator. The main parameters are mentioned in the diagram, the spectrometer is symmetric such that it can be also used mirrored. Because the grating produces multiple orders they can overlap and cause false images at double the wavelength (150 nm is imaged at 300 nm as well). The zeroth order is imaged on the wall, which can cause stray light (in reality it is much closer to the first order). The focal plane is under a 32° angle, which is important if one installs a camera as a detector.

In general in the VUV region both flat and curved gratings are used to build spectrometers, examples are the Czerny-Turner[195] and Seya-Namioka [194] spectrometers. Examples of suppliers are McPherson, HP Spectroscopy, Resonance and Horiba. Still, few high efficiency spectrometers in the VUV range are available on the market. The development of high efficiency and precision VUV spectrometers is still underway and its not clear which optical design performs better in which situation. Also gratings can produce spectral defects that reduce performance, such as Roland ghosts [196]. The optical design of the spectrometers is based on mathematical approximations, which in the end also limits their maximum resolution. Due to these mathematical approximations the slit images have multiple orders and odd shapes [194].

In the end the resolution of a spectrometer is mostly determined by its grating. The exact shape of the grating surface changes the spectral efficiency of a grating. Ruled gratings have a sawtooth shaped surface, and provide the highest efficiency in the VUV. By changing the facet angle the maximum of the spectral efficiency can be shifted, which is the so called blaze angle. This is schematically represented in figure 4.2. In the performed experiments all gratings have a blaze angle such that the most efficient output wavelength is 147 nm. When measurements are made with a precision $\Delta\lambda <$ 1 nm, temperature stabilization of the entire system might be needed. The grating also can (de)magnify the image of the slit, and in general will modulate its straight shape to a more curved one.

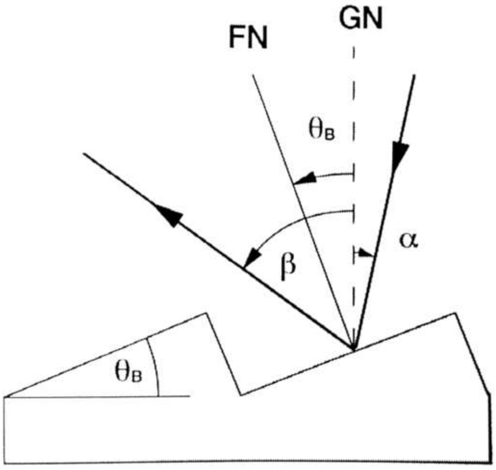

FIGURE 4.2: Magnification of the surface of a grating showing two grooves. Here GN is the grating normal, FN the facet normal, θ_B the facet angle and α/β the angle of incidence and angle of diffraction. The rule of thumb for the angle of maximum efficiency of the grating, the blaze angle, is if the FN bisects the angles of incidence and diffraction. Adapted from [196].

In the experiments detailed here only the aberration-corrected modified Seya-Namioka McPherson 234/302 VUV spectrometer was used. It is a $f = 0.2\,\mathrm{m}$ focal length spectrometer designed for 30 nm to 2200 nm. The sum of incident and outgoing angle is $\alpha + \beta$, which is in total always 64°. The Seya-Namioka design makes it such that only the grating needs to be rotated in order to change the imaged center wavelength on the exit of the spectrometer. Figure 4.1 is a schematic representation of this spectrometer.

The maximum resolution is stated to be ±0.1 nm FWHM for a 1200 lines/mm grating, ±0.05 nm reproducibility, grating size is $w \cdot h = 40$ by 45 mm and the f number is 4.5 (ratio between grating size and focal distance f). The f number is a figure of merit of the acceptance angle of the spectrometer, and thus determines how much signal one can capture in terms of solid angle. The actual resolution of the system is determined by entrance and exit slit, as described in section 4.1.4 and equation 4.4. The resolution improves with decreasing slit size, but also the signal decreases. This trade-off is at the basis of these grating spectrometers. The alignment of the light source before the entrance slit can be important, as it can affect calibration and the absolute measurement of wavelengths [197]. The inside of these spectrometers is often anodized black, or painted with black Aeroglaze z306 to reduce reflections of stray light. Aeroglaze z306 is also used on the Hubble telescope to reduce reflection of light [198].

The amount of light captured in the spectrometer emitted by an isotropically emitting point source directly in front of the slit can be calculated and used as a measure of efficiency, η of the spectrometer. The efficiency of grating and detector (see figure 4.3) can be added to that as well which estimates the total efficiency η_{tot}. The captured fraction of light is described by the ratio of the visible surface of the grating as seen from the entrance slit, $wh\cos\alpha$, and a sphere at the grating position, $4\pi f^2$, which we can estimate for the 0th order incoming angle $\alpha_0 = 32°$

$$\eta = \frac{wh\cos\alpha_0}{4\pi f^2} = 0.3\,\%. \tag{4.1}$$

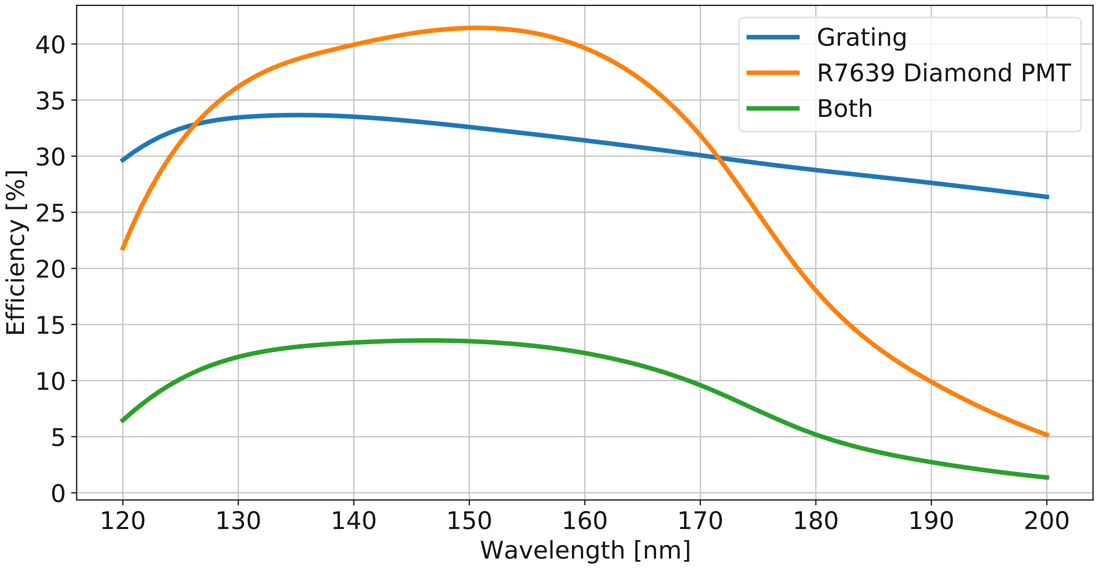

Figure 4.3: Spectral efficiency of the grating and the diamond PMT used in the experiments. These are non-verified datasheet values provided by McPherson Inc. (grating) and Hamamatsu Photonics (R7639 diamond PMT).

The efficiency at 150 nm is then for an outgoing angle of $\beta = 20.5°$, $\alpha = 43.5°$: $\eta = 0.26\,\%$. The total efficiency is then $\eta_{tot} \approx 0.05\,\%$. As can be seen from equation 4.1, the best way to increase the η of a spectrometer is reducing the focal length, and increasing the surface area of the grating. By using reflective optics on the opposing side of the isotropic emitter the efficiency of the system can be doubled. One cannot increase efficiency further using focusing optics due to their linearity. One is limited by the numerical aperture defined by the spectrometer. In equation 4.1 the (de-)magnification by the grating of the image on the exit slit was not taken into account. In the case of a CCD, this is also not relevant. It is also unclear what the grating manufacturer means with grating efficiency which will affect the total efficiency, as it matters how this value is measured.

4.1.2 Hamamatsu D_2 Arc Discharge Lamp

Deuterium lamps are very bright and stable light sources ranging from 115 to 400 nm [199]. Many companies build D_2 lamps, in these experiments only those produced by Hamamatsu are used [200]. More specifically the L1835, and L15094 with an H2D2 lamp by Hamamatsu.

The general operating principle is that a cathode is heated by a current and then a trigger voltage is applied between 300 and 500 V to release electrons from the cathode and ignite an arc. There is a focusing electrode that keeps the arc from discharging on any of the other parts and guiding it towards the anode. This arc discharge will create a plasma and excite the D_2 molecules which will release their energy in the form of heat and photons. Deuterium is used as opposed to hydrogen due to the higher intensities at lower wavelengths it can produce. Due to the higher atomic weight the plasma behaves differently and produces more VUV light.

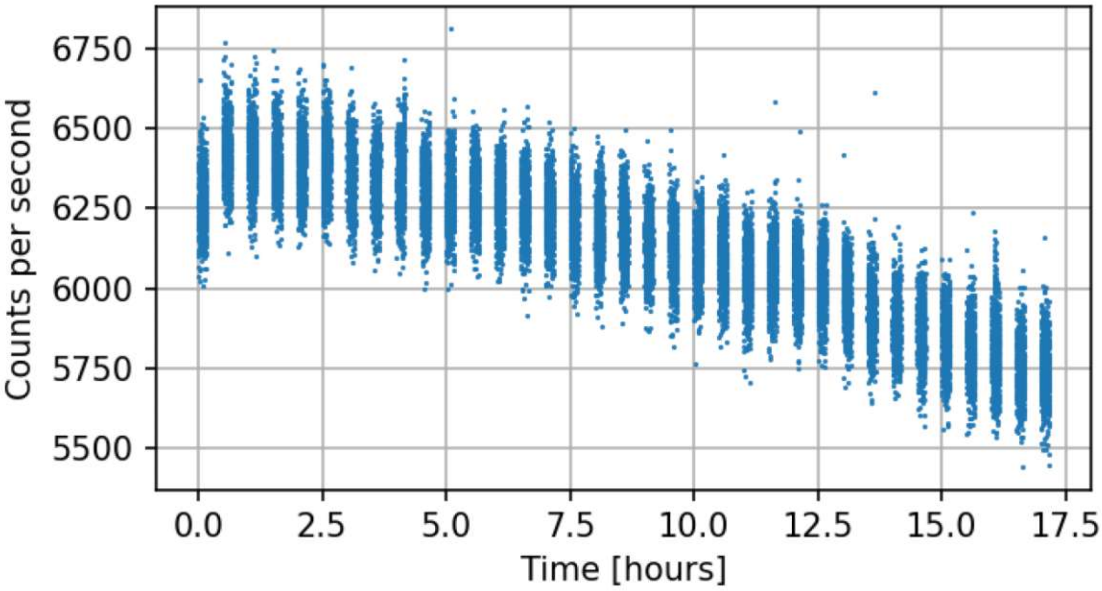

FIGURE 4.4: Drift of the L15094 as measured after the VUV light passing the MgF$_2$ window of the lamp itself, a mirror, a grating and ultimately measured by a CsI R6835 Hamamatsu PMT with a mg$_2$ window. Each optical element will degrade over time, which contributes to the decrease in signal. The noise on the PMT is not averaged out in this figure to show the spread of points measured for each measured time point.

Deuterium lamps have an excellent intensity stability, the Hamamatsu L15094 has a fluctuation of 0.05 % peak to peak, drift of ± 0.3 %/h and the L1835 fluctuations of 0.5 % peak to peak and drift of 1 %/h. The actual drift on target is larger due to the detrimental effects VUV irradiation has on optics along the path. Over time windows and mirrors will be damaged internally and coated by VUV-cracked leftover hydrocarbons that are still present in the vacuum system. A typical drift seen in our setup is displayed

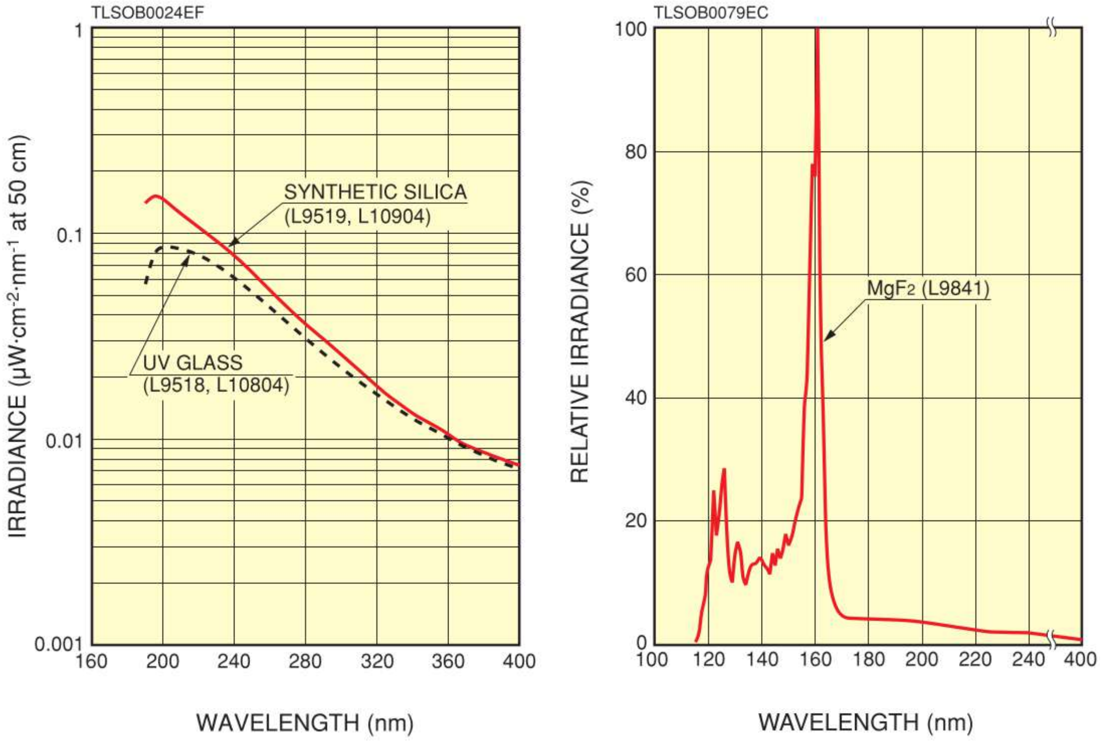

Figure 4.5: Irradiance in the UV range and relative irradiance in the VUV range of a D_2 lamp. From these one can estimate the photon flux per wavelength by extrapolating the UV irradiance to the VUV relative irradiance $\frac{dN}{d\lambda dt} \approx 10^{15}\,\mathrm{nm}^{-1}\mathrm{s}^{-1}$.

in figure 4.4. The VUV and UV spectral distribution of these lamps can be seen in figure 4.5.

The spectrum of a D_2 lamp is built up out of many narrow lines [202]. If one had a spectrometer with a very high resolution, the spectrum would look as in figure 4.6. Note that because the D_2 spectrum consists of many thin lines instead of a continuous spectrum it is not considered to be used as excitation source for the nucleus, although the photon flux per nanometer is theoretically higher than for other sources. If the nuclear excitation does not overlap with any of the D_2 lines, then excitation will not be possible regardless of the photon flux. That is why the excimer lamp, described below, was chosen as excitation source: It has a continuous spectrum. Another benefit is that the excimer lamp is has a more confined spectral output. The broad spectrum of the D_2 lamp excites many states in the crystal which can contribute to background and damage in the crystal, both unwanted, when trying to measure the extremely weak nuclear fluorescence.

The D_2 lamps of Hamamatsu conveniently come with their own power supply, and turn on with the switch of a button. The L1835 needs water cooling, the L15094 only air cooling (see figures 4.7 and 4.8).

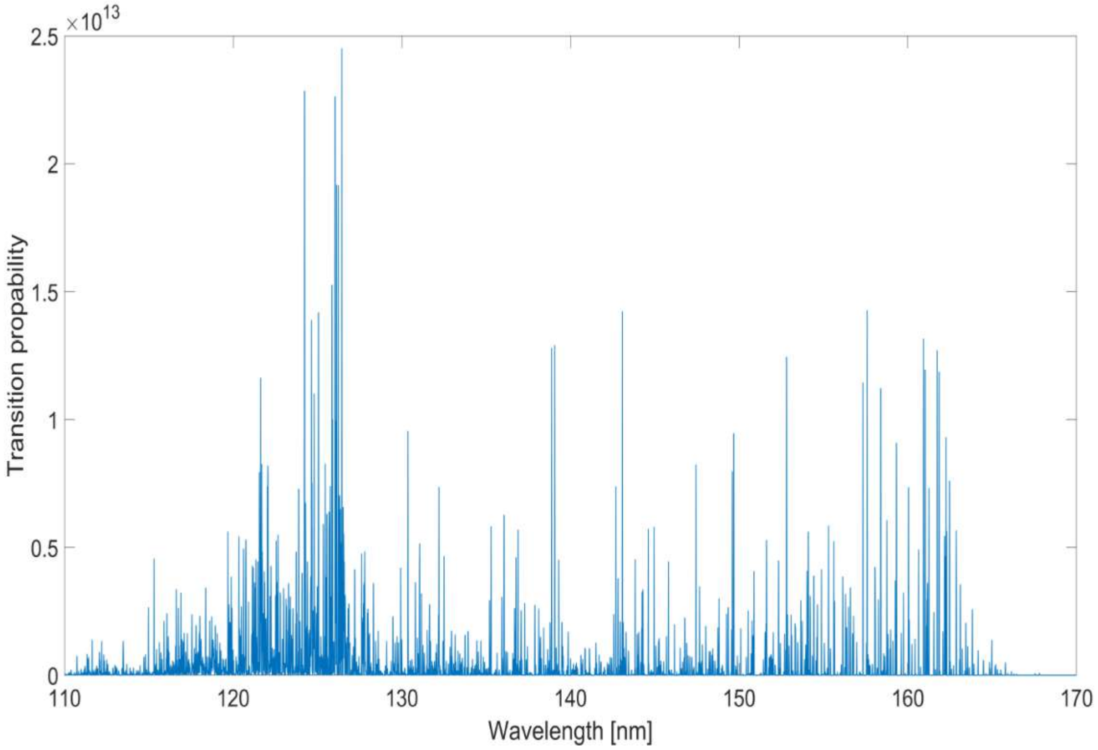

FIGURE 4.6: D$_2$ arc discharge spectrum for an almost infinitely narrow linewidth. Above 170 nm the D$_2$ continuum starts. Data from [201]

FIGURE 4.7: D$_2$ arc discharge Hamamatsu L1835 lamp. Connector to KF40 vacuum connection is shown together with water cooling tubes.

4.1.3 Excitech Elux Electron Beam Lamp

The electron beam excited noble gas plasma lamp was first conceived in 1997 [203] as a prototype. By now this light source has matured to a product sold by Excitech GmbH. The main feature of this lamp is the cold excitation via an electron beam of the gas as

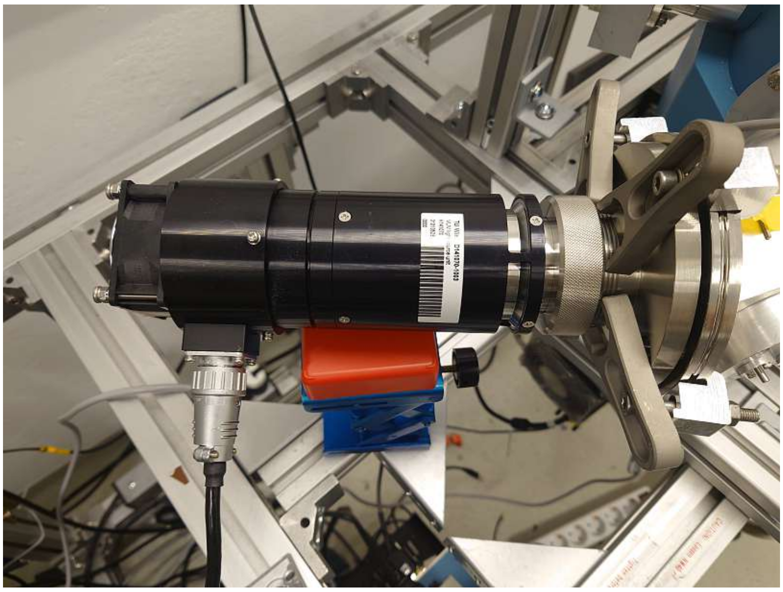

FIGURE 4.8: D$_2$ arc discharge Hamamatsu L5309 lamp. An improvised connector to ISO-KF 100 vacuum connection is shown and on the back the air cooling fan can be seen.

opposed to the arc discharge plasma. This ensures high efficiency conversion of input power to output VUV emission. The consumed power of this device is around 10 W as opposed to the 110 W of the D$_2$ lamp while providing approximately the same total power (the excimer spectrum covers 10 times less wavelengths than the D$_2$ spectrum). The produced photon flux is $\frac{dN}{dtd\lambda} \approx 10^{14}\,\mathrm{nm}^{-1}\mathrm{s}^{-1}$.

A schematic representation of the lamp is shown in figure 4.9. The electron beam is produced by heating a BaO cathode in vacuum and applying 12 kV between cathode and anode. This beam of several μA is collimated by an electrode G1 with a small negative voltage. It then is accelerated towards the first anode G2. This anode is needed to pull electrons out of the cathode and overcome the work function of the BaO. The beam is further focused to a parallel beam by a focusing electrode G3. The final acceleration stage to 12 keV of kinetic energy takes place towards the anode. After the anode the electrons fly freely, and are steered by steering coils M$_x$ and M$_y$ to the membrane. A SiN$_x$ 300 nm membrane with a surface area of 1x1 mm is produced by ion etching a 0.5 mm Si wafer and afterwards depositing SiN$_x$ on it via vapor deposition [204]. Due to the thin ceramic membrane the 12 keV low energy electrons retain much more of their energy ($\approx$ 70 %) while passing through as opposed to conventional low atomic weight membranes like titanium.

The electrons then collide with a noble gas in the gas cell which excites the atoms. The excited noble gas atoms now have an unbound valence electron, and are able to form a metastable molecule with a ground state atom, called an excimer. When this excimer decays it produces characteristic light depending on the species used. This

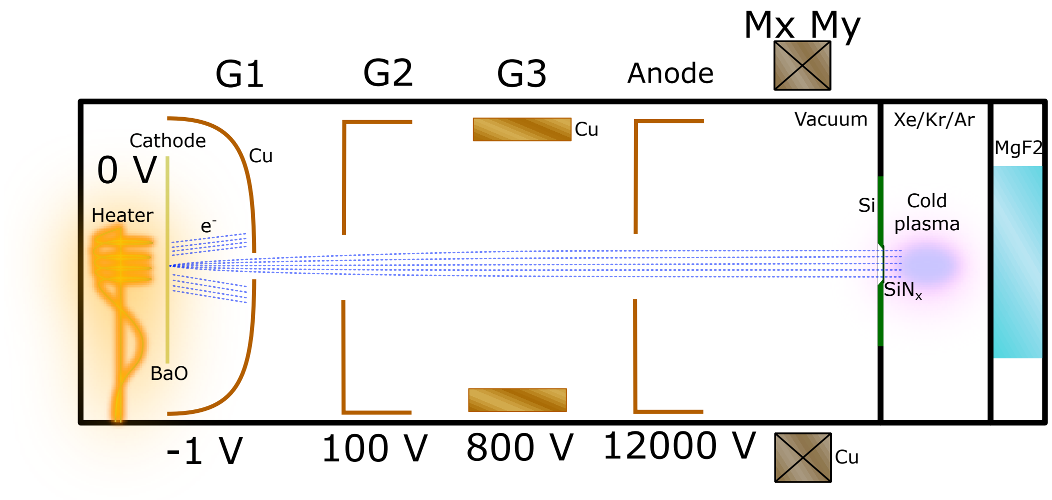

FIGURE 4.9: Inner construction of the Excitech lamp. Electron optics, membrane, vacuum cell, gas cell, heater and window are shown. The electron beam moves from the BaO cathode to the anode while being collimated by G1, accelerated to G2, focused to a parallel beam by G3 and aimed through the Mx My steering coils through the SiN membrane into the noble gas which produces excimers. An ion pump keeps the vacuum in the electron gun side to better than 10^{-9} mbar and another ion pump keeps the noble gas side free of contaminants that leak in such as H_2O, O_2 and hydrocarbons. Species other than noble gasses and CH_4 are pumped more efficiently by ion pumps due to their lower ionization energy.

excitation is broad and quasi-continuous due to the nature of the decay, see figure 4.10. The potential between the excited and ground state atom is attractive, but for two not excited atoms repulsive. Depending on the separation between the atoms upon decay the energy released changes significantly.

In figure 4.11 the different emission spectra can be seen for different noble gas species [203]. In order to increase light emission efficiency different mixtures of gasses are used. For the argon excimer 1 bar of argon is used. For the krypton excimer 100 mbar of krypton is backed by 1 bar of argon. For the xenon excimer 100 mbar of xenon is backed by 1 bar of argon. These mixtures reduce the probability of collisions between same species noble gas but still provide high cooling rates (aside from the light argon). In figure 4.11 one can see lines from different contaminants in the noble gas chamber, these can conveniently be used for calibration. The xenon spectrum was taken using a 700 micron slit due to the low intensity, other spectra with a slit of 200 microns. This can be recognized by the width of peaks in the spectrum. Later it was found out that the lower intensity was due to a broken membrane which was leaking out xenon, obstructing both the electron beam and reducing the gas pressure in the noble gas chamber. The plasma does not only produce VUV light, but also some visible as can be seen in figure 4.12. A krypton plasma is orange, argon is blue, and xenon is weak pinkish.

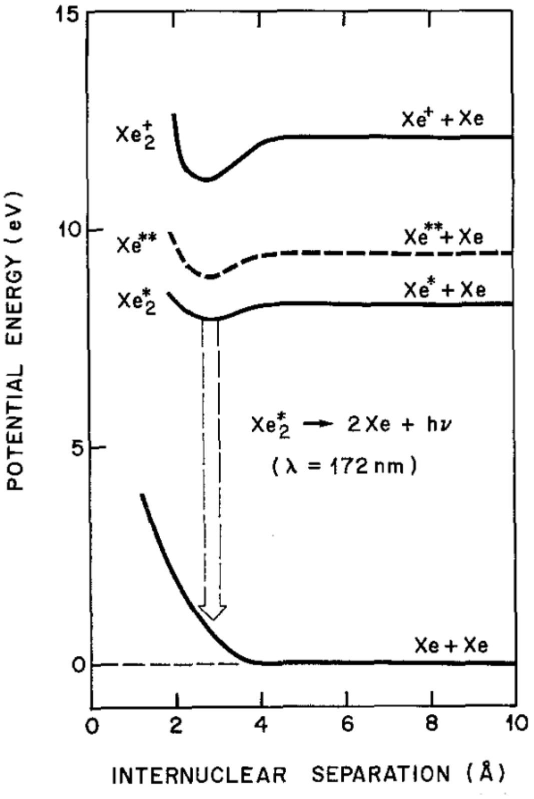

FIGURE 4.10: Simplified potential energy diagram of molecular xenon. The bound excited state decays to the repulsive ground state for which the potential energy significantly changes depending on internuclear separation. Because of this the de-excitations of excimers is broad. For higher excitation of xenon different excimer emission is observed, but the higher excitations are more unlikely to be produced.

Intensity drift with time of this lamp was tested, and seem to behave excellent over time as can be seen in figure 4.13. A part of the electron beam will hit the walls of the system, leaked in contaminants, and the electrodes. This can sputter and release atoms in the system, which can be ionized by the beam. Because the beam is negatively charged the positive ions will be accelerated to the beam and ultimately towards the BaO cathode. There the ions can sputter the BaO and create more contaminants. These processes create the possibility for more reactions in the electron gun chamber which can have a variety of effects. The cathode can become poisoned. This means that a layer of a different material has formed on top of it which strongly increases the work function and prevents electrodes from escaping the cathode.

By heating the cathode to extreme temperatures, the layer can be removed. By applying high voltage in a bad vacuum this layer can also be removed by sparking. A last option is to put a large negative voltage on G1 and reflect electrons back onto the cathode to sputter the layer. Often the layer is only formed in the center where the ions can pass the collimator and electrons produced elsewhere on the cathode can contribute to sputtering the layer.

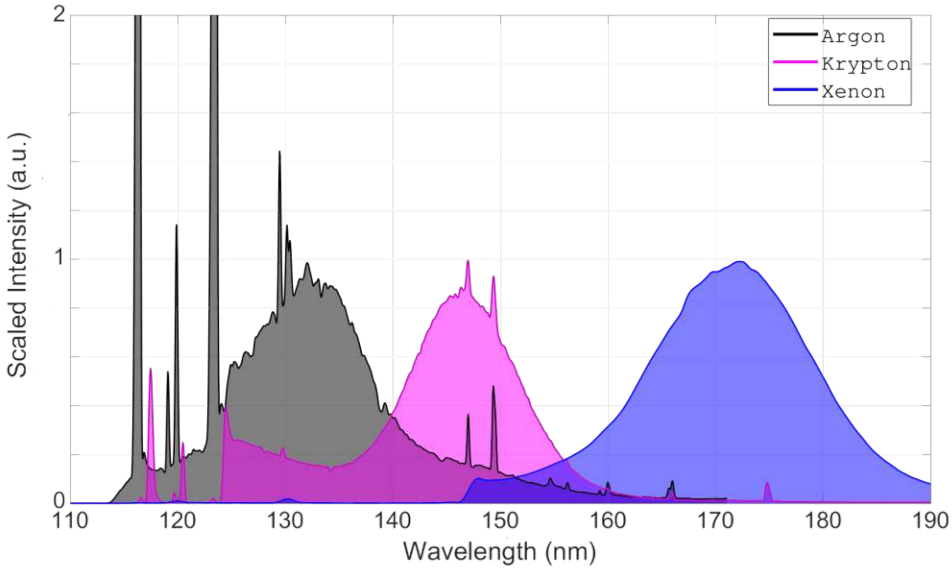

Figure 4.11: The spectra produced by the Excitech lamp for different noble gasses in the gas cell at the end of the electron beam. These spectra were measured in house. It can be seen that there is cross contamination of Xe in the Kr spectrum, and Kr plus Xe in the Ar spectrum. These contaminations decrease the ultimate light output. Argon and Krypton spectrum were taken with a 200 micron slit, xenon spectrum was taken with a 700 micron slit using the 234/302 McPherson spectrometer and a CCD camera.

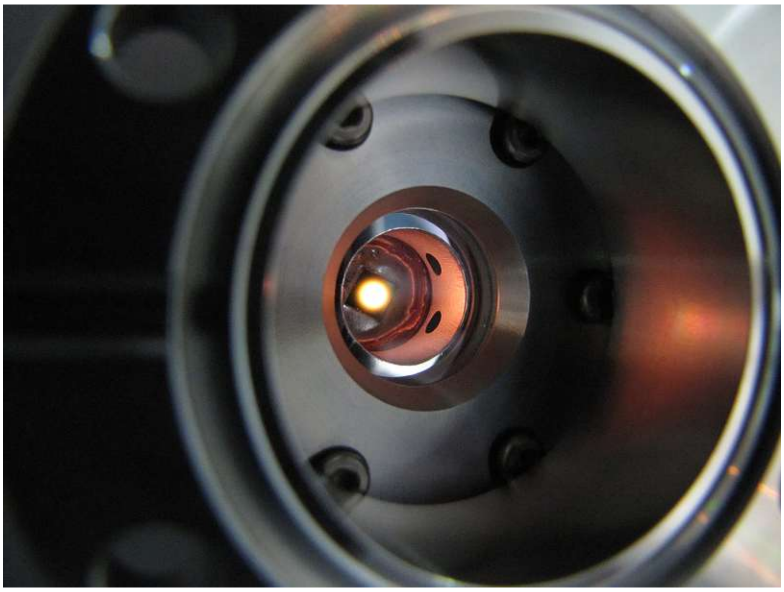

Figure 4.12: Orange krypton lamp plasma taken with a normal camera. The two holes for the ion getter pump are visible as well as the square silicon wafer. Behind the orange plasma the silicon nitride membrane is situated.

Another effect is due to the dissociation of hydrocarbons. The free carbon can form carbon nanotubes on the electrodes. These nanotubes start sparking under high voltage, which damages the system. They can be removed by electron irradiation or 'burning' them in a bad vacuum using high voltage sparks.

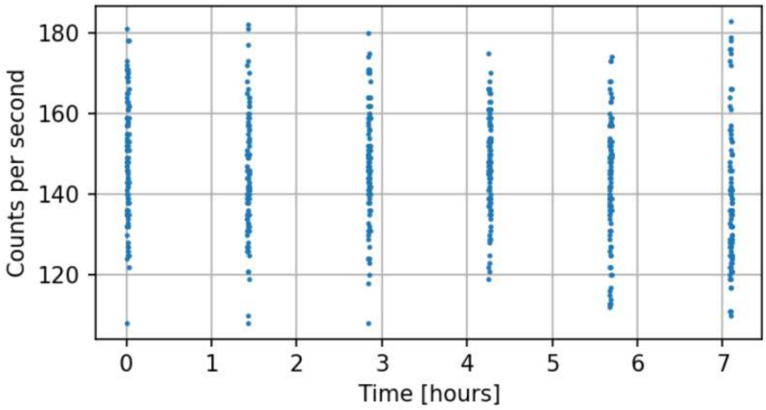

FIGURE 4.13: Drift of the L15094 as measured after the VUV light passing the MgF$_2$ window of the lamp itself, a mirror, a grating and ultimately measured by a CsI R6835 Hamamatsu PMT with a mg$_2$ window. Each optical element will degrade over time, which contributes to the decrease in signal. The noise on the PMT is not averaged out in this figure to show the spread of points measured for each measured time point.

4.1.4 Calibration of a VUV Spectrometer

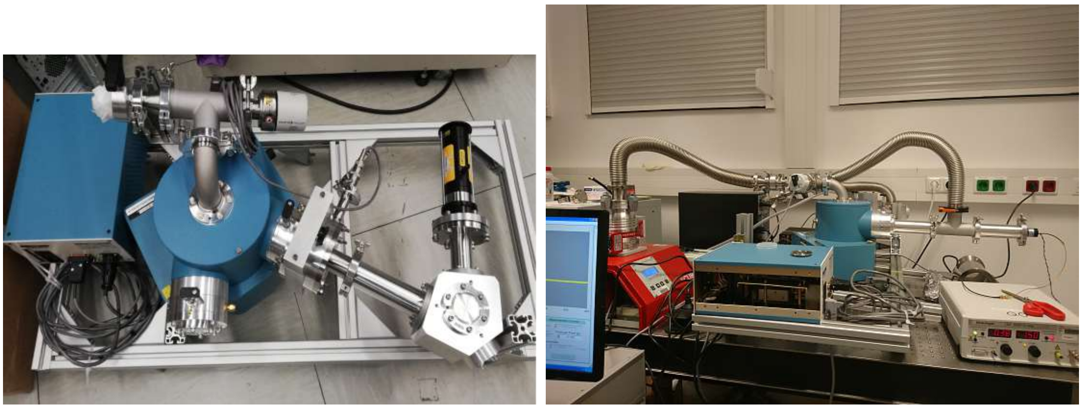

FIGURE 4.14: Top (left) and side view (right) of setup to calibrate the McPherson 234/302 spectrometer. Only in the side view a pump and detector (Hamamatsu CsTe R6836 PMT) is attached, in the top view these were not attached. The entire setup was mounted on an easily transportable rack. A shutter and filter wheel were installed to block the light remotely and reduce the light intensity. The light of the D$_2$ L1835 lamp was focused on the entrance slit of the spectrometer to increase intensity.

To have an accurate measurement of the wavelength of a measured spectrum the spectrometer needs to be calibrated. The McPherson spectrometer comes with a rough built-in calibration which is displayed by a dial on the chamber. This calibration is only correct for a 1200 lines/mm grating. A D$_2$ lamp was used in combination with a PMT that was far away from the exit slit to calibrate the setup as shown in figure 4.14. Calibration with a D$_2$ lamp is difficult, because the position of the peaks depends on the resolution [205] as can be seen in figure 4.15. To properly calibrate a setup using a D$_2$ lamp, one needs to measure the entire spectrum and fit all lines simultaneously for resolution with a simulated spectra produced from known calibrated data. The difficulty

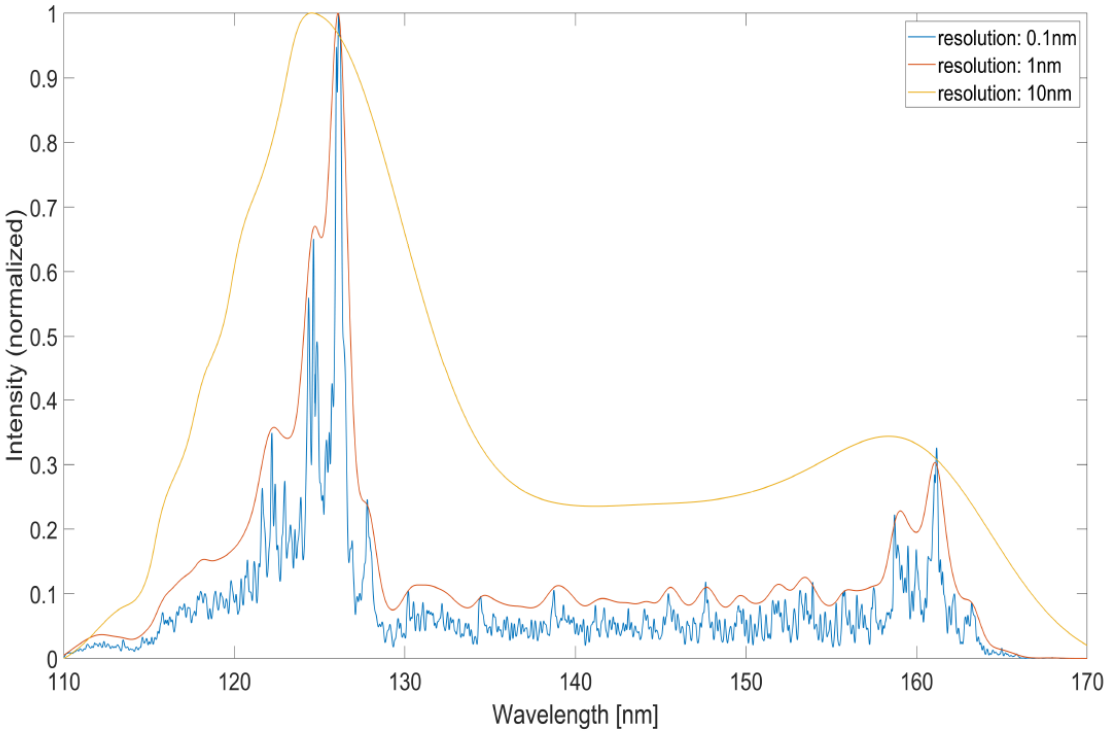

FIGURE 4.15: Simulated D_2 VUV spectrum using data from [202] for 3 different resolutions. Note the apparent shift in peak position.

in this is that the optical components have an unknown spectral behavior due to their constant degradation in vacuum under VUV radiation. Mostly the short wavelengths are affected by this. The actual spectral efficiency of the grating is also poorly known.

The resolution limit (minimum peak separation) $\Delta\lambda_R$ of a grating in Seya-Namioka configuration is a combination of the minimal resolvable resolution of the grating $\Delta(\lambda)_r$ and $\Delta(\lambda)_s$, the resolution reduction caused by the size of the slit.

$$\Delta(\lambda)_R = \sqrt{\Delta(\lambda)_r^2 + \Delta(\lambda)_s^2}. \tag{4.2}$$

The minimal grating resolution $\Delta(\lambda)_r$ can only be calculated numerically and the entrance slit width (Δs) can be modeled according to Namioka [194]:

$$\Delta(\lambda)_R = \sqrt{\Delta(\lambda)_r^2 + \left(\frac{\Delta s \cos\beta}{gnr'}\right)^2}, \tag{4.3}$$

where β is the outgoing angle, n the order, r' the distance from grating to exit slit and g the line density of the grating (mostly $g = 1200\,\text{lines/mm}$ was used). Normally, the resolution is defined through the Rayleigh criterion but often the FWHM of a peak is used to simplify measurements. The difference is a factor $\frac{0.61}{0.4}$, we will only use the

FWHM definition which is smaller than the Rayleigh criterion. To add the exit slit width (Δs_{exit}) in the equation:

$$\Delta(\lambda)_R = \sqrt{\Delta(\lambda)_r^2 + \left(\frac{\Delta s_{entrance}\cos\beta}{gnr'}\right)^2 + \left(\frac{\Delta s_{exit}\cos\alpha}{gnr}\right)^2}, \tag{4.4}$$

where r is the distance from entrance slit to grating. The experimental resolution was determined by simulating the D$_2$ spectrum $f'(\lambda)$ by convoluting each molecular line with a gaussian shape and summing all of them, then calculate, which of these spectra had the smallest normalized integrated overall distance to the experimental spectrum $f(\lambda)$. This is mathematically described by

$$R = \min \frac{\int_{-\infty}^{\infty} \sqrt{(f(\lambda) - f'(\lambda))^2}}{\int_{-\infty}^{\infty} f'(\lambda)}, \tag{4.5}$$

where practically the bounds of the integral run from 110 nm to 170 nm. For this a MATLAB code was developed. While fitting this spectrum, one could extract the resolution of the system and the shift of the wavelength as opposed to what the McPherson dial shows. The D$_2$ spectrum was measured by measuring the PMT count rate in 0.1 s bins while continuously rotating the grating with an angular speed that represents 4 Å/min from 110 nm to 170 nm. In table 4.1 the calibration results for different slit openings are shown.

Slits (μm) entrance/exit	Offset (nm)	Theoretical $\Delta(\lambda)_R$ (nm)	Experimental R (nm)
20/20	-0.81	0.12	0.12
100/100	-0.75	0.36	0.28
150/150	-0.70	0.52	0.56
100/150	-0.72	0.47	0.47
150/100	-0.68	0.42	0.41

Table 4.1: Calibration of a McPherson 234/302 VUV spectrometer with a D$_2$ lamp by comparing a simulated D$_2$ spectrum to an experimentally measured one. A small drift can be seen in the offset depending on slit size. This drift is probably due to the non-homogeneous illumination of the slit with the deuterium lamp and thus the grating. These optical misalignments can cause shifts in the range of 0.5 nm [197]. The experimental resolutions match up very well to the theoretical values, calculated by equation 4.4. Exception is the 100/100 measurement, here the measurement is consistent with a 100/20 slit size setup. Possibly hysteresis in the slit opening caused a smaller slit size than what was set.

4.1.5 Photomultiplier Tubes

The Photomultiplier Tube, or PMT was invented somewhere in the 1930s but its first inventor is contested [206]. The PMT uses the photoelectric effect to produce an electron from a cathode that is hit by a photon. In order to manipulate the electron, the inside of the tube is a vacuum. This electron is then accelerated to the next stage (dynode) where it kicks out many secondary electrons on the dynode. These are then accelerated towards the second dynode, where more secondary electrons are created and accelerated towards the third dynode. This process amplifies the photoelectron from the initial single photon via an electron avalanche by many orders of magnitude (gain of 10^6 to 10^7).

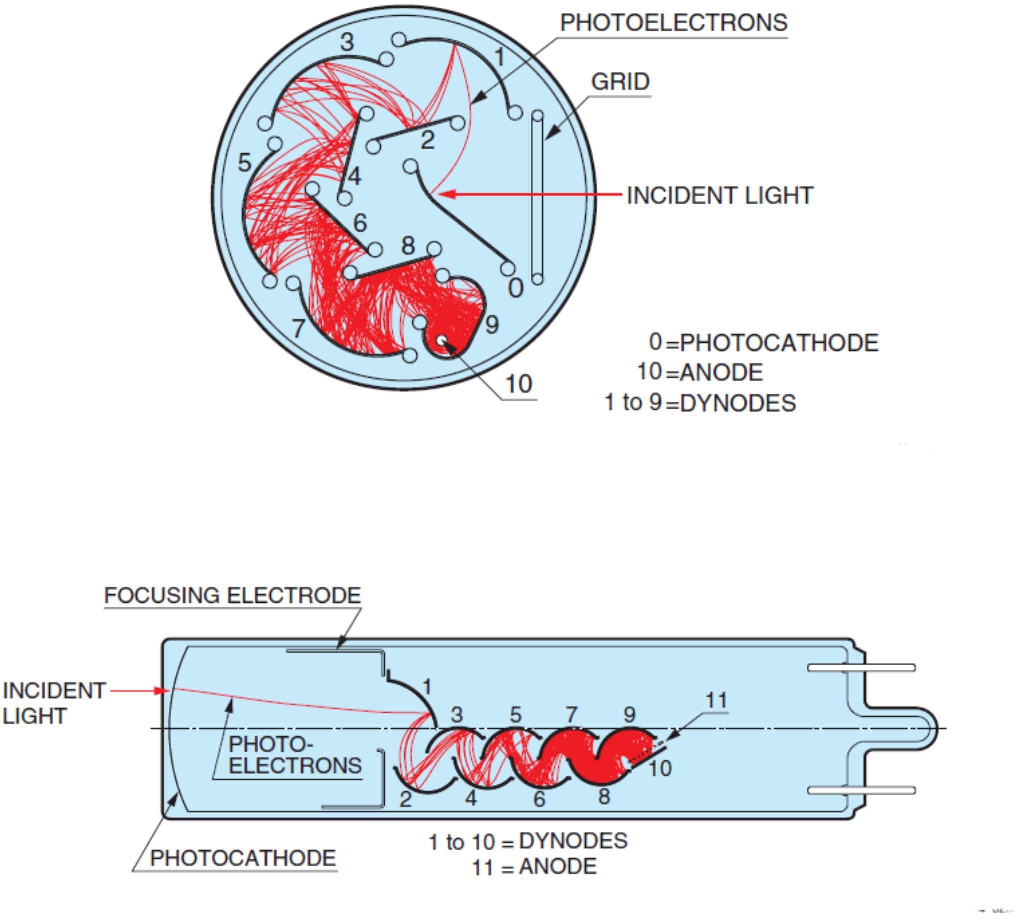

Figure 4.16: Two different designs of PMT. A side-on (upper figure) and head-on (lower figure) PMT; red arrow: incoming photons; red lines: electron trajectories. Taken from [207].

In the end, the electrons are captured by an anode and continue as a current signal. In the case of many photons, a constant current will be created. In the case of single photons very short pulses will be created (≈ns). By measuring this signal, photons can be measured extremely efficiently, even single photons can be counted. By looking at pulse height and shape, some background can be filtered out if the size and shape of a signal pulse is very well known. The electronic signal strength is then very linearly proportional to the input photon flux [207]. Two PMT designs are often used, so called side-on and head-on. These are illustrated in figure 4.16.

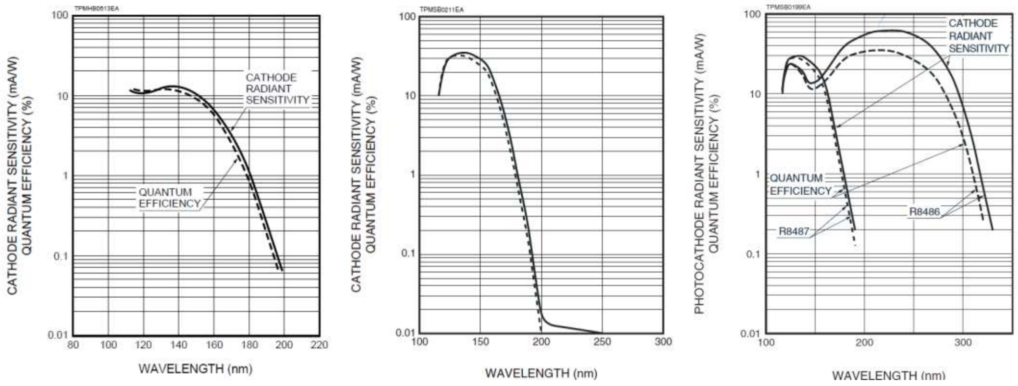

Figure 4.17: Spectral efficiency of three different CsI PMTs (from left to right: R6835 HO, R10454 SO, R8487 SO). Taken from [207].

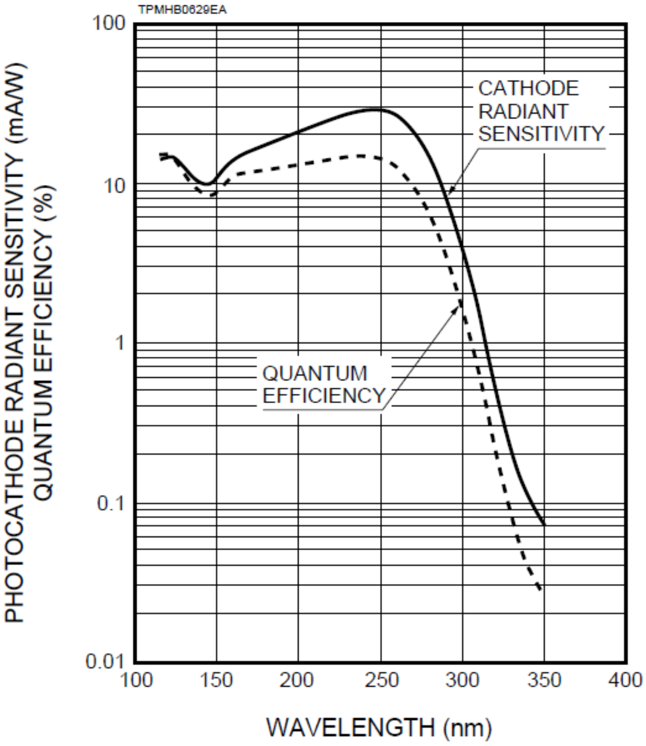

Figure 4.18: Spectral efficiency of a CsTe PMT (R6836 HO). Taken from [207].

In the experiments described here, both side-on (SO) and head-on (HO) were used and three different cathode materials, all from Hamamatsu Photonics [207]: Diamond (R7639 SO), Cesium Iodide (R6835 HO, R10454 SO, R8487 SO) and Cesium Tellurium (R6836 HO). The different cathode materials and designs change the spectral efficiency

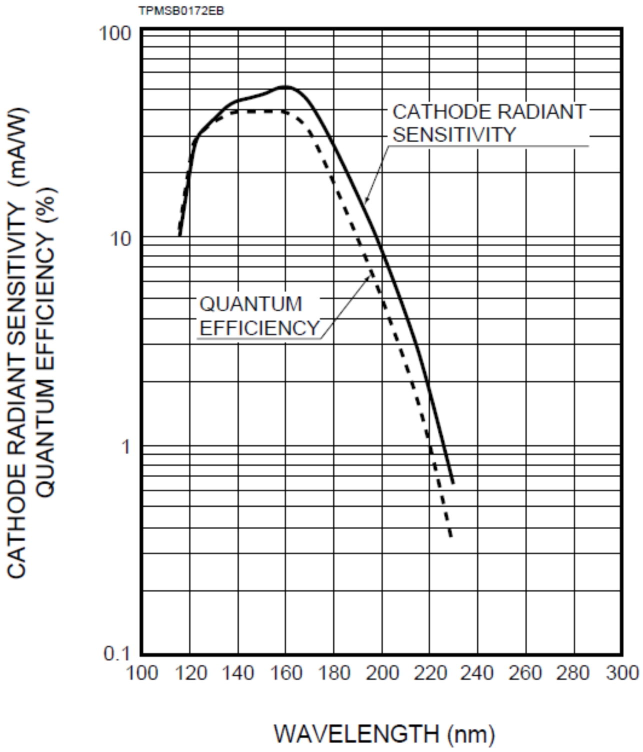

FIGURE 4.19: Spectral efficiency of a Diamond PMT (R7639 SO). Taken from [207].

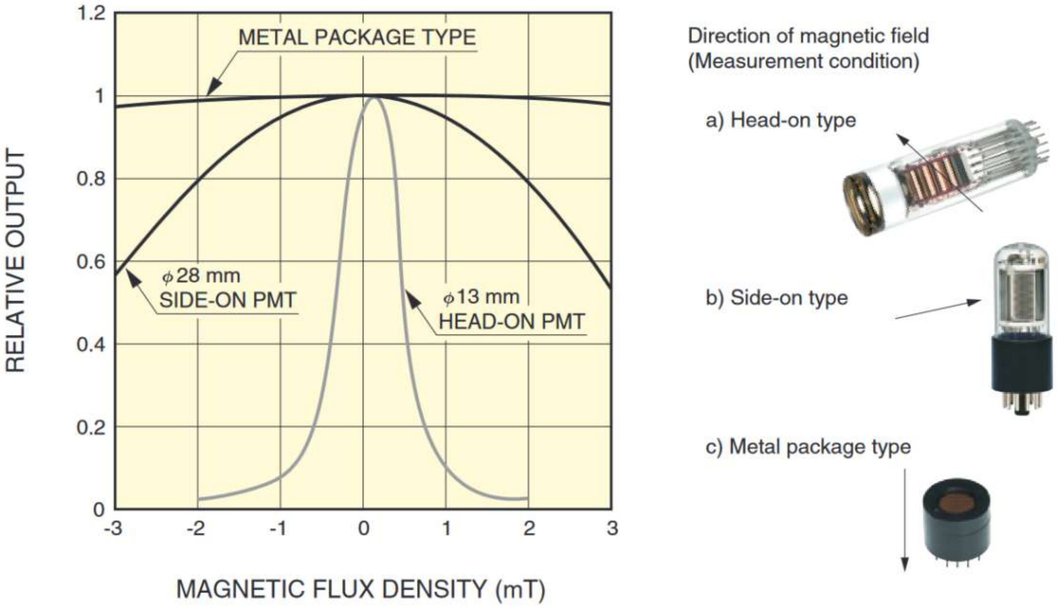

FIGURE 4.20: Change in PMT efficiency due to an external magnetic field. Taken from [207].

of the PMT as can be seen in figures 4.17, 4.18 and 4.19. The two designs (HO and SO) mainly change the efficiency of the system and its susceptibility to external magnetic fields. Because the SO is circular, it is less susceptible to magnetic fields than the linear HO as can be seen in figure 4.20. In all experiments, breeder circuit plugs from

Hamamatsu were used to distribute voltage over the electrodes of the PMTs. These circuits are effectively voltage dividers and take a high voltage and divide it over the respective dynodes in the correct ratio. Aside from providing the voltages they also compensate for nonlinearities in the PMT by using buffer capacitors for example, see [207]. For the SO PMTs E717-74 breeder circuit plugs were used and for the HO E717-63. Positive and negative high voltage plugs were used. The benefit of running the PMT at positive high voltage is that no electrons will find ground towards the walls of the PMT instead of the anode. A downside is that the signal is at high voltage so a outcoupling capacitor needs to be used.

Even when no photons reach the PMT, a current will run, which creates a background for any photon counting measurement. This background is called dark current and occurs due to:

- Thermionic emission from cathode and dynodes.
- Leakage current between the different pins on the PMT.
- Field emission current.
- Scintillation of the PMT glass producing photons that produce a current.

The thermionic emission current I can be characterized by [207]

$$I = AT^{5/4}e^{-\frac{q_e\Psi}{k_BT}} \tag{4.6}$$

where A is a constant, T the absolute temperature of the cathode/dynode, q_e the elementary charge, k_B the Boltzmann constant and Ψ the work function of the material. The work function is the amount of energy needed for an electron to leave the material. Naturally this is a very material-dependent parameter, so different PMT materials have different thermionic emission rates. From equation 4.6 we can see that reducing the temperature, the dark current is reduced exponentially. When a PMT is cooled down the thermionic emission current and thus the total dark current will reduce, until another background source dominates. It has been shown that when a PMT is cooled down too much, dark current increases again and the reason for this is still unclear [208]. The exact temperature of this depends on the used cathode material but in general are lower than -30 °C.

Leakage current is a result from imperfect isolation and the low currents that are involved in photon counting. A very high resistance ($10^{12}\,\Omega$) will still at high voltage produce a nA current according to Ohm's law. This will then be linearly dependent on the voltage put over the PMT.

When a high voltage is applied on the PMT, electrons can possibly be pulled directly from the cathode and produce a current. This is called field emission current. To counter this a PMT should not be operated more than its recommended maximum supply voltage, and ideally only 70 to 80 % of the maximum.

Most PMTs are made of VUV fused silica, and have a window of either VUV fused silica or MgF$_2$. When the glass is hit by a high energy particle the fused silica and MgF$_2$ are known to scintillate, just as CaF$_2$.

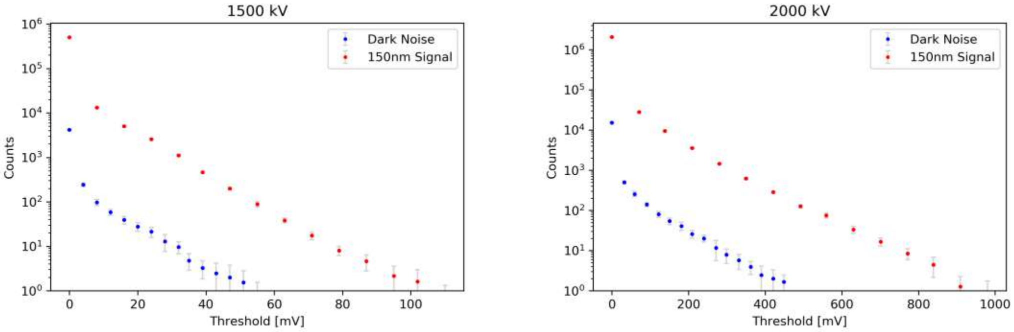

FIGURE 4.21: The L1835 Hamamatsu D$_2$ lamp was measured at 150 nm using different threshold voltages. The ratio between dark current and signal was studied to find the optimum signal-to-noise-ratio for different voltages applied on the R6836 HO CsTe PMT.

The HO CsI and CsTe PMTs were characterized for their dark current behavior as a function of temperature and threshold voltage setting. The threshold voltage is the minimum height a current or voltage peak needs to have in order to be registered as a signal. This is done to discriminate thermionic emission from the dynodes, which in general has a lower pulse height, than from photoelectrons from the cathode. The threshold voltage was characterized in figure 4.21. The dark current behavior of two types of PMT were tested because no data was available. The vacuum cooling setup for this is described in section 4.3. The results can be seen in figures 4.23, 4.24 and 4.22 and the stability of dark counts can be seen in figure 4.25. The photon counting in our experiments is done by using the Becker and Hickl PMS400A counting cards. These convert the electronic pulses to a digital computer signal.

4.1.6 CCD and MCP Cameras

In some of the experiments, the PMT was replaced by a CCD camera, the Andor Newton SO BN940. The camera is placed under a 32° angle such that it is in the focal plane

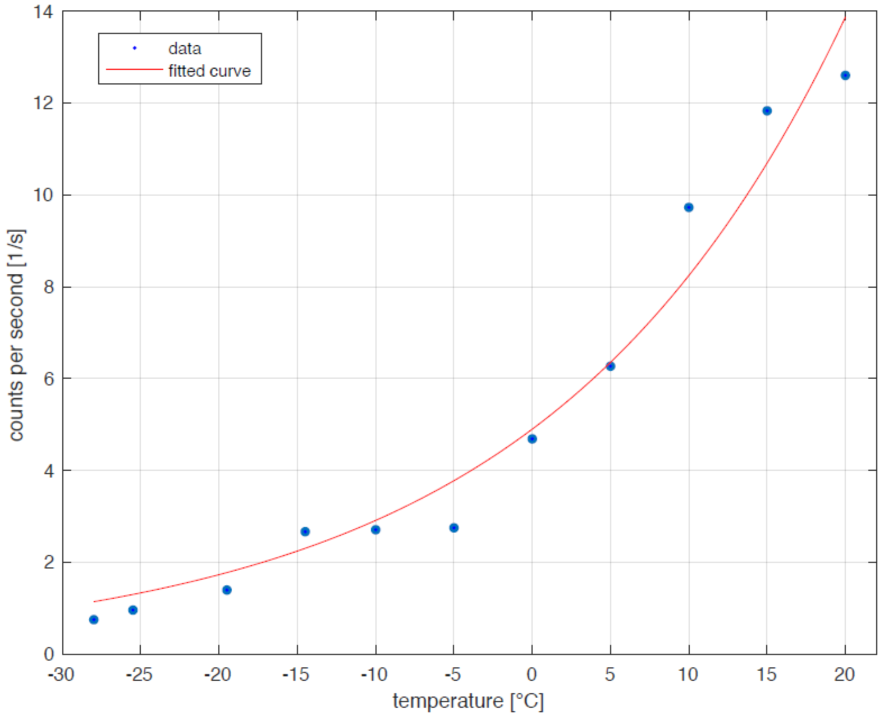

Figure 4.22: Dark current pulses per second as a function of temperature for the R7639 HO Diamond PMT. Each point was measured for 4 minutes. The red line is an exponential fit.

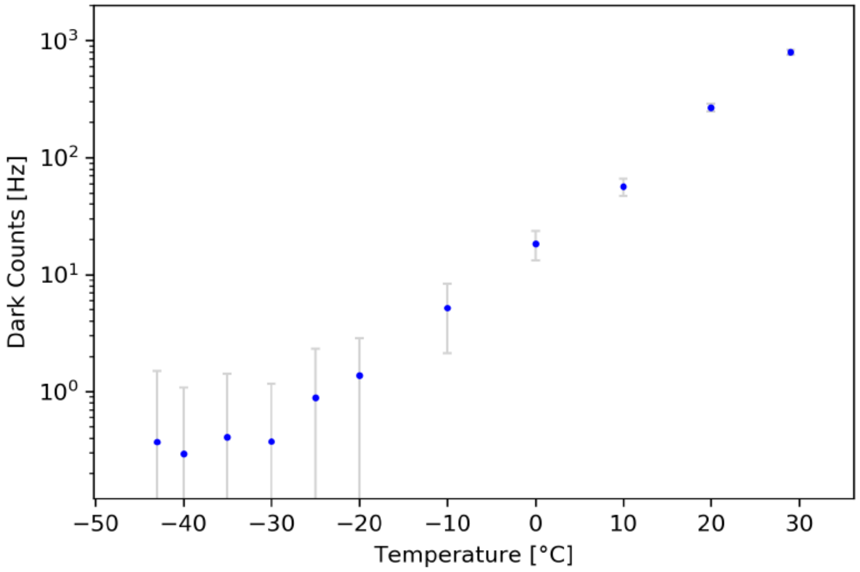

Figure 4.23: Dark current pulses per second as a function of temperature for the R6836 HO CsTe PMT. Each point was measured for 17 minutes and 30 seconds.

of the McPherson spectrometer (see figure 4.1). The benefit of using a camera is that a complete spectrum with a width between 50 and 200 nm can be instantly recorded. Normally the 1200 lines/mm grating is used which has a dispersion of 4 nm/mm and thus produces a spectrum with a width of 110 nm on the 27.6 mm CCD chip. In practice the width is reduced because the edges of the diffracted light spectrum from the grating

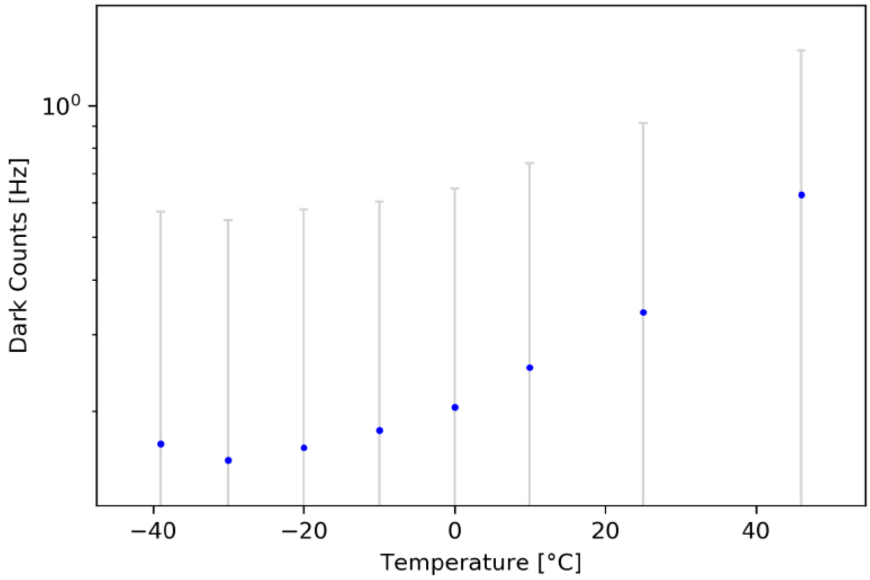

FIGURE 4.24: Dark current pulses per second as a function of temperature for the R6835 HO CsI PMT. Points were measured for between 4.5 and 16 hrs.

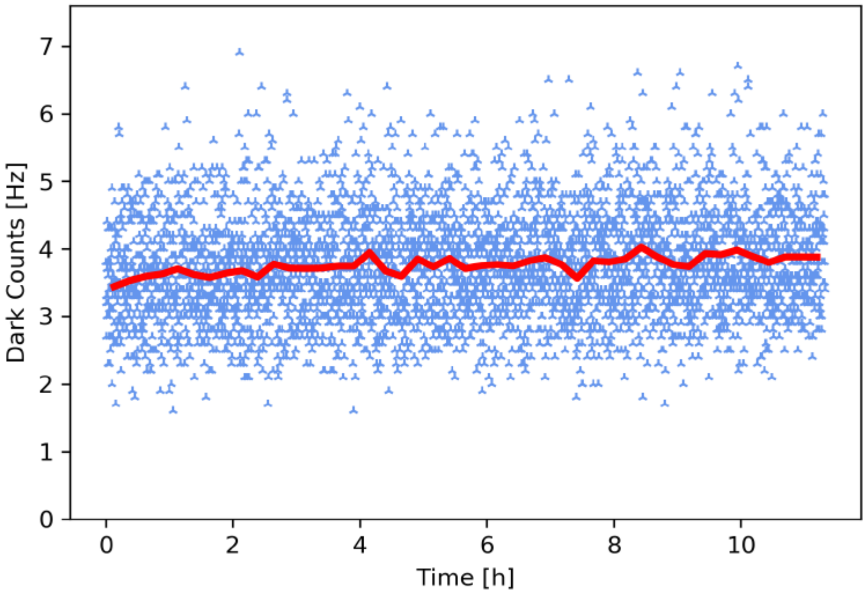

FIGURE 4.25: Dark current time stability for the R6835 HO CsI PMT at -10 °C, the red line indicates the mean every 15 minutes. The total mean is 3.76 ± 0.13 Hz.

are blocked by the walls of the vacuum system. The efficiency of the CCD is quite flat from 5 to 10 eV (248 to 124 nm) and around 15 %. To compare, PMTs have a more peaked efficiency profile in this region (see figures 4.18, 4.19 and 4.17) but also have higher efficiencies (up to 40 % for diamond).

The image of the CCD is not purely the photons falling onto the detector. Different effects create a signal independent of photon illumination and determine how a CCD image appears. Here a brief overview:

- Bias differences. Due to minor differences in applied voltage across the CCD chip a different constant offset value is measured at each pixel.
- Dark current. Even when no light hits the CCD it will accumulate counts due to thermally excited electrons. By cooling the CCD to -100 °C the dark counts can be exponentially suppressed to $5.5 \cdot 10^{-5}$ e$^-$/pixel/s.
- Readout noise. The analog to digital converter that reads out the pixels and converts the amount of electrons in there to a count will induce some noise, for example sampling noise. Pixels can be binned to reduce readout noise per pixel. Binning means that a larger square of pixels is read out at the same time and thus only once readout noise is added to the signal. This increases signal to noise ratio.
- Flat field differences. The pixels on the CCD are almost exactly the same, but slight differences in efficiency occur (up to 10 %). A flat field image can be (homogeneously illuminated chip) in order to compensate for this effect.
- Overexposure/burning in of light [209]. If a cooled CCD is hit with intense enough high energy photons, defects will be created in the silicon of the chip which will create an artificially higher dark count in the affected region until the chip is heated up again and thus annealed.

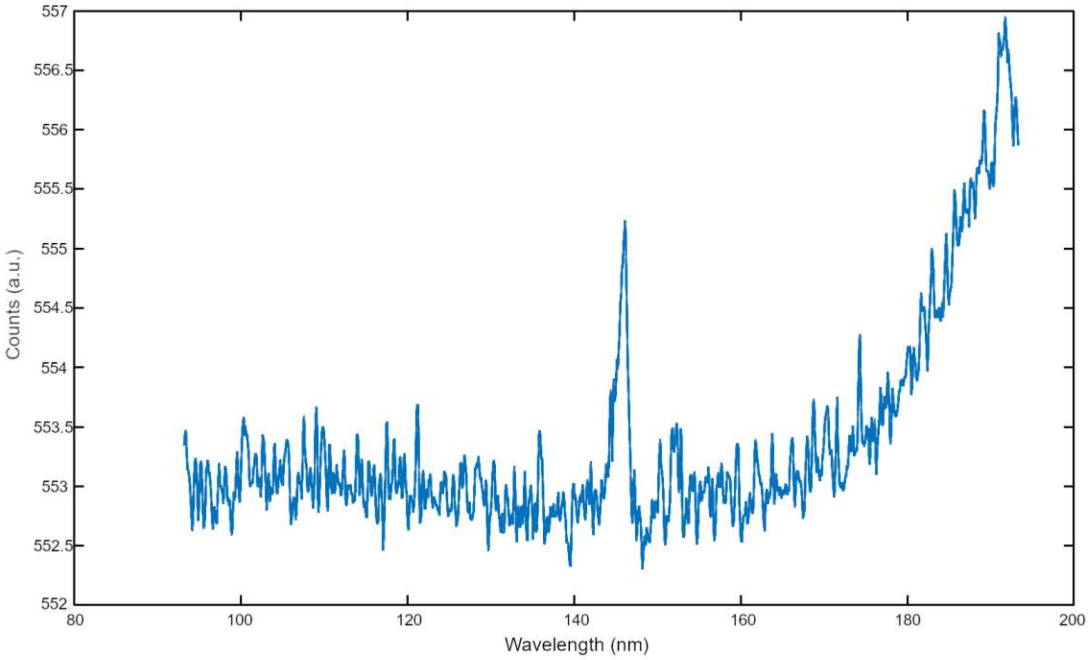

FIGURE 4.26: Narrow signal caused by the overexposure of a CCD chip by the 147 nm xenon atomic line in a measured spectrum. On the higher wavelength side STE radioluminescence can be seen caused by a ^{229}Th:CaF$_2$ crystal in the system.

The overexposure can give a signal very similar to a fluorescence signal on a CCD, if the light that overexposed the camera is a narrow feature as well. The overexposure creates

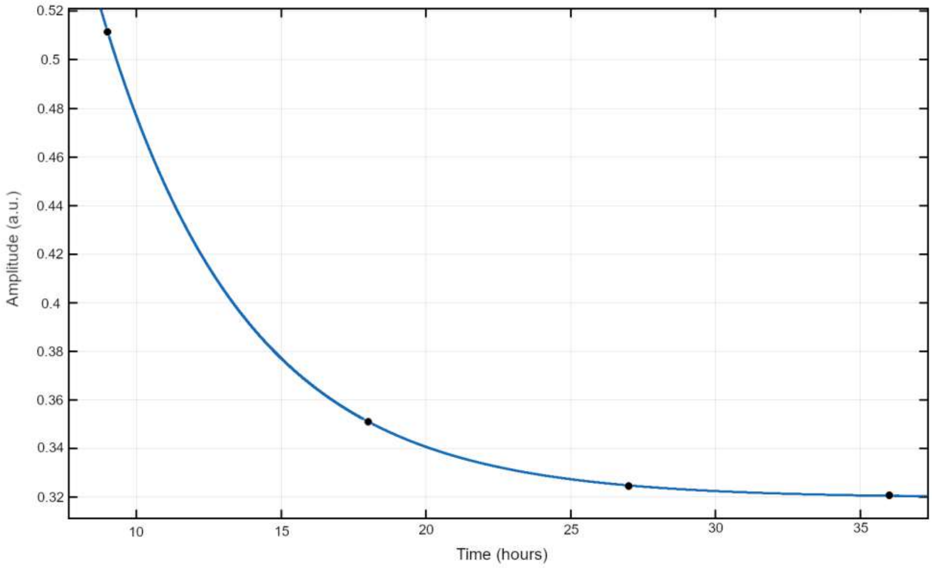

FIGURE 4.27: Overexposure signal lifetime from the signal in figure 4.26. The amplitude of the peak at 147 nm follows an exponential decay with a lifetime of 3 hours but decays to a constant amplitude, which would not be expected of any photon signal but would be expected from defects.

defects in the silicon crystal that are stable at the temperatures of the cooled CCD chip. These defects produce more dark noise which changes over time, see figure 4.26 and 4.27 to see a typical burn-in signal from the 147 nm xenon atomic line. Also PMTs and MCPs can be overexposed.

Aside from a CCD, one could install a microchannel plate (MCP). The MCP is based on the same operating principle as a PMT, but has spatial sensitivity. A schematic representation can be seen in figure 4.28. The MCP uses a plate with many microchannels (μm sized) in it. When a photon hits the inside of one of the channels a photoelectron is released, just as with the PMT. The electron will be accelerated towards the exit of the MCP because of the high voltage V_D applied to the front and back of the plate. The electron will hit the wall of the channel before reaching the end, creating more secondary electrons. This process causes a cascade in the small channel, resulting in a large amount of electrons leaving the channel at the other side of the plate. These electrons are then accelerated towards a phosphor screen by a high voltage applied between MCP and phosphor plate. The phosphor plate converts the electrons into photons which are then imaged by a CCD camera.

If one calculates the amount of background counts per surface for a PMT, CCD and MCP we can compare their performance. The results can be seen in table 4.2. The Andor Newton 940BN CCD chip cooled to -100 °C has $5.5{\cdot}10^{-5}$ e$^-$/pixel/s, which for 2048x512 pixels is 31 s^{-1}cm^{-2}. The efficiency is approximately 15 % at 150 nm. The dark

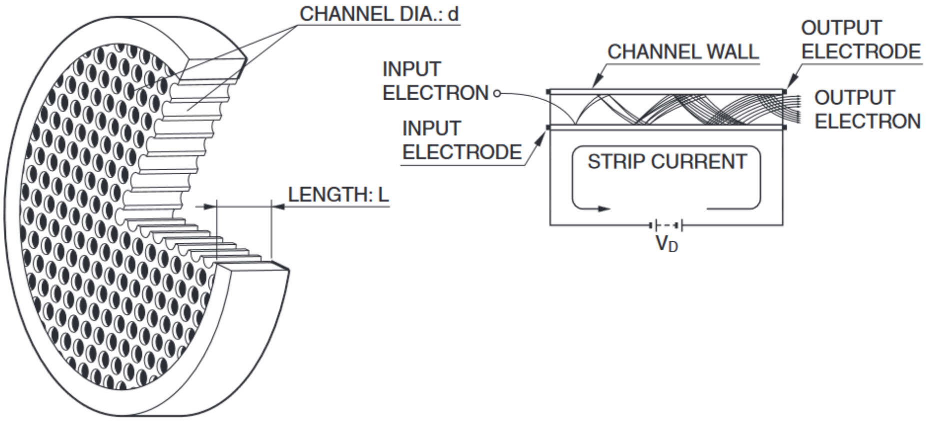

FIGURE 4.28: Left, the structure of an MCP plate. Many small channels in the material provide the avalanche amplification of any electron that is absorbed by the channel, see the image on the right. For VUV photon detection the photon would hit the inside of a channel and produce a photoelectron there, which is subsequently amplified as well. The electron avalanche can then be detected by for example a phosphor plate. Taken from [207].

noise of an MCP is 0.5 s^{-1}cm^{-2} [210]. The efficiency of an MCP depends on the material used to produce electrons, for CsI it is 20 % and for GaN it is 50 %. It was measured in figure 4.23 and 4.24 that minimal dark noise in the used PMTs is less than 0.5 s^{-1}. The active surface are of these PMTs is 23 mm in diameter, thus 0.1 s^{-1}cm^{-2}. The SO types of CsI have even less dark noise [207] and an efficiency of 25 %, the diamond PMTs an efficiency of 40 %.

TABLE 4.2: Characteristics of different VUV detectors

Detector	Background (s^{-1}cm^{-2})	efficiency (%)
PMT	0.1	25/40
CCD	31	15
MCP	0.5	20/50

In conclusion, the PMT has the least noise but no positional sensitivity to that noise. The MCP has the best efficiency and has spatial resolution, allowing to measure any spectrum in one image. The spatial resolution for all these detectors is limited by the grating resolution, not exit slit size for the PMT, CCD pixel size or MCP microchannel size. The dispersion of the 1200 lines/mm grating is 4 nm/mm and its minimum resolution is 0.1 nm. Any narrow peak will thus be at least 25 μm FWHM which is twice the size of the CCD pixels, MCP microchannels and the first increment on the micrometer screw. For taking spectra of low intensity signals an MCP seems most suited, because it avoids wavelength scanning that is needed for a PMT.

4.2 VUV Absorption Measurement Setups for (doped) CaF$_2$

For the crystal to be a useful host matrix for the thorium nucleus it needs to be transparent to the wavelength of the first nuclear excited state. To characterize optical/VUV transparency, the transmission/absorption of the grown crystals is measured. Several setups were built to measure the absolute transmission of these crystals.

To measure the absorption of the crystal, the intensity of a VUV light source was measured while passing through the crystals and compared to the unperturbed light source. A grating is used to spatially disperse the light into its components in order to measure the transmission for different wavelengths, effectively using the McPherson 234/302 as a monochromator. By measuring the wavelength-dependent absorption of the grown crystals, defect centers can be identified. As discussed in chapter 2, many have a studied characteristic wavelength at which they absorb. By identifying the centers, the growth processes and condition of the crystal can be understood.

To properly measure the absorption, the optical path of the light needs to be carefully controlled and the light source intensity needs to drift as little as possible over the measurement period. Reached reproducibility for the transmission is ±5 %. Three types of absorption setups were built:

- A setup to measure the absorption over the complete VUV spectral range (4.2.1), with results in section 4.3.
- A setup to measure the absorption over the complete VUV spectral range while heating the crystal to 620 °C (4.2.2). This setup was built to study the transmission behavior of crystals under heating (section 4.2.2) and their reaction to annealing after VUV irradiation damage (section 5.5.1).
- A setup to only measure the absorption around 150 nm for quick progress in growing transparent Th:CaF$_2$ (4.2.3), with results reported in table 3.2.

Annealing of crystals is an often used process. As explained in section 2.2.2, the mobility of F centers is greatly increased at higher temperatures. As the main defect in CaF$_2$ these F centers will naturally find H centers and annihilate. For other crystals the exact process is different, but the concept is equivalent. When supplied with enough thermal energy, defects become mobile and will quickly return to the thermal equilibrium defect concentration. The exact details on defect mobility are explained for CaF$_2$ in section 2.4.1, as the mobility and thermal formation of F and H centers changes relatively with temperature.

In the following sections the used absorption/transmission setups are detailed. Mostly a spectrally resolving transmission setup was used, as this could identify possible defect centers. A setup purely designed to measure absorption around 150 nm was built to quickly check the transparency of newly grown crystals during the optimization of the growing process. Lastly a heated holder was designed and used in these setups to measure absorptions at temperatures up to 620 °C and to anneal the crystal. The vacuum in all systems was held better than 10^{-6} mbar.

4.2.1 Spectrally Resolving Transmission Setup

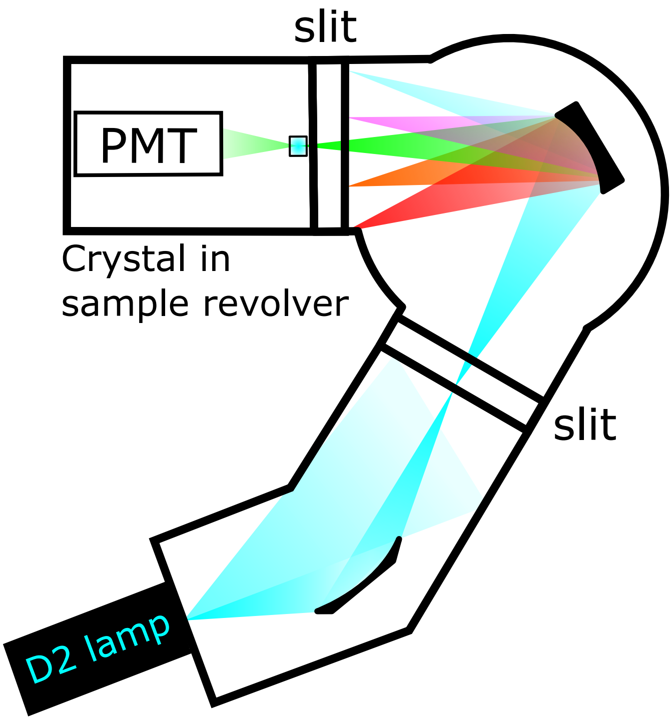

FIGURE 4.29: Experimental setup to measure the wavelength-dependent transmission of a crystal. The light of a Hamamatsu L15094 D$_2$ lamp is focused with a toroidal mirror onto the entrance slit of a McPherson 234/302 monochromator. Part of the light does not hit the focusing mirror, some part does. The light is separated into its spectral components by the grating and is focused onto the exit slit. By rotating the grating the exit wavelength can be selected. The exit slit cuts out a small portion of the spectrum effectively creating a narrow wavelength source with a linewidth down to 0.1 nm. The linewidth can be changed by changing the entrance/exit slit width (0.01 mm to 2.50 mm) as discussed in chapter 4.3.5. This light travels through the crystal, and is recorded by a HO PMT which is mounted close to the crystal. By comparing the light output with and without crystal in the optical path and scanning the grating a transmission spectrum can be measured.

In practice such a device for the VUV region looks as in figures 4.29 and 4.30. In a vacuum system, a wavelength selected by the monochromator grating setting is sent through a crystal and the transmission is measured. By scanning the monochromator

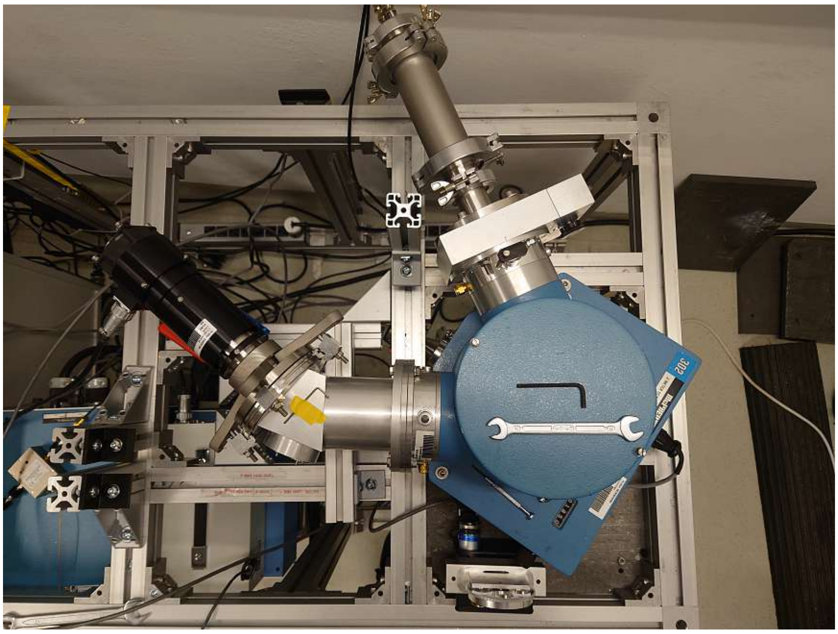

FIGURE 4.30: The transmission setup as built in the lab.

grating one can record a spectral transmission. As a light source we use the broadband D_2 lamp.

In this setup, the D_2 lamp is focused on the entrance slit to increase signal and improve resolution (up to 0.1 nm). The PMT was mounted as close to the crystal as possible to capture all the light that exits the crystal. Not only the light produced by the D_2 lamp exits the crystal, part of the light is absorbed and emitted again as STE luminescence (see chapter 2). This crystal luminescence will distort the transmission spectrum due to its spectral shape: Light emission begins at 200 nm, peaks at 280 and 300 nm and continues into the UV. The Hamamatsu CsI R6836 HO PMT was used in this setup to be blind to this luminescence in CaF$_2$. This PMT is very insensitive to light with wavelengths above 200 nm. The same setup can also be built with a CCD or MCP instead of a PMT, imaging the entire transmission spectrum at once and using the McPherson 234/302 as a spectrometer. In this case the crystal would be moved in the beam path before the entrance slit such that all light can pass through it at once.

The crystals are mounted in a filter wheel to allow transmission measurements of several crystals without breaking vacuum. They are mounted in sample holders with a 2 mm pinhole as can be seen in figure 4.31.

4.2.2 Heating/Annealing Crystal Holder

To anneal/heat CaF$_2$ crystals and not oxidize or hydrolyze them, all heating is done under vacuum. For annealing, the crystal growing device as described in section 3.2.6

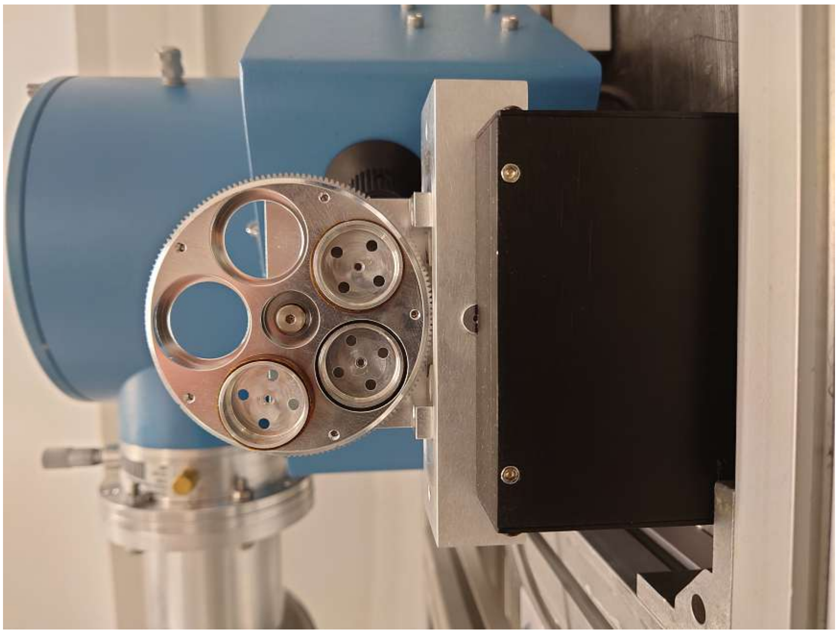

Figure 4.31: Holders for 3.2 mm diameter crystal in a filter wheel. The 4 holes surrounding the center pinhole are for screws to sandwich the crystal between two plates. The pinholes are 2 mm in diameter.

was sometimes used, as annealing is part of the growing process. Aside from that, an ohmic heating holder was designed which allowed for simultaneous heating and transmission/damage measurements. This holder is shown in figure 4.32. In figure 4.33 the holder can be seen in the vacuum system in operation. The vacuum during annealing was held better than 10^{-6} mbar.

The requirements for the holder were stringent. It needed to be compatible for use in vacuum at low and high temperatures, be able to withstand over a 1000 °C, have a large contact area with the crystal for thermal conductivity, high material electric resistance to function as an ohmic heater, have in-vacuum vertical translation and be able to measure the temperature as close to the crystal as possible. To do this the holder in figure 4.32 was designed. Stainless steel was the material of choice due to the high electrical resistance compared to other common metals ($6.9{\cdot}10^{17}\,\Omega$m). A K-type thermocouple was spot-welded as close to the crystal as possible and lead via a feedthrough through the CF40 flange. The top was cooled with a fan as to get a relatively accurate temperature measurement with the thermocouple.

The CF40 feedthrough was mounted on vertical translation bellows to move the crystal in and out of a collimated VUV light beam created by an excimer lamp (4.1.3). The area where the crystal was held was made as thin as possible, 1 mm, to increase resistance of that area. In figure 4.33 one can see that these areas are particularly hot. The semaphore that sandwiched the crystal was screwed onto the holder using brass screws and springs to provide dynamic pressure while the holder expands due to heating. After

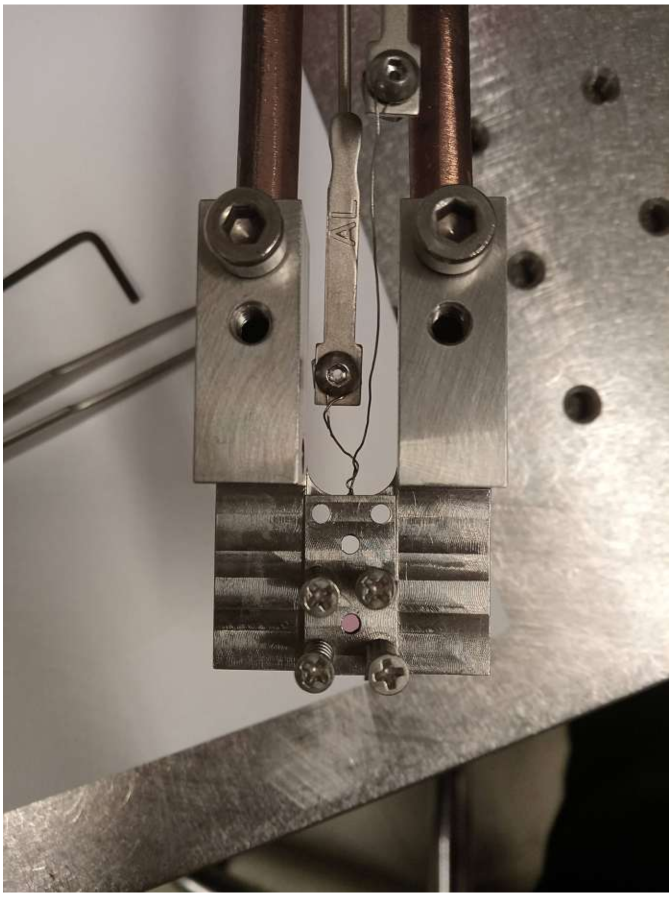

FIGURE 4.32: Ohmic heating crystal transmission holder. Thick copper leads go through a CF40 vacuum feedthrough flange for mounting on a vacuum system. Through the thick leads high currents (up to 40 A) can be run through the transmission holder to heat the crystal held inside. Two equal sized holes are used, one holds the crystal and one is empty. By measuring the VUV light output through both and comparing the transmission of the crystal can be determined as a function of temperature. The lower hole is filled with a red Uranium crystal to show how it can be used.

the first use of the brass screws at 1000 °C in vacuum almost all zinc was evaporated out of the screws. The copper parts were covered in a zinc layer and the screws turned to copper. In figure 4.34 one can see Newton rings which were produced by VUV irradiation. Possibly material produced by outgassing of the hot steel holder underwent a photochemical reaction which produced these rings on the holder.

This holder was incorporated in a VUV transmission setup in order to measure the crystal transmission. A PID controlled heating system was used to stabilize the temperature of the holder. A computer would read out the thermocouple via an amplifier and a NI USB6000 analog to digital converter. The read out temperature was used real time in a MATLAB script that would apply a PID system to determine the current that needed to be used to heat the system. This information was transferred via a GPIB connection to a HP6574A 35 A power supply to stabilize the temperature. This setup reached a temperature stability of ±0.25 °C at 300 °C as can be seen in figure 4.36. A schematic

FIGURE 4.33: Zoom through a vacuum viewport of the annealing holder while in operation. Temperatures above 800 °C were reached to create this glow.

representation of the setup can be seen in figure 4.35, a more detailed description of the Excitech Elux 147 nm light source and VUV transmission setup can be found in section 4.1. With this system the heated transmission and annealing experiments were performed, in sections 4.4.4 and 5.5.1 the results are described.

4.2.3 150 nm Transmission Check setup

Due to experimental setbacks a setup was built to measure the transmission of newly grown crystals at 150 nm rapidly instead of recording a full spectrum. Using this setup the 150 nm transmission of freshly grown 3.2 mm diameter crystals could be verified which would stimulate fast development of good Th:CaF$_2$ crystals.

The simple setup consisted of the D$_2$ L1835 VUV light source, a collimator, bandpass filter and a detector as shown in figures 4.37 and 4.38. The bandpass filter used was from esource optics and had a peak transmission at 150 nm of 15 % and a FWHM of 20 nm. Using the filter an effective average transmission from 140 to 160 nm was measured, the region that is crucial for the experiments. The collimator was a stack of 4 mm apertures with 5 mm gap between them. The space in between the apertures was painted using Aeroglaze z306 to reduce internal reflections. Instead of photon counting using the Becker & Hickl PMS400A card, the current of the PMT was read out directly. A voltage of 2500 V was used on the HO R6836 CsI PMT of Hamamatsu.

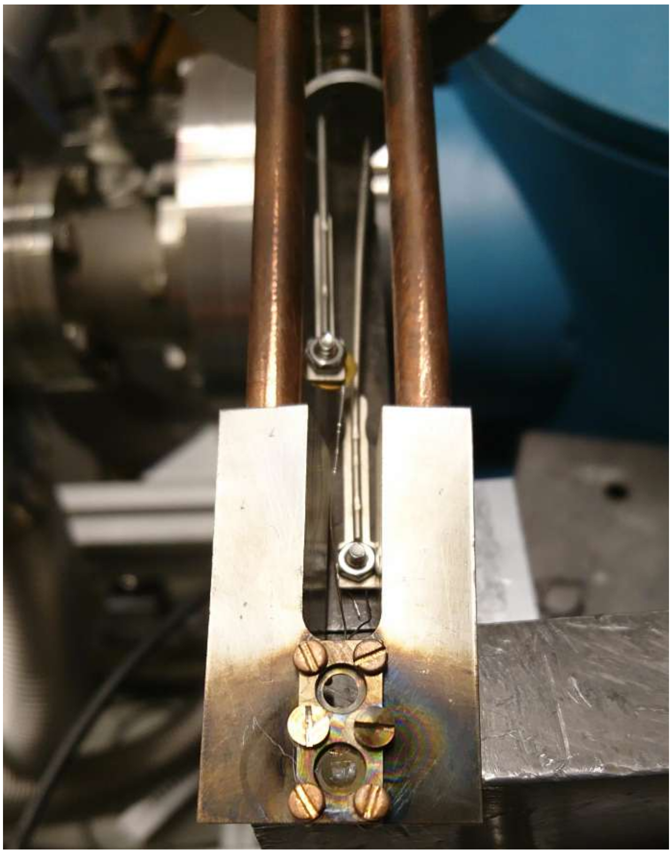

FIGURE 4.34: Ohmic heating crystal transmission holder after focused VUV illumination and simultaneous heating.

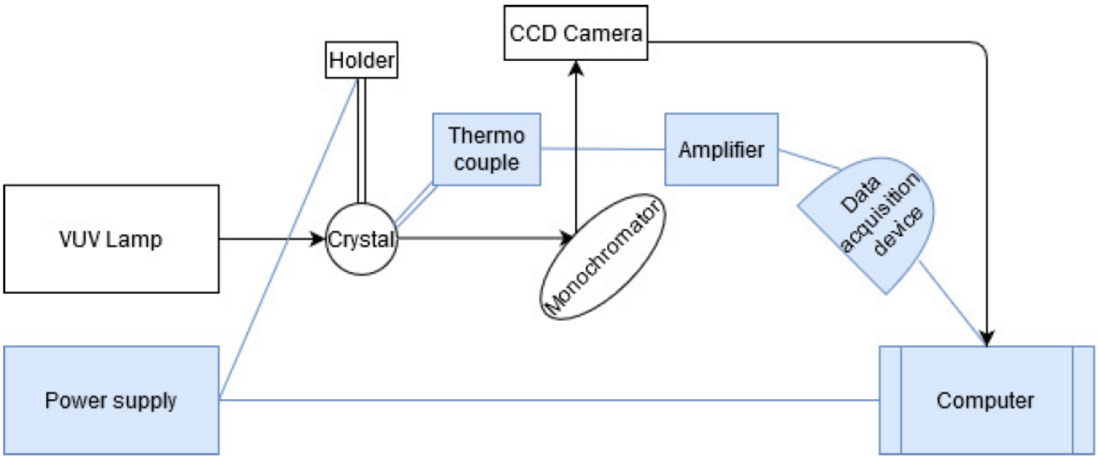

FIGURE 4.35: Schematic representation of the annealing and transmission measurement system. The transmission could be measured while the crystal is hot or after an annealing period. The blue cycle is the closed circle controlled by a PID scheme.

4.3 Long Integration VUV Luminescence Setup

CaF$_2$ is an excellent scintillator, it produces light when it absorbs high-energy photons or is bombarded by particles (see chapter 2). This means that the radioactivity inherent

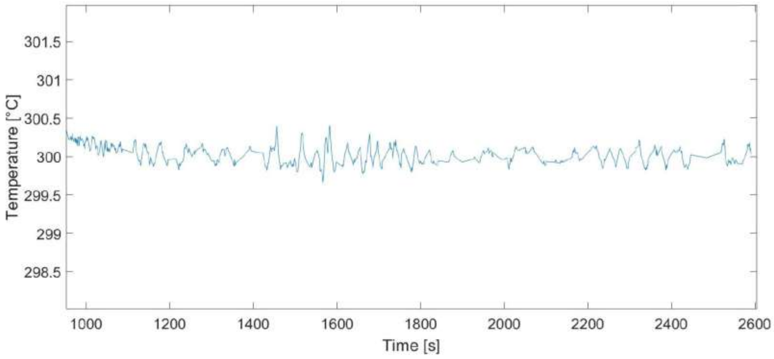

Figure 4.36: Measured temperature of the holder over time when PID stabilization is turned on for 300 °C.

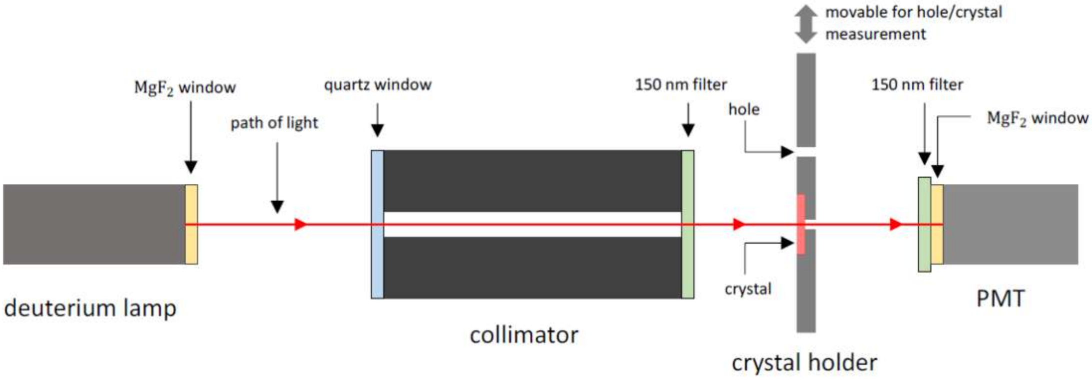

Figure 4.37: Schematic representation of a setup that measures the transmission of a crystal at 150 nm. Light from a Hamamatsu L1835 D$_2$ lamp is collimated and passes through a quartz window which effectively cuts the light below 147 nm. This is done to reduce VUV damage to the filters and sample. Secondly the light passes through a 150 nm band pass filter. The filtered 150 nm light passes through a cut and polished crystal and afterwards through another filter. The second filter removes any fluorescence that would contribute to counts on the PMT. In the end a Hamamatsu R6836 CsI HO PMT is used to detect the amount of light. The measurement is repeated for an open hole and compared to obtain the transmission of that crystal.

to the ^{229}Th and ^{233}U doped crystals will produce light. Light will be emitted in the VUV (120-200 nm) in the form of Cherenkov radiation (and hopefully isomer photon emission) and in the UV (200-400 nm) in the form of STE annihilation.

To characterize the radio-induced luminescence in the grown crystals a setup was designed to measure low photon fluxes. Since the interest of this research is mainly in the VUV, the UV light will be blocked by using solar blind PMTs (see section 4.1.5). These same PMTs also provide one of the highest photon detection efficiencies to measure the low photon fluxes involved. The setup is designed to provide spectral sensitivity to be able to distinguish between Cherenkov emission, STE emission and other possible sources. This same setup is also used to characterize the light produced by neutron activated crystals and might possibly one day measure the isomer photon emission from ^{233}U:CaF$_2$ or ^{228}Ra:CaF$_2$ crystals (see chapter 6).

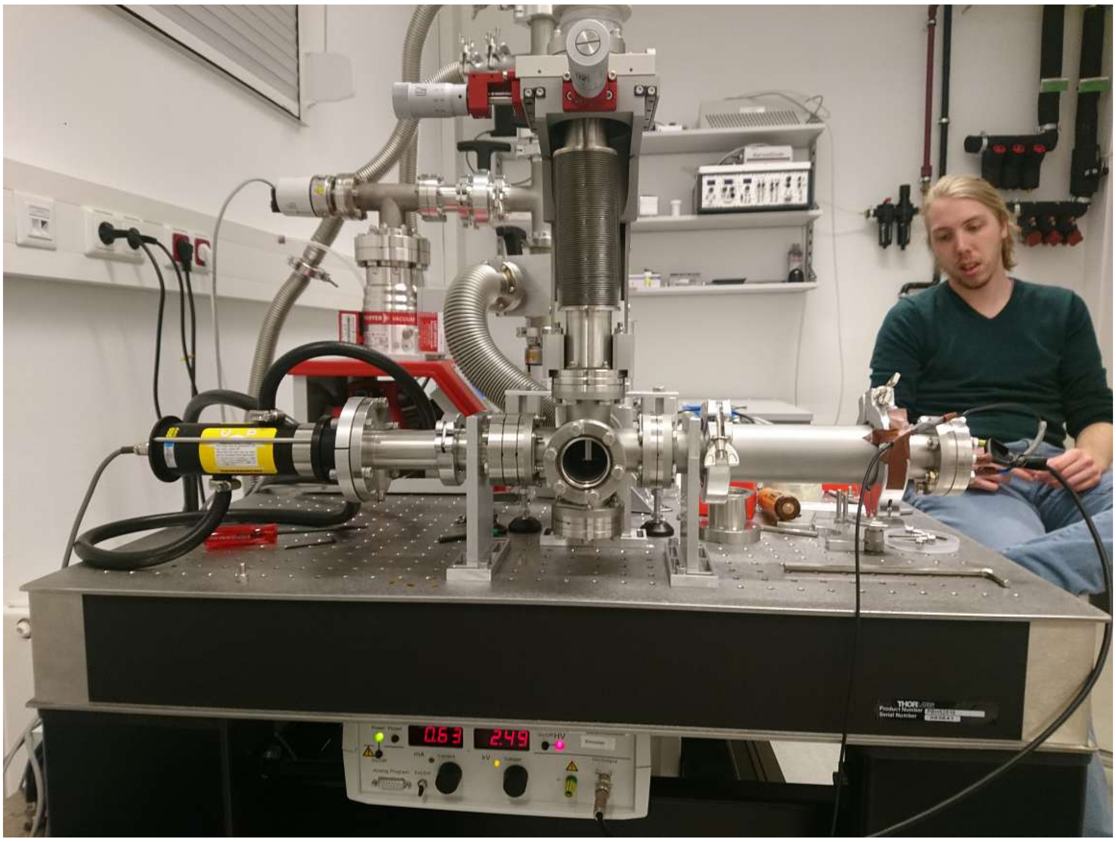

FIGURE 4.38: The 150 nm transmission setup as built in the lab.

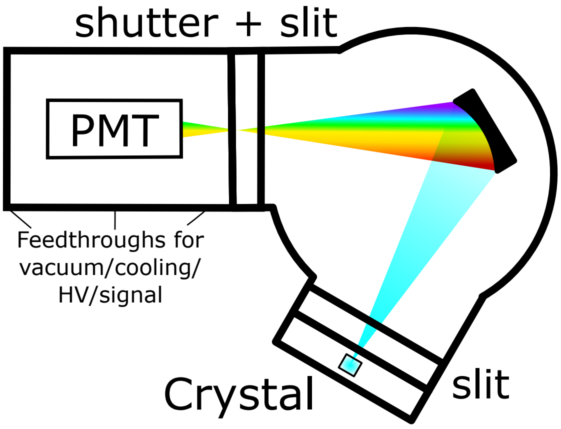

FIGURE 4.39: Schematic drawing of the detector-spectrometer combination used to measure the fluorescence of activated crystals. The fluorescence produced by the crystal goes through the entrance slit and is then imaged by a focusing grating in a Seya-Namioka spectrometer model onto the exit slit. Only a slit size-dependent fraction of wavelengths will fall onto the PMT. Directly after the exit slit a fast (18.0 ms opening time) shutter is installed.

To characterize the grown crystals, the Seya-Namioka design McPherson 234/302 VUV reflective grating spectrometer was used in combination with a PMT, illustrated in figure 4.39. This provides spectral sensitivity and high detection efficiency, while blocking out all STE luminescence due to the solar blindness of the PMT spectral sensitivity

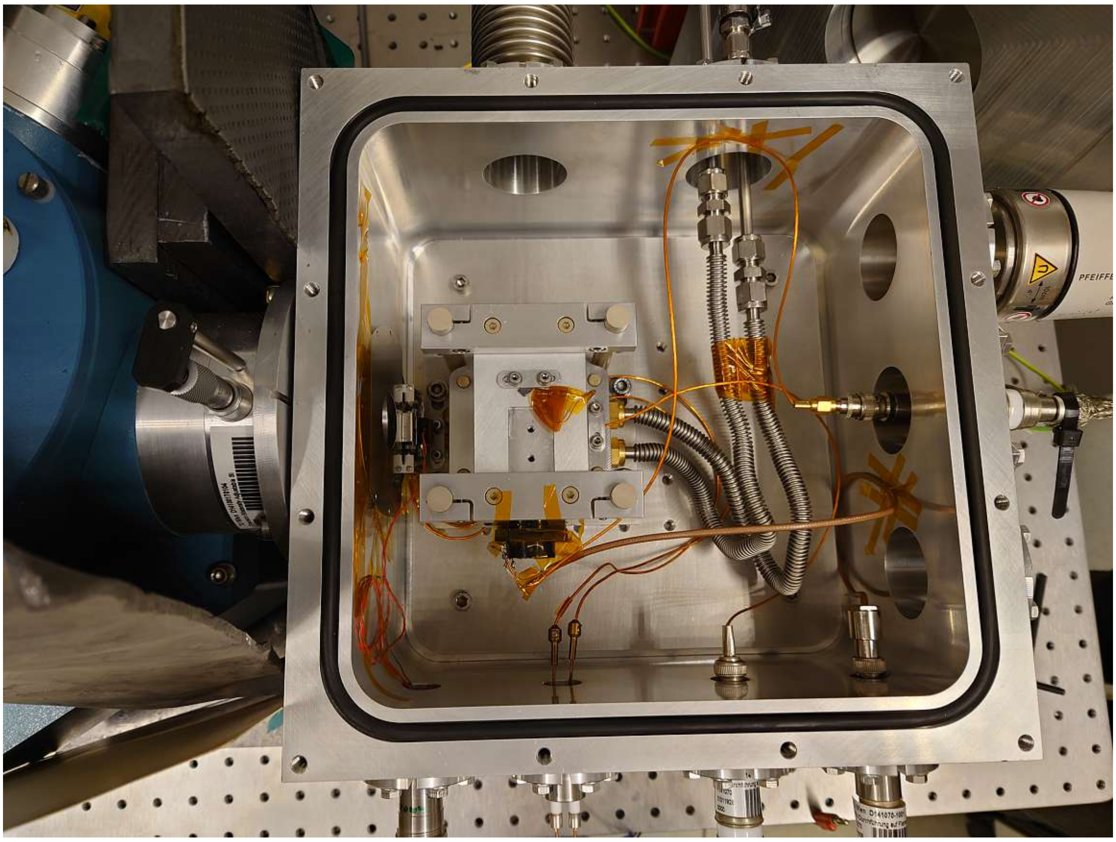

FIGURE 4.40: Long integration setup open in the lab. From left to right, the McPherson 234/302 VUV spectrometer, a VS35 shutter, a cooled diamond PMT and the wiring needed for that. The PMT cooling is water-cooled from the outside using 11 °C water, see tubes. It is important to avoid loops in the signal wire as to reduce noise on the signal line.

(figure 4.3). A more detailed image of the PMT chamber is shown in figure 4.40, and the total setup in the lab in figure 4.41. The vacuum during measurement was held better than 10^{-4} mbar.

By rotating the grating in the spectrometer, the detected wavelength changes. The crystal is put in the focal point of the grating, behind the entrance slit. Increasing the width of the entrance slit increases the amount of signal that reaches the grating, but reduces the resolution of the spectrometer. The detector on the exit slit is a diamond PMT (Hamamatsu SO diamond R7639). A shutter (Uniblitz VS35) is installed in between the PMT and exit slit to take background measurements (shutter closed) simultaneous with signal measurements (shutter open).

The percentage of photons produced by the crystal that fall on the detector is calculated to be 0.3 %, and the efficiency of the PMT and grating combined is 14 % at 150 nm (see section 4.1.1). In total, the system efficiency is 0.05 % at 150 nm. Due to the grating's and PMT's wavelength dependent efficiency this will be different for other wavelengths (figure 4.3). By using different slit openings more light can be put into the system and

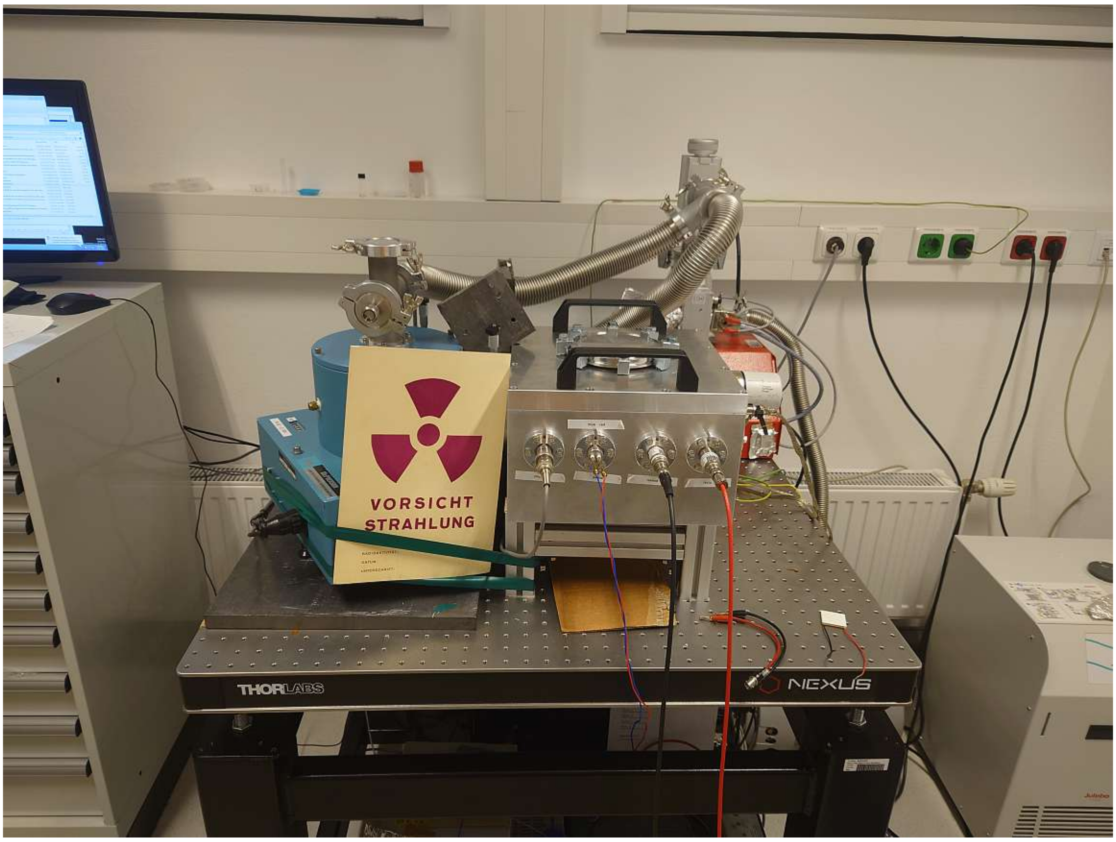

FIGURE 4.41: Long integration setup in the lab, as in 4.39. Note the lead shielding between crystal and detector. This was needed due to the high activities produced through neutron irradiation of CaF$_2$ crystals.

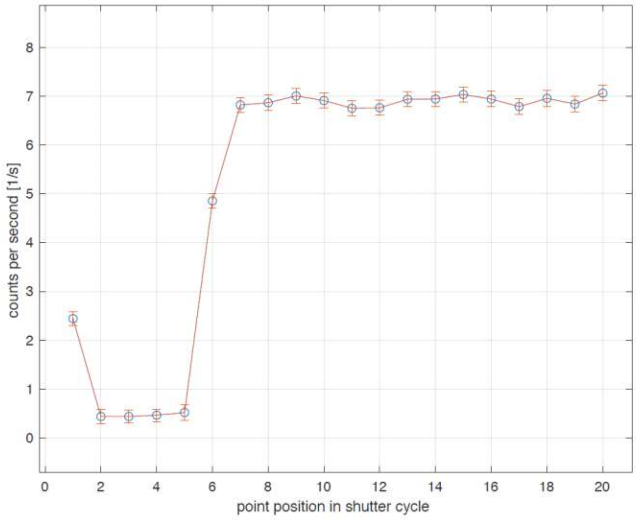

FIGURE 4.42: Shutter cycle as measured by the setup in figure 4.39. For the first 5 points the shutter is closed, for the last 15 points, the shutter is open. Total measurement time of this cycle is 2 s. The opening time of the shutter is 0.018 s which causes the not completely dark measurement of point 1 and not completely exposed measurement of point 6. In the data processing these points are removed. By using this measurement cycle every 2 s dark and light measurements are recorded.

thus increase signal strength. This assumes that the crystal is a point source and is exactly in the position of the entrance slit. Since both do not hold, the real efficiency of the total system will be lower. Other factors reducing the efficiency are lensing of the crystal, absorption by the crystal and the critical angle of total internal reflection ($\theta_c = 39.21°$) of the crystal.

This setup was used to record the spectrum produced by:

- ^{229}Th:CaF$_2$ crystals
- $^{233/232}$U:CaF$_2$ crystals with the possible de-excitation of the ^{229}Th isomer
- A ^{32}P irradiated CaF$_2$ crystal producing Cherenkov radiation
- Neutron activated CaF$_2$ producing Cherenkov radiation and STE luminescence to characterize the background for a measurement as described in section 6.2.1

In these measurements long integration times are used: hours for activated crystals and days for ^{229}Th/^{233}U:CaF$_2$ crystals. In order to register unavoidable drifts in dark counts, the shutter was used to measure the current dark counts. Effectively each measurement was done by repeating a measurement cycle of 20 points of 0.1 s integration time where 5/20 are shutter closed measurements and 15/20 are shutter open measurements. A representation of such a measurement cycle can be seen in figure 4.42. A PMT cooling jacket was designed to cool the PMT to reduce dark counts during these long measurements. A heated holder was designed to measure the effect of heating on the radioluminescence.

4.3.1 PMT Cooling Jacket

As can be seen from equation 4.6, and from the characterization curves in section 4.1.5, cooling the PMT reduces the background and thus increases the probability of measuring the nuclear isomer (or other faint signals). For this purpose a vacuum compatible cooling jacket was developed as this was not available from the PMT supplier. The only question that remains open about cooling is how it affects the sensitivity of the PMT; this was not characterized by the supplier. Cooling the PMT using a metal jacket creates issues. Under negative high voltage the PMT will direct any photoelectrons from the front cathode to the back grounded anode. Since now ground is all around the electrodes in the form of the metal jacket electrons will be deflected towards the walls and create luminescence in the walls. This effect increases background and can be avoided by running the PMT on positive high voltage.

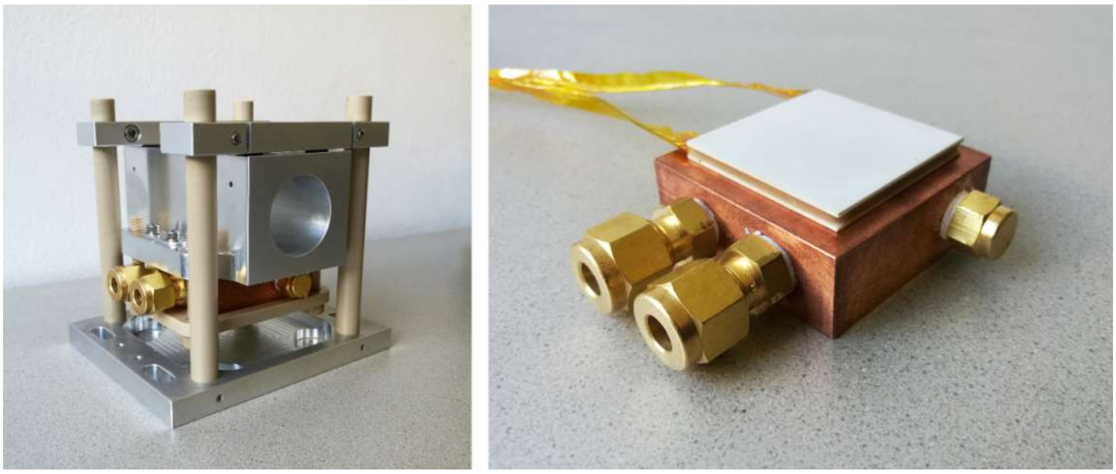

FIGURE 4.43: Total PMT cooler with aluminum cooling jacket and zoom of copper block with Peltier element. In between the Peltier element and copper block a sheet of graphene was added for thermal conductivity. The graphene sheet was chosen because of its vacuum compatibility and high thermal conductivity of 18 W/(m·K). Both a head-on and a side-on PMT can be mounted in the holder.

The PMT is cooled through an aluminum jacked which is connected to a Peltier element in combination with a water cooled copper block, see figure 4.43. The Peltier element uses current to move heat from one side of the element to the other, and the water through the copper block transports that heat away. As a rule of thumb, the PMT can create a temperature difference of 40 °C depending on the temperature on the cold side of the Peltier. The resulting minimum temperature is then around -40 °C.

For water tubing, Swagelok vacuum tubes were used. The water connections on the copper block were sealed using tapered pipe threads (NPT) in combination with teflon tape wrapped around the threads. A closed cycle lab water cooler is used to keep the copper block cooled. Electric wires were coated in kapton. The copper block with Peltier element is pressed onto the cooling jacket with PEEK screws and a PEEK plate to avoid heat leaking from the copper block to the colder aluminum jacket.

The aluminum jacket is again isolated from the top support structure with PEEK washers, and 4 PEEK pillars hold the structure at the appropriate height to reduce heat leaks from the vacuum chamber as much as possible. PEEK is chosen because of its vacuum compatibility and its low thermal conductivity (0.25 W/(m·K)). The structure is made to be mounted on an optical table. Every drill hole goes completely through the material to avoid trapped air in vacuum.

On top of the aluminum jacket a PT1000 thermistor is pressed using screws. The temperature is read out using a NI USB6000 and a python script feedbacks this information to a controllable power supply that determines the Peltier elements power. Using this setup a temperature stability of ±0.3 °C can be achieved and a minimum temperature of -43 °C.

4.3.2 Crystal Heating Holder for Luminescence Measurements

A simple ohmic heating setup was installed to measure the radioluminescence of a ^{229}Th:CaF$_2$ crystal in a long integration setup with a camera instead of PMT while heating the crystal. The suspension heating coil and the ^{229}Th:CaF$_2$ crystal can be seen in figure 4.44. The results obtained with this setup are discussed in section 4.5.3.

FIGURE 4.44: Simple ohmic heating holder. The V057 ^{229}Th:CaF$_2$ crystal was wrapped in a kapton isolated copper wire effectively producing a coil. The coil, a temperature sensor and holding mechanism were secured using torrseal. Using a vacuum electrical feedthrough and a 12V power supply the crystal was heated. The crystal was put in front of a McPherson 234/302 spectrometer with a camera at the end to measure the temperature dependent radioluminescence.

4.4 VUV Absorption of Th:CaF$_2$ and U:CaF$_2$

To serve as a platform for a future nuclear optical clock, the crystals need to be transparent to VUV photons. In principle CaF$_2$ should be transparent, but the doping and produced defects can change this fact (see chapter 2). Therefore the VUV transmission of the $^{229/232}$Th:CaF$_2$ crystals was characterized (4.4.1) using the setups described above.

The crystals grown using high activity possibly showed signs of fluoride deficiency, so fluoride annealing was attempted to increase transmission after growth (4.4.2). To assess the viability of measuring the photon emission of $^{229\mathrm{m}}$Th through ^{233}U decay in CaF$_2$ the transmission of these crystals grown in [172] were remeasured (4.4.3). The behavior of the crystal transmission under heating and cooling was studied to improve characteristics for any future experiment (4.4.4). In the end the damage created by the radioactive dopant in the crystal itself is assessed (4.4.5).

4.4.1 VUV Absorption of $^{229/232}$Th:CaF$_2$ and Color Centers

In order to ensure a good transmission after growth, the crystals were characterized in a series of experiments described below. The spectral features were studied to learn more about defects in the crystal, produced during and after growth. The transmission efficiency using the setup detailed in section 4.2.3 are reported in table 3.2. Here we discuss the spectral transmissions measured using the setup described in section 4.2.1 and compare different concentrations of crystals doped with ^{232}Th and ^{229}Th.

In a spectral transmission measurement the wavelength-dependent absorption of a material is measured. To explain the intricacies of transmission measurements we follow a 150 nm photon encountering a material. A photon traveling in vacuum encounters a material, in our case CaF$_2$. On the interface between the two optical media it is subjected to the Fresnel equations that describe reflection and transmission. In the case of unpolarized light that arrives at normal incidence the equation for reflection R_1 simplifies to

$$R_1 = \left| \frac{n_1 - n_2}{n_1 + n_2} \right|^2 , \tag{4.7}$$

where n_1 is the refractive index of the material the photon is leaving and n_2 the refractive index of the material to which the photon arrives. About 5.15 % of the incoming photon will be reflected and 94.85 % will be transmitted while going into CaF$_2$. In the CaF$_2$ the photon will interact with any available electronic and nuclear states. The bandgap of undoped CaF$_2$ is large, so photons from approximately 12 μm to 122 nm will not be absorbed and leave the material at the next interface. If due to doping, or the creation of defects, new electronic states emerge the photon can interact with them and be absorbed. At the next interface again 5.15 % will be reflected back, and 94.85 % will be transmitted. Of the 5.15 % that is reflected back into CaF$_2$, again some is reflected back towards the traveling direction of the photon and will contribute to the transmission. The total reflection losses R_2 including these multiple reflections is then

$$R_2 = \frac{2R_1}{1+R_1}, \tag{4.8}$$

which means the total transmission T is then

$$T = 1 - R_2. \tag{4.9}$$

So disregarding other absorption processes, ≈90 % of the photons will make it through the medium and in our case will fall on a detector.

Now we compare the photons that are transmitted by the crystals to the photons that do not travel through a crystal. The ratio between the signal strengths detected by the detector is then the transmission, assuming a linear detector. From the description above one can see that a maximum transmission of 90 % can be measured using this method. Any deviation from this value would mean that an absorption is present in the material or on the surface. By looking at absorption in the crystal one can learn of the presence of defects and doping in the material.

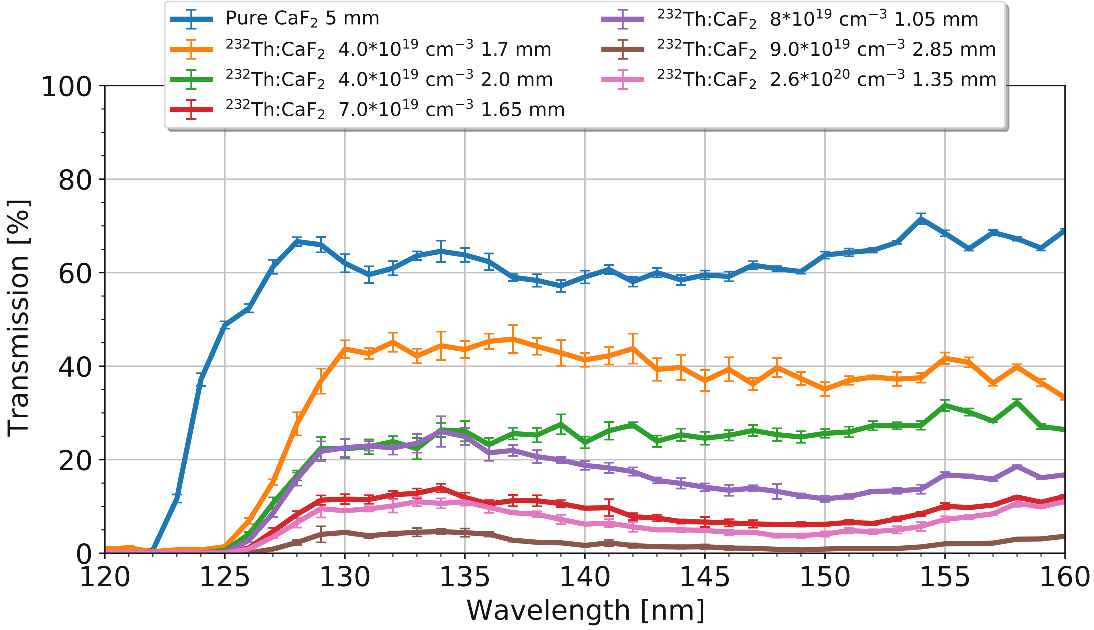

Figure 4.45: Spectral transmissions of ^{232}Th:CaF$_2$ with different thicknesses and concentrations for different wavelengths. A sample of RAMAN/Excimer grade CaF$_2$ produced and polished by Korth GmbH is displayed for comparison, thickness 5 mm. It can be seen that the thorium doped crystals all absorb heavily below 130 nm, but pure CaF$_2$ only below 125 nm. By not taking into account the thickness, volume absorption is not taken into account properly. Crystals measured here are V9.1, V10.1, V11.1, V12.1, V14.2 and V15.2. The powder for these crystals was prepared through mixing (see section 3.2.3).

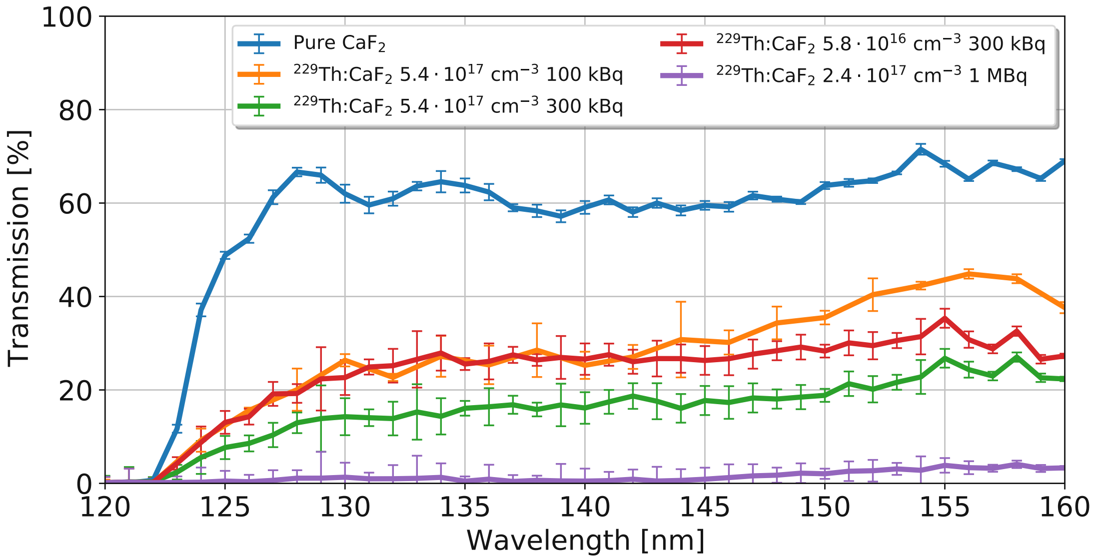

FIGURE 4.46: Spectral transmissions of ^{229}Th:CaF$_2$ with different thicknesses and concentrations for different wavelengths. A sample of RAMAN grade CaF$_2$ produced and polished by Korth GmbH is displayed for comparison (not remeasured), thickness 5 mm. It can be seen that the thorium doped crystals consistently transmit less than pure CaF$_2$, but otherwise follow the same behavior. By not taking into account the thickness, volume absorption is not taken into account properly. Crystals measured here were C10.5, C13.2, C13.5 and X2u.

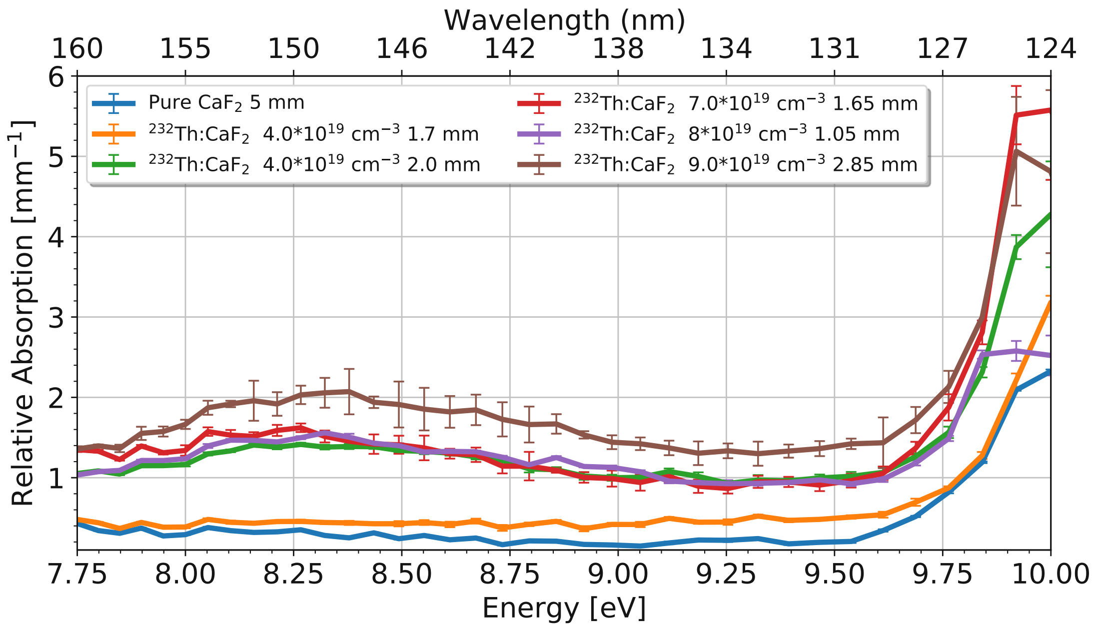

FIGURE 4.47: Relative absorption coefficient of ^{232}Th:CaF$_2$ with different concentrations for different energies and wavelengths. Main features are general increase in absorption for higher concentrations, absorption around 150 nm and below 130 nm or after 9.5 eV. The thickness of the crystal limits how well high absorption can be measured which is visible in the figure: the thinnest crystals have the highest absorption around 10 eV. Crystals measured here are V9.1, V10.1, V11.1, V12.1, V14.2 and V15.2.

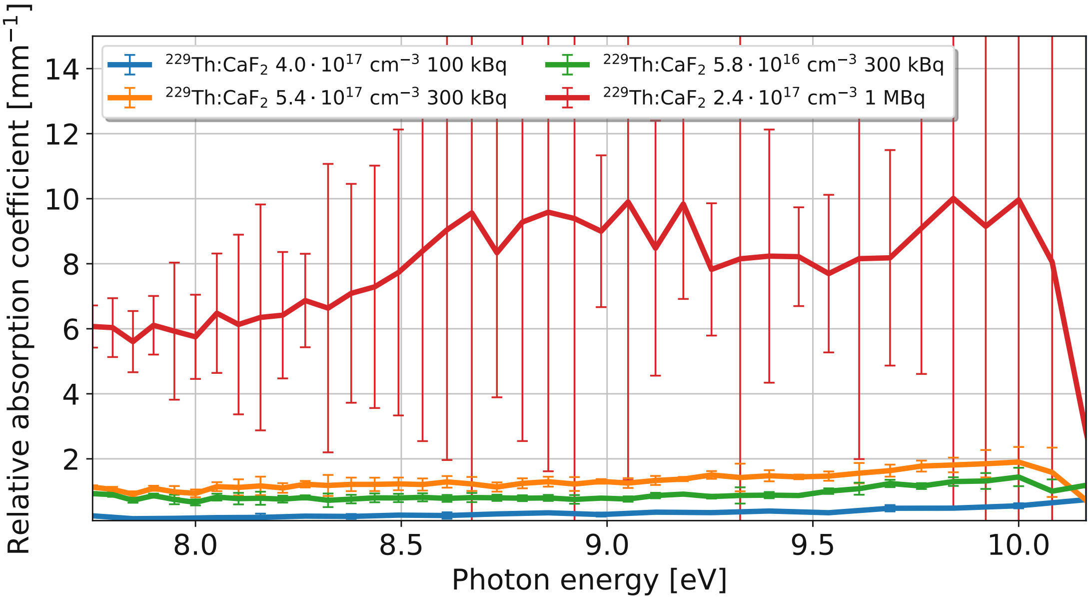

FIGURE 4.48: Relative absorption coefficient of ^{229}Th:CaF$_2$ crystals with different concentrations for different energies and wavelengths. Crystal X2u, grown under 1 MBq activity, was only 0.5 mm thick. The thickness allowed an absorption measurement with high uncertainty. The absorption profile of these crystals is flat with few features. The bandgap edge of CaF$_2$ after 10 eV is seen. With higher activity during growth, more absorption is observed independent of concentration. The crystals measured were C10.5, C13.2, C13.5 and X2u

Measuring the absolute wavelength-dependent absorption is a challenging task. The systematic uncertainty on the measured transmissions is hard to estimate, but was measured to be ±5 %. Small changes in the optical path of the light when it passes through a crystal and when it doesn't, changes the measured intensity. With it, the resulting transmission can change in absolute value. The spectral shape of the transmission is not affected by this due to the nature of the optical elements. Due to this, crystals were always measured in close succession within the same measurement such that experimental parameters were kept consistent.

To compensate for the thickness of the crystal, surface reflections, and absorption at the surface we calculate the absorption coefficient relative to pure CaF$_2$, μ_{rel}. This relative absorption coefficient then is a measure for the absorption caused by Th doping in the bulk and surface. Here we assume that the bulk of undoped CaF$_2$ absorbs very little, which is true for thin samples ($d < 6$ mm) [91]. It is assumed that due to the low intensities used in our experiments, two-photon absorption plays a small role, although it has been shown that this process is significant in CaF$_2$. It is assumed that surface quality is similar for all measured crystals, which is hard to guarantee due to the aging process [93]. The relative absorption coefficient is then

$$\mu_{rel} = \frac{-\log\left(T/T_{CaF_2}\right)}{d}, \tag{4.10}$$

where T is the transmission, T_{CaF_2} the transmission of pure CaF$_2$ and d the thickness of the crystal. We measured the transmission and subsequently calculated the relative absorption of $^{229/232}$Th:CaF$_2$, which can be seen in figures 4.45 and 4.46 for transmission and figures 4.47 and 4.48 for the relative absorption respectively.

From figures 4.45 and 4.46 it can be clearly seen that all grown crystals have a transmission above 1 % around 150 nm, some reaching ≈40 %. Doping concentrations up to $2.6{\cdot}10^{20}$ cm^{-3} for ^{232}Th and up to $5.4{\cdot}10^{17}$ cm^{-3} ^{229}Th were grown with good transparency.

The ^{232}Th doped crystals often show an absorption around 150 nm, possibly due to Ca metallic particles [211]. Normally they absorb around 160 nm but the presence of Th might change the refractive index of the crystal and possibly the electron density in the metal particle thereby changing the absorption wavelength (see section 2.2.3). Higher concentrations seem to give more absorption. All crystals seem to absorb starting from 130 nm and have very low transmission below 125 nm, earlier than the transmission edge of CaF$_2$ which starts at 125 nm and has little transmission below 122 nm.

In the absorption of ^{232}Th (figure 4.47) it can be seen that crystals with similar concentration have similar absorption. Three features can again be identified: Increasing absorption around 150 nm or 8.2 eV, general increase of absorption with increasing doping concentration and very strong absorption starting at <130 nm or 9.5 eV. These features are all compared to pure CaF$_2$, so they are an effect of growing a doped crystal.

In figure 4.46 it can be seen that the ^{229}Th doped crystals transmit up until the transmission edge of undoped CaF$_2$. The overall transmission of these crystals is lower. In the absorption of ^{229}Th:CaF$_2$ (figure 4.48) some common features can be detected. Similar concentration does not give similar absorption and the absorption profile is flat. The measurement of the crystal grown with the highest activity is uncertain due to its strong absorption. Following the spectral absorption of the other crystals we can expect its profile to be flat as well with a relative absorption higher than 6 mm^{-1}. From figure 4.48 it can be concluded that crystals grown using similar activity have similar absorption and at these low concentrations (compared to figure 4.47) the absorption does not heavily depend on concentration.

The ^{229}Th doped crystals display a different behavior from the ^{232}Th doped crystals, which can be clearly seen when comparing figure 4.45 and 4.46, which is shown in figure 4.49. This was not expected as it is assumed that different isotopes behave identical

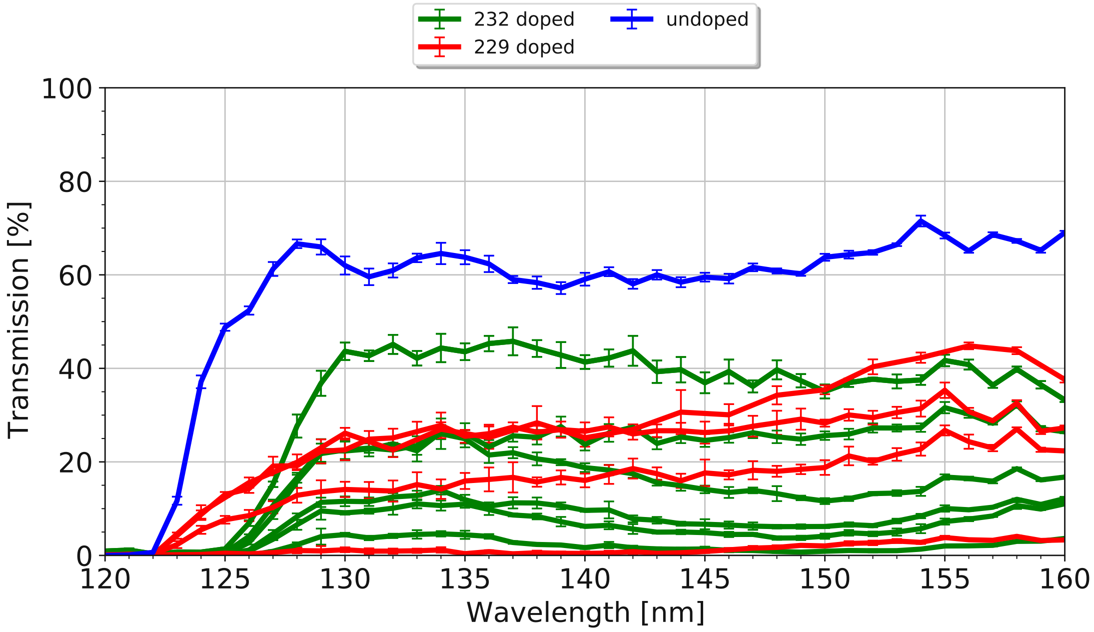

FIGURE 4.49: Comparison of VUV transmission spectra between undoped CaF$_2$, ^{229}Th:CaF$_2$ and ^{232}Th:CaF$_2$.

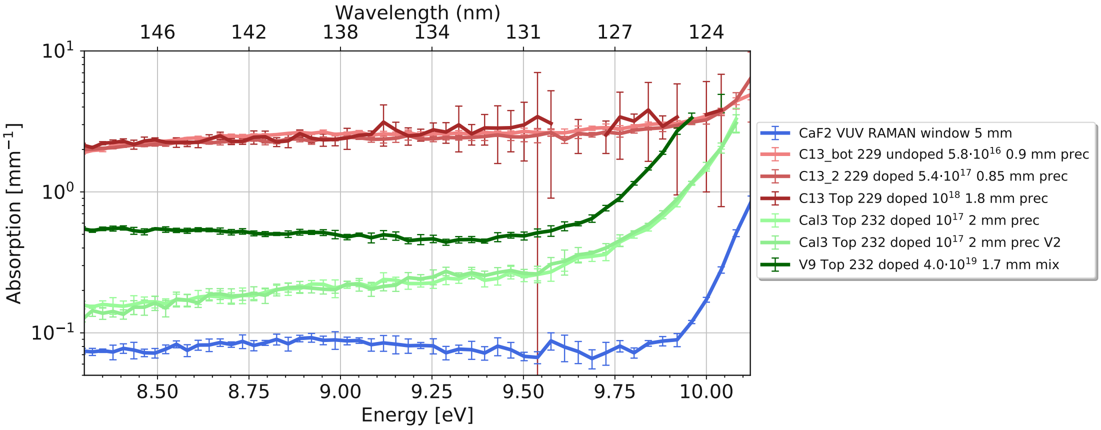

FIGURE 4.50: Absorption coefficient of Th:CaF$_2$ and undoped CaF$_2$ crystals with different concentrations for different energies and wavelengths. Crystal Cal3 was measured twice, once at the start and end, to show drifts in the system between measurements. In the legend the crystal number, doping concentration, thickness and production method of the initial growing powder is indicated. The very highly doped crystal was made by manually mixing ThF$_4$ with CaF$_2$, not by coprecipitation as described in section 3.2.2.

concerning the chemistry. Most probably, the isotope itself does not change the characteristics but the radioactivity of the isotope does. The ^{229}Th doped crystals only stop transmitting at the bandgap edge of CaF$_2$, the 125 nm absorption is not observed. The absorption around 150 nm seems to have disappeared. The general transmission of the ^{229}Th doped crystals is lower, despite the lower doping concentration.

To confirm the different absorption spectra of ^{229}Th and ^{232}Th doped crystals, drifts and changes between measurements of the VUV transmission setup were excluded. For this, a low doped ^{232}Th:CaF$_2$, a high doped ^{232}Th:CaF$_2$ and a high doped ^{229}Th:CaF$_2$ were measured in the same experimental run. The result is seen in figure 4.50. Here we can see several effects. There seems to be an activity-related broadband VUV absorption, independent of doping concentration. Both the undoped CaF$_2$ and ^{229}Th:CaF$_2$ heavily absorb at >10 eV, the transmission edge of CaF$_2$. The ^{232}Th:CaF$_2$ absorbs heavily at >9.5 eV, earlier than the other crystals. The intensity of this absorption is concentration-dependent.

If we now combine the knowledge of all figures, a few observations can be made:

- Crystals grown with increasing activity have an activity-dependent broadband VUV absorption, independent of Th concentration. This is clearly seen in the absorption of ^{229}Th doped crystals and even in ^{232}Th doped crystals probably due to the small amounts of added ^{229}Th in combination with the weak activity of ^{232}Th. The activity of the crystal with the highest ^{232}Th doping concentration is 1 Bq.
- Thorium doping with low activity creates a concentration-dependent absorption around 150 nm and a strong absorption around 124 nm. This is mainly visible for crystals with doping concentration of $>7\cdot10^{19}$ cm^{-3}.

The thorium-related absorption does not seem to be present in crystals grown with high activities. It seems that the thorium is in a different electronic state, either oxidation state or paired with a defect, if a crystal is grown under high radioactivity. Because of this change in electronic state, the absorption around 125 nm disappears. The hypothesis of this observation is that the activity induces loss of fluoride which produces non-stoichiometric, or fluoride-deficient crystals. Section 4.4.2 covers the early investigations in this direction.

4.4.2 Effects of Annealing and Fluoride-Deficiency on the Absorption

Above observations led to the hypothesis that the ^{229}Th:CaF$_2$ crystals were possibly fluoride deficient. The strongest observation was the transmission of crystal X2, the crystal grown under high activity. A thin slice taken from the undoped side of X2, X2u (see figure 4.51), was measured to be completely VUV opaque. At first the suspicion was radiation damage: Annealing to 600 °C did not decrease absorption whereas it normally removes radiation damage. The annealing did remove the orange color of the doped part. This indicated that the VUV opaqueness of X2u was not radiation induced defects in the crystal. Another observation was that when growing CaF$_2$ crystals in vacuum (doped or not) outgassing of F$_2$ was measured by a mass spectrometer.

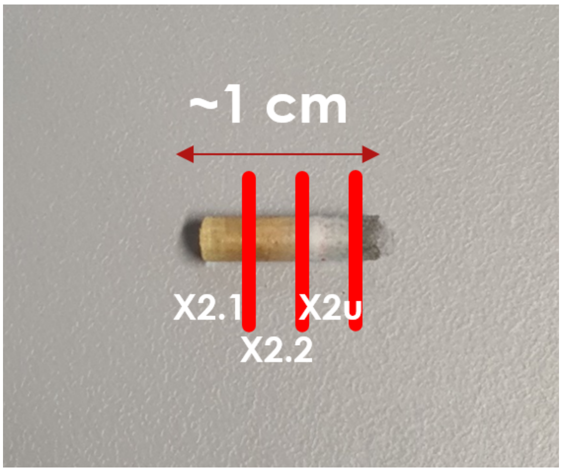

FIGURE 4.51: Cuts made in the X2 crystal

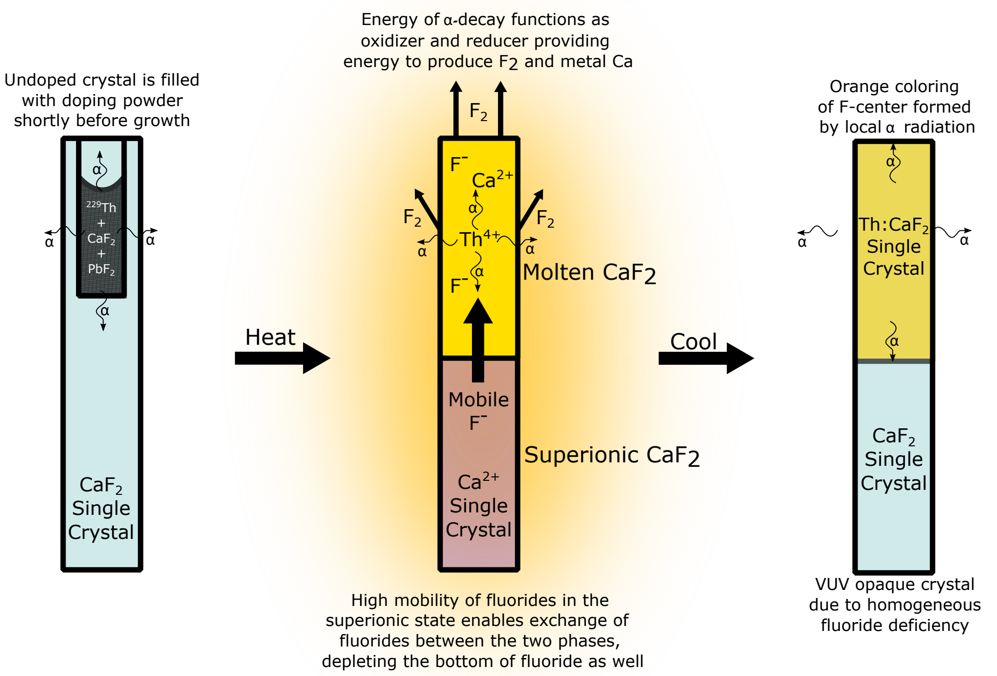

FIGURE 4.52: Schematic representation of the radioactively induced loss of fluoride during the growth process, taking crystal X2 as an example (see figure 4.51). First the crystal is filled with the radioactive powder. During growth, a part of the crystal is molten and a part of the crystal is in the superionic state. In the liquid, the ^{229}Th is dissolved and the α-decay locally provides the energy to dissociate CaF$_2$, producing F$_2$. The superionic crystal has extremely mobile F$^-$ atoms which will diffuse to the liquid phase, supplying it with more F$^-$. The resulting crystal will have a homogeneous deficiency of F in its lattice due to their high mobility, but only a partial doping of Th due to its low mobility. As is seen from activity measurements, only a small fraction of the Th penetrates the superionic crystal.

Our conjecture of the process that leads to the fluoride deficient crystals is depicted and detailed in figure 4.52. By growing CaF$_2$ with radioactive materials, the loss of fluoride in the liquid is enhanced and non-stoichiometric crystals are produced. The dissociation of fluoride compounds to produce gaseous F$_2$ through radioactivity, radiolysis, has been observed in UF$_6$ [212]. The nuclear chemical reaction describing this process is

$$\mathrm{CaF_2} \xrightarrow{\alpha\ 5\ \mathrm{MeV}} \mathrm{Ca}^s + \mathrm{F}_2^g, \tag{4.11}$$

where the metallic Ca is in the solid phase, and F$_2$ leaves the material as a gas. The energy for a chemical reaction is ≈eV, the energy of α-decays is ≈MeV. Because of this every single α-decay could drive many chemical reactions. In a conservative estimate, if 1 % of all reaction with an α particle drive radiolysis which costs 10 eV per reaction, then 5000 dissociation can take place per α-decay. At an activity of 1 MBq of ^{229}Th this would mean at least $5{\cdot}10^9$ radiolysis events per second. In a growing cycle where a part of the crystal is molten for 22 hours, there are $2{\cdot}10^{15}$ radiolysis events as compared to the $\approx 10^{21}$ F atoms in the crystal. This would lead to a defect concentration of $4{\cdot}10^{16}\,\mathrm{cm}^{-3}$, which should indeed be visible in a transmission measurement.

Due to the phase transition in CaF$_2$ (see section 3.1.5) to a superionic state, the fluorides become highly mobile even in the undoped part of the crystal. When the top liquid loses fluoride the mobile bottom fluorides evenly spread throughout the solid and liquid crystal causing homogeneous fluoride-deficiency throughout the crystal. The observations suggest that this causes broadband absorption in the VUV region.

To confirm this hypothesis, and increase transparency of the ^{229}Th:CaF$_2$ crystals, it was attempted to add fluoride to the crystals during annealing. This was done by sandwiching the crystal between undoped CaF$_2$ crystals: The fluoride-deficient crystal was put into contact with undoped CaF$_2$ and together they were heated in the crystal growing machine described in section 3.1.6 to superionic temperatures, 1200 °C.

Two methods of fluoride transfer at superionic state were envisioned: One, the immobile but soft Ca^{2+} lattice of the two crystals would connect and the highly mobile F$^-$ would diffuse throughout both crystals decreasing the fluoride deficiency in the ^{229}Th doped crystal but increasing it in the undoped crystal. Two, the undoped and doped crystals will naturally start outgassing F$_2$ at these high temperatures. If the F$_2$ outgassing of the deficient crystal is less than the not deficient crystal, effectively fluoride can be added to the fluoride deficient crystal through outgassing of the undoped crystal. The results of this superionic fluoride transfer experiment are shown in figure 4.53.

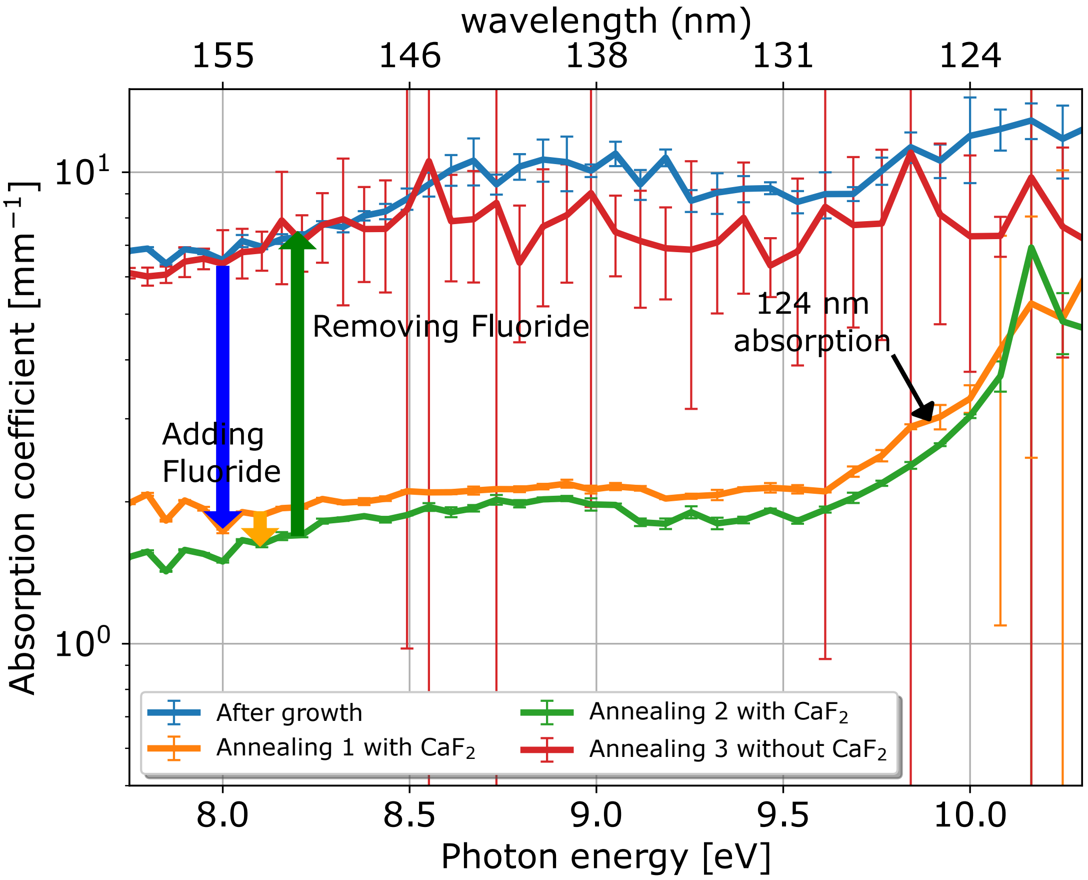

FIGURE 4.53: Spectral absorption taken of the X2u crystal before annealing, after annealing with pure CaF$_2$, same again and after annealing the crystal without the presence of an undoped CaF$_2$. The last attempt was to try and boil out fluoride of the X2u crystal. The fluoride transfer caused the relative absorption to decrease homogeneously by a factor of 4, and after annealing without the presence of undoped CaF$_2$ returned to its previous state. Increase in the absorption after 9.5 eV (as seen in figure 4.47 and 4.50) is observed for fluoride annealed crystals.

The experiment showed that most probably fluoride was transferred to the deficient crystal, and the absorption reduced greatly. The effects of the used experimental procedure gave results very similar to fluorine oxidation annealing [213]. It was also observed that the crystal could be returned to its original fluoride-deficient state by heating the crystal to superionic state without undoped CaF$_2$, indicating that it outgasses the fluoride again at these temperatures. Another observation was that the concentration dependent 124 nm absorption in ^{232}Th:CaF$_2$ returned to the fluoride annealed ^{229}Th:CaF$_2$ crystals (see section 4.4.1 and see figure 4.50). The defect responsible for this absorption seems to disappear and appear through removal or addition of fluoride.

An explanation for the appearance and disappearance of the absorption around 124 nm is the change of oxidation state from Th^{3+} in fluoride deficient crystals (non-stoichiometric) to Th^{4+} in fully charge-compensated crystals. The change of oxidation state due to stoichiometry has been observed in Th:LiF crystals [59]. The change of oxidation state due to fluorine oxidation annealing has been observed in Eu:CaF[214].

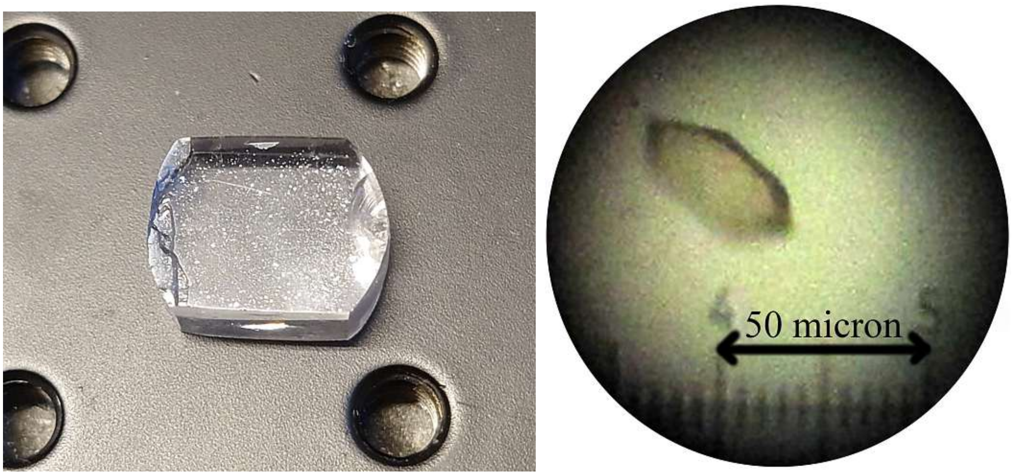

FIGURE 4.54: Glitter observed in ^{229}Th:CaF$_2$ crystal V057 after growth and a microscope image of an individual glitter. This crystal was contaminated with Zr with a 1:1 ratio to ^{229}Th. Probably the fluoride deficiency allowed the Zr and Th in this crystal to produce these microscopic hexagonal crystals that reflect the light. The glitter was never observed in the current series of ^{229}Th:CaF$_2$ crystals so Zr must play an active role.

FIGURE 4.55: ^{229}Th:CaF$_2$ crystal V057 after fluoride annealing (no glitter observable) and subsequent damaging using a krypton excimer lamp for 24 hrs. The glitter must have prevented this type of damage by restricting motion of fluorides because this was not observed in the experiments in section 5.6.1. Annealing to 550 ℃ removed the visible damage but never the glitter.

Another indication of changes in the crystal due to fluoride transfer: The V057 crystal (see [172]), the crystal grown under the highest total activity of ^{229}Th in that series, displayed glitter after growth. The glitter and a microscopic image of it is displayed in figure 4.54. Here again, superionic fluoride transfer was applied as described which removed the glitter. Annealing it without the presence of undoped CaF$_2$ brought back the glitter.

By removing or adding fluoride to CaF$_2$, the crystal can supposedly be brought out of stoichiometry and create different populations of defects with different electronic and absorptive properties. In VUV damaging experiments similar to those described in section 5.6.1 the fluoride annealed crystal was subjected to 24 hrs of krypton excimer lamp irradiation. This created a heavy purple colored damage in the crystal, as seen in figure 4.55. This same behavior was not observed when the crystal was still fluoride deficient and had glitter.

4.4.3 VUV Absorption of U:CaF$_2$ Crystals

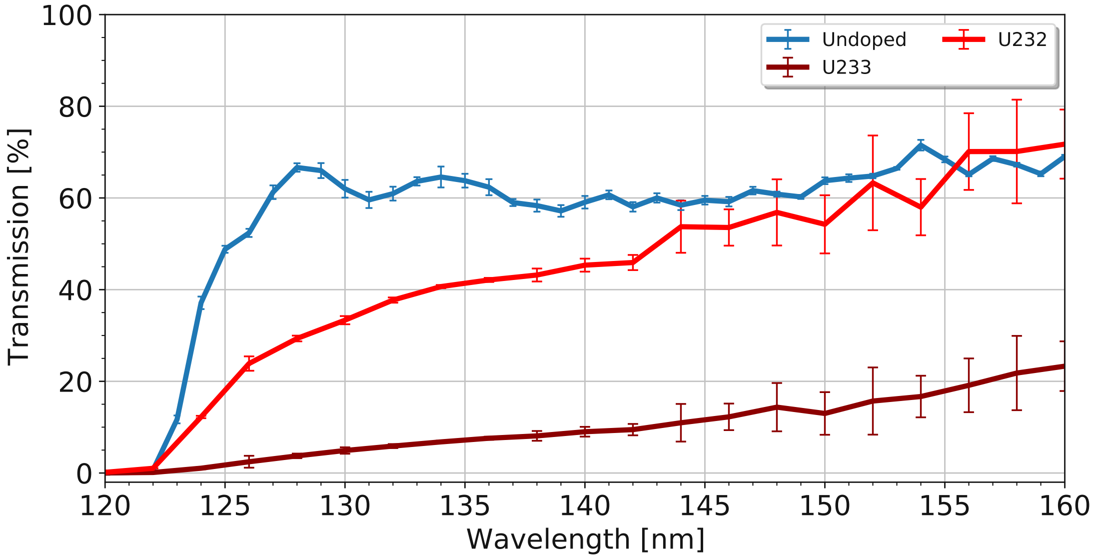

FIGURE 4.56: VUV transmission of a $^{232/238}$U:CaF$_2$ and a $^{233/232}$U:CaF$_2$ crystal compared to an undoped Korth CaF$_2$ crystal. Doping concentration of $^{232/238}$U:CaF$_2$ is $10^{13}/10^{18}$ cm^{-3} and of $^{233/232}$U:CaF$_2$ is 10^{19} cm^{-3} (remeasured compared to [172]). The ^{232}U crystal was grown such that it mimicked the 1 ppm ^{232}U contamination in the ^{233}U. This was done to separate the VUV background produced by ^{232}U from ^{233}U decay. Both crystals are 2 mm thick.

The VUV transmission of a ^{232}U:CaF$_2$ and a ^{233}U:CaF$_2$ crystal was measured in the setup described in section 4.2.1 using the excimer lamp of section 4.1.3 filled with argon as a light source. It can be seen in figure 4.56 that both crystals have reduced transmission as compared to an undoped crystal. The crystals have a different doping concentration and a different transmission.

The difference in transmission either stems from VUV absorption due to U doping concentration differences or through radioactivity induced loss of fluoride as described in the previous section. The ^{233}U:CaF$_2$ crystal was grown with about 1000 times more α activity as compared to the ^{232}U:CaF$_2$ crystal and thus the more active crystal would have lost more fluoride. These characterizations are used to assess the viability of using ^{233}U:CaF$_2$ crystals to produce ^{229m}Th in CaF$_2$ and measure the subsequent isomer photon emission, see section 6.1.

4.4.4 Temperature Dependent Absorption of (Th:)CaF$_2$

The temperature dependent bandgap of cooled undoped CaF$_2$ and ^{232}Th:CaF$_2$ (10^{20} cm^{-3}) was measured. The cooling of the crystal will reduce the probability of indirect bandgap excitations by decreasing the population of phonons, thereby increasing the transmission. It was observed that the transmission window increases with colder temperatures for both undoped and Th doped CaF$_2$ crystals (see figure 4.57).

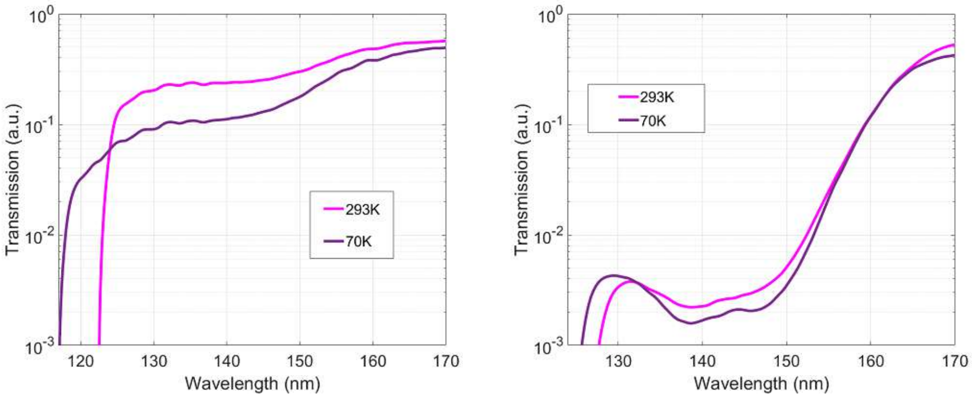

FIGURE 4.57: VUV transmission of (left) an undoped IR quality Korth CaF$_2$ crystal at 70 K and 293 K and (right) a ^{232}Th:CaF$_2$ crystal at 70 K and 293 K. Spectra were measured using an argon excimer lamp with leftover krypton, covering the entire spectrum. A McPherson 234/302 and a CCD camera were used to detect and create the spectrum after the light passed through the crystal. Reduction in transmission between warm and cold measurements is most likely due to water in the vacuum system freezing on the crystals.

During VUV irradiation F and H center pairs are created, and if these remain in the crystal the transmission can decrease during irradiation. At higher temperatures these might anneal more readily during irradiation, re-increasing the transmission. To test this hypothesis, the transmission of a ^{232}Th:CaF$_2$ crystal was measured at different temperatures with low intensity irradiation. Due to the large amounts of infrared radiation the background as measured by the CCD increased for increasing temperatures, which prevented going to higher temperatures.

It can be observed in figure 4.58 that for temperatures up to 400 °C the transmission decreases by a factor of 4 at 150 nm as opposed to room temperature. After this point the transmission increases up to 4 times that of room temperature at 600 °C. Observations at the same temperatures were made in the annealing experiment described in section 4.4.4, indicating that these signify important steps in the mobility of F and H centers or larger defect centers.

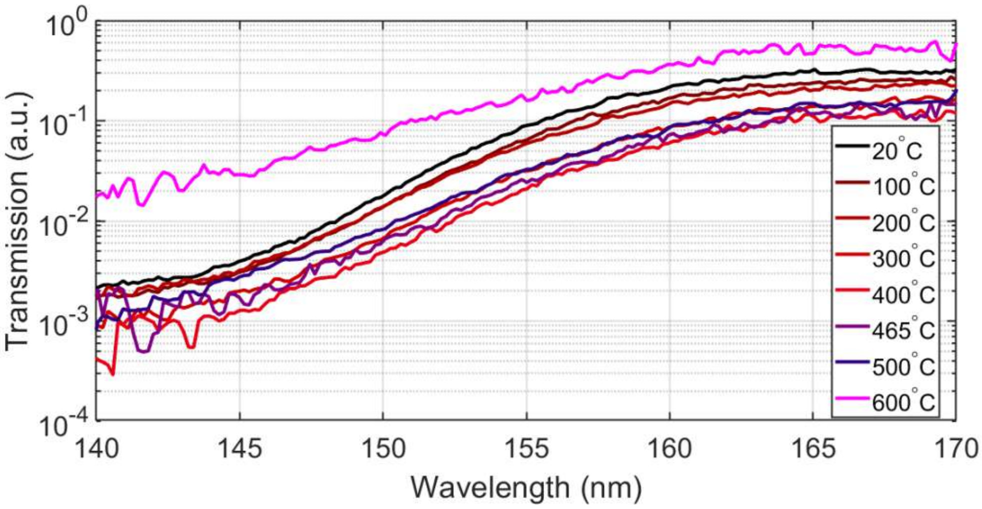

FIGURE 4.58: Spectral transmission measured for a highly doped ^{232}Th:CaF$_2$ crystal at different temperatures. The setup described in section 4.2.2 was used to measure the heated transmission. Up until 400 °C the transmission decreases after which it starts increasing to 4 times its original transmission at 600 °C.

From figure 2.17 it can be seen that at 400 °C, the mobility of F and H centers are approximately equal which correlates with the first step. An explanation would be that at these temperatures the probability of created F and H pairs annihilating directly after creation is lowest, thus decreasing transmission. This would also mean that annealing at higher temperature, the mobility of F and H centers is not further increased and thus a plateau in annealing is reached.

Another defect probably gains more mobility above 600 °C which explains the increase in transmission during irradiation. The larger agglomerations of F centers might need higher temperatures to anneal, as was discovered for undoped CaF$_2$ in [47, 72]. Here a temperature of 500 °C was needed to anneal the smallest of colloids. Possibly in Th:CaF$_2$, this increases to 600 °C.

Thus heating the Th:CaF$_2$ crystals to 600 °C increased the transmission around 150 nm, but probably decreases transmission close to the bandgap. Cooling increased transmission around the bandgap. When designing an experiment that attempts to excite the ^{229}Th nucleus in CaF$_2$, the temperature can be chosen to either increase transmission close to the bandgap by cooling or to increase transmission and continuously heal damage by heating. Decreasing the phonon population by cooling might also reduce the non-radiative decay of the nucleus: In a crystal, most non-radiative decays are induced through defect states which need a phonon to conserve the momentum.

Characterizing how the transmission behaves at the bandgap could be used to study why ^{232}Th:CaF$_2$ crystals absorb heavily <130 nm and undoped CaF$_2$ absorbs heavily <122 nm. A bandgap would display an exponential broadening behavior and a color center (as measured in section 4.4.1) would display a gaussian broadening behavior.

4.4.5 Radioactive Decay Induced Damage/Absorption in ^{229}Th:CaF$_2$

Due to the inherent radioactivity of ^{229}Th and ^{233}U, crystal damage through radioactive decay is inherently present in the grown crystals. The most important processes are detailed in section 2.4.1. Most of the damage will be created due to α-decay and will thus be highly localized. CeO$_2$ is analogous to CaF$_2$: both have the fluorite structure and show non-stoichiometry in their anions. CeO$_2$ has been studied extensively and there it is seen that swift heavy ions produce local anion deficient regions surrounded by anion enriched regions. The exact mechanisms are however complicated and most likely cannot be mapped exactly onto CaF$_2$ [215].

No significant reduction in VUV transmission was observed for radioactively doped ^{229}Th:CaF$_2$ crystals, at most a reduction of 5 % at 150 nm as compared to the original transmission. Reduction in transmission due to aging of the surface, or other damages seems to be dominant. The production of F, M or N centers and with it an orange coloring (figure 3.21) was observed in C13, X1 and X2. These however do not seem to affect the VUV transmission significantly as annealing does not recover the undoped CaF$_2$ transmission but removes the orange coloring. Annealing aged ^{233}U crystals also did not increase the VUV transmission at 150 nm by more than 5 %. The fluoride deficiency dominates the transmission characteristics of these crystals.

4.5 VUV Luminescence of Radioactively Doped CaF$_2$

The VUV luminescence produced by excited defect centers and the radioactive decay of the dopants produce a background for any experiment attempting to measure the photon emission of $^{229\mathrm{m}}$Th. Therefore the VUV Cherenkov emission and the UV radioluminescence (see section 2.4.3) of the U and Th doped crystals was characterized (VUV: sections 4.5.1 and 4.5.2, UV: Section 4.5.3). The UV luminescence was characterized as a function of temperature. In the end it is shown that a 405 nm laser pointer can excite F centers in highly damaged ^{229}Th:CaF$_2$ and produce orange luminescence.

4.5.1 VUV Radioluminescence of ^{229}Th:CaF$_2$

As was established in section 2.4, the dominant photon background in any attempted measurement of the photon emission of the ^{229}Th isomer is Cherenkov radiation. To characterize the Cherenkov background of doped CaF$_2$ crystals, the setup described in section 4.3 was built. Here, the Cherenkov radiation of a ^{229}Th:CaF$_2$ was measured.

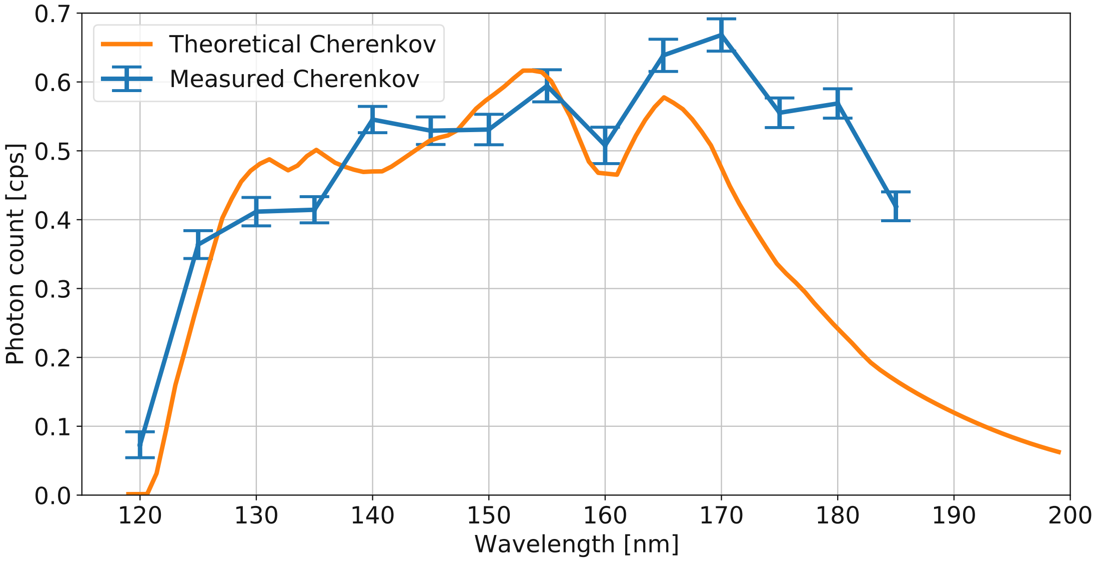

FIGURE 4.59: The detected VUV spectrum of C10.5 a 1 mm long 3.2 mm diameter ^{229}Th:CaF$_2$ compared to a theoretically computed Cherenkov spectrum that takes into account the spectral efficiency of the system and the measured transmission of the crystal (see figure 4.46). A 1 mm slit size was used for the measurement. The maximum count rate was 0.7 cps. The transmission cutoff of CaF$_2$ below 122 nm can be seen, as well as loss in efficiency of the PMT and grating for higher wavelengths. The measured transmission of the C10.5 crystal was used to calculate the theoretical Cherenkov spectrum. The small fluctuations in the theoretical spectrum are due to lines in the D$_2$ lamp used to measure the transmission of this crystal. Remarkable are the higher light outputs at 170 and 180 nm.

The VUV Cherenkov background, induced mainly by β^--decay of the ^{229}Th daughters [45], was characterized for the C10 ^{229}Th:CaF$_2$ crystal (see figure 4.59). The Cherenkov background at 150 nm was measured to be 0.5 cps. As calculated in figure 2.20, every Bq of ^{229}Th produces 0.1 Cherenkov photon per second at 150 nm in a 1 nm bin. Considering 9.4 kBq (as measured on a γ spectrometer) of ^{229}Th in C10 within the slit, and 0.05 % total efficiency of the system it would result in ≈0.4 cps. The small discrepancy can lie in the accuracy of the measured amount of ^{229}Th in the crystal, or characterization of the experimental efficiencies. This was done using activity determination using a γ spectrometer in a calibrated geometry.

The calculated Cherenkov spectrum does not match the measured values well for higher wavelengths, especially when compared to the Cherenkov calibration source in section 6.5.2. This could be caused by measurement errors in this experiment or in the transmission of C10 which is used in the calculation of the spectrum. Another explanation would be VUV luminescence of color centers induced by the radioactivity, radioluminescence. It is known that due to the scavenger all crystals are contaminated with Pb, which has a luminescence peak at 180 nm [124]. The 170 nm peak is not seen in Pb doped CaF$_2$ and is more likely to come from Th doping. Because of the electronic configuration of Th^{4+} it is not expected to fluoresce at this wavelength.

An explanation for the 170 nm luminescence is that in this crystal the oxidation state is changed due to the fluoride deficiency (4.4.2) or due to capturing electrons excited by the radioactivity. The first hypothesis, oxidation change through non-stoichiometry, is known to happen for Ce and Th in other compounds [59]. The last hypothesis, reduction through self irradiation, is a known effect in CaF$_2$ for many actinides [49] (see section 2.5.2). Lower oxidation states of Th have lower excited states of the outer electron(s) and could fluoresce at these energies. The Th^{3+} free ion for example has excited states in the VUV [216]. A last possibility is a change in the crystal lattice using larger defect structures to compensate for the loss in fluoride (see figure 2.12) which could absorb and fluoresce.

4.5.2 VUV Radioluminescence of $^{232/233}$U:CaF$_2$

The VUV radioluminescence of U:CaF$_2$ crystals was measured to determine a background for future experiments. Due to the low transmission of the ^{233}U:CaF$_2$ crystal (see section 4.4.3), its VUV radioluminescence was not detected. It was therefore attempted as well for the more transparent ^{232}U:CaF$_2$ which should produce more Cherenkov photons (figure 2.20).

A ^{232}U:CaF$_2$ was put in front of the slit of the long integration setup (see section 4.3) and the (V)UV spectrum was recorded. Luminescence was integrated for a week. In this measurement, radioluminescence above 200 nm was measured, and 0.3 cps of Cherenkov radiation at 150 nm as can be seen in figure 4.60. This weak signal indicates that the Cherenkov radiation produced by ^{233}U:CaF$_2$ is not measurable in this setup. With little improvement however it should be possible.

4.5.3 UV Radioluminescence of Radioactively Doped CaF$_2$

Due to the radioactivity of the dopant, defects will be constantly created which will annihilate and produce luminescence, as detailed in section 2.4.2. The α and β^--decay will produce STE luminescence. In figure 4.61 the radioluminescence emitted by a ^{233}U:CaF$_2$

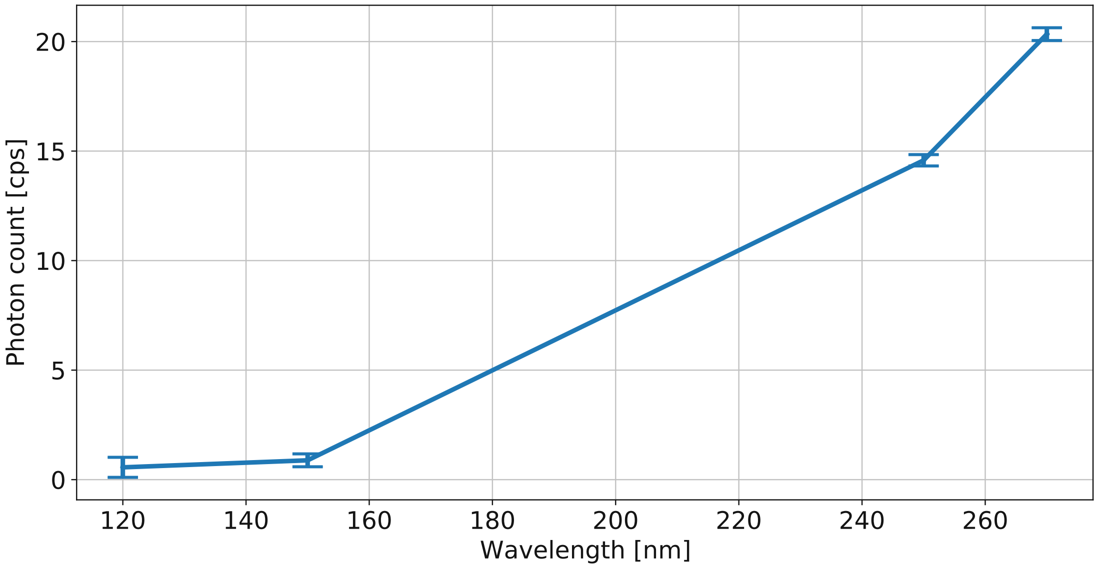

Figure 4.60: Radioluminescence produced by a ^{232}U:CaF$_2$ crystal. At 150 nm 0.3 cps of Cherenkov radiation was detected. Due to the high radioactivity of the sample, especially the high energy γ-ray of thallium-208, the background at 120 nm was higher than in previous experiments.

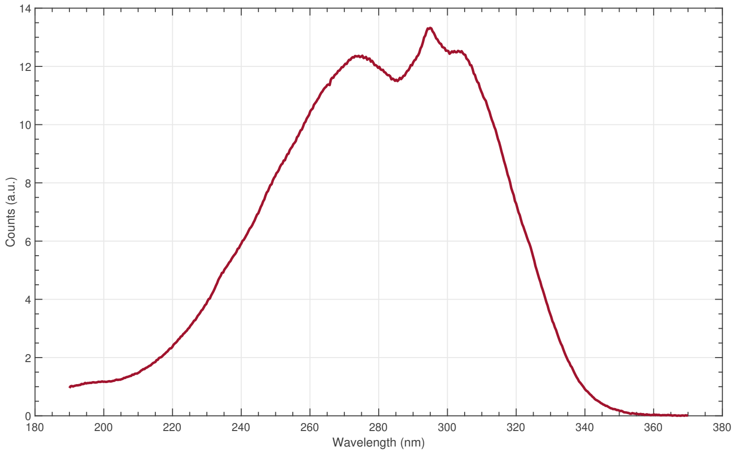

Figure 4.61: Radioactivity induced STE luminescence in a ^{233}U doped CaF$_2$ crystal (1 mm slit size, 1 min integration). Typical large broad peaks at 275 and 305 nm can be seen. A smaller peak around 295 nm can be observed. A similar peak is observed in Tm doped CaF$_2$, but also in Ce doped CaF$_2$ where it is explained as a dopant stabilized V$_k$ center annihilating with an electron [86].

crystal is shown, measured in a McPherson 234/302 spectrometer with Newton CCD attached and crystal positioned at the entrance slit.

When measuring the radioluminescence of ^{229}Th:CaF$_2$ a similar spectrum is produced, see figure 4.62. The radioluminescence spectrum needed a longer integration than a U:CaF$_2$ spectrum before reaching sufficient signal to noise ratio due to the difference in α-decay activity. During long measurements of the radioluminescence spectrum, it

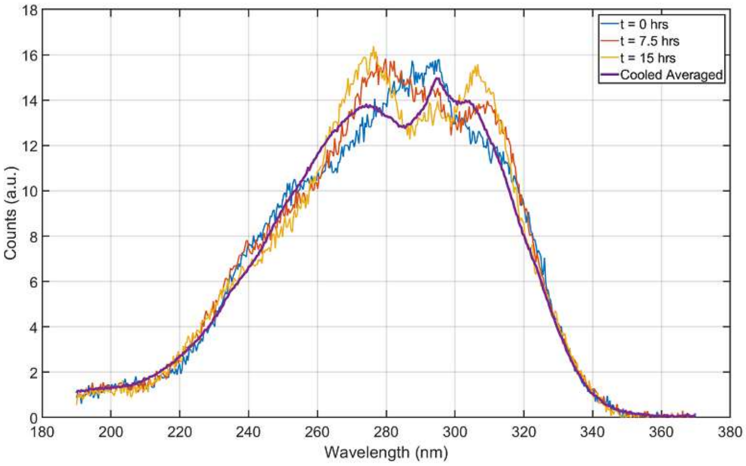

Figure 4.62: Radioactivity induced STE luminescence in a ^{229}Th doped CaF$_2$ crystal (1.2 mm slit size, 30 min integration). The spectrum was shifted due to temperature instabilities in the spectrometer, as can be seen from the first three spectra taken 7.5 hours apart. After cooling the setup to a stable temperature the fluctuations were not observed anymore and a spectrum similar to figure 4.61 was observed. Again, typical large broad peaks at 275 and 305 nm can be seen. A smaller peak around 295 nm which is a dopant stabilized hole (V$_\text{k}$ center) annihilating with a conduction electron [86].

was observed that the spectrum would be periodically distorted due to temperature changes in the spectrometer. This issue was resolved by stabilizing the temperature of the McPherson 234/302 spectrometer.

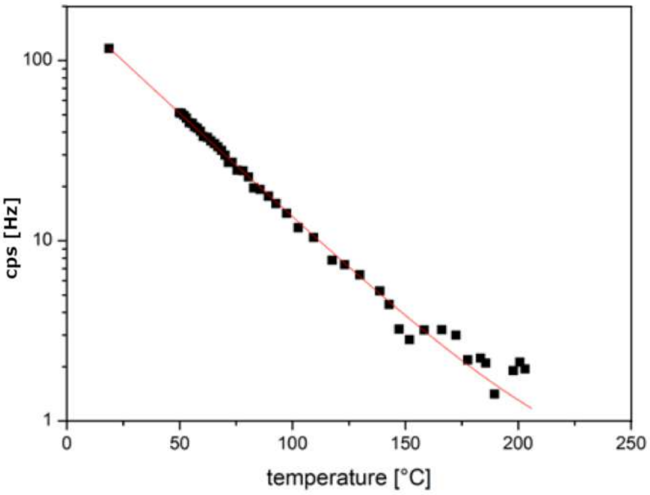

Figure 4.63: Amplitude of the radioluminescence spectrum between 230 and 330 nm as a function of temperature. A single exponential function is fitted to the data. Measurements were taken with the ^{229}Th:CaF$_2$ crystal V057 in the setup described in section 4.2.2 in picture 4.44.

The temperature dependence of the radioluminescence was measured independently in Vienna and Japan to explore if it can be minimized. It was observed that the radioluminescence can be shifted towards higher wavelengths for higher temperatures, as seen

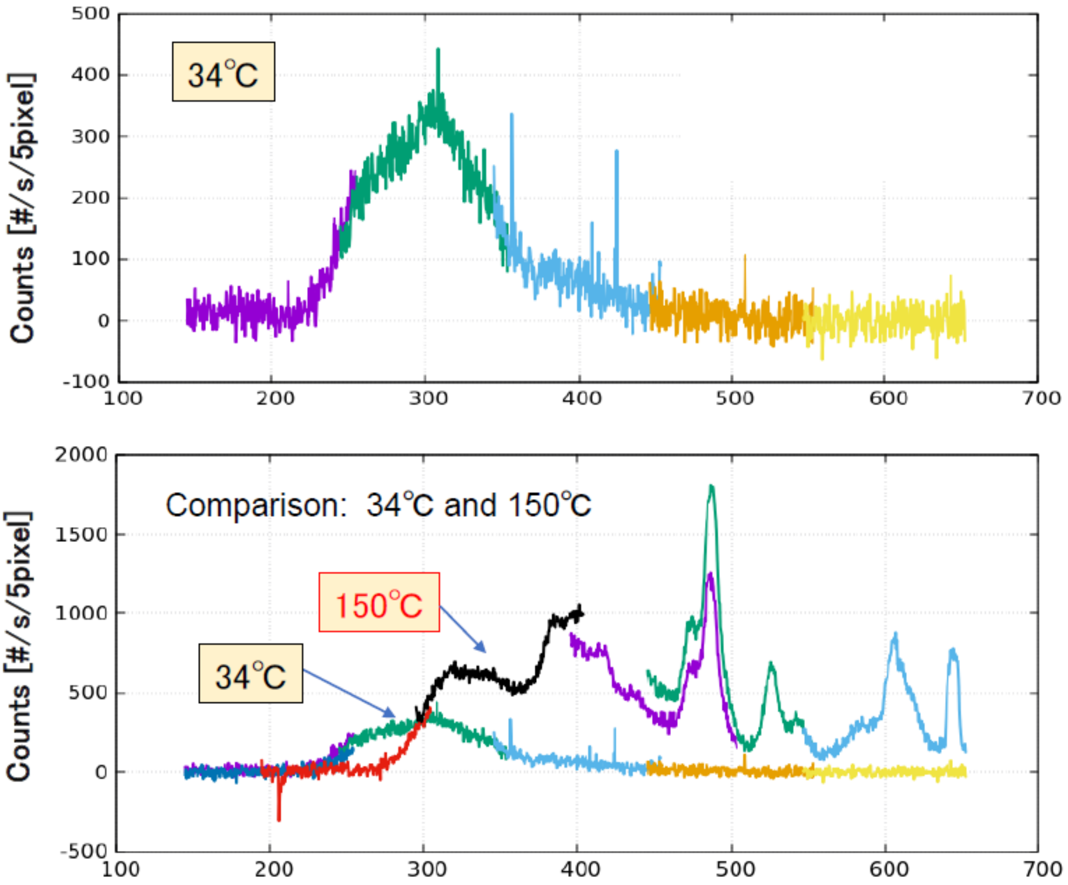

FIGURE 4.64: Comparison of the radioluminescence spectrum of V057 in Japan for 34 °C and 150 °C. It can be seen that the luminescence is shifted towards higher wavelengths, reducing the intensity in the 230 nm to 330 nm region. Many defects can be seen similarly to the photoluminescence measurements in section 5.6.1.

in figures 4.63 and 4.64.

4.5.4 The UV Laser Pointer Excitation of ($^{229/232}$Th:)CaF$_2$

Due to the availability of 405 nm laser pointers such a laser was aimed at a ^{229}Th:CaF$_2$ crystal. It was observed by eye (figure 4.65) that this crystal fluoresced in the orange. The absorption at 405 nm and emission in the orange matches with M centers as seen in table 2.5.3. It is very likely that the high radioactivity produces many F centers that conglomerate to M centers.

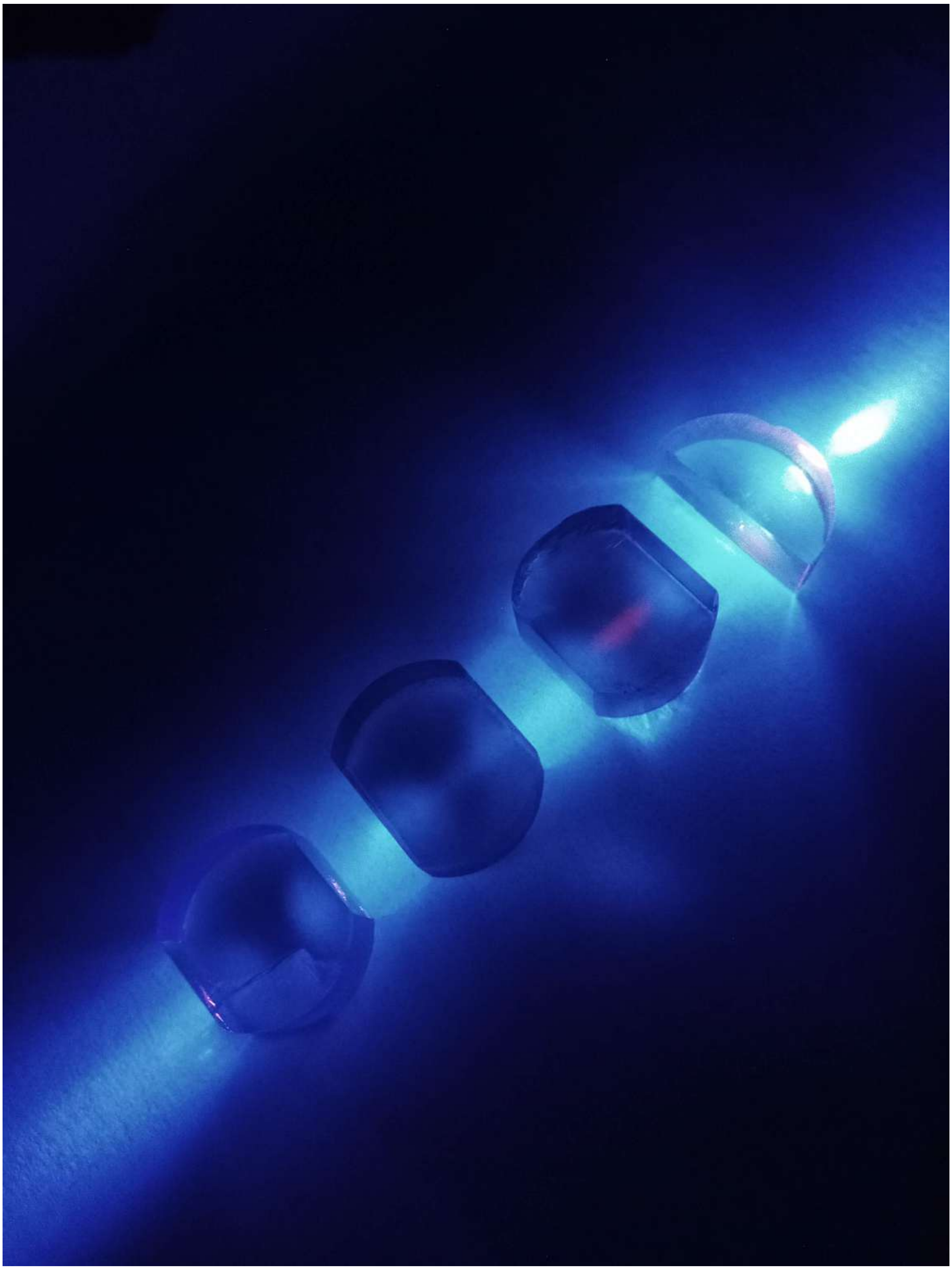

FIGURE 4.65: A 405 nm blue laser was shot through a (from left to right) undoped, low ^{232}Th doped, ^{229}Th doped and high ^{232}Th doped CaF$_2$. Due to the high amount of F centers created in the radioactive crystal orange (600 nm 2.5.3) fluorescence is seen.

4.6 AFM, Electron microscope, EPR and NAA Measurements

Over the many years performing experiments on Th:CaF$_2$ occasional opportunities presented themselves to microscopically characterize Th:CaF$_2$ crystals, sometimes in cooperation with other groups. These measurements should be expanded on in the future.

A ^{232}Th:CaF$_2$ was measured in a cryogenic atomic force microscope (AFM). Here the crystal was cooled to cryogenic temperatures and then cleaved in vacuum. The freshly cleaved surface was then probed with the AFM. The AFM can image single atoms on the single atomic layer. In figure 4.66 these images can be seen. Only in the doped crystal features on the surface can be seen. In light of the measurements done on fluoride deficiency these features are probably Ca metallic nanoparticles compensating for the fluoride deficiency. These images look very similar to an AFM image of damaged undoped CaF$_2$ [211] in size and shape.

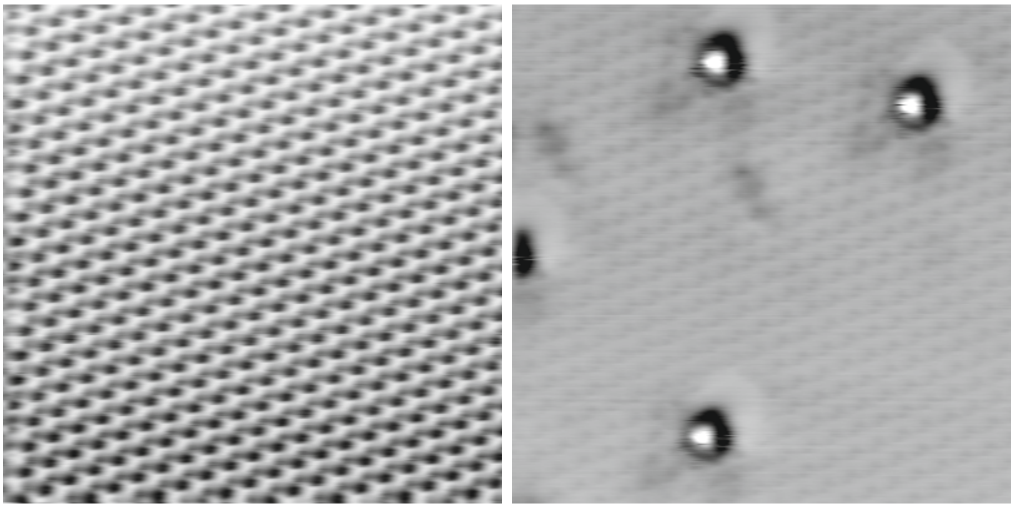

FIGURE 4.66: AFM pictures of cryogenic cooled undoped CaF$_2$ (left) and ^{232}Th:CaF$_2$ (right). The undoped crystal shows its regular crystal structure. The doped crystal has protrusions of about 7 nm in size that are most likely due to the Th doping or they are imprints left by metallic Ca nanoparticles. When the crystal is heated, these defects disappear. Either the dopant moves to the inside of the crystal or the hole or protrusion of the Ca nanoparticle is healed by hopping.

Following above publication, during damaging, F centers are created which is equivalent to a fluoride vacancy. When many vacancies are produced at the same location due to focused irradiation only Ca is left and thus metallic nanoparticles can be formed. In the growth process of Th:CaF$_2$ it has been observed that more fluoride is lost to the vacuum then for undoped CaF$_2$. This process is probably driven by the radioactivity of the dopant. The result is a fluoride deficient crystal that forms Ca nanoparticles. Thus the AFM image of a doped crystal (figure 4.66) and damaged crystal in [211] show the same metallic nanoparticles.

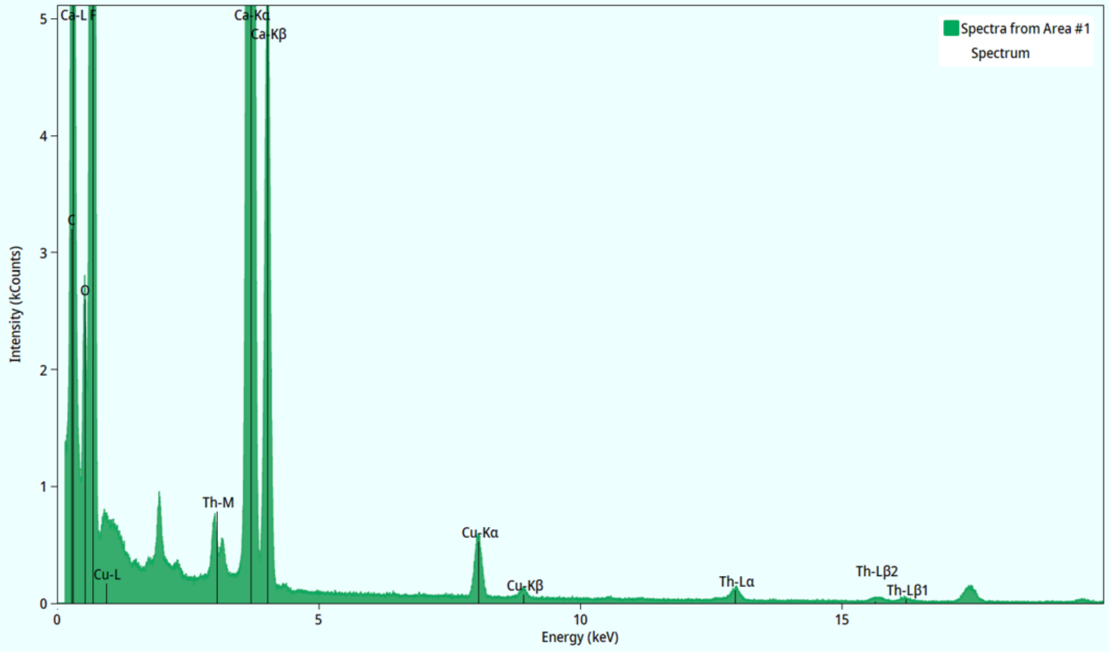

FIGURE 4.67: An EDXS spectrum taken of ^{232}Th:CaF$_2$ crystal V15. The different X-ray lines of Ca, F, Th, O can be discerned. This information is used together with focusing of the electron beam to determine the position of these elements in the crystal in figure 4.68

TABLE 4.3: Measured fractions of major elements in the ^{232}Th:CaF$_2$ crystal. The errors are in absolute percentages. The amount of Th in the sample is one order of magnitude lower than expected. Possibly this is due to uncertainties in using gamma spectroscopy to determine the doping concentration or using EDXS to determine concentrations.

Z	Atomic fraction [%]	Atomic error [%]	Mass fraction [%]	Mass error [%]
F	71.52	6.62	53.74	3.21
Ca	28.33	4.59	44.91	6.55
Th	0.15	0.02	1.34	0.17

The ^{232}Th:CaF$_2$ crystal V15 was imaged under an electron microscope by Transmission Electron Microscopy (TEM) and simultaneously Energy Dispersive X-ray Spectroscopy (EDXS) was performed. This allowed to visualize the surface and to visualize the distribution of elements on the surface. To perform this measurement the crystal was polished down to a few nm and put in the sample chamber of an electron microscope. The EDXS spectrum can be seen in figure 4.67, an electron microscope picture and element positions in figure 4.68.

In figure 4.68, some features were detected. The two circles in the top three images seem to be a Ca metallic nanoparticle and a hole left by one that must have been removed during polishing. It can be seen respectively that one has only Ca, whereas the other no F and Ca. It also seems a line element was grown, as was also observed in [84]. A

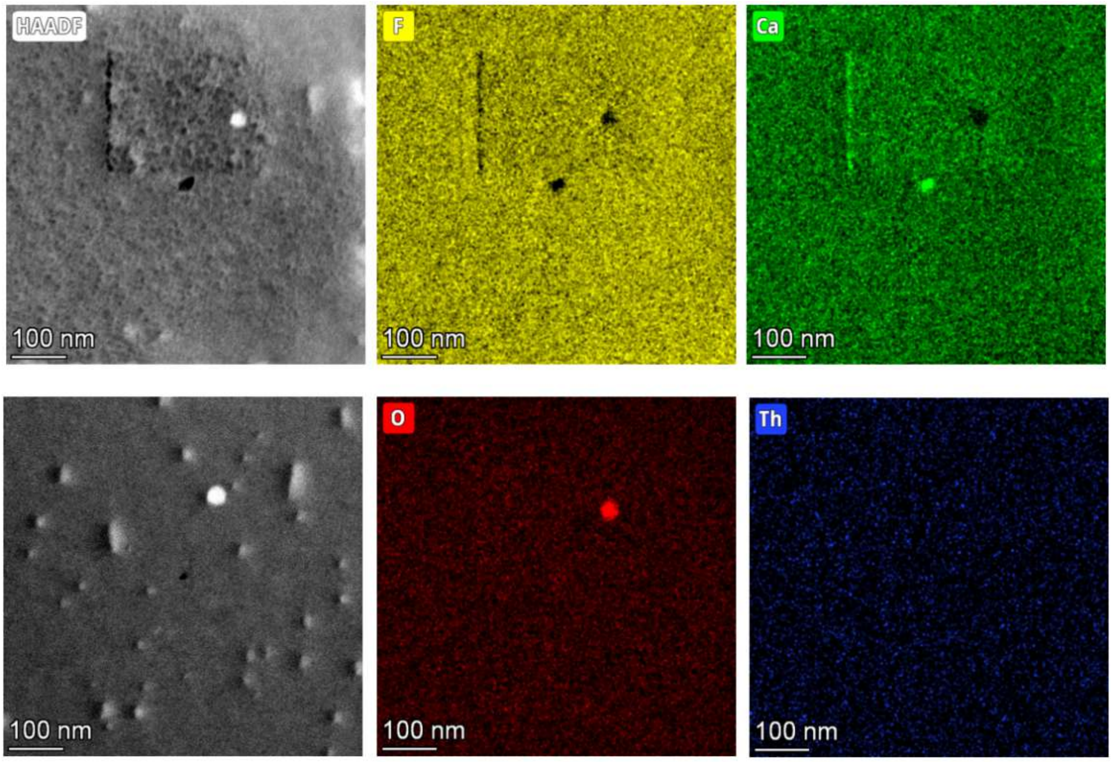

FIGURE 4.68: On the left, two images taken at different locations of the ^{232}Th:CaF$_2$ V15 crystal. On the right are positions of elements found with EDXS and electron beam focusing.

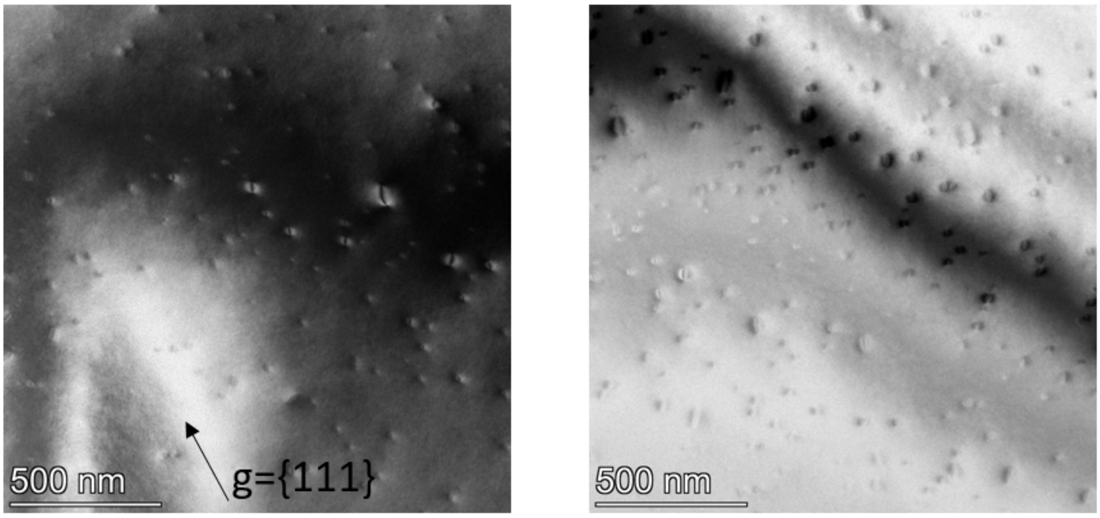

FIGURE 4.69: Bright field and dark field image of the ^{232}Th:CaF$_2$ crystal V15. The loop features observed are typical dislocation loops. The crystal [111] axis is shown.

square structure can be discerned in these pictures, this was damaged due to a more intense electron beam irradiation because this area was used to produce the spectrum in figure 4.67.

In the bottom three images it can be seen that the Th is homogeneously dispersed throughout the crystal. The fractions of the elements observed is shown in table 4.3. Oxygen is also observed, which is most likely water that reacted with the surface [217] or is absorbed [95]. A spot of oxygen can be observed, this is a spot where the electron beam was focused on for a longer time. It seems the energy of the electron beam drives the reaction of water or oxygen with the surface and thus incorporates oxygen.

In these same measurements it was discovered that the crystal contained many dislocation loops. Dislocation loops are image artefacts in electron microscopy that are formed by stabilized rows of defects. In figure 4.69 these can be seen. These loops were also observed in ^{232}Th:CaF$_2$ in [52]. Here the formation of the loops is explained as follows: F centers or fluoride vacancies hop around the lattice due to thermal fluctuations. They preferentially move along the [111] axis because the energy barrier is lowest. Once they encounter a Th atom they are trapped, because the energy needed to pass a Th atom is much larger than to pass a Ca atom. Over time more and more vacancies follow and pile up near a Th atom. This creates a stabilized row defect around a Th atom. This effect was not observed for U atoms, probably because the energy needed to change its oxidation state is lower.

The theoretical prediction [57] that in the ground state, the Th^{4+} will substitute the Ca^{2+} in CaF$_2$ with two fluoride compensation atoms, was tested in collaboration with the group of Lino da Costa Pereira in Leuven and mainly the work of Janni Moens[1]. Due to the large difference in mass between thorium and calcium, 2D Rutherford backscattering/channeling (RBS/C) scans could detect doping concentrations of less than 1 %. In these measurements a highly doped ^{232}Th:CaF$_2$ (V14/V15) was sent to be characterized. It was measured that a fraction of 1.01 ± 0.02 Th substitutes Ca.

Electron paramagnetic resonance (EPR) measurements were performed on V14/V15 in collaboration with the above group which originally did not yield any signal, indicating no unpaired electrons are present in the crystal. This concluded that almost all ^{232}Th is substitutional and is Th^{4+}. After annealing these crystals to 1100 °C and back to room temperature, an EPR signal was measured. It is ongoing research if this is due to inducing fluoride deficiency as detailed in section 4.4.2.

Using Neutron Activation Analysis (NAA), contaminants that are susceptible to neutron capture and subsequent gamma detection were identified in undoped CaF$_2$ crystals. In these measurements the following elements were detected: Na, Si, K, Mn, Sr and Au. Most of these elements are alkali and alkali halides which are chemically similar to Ca and thus hard to separate. Others contaminants probably byproducts of the production process, possibly to remove metal contaminants like rare earths which cause more issues in CaF$_2$ [218].

---

[1] Publication pending

Chapter 5

The Nuclear Excitation of ^{229}Th with Resonant VUV photons

To date, excitation of a nucleus with photons in the optical range has not been shown. Excitation with x-ray photons has been shown, and is covered in chapter 7. Excitation by low energy photons, close to optical range, is only known to be possible with ^{229}Th, but other neighboring isotopes may display similar behavior [219, 220]. These isotopes however mostly have a much shorter half-life, making practical optical excitation experiments challenging. Excitation with photons in the optical range is interesting due to the unparalleled precision of lasers. Applications, such as a nuclear clock, are only possible due to the major advances in laser technology. The VUV region however, is somewhat underdeveloped. The energy of the ^{229}Th isomer of around 8 eV (≈150 nm) puts it in the vacuum ultraviolet region, or VUV.

Light sources in the VUV are few, mainly due to little interest for industry. Possible light sources are synchrotrons, plasma lamps and pulsed lasers. To our best knowledge, no tuneable continuous wave lasers have been developed. Synchrotrons and lamps have a broadband spectrum of light and high intensities which can effectively excite the isomer but will not help to narrow down its exact energy. They can however help determine its wavelength up to the (≈Å) level. To obtain a high precision value of the nuclear excitation energy, a laser is needed. A narrowband laser would ultimately allow the development of a clock. Important is the linewidth of the laser, which dictates to which precision the nuclear excitation energy can be determined. Frequency combs can have linewidths down to at least 1 MHz [26, 221], possibly down to the Hz level using the individual comb teeth. This narrow band light should be able to probe the nuclear excitation to a high degree of precision and accuracy. Any other excitation method does not have this kind of precision and thus the fundamental physics that can be probed with the nuclear transition will be invisible to them. Currently, no VUV CW laser is as precise as these frequency combs. To build the best clock, or probe the isomer extremely precisely, the limiting element is the laser linewidth, not the nuclear excitation linewidth.

In the past, continuous wave (CW) VUV lasers were actually considered using excimer molecules and liquid or solid noble gasses and this recently has gathered attention again [222–225]. To input enough power continuously to excite enough excimers for CW operation one needs to input at least 1 gigawatt of irradiation power per gram of gain medium. To input this amount of 1 GW/g, a Febetron [226] could be used which can deliver electron beams with currents up to 6 kA.

Another approach is frequency doubling or wavelength conversion of lasers in non-linear media. This has produced 149.8 nm [227] light and could be used to develop VUV lasers. The limiting factor in terms of producing VUV light of these non-linear crystals is their bandgap which starts to absorb in this wavelength region. KBBF has the largest bandgap at the moment, with a transmission up to 165 nm [228]. The main difficulty for producing CW VUV lasers is the amount of power that needs to be put into the gain medium continuously. The necessary pumping power density in a gain medium scales approximately with $\frac{1}{\lambda^5}$, therefore making development of a laser harder the shorter the used wavelength.

To solve these issues, the most widely used VUV lasers are pulsed, and often more specifically frequency combs. These can pump a lot of power in a short period of time into a medium, inducing higher harmonic generation (HHG). Media used are noble gasses in cells, jets and capillaries [229–231] or large bandgap crystals [232]. Downside is that the ultimate linewidth one can have is in the tens of MHz range [221] which would not be sufficient for a next generation clock. It is however useful for precisely determining the energy of the nuclear transition. A tuneable VUV frequency comb, currently in development at PTB Braunschweig, is characterized to have 394 μW average power at 150 nm with a linewidth of 250 MHz, which is $\frac{dN}{dtd\lambda} \approx 10^{26}$. Due to the pulsed nature the excitation rate of this laser is similar to the other methods considered (see section 5.1.1).

In the end, exciting the nucleus through VUV photon excitation is undoubtedly needed for development of a clock, and through proper engineering this is a viable option (5.1.1). We call this the direct excitation experiment. If an electronic defect state in the crystal host can be coupled to the nucleus, the photon excitation can be enhanced further [42] (5.1.2). We call this the color center excitation experiment. The nuclear excitation through defect coupling is a version of the electron bridge (EB) process. The EB process uses an excited electronic state, energetically near the thorium isomeric excitation energy and couples that via a virtual state to the nucleus using a strong laser field such that the total energy of excited electron and photon is the isomer energy (2.3.1). The closer the energy of the excited state of the electron is to the isomer, the stronger the coupling will be [31]. This EB process can be extended to any electronic excited state that has some wave function overlap with the nucleus. Excitation via a defect state is an example of this.

Other examples use the EB process in any thorium ion (1+ [233], 2+ [31], 3+ [234]) or via the continuum [235, 236]. One could investigate changing the Th oxidation state to create defects at the right energy for EB excitation, as the oxidation state for Eu in CaF_2 was changed [214]. Implementing the continuum EB process in a crystal by using the conduction band as continuum might also be possible: Trapping of conduction electrons by impurities is a well known effect in lanthanides and actinides [49, 115]. Scattering of electrons of the Th atom in a solid or outside of it could also produce isomeric thorium [237]. These methods are not considered further in this chapter.

In any practical experiment, the excitation of the nucleus needs to be verified. The most straightforward verification is measuring the photon from the de-excitation of the nucleus. Because of the slow decay rate (long lifetime) and the isotropic emission of the photons detection above the noise threshold is challenging. By using many nuclei and intense excitation sources this problem can be overcome. For that reason we grow large bandgap crystals with high doping concentration and use intense light sources focused on the crystals.

There are also options to determine the nuclear state without waiting for the de-excitation. An example is that once excited, the nuclear magnetic moment changes and therefore the hyperfine splitting of electronic excited states of the ion/atom. For ion traps the monitoring of the hyperfine splitting of electronic excited states can thus determine the nuclear state [21]. Monitoring hyperfine splitting is much more reliable because an electronic excited state can be chosen for which intense narrow lasers have been developed (optical region) with which such a spectroscopy can be done.

The optical region can be chosen for hyperfine splitting spectroscopy because in ion traps or beams the ion is in the 2+ oxidation state and has optically active electrons. In the crystal this is not possible because the thorium is in the 4+ oxidation state and has no electronic excited states in the optical region. Another example is that in a crystal the nuclear magnetic properties of ^{229}Th interact with electric field gradients which together create a quadrupole structure depending on the excitation state of the nucleus [22]. Monitoring the state of the nucleus in the crystal thus comes down to spectroscopy of the nuclear quadrupole structure, which has not been demonstrated. Due to the oxidation state of Th in a crystal, monitoring the hyperfine splitting is not possible. Pursuing the only option, many nuclei need to be excited to detect a nuclear photon emission.

In order to ensure that many nuclei are excited the viability of the direct excitation and color center excitation experiment are investigated (section 5.1). After identifying the necessary experimental characterizations for a full analysis, the characterization setups (sections 5.2,5.3 and 5.4) and results (sections 5.5,5.6) are presented. Concluding this chapter is a revisit of the viability calculations.

5.1 Viability of Excitation of ^{229}Th with VUV Photons

Excitation of the ^{229}Th nucleus can be done directly by resonant photons or indirectly: For example using electron bridge (EB) processes and charge transfer state electron bridge (CTS-EB) processes. The EB method is used by the group of Peik at PTB, in Vienna direct excitation is attempted and CTS-EB is investigated theoretically and reported on in this thesis.

First of all, the Cherenkov background due to β^--decays from the daughters of ^{229}Th can only depends on the crystal used, not the excitation approach. To calculate the produced Cherenkov radiation, we use the results in section 2.4.3. A more detailed analysis of the Cherenkov radiation produced through β^--decay of each ^{229}Th daughter can be found in section 6.1. From equation 6.2 we can calculate the Cherenkov flux at 150 nm in a 1 nm bin for a certain concentration of ^{229}Th n_{Th}:

$$\frac{\Phi_{cher}}{\Omega} = 0.59\lambda_{229}\frac{V_c n_{th}}{4\pi} = 1.31 \cdot 10^{-13} V_c n_{Th}\ \text{sr}^{-1}\text{Hz}, \tag{5.1}$$

where Φ_{cher} is the Cherenkov photon flux, Ω the solid angle, λ_{229} the α-decay constant of ^{229}Th, and V_c the volume of the used crystal. The factor 0.59 is the amount of Cherenkov photons produced per ^{229}Th decay taking into acount all daughters. This result is around 100 sr^{-1}Hz for a 1 mm^3 cube of 10^{18} cm^{-3} ^{229}Th:CaF$_2$. Now we consider the nuclear excitation and decay rates for ^{229}Th nuclei in CaF$_2$ crystals.

5.1.1 Direct Excitation Experiment

Assuming there is only radiative decay (with rate Γ_m of the nuclear isomer), the number of excited nuclei N_m will grow under photon flux $\frac{dN_\gamma}{d\lambda dt}$

$$N_m = N_{eq}(1 - e^{-\Gamma_m n^3 t}) \tag{5.2}$$

where n is the refractive index of the material [238]. The equilibrium or asymptotic number of excited nuclei, $\mathrm{N_{eq}}$, can be described by

$$N_{eq} = N_{Th}\frac{W_{VUV}}{\Gamma_m n^3} = \frac{N_{Th}}{s_{beam}}\frac{\lambda^4}{12\pi c n^3}\frac{dN_\gamma}{d\lambda dt} \approx 10^{-23} N_{Th}\frac{dN_\gamma}{d\lambda dt}. \tag{5.3}$$

Here we use s_{beam} is 1 mm^2, λ is 152.1 nm and $n(\lambda)$ is 1.575 for the estimate while W_{VUV} is defined as

$$W_{VUV} = \frac{\lambda^5\Gamma_m}{24\pi^2 c^2\hbar}\frac{dI_0}{dt} = \frac{\lambda^4\Gamma_m}{12\pi c s_{beam}}\frac{dN_\gamma}{d\lambda dt}. \tag{5.4}$$

In these equations W_{VUV} is the VUV excitation rate, s_{beam} is the cross-section of the beam, N_{Th} the number of irradiated thorium nuclei, c the speed of light and $\frac{dI_0}{dt}$ the beam intensity in the crystal. In equation 5.3 we can see that the equilibrium number of excited nuclei is independent of lifetime of the isomer state. The time needed to reach this equilibrium however obviously depends on lifetime: The shorter the lifetime the faster equilibrium is reached. Here it is assumed that the value of $\frac{dN_\gamma}{d\lambda dt}$ is taken for on-resonant photons. With these equations we approximate the produced nuclear photons per second, Φ_γ as a function of photon flux and excitation time t

$$N_m \approx 10^{-23} N_{Th}\frac{dN_\gamma}{d\lambda dt}(1 - e^{-\Gamma_m n^3 t}), \tag{5.5}$$

$$\Phi_\gamma = n^3\Gamma_m N_m \ \mathrm{s^{-1}}. \tag{5.6}$$

If a pulsed VUV laser is used we cannot make the assumption of a continuous stream of photons. Assuming that the spectrum of a single pulse is a Lorentzian profile with a full width half maximum (FWHM) equal to $\Delta\omega$ the spectral energy density of a pulsed laser can be modelled as

$$\left.\frac{dE}{d\omega}\right|_{\text{1 pulse}} = \frac{E_{pulse}}{\pi\Delta\omega}. \tag{5.7}$$

Since many pulses are fired in rapid succession any nucleus will feel an average spectral density

$$\left.\frac{dE}{d\omega}\right|_{\text{av}} = \left.\frac{dE}{d\omega}\right|_{\text{1 pulse}} 2\sum_{n=-N}^{N}\frac{1}{1 + (2\frac{\omega-\omega_m+n\Delta\omega}{\Delta\omega})^2} \approx \frac{E_{pulse}}{\Delta\omega}. \tag{5.8}$$

The above equations can be used to estimate the excitation probability R of a single thorium nucleus that is in this pulsed beam

$$R = \frac{2}{3}\frac{c^2\Gamma_m\pi^2}{s_{beam}\hbar\omega^3}\frac{dE}{d\omega}\bigg|_{\mathrm{av}}. \tag{5.9}$$

To compare between excitation methods, above equations can be used to calculate the nuclear photon emission flux Φ_γ per 4π steradian Ω for each method. We assume that the isomer decay rate is $\Gamma_m = 2.8{\cdot}10^{-4}$ Hz [16], $\lambda = 152.1$ nm, $n(152.1) = 1.575$ [56], s_{beam} $= 1\,\mathrm{mm}^2$ and $N_{Th} = 10^{16}$ ($\approx 10^{18}$ cm^{-3} doping in $1\times1\times10$ mm crystal). The different light sources available in Vienna with corresponding excited nuclear photon flux are then:

- D_2 lamps [200] with a photon flux at 150 nm of $\frac{dN_\gamma}{d\lambda dt} \approx 10^{15}$ nm^{-1}s^{-1}.
  $\frac{\Phi_\gamma}{\Omega} = \frac{n^3\Gamma_m N_{eq}}{\Omega} \approx 10^4$ sr^{-1}s^{-1}
- Excimer lamps [239] with a photon flux at 150 nm of $\frac{dN_\gamma}{d\lambda dt} \approx 10^{14}$ nm^{-1}s^{-1}.
  $\frac{\Phi_\gamma}{\Omega} = \frac{n^3\Gamma_m N_{eq}}{\Omega} \approx 10^3$ sr^{-1}s^{-1}
- A pulsed VUV laser currently being developed at PTB. The pulsed laser has a high intensity pulse, but low power on average. The characteristics of this laser are: 10^{13} photons/pulse, 30 Hz pulse repetition and 250 MHz linewidth ($\Delta\nu = \frac{\Delta\omega}{2\pi}$). $R \approx 6.78 \cdot 10^{-9}$ and then $\frac{\Phi_\gamma}{\Omega} = \frac{n^3\Gamma_m R N_{Th}}{\Omega} \approx 6 \cdot 10^3$ sr^{-1}s^{-1}

The downside of using D_2 lamps is that their spectrum consists of extremely many sharp lines rather than a continuum as is the case for excimer lamps. This creates the possibility that the nuclear state cannot be excited via a D_2 lamp. The excimer lamp thus seem favorable, although the nuclear photon flux is one order of magnitude lower. The pulsed laser is tuneable, produces a higher photon flux than the excimer lamp and in a successful measurement would be able to precisely determine the wavelength of the isomer excitation. The pulsed VUV laser thus seems to be the most favorable to use, if the isomer energy falls into the operating range of the tuneability of the laser.

5.1.2 Charge Transfer State Electron Bridge

The direct excitation of a thorium nucleus is very inefficient, the required photon flux to excite a single nucleus is 26 orders of magnitude larger than the signal flux it produces in a crystal, 27 orders of magnitude larger in an ion trap. The coupling of photons to the nucleus seems to be a more inefficient process than coupling electrons to the nucleus. For example, this has been calculated and validated for plasma excitation [237].

We propose to use a color center, a charge transfer state (section 2.3.1), that is created in the crystal by doping it with Th [42]. This charge transfer state can be seen as an excitation where the negative charge of the interstitial F^- is excited to an orbit around the Th^{4+}. Effectively the F becomes neutral and the Th gains an oxidation state of 3+. This excited electron would normally have a very low probability to excite the nucleus by transferring its energy. By sending in an additional laser, the CTS electron can be coupled to a virtual state at exactly the same energy as the thorium nuclear excited state. The electron can now under the emission of a lower energy photon transfer its energy to the nucleus via the virtual state, creating an excited nucleus (see figure 2.14).

The characteristics, such as wavefunction, of these CTS can be calculated by using DFT theory as described in chapter 2. The charge transfer of the electron that moves from fluoride to thorium results in the electron being in a certain orbital. There are several possibilities for these orbitals which have different total energy and wavefunction. Each one thus has a different probability to excite the nucleus through CTS. According to [29] there are 8 states possible, depicted in figure 2.13. The result of these calculations is that the excitation rate of the nucleus can be increased by at least 2 orders of magnitude if this type of scheme is used. The closer the defect state energy to the isomer energy, the more the enhancement increases.

Independently, preliminary calculations were done on these CTS by L. Seijo [102] that predict two type of CTS: One from the interstitial F^- that is used for charge compensation of the Th^{4+} and one from the lattice F^-. These two were estimated to be at 125 nm and 300 nm, where the first one is in close agreement to the prediction by [29]. These colour centers can also be used to de-excite the nuclear excited state faster, increasing the rate by 3 orders of magnitude. If these CTS can be characterized experimentally, which was possibly done in sections 4.4.1 and 4.4.2, they can be used as a novel approach to excite the ^{229}Th nucleus.

These calculations purely take into account excitation of the ^{229}Th nuclei in CaF_2 and not the surrounding crystal and detection setup. The transmission needs to be taken into account, the damaging effects of VUV irradiation characterized and mitigated, background needs to be measured and the detection setup efficiency needs to be evaluated. The crystal transmissions were evaluated in chapter 4. The setups to measure the other aspects are presented in the following sections: The cooling setup to characterize and mitigate VUV irradiation damage and the direct excitation setup meant to measure the photon emission of the isomer and to characterize background in a realistic setting.

5.2 VUV Irradiation Damage Characterization Setup

As described in section 2.4.1 damage in undoped CaF_2 is mainly produced by creating F and H centers. If they do not annihilate, they will separate. The F centers can then agglomerate to form Ca metallic nanoparticles which scatter light in the VUV region (see figure 2.16). This effect needs to be characterized as well for Th:CaF_2. Non-radioactive (^{232}Th doped) crystals will be used for this.

In [47] it is described that cooling can possibly prevent F and H centers from separating, and thus they will more likely annihilate after formation preventing any formation of larger colloids which absorb in the VUV. Thus a setup was designed to measure the effects of temperature on damage formation of the Th:CaF_2 under VUV irradiation. For this a holder was designed to cool a crystal to cryogenic temperatures while simultaneously damaging it. Also the holder from section 4.2.2 was used to anneal the crystals after damaging.

5.2.1 Cooled VUV Irradiation Setup

Building and designing a crystal VUV transmission holder that can also be cooled brings with it a unique set of boundary conditions. The holder needs to be cooled to low temperatures (35 K), need to have temperature control, materials that withstand the cold temperatures, low thermal conductivity to prevent heating, temperature read out, vertical translation, vacuum compatibility and two openings for crystal and reference measurement.

The end result is shown in figures 5.1, 5.2 and 5.3. The entire holder is connected to a CF40 flange which is connected to an XYZ bellows translation stage for moving the holder. The flange has a D-type socket feedthrough for the electronics. An NTC resistor is connected as close to the crystal as possible for temperature measurement. A ceramic heating element is sandwiched in between the long plate and the actual crystal holder to function as isolation and as a possible heater. The wiring for the heater and NTC is coiled around the long plate and fastened with screws. As thin leads as possible are used for the NTC resistor to reduce heat leaking into the crystal holder. At the top of figure 5.2 3 thick copper wires can be identified that will be connected to the cold finger to cool the crystal holder.

This crystal holder needed to be incorporated into a setup where at the same time the holder could be cooled and a VUV light source could damage the crystal. In this damaging setup, a Sunpower cryocube is used as cold finger. The cryocube is an inverse Sterling engine that can cool down to 35 K. Three copper wires are attached to the

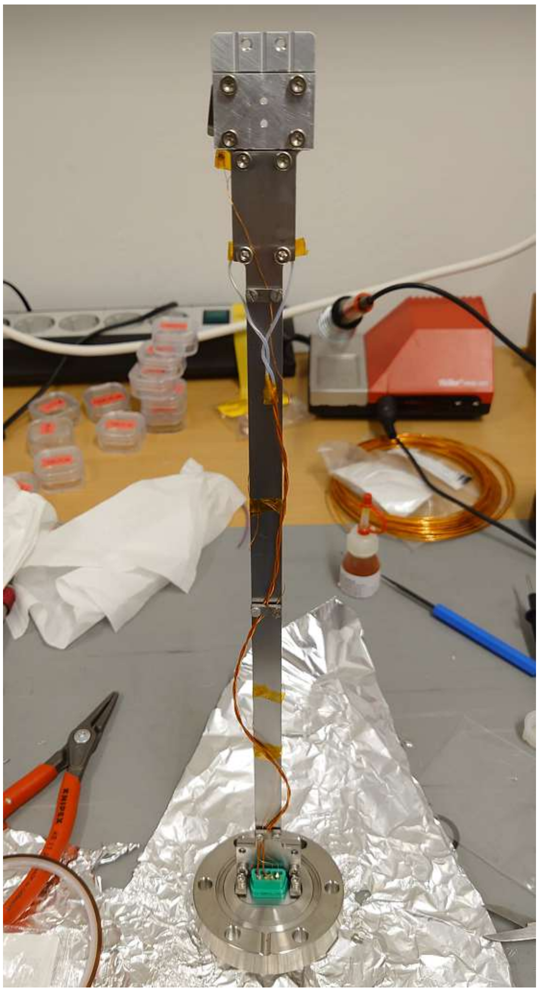

FIGURE 5.1: Cryogenic VUV transmission crystal holder.

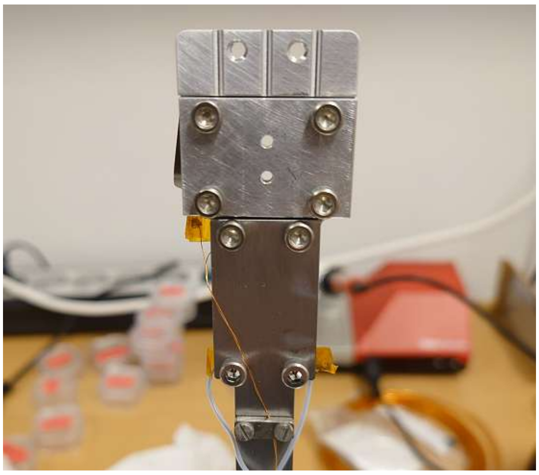

FIGURE 5.2: Zoom of cryogenic holder.

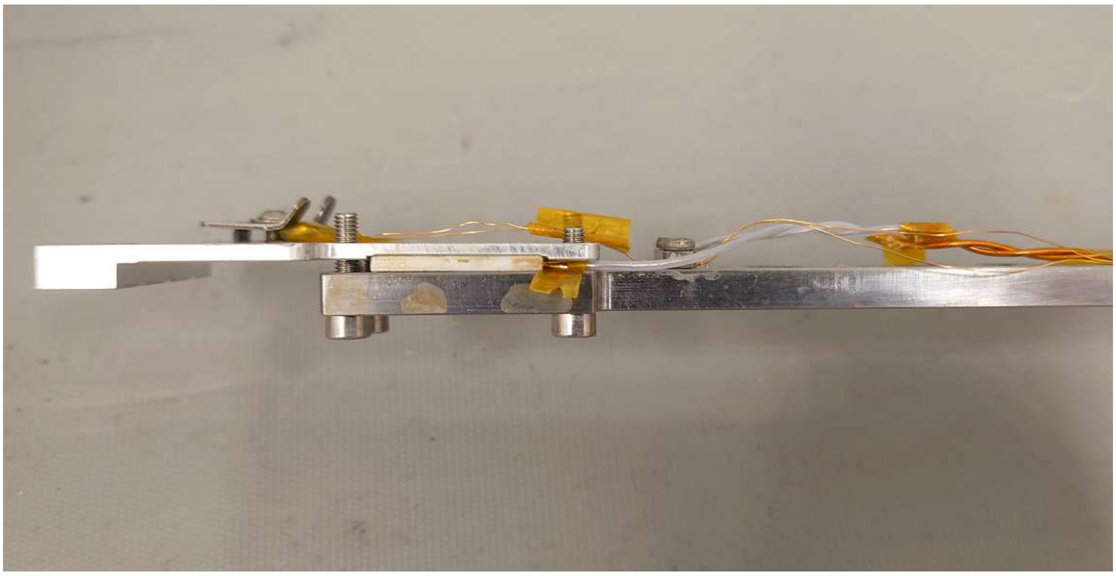

FIGURE 5.3: Side view of the cryogenic holder to show the NTC and heater.

FIGURE 5.4: Sunpower cryocube suspended with rope and a piece of lead of the same weight as the cube. This contraption was needed to avoid pressure on the vacuum connection on the cube, as it was too weak to resist any stress. The whole suspension and bellows system was designed such that it could be moved, as the holder needed to be able to move up and down for transmission measurements. The copper wires that are meant to cool the holder were shaped into a spring to provide some longitudinal motion freedom.

cryocube cold finger and the crystal holder to provide cooling of the crystal, see figure 5.4. Since the PID system of the cryocube expects a large cooling load, the ceramic heater was installed to provide the cryocube with the appropriate load to stabilize on any desired temperature between 50 K and room temperature. Later, holes were drilled into the long plate to reduce thermal conduction through this connector, which limited the ultimate temperature that could be reached. The holder in the open damaging system can be seen in figure 5.5, and the entire cooled damaging setup can be seen in figure 5.6.

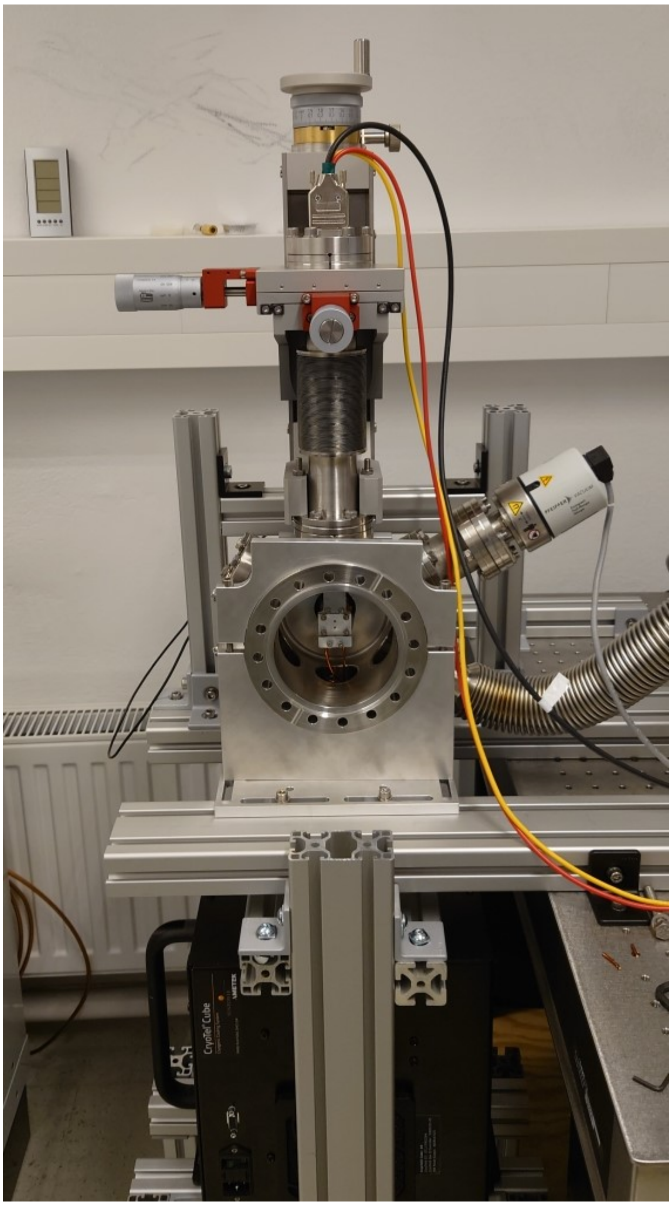

FIGURE 5.5: Cooled damaging setup with the focused VUV light source removed to show the holder inside the system. Here one can also see the copper cooling wires connected to the holder. On the top the XYZ vertical translation bellows can be seen. A gauge is added to measure the pressure.

The vacuum during cooling was held better than 10^{-6} mbar.

5.3 Direct VUV photon Excitation Setup

To directly excite the ^{229}Th isomer in a CaF_2 crystal, a setup was designed to focus as much VUV light onto a crystal and detect the fluorescence. The excitation probability was calculated above, which yielded $\approx 10^3$ sr^{-1}s^{-1} for an excimer lamp focused on a

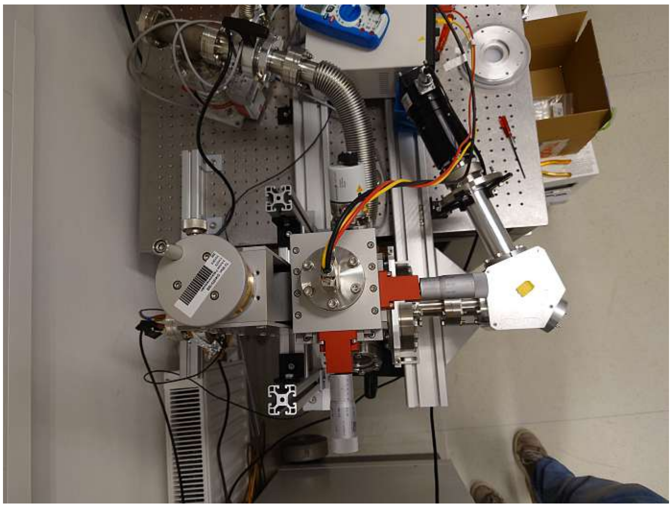

FIGURE 5.6: Damaging setup top view with the focused L15094 VUV light source D_2 lamp of Hamamatsu. The whole system is pumped with a rough pump/turbo pump combination from Pfeiffer. The NTC resistor is read out through a multimeter, heater is powered by a DC power supply (red, yellow and black wires).

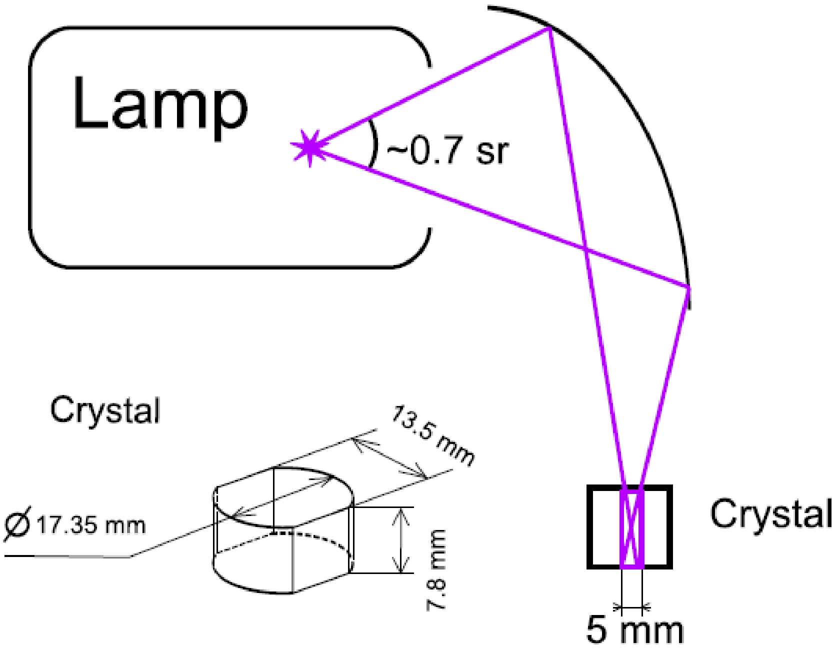

FIGURE 5.7: Schematic representation of the lamp and its emission angle. The 100 mm diameter elliptical mirror ($f_1 = 100\,\mathrm{mm}$, $f_2 = 100\,\mathrm{mm}$) focuses the light onto the crystal to an approximately 1.2 mm spot at the tightest focus, which is a 5 mm spot on the top of the crystal. The crystal used was the V057 ($8{\cdot}10^{15}\,\mathrm{cm}^{-3}$ ^{229}Th and $1{\cdot}10^{17}\,\mathrm{cm}^{-3}$ ^{232}Th) grown in [172] cut to the shown dimensions. The cut sides and top were polished to excite and image the fluorescence.

$10^{18}\,\mathrm{cm}^{-3}$ doped ^{229}Th:CaF$_2$ of dimensions 1x1x10 mm. A setup was designed to ensure this focusing and detection with a large acceptance angle.

The entire setup in the lab can be seen in figure 5.9, where an excitech lamp filled with krypton is attached to a large vacuum chamber with a ^{229}Th:CaF$_2$ crystal and focusing

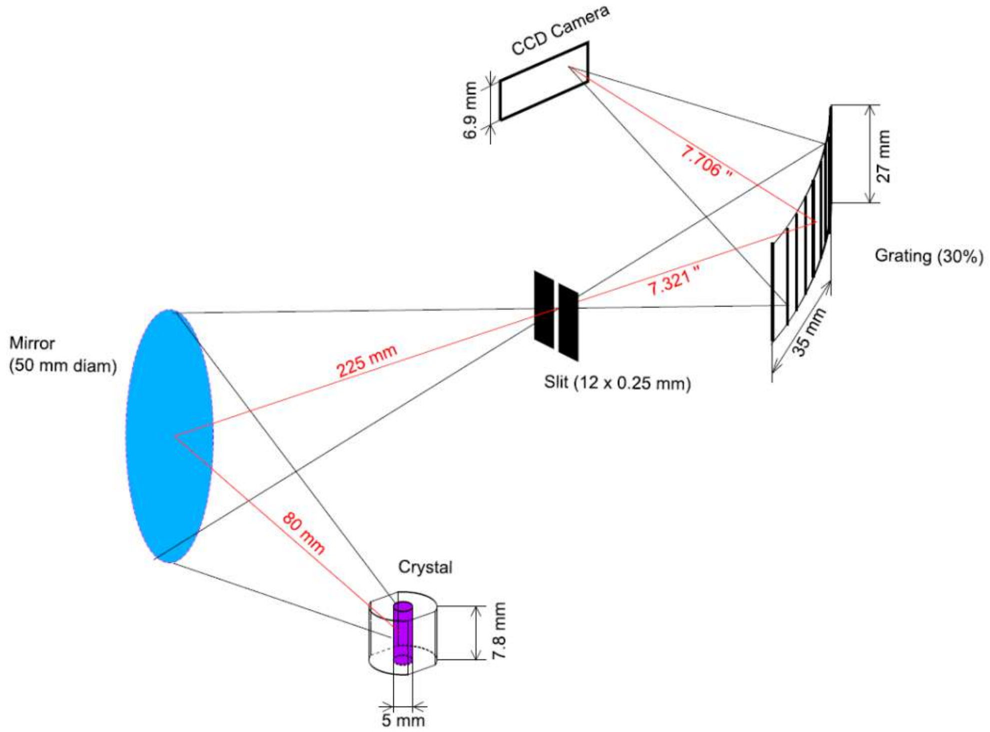

FIGURE 5.8: Imaging system of the irradiated volume from figure 5.7. A 50 mm diameter elliptical mirror ($f_1 = 80$ mm, $f_2 = 225$ mm) focuses the light onto the slit of the 234/302 McPherson spectrometer and is then diffracted and focused by the grating onto the CCD camera.

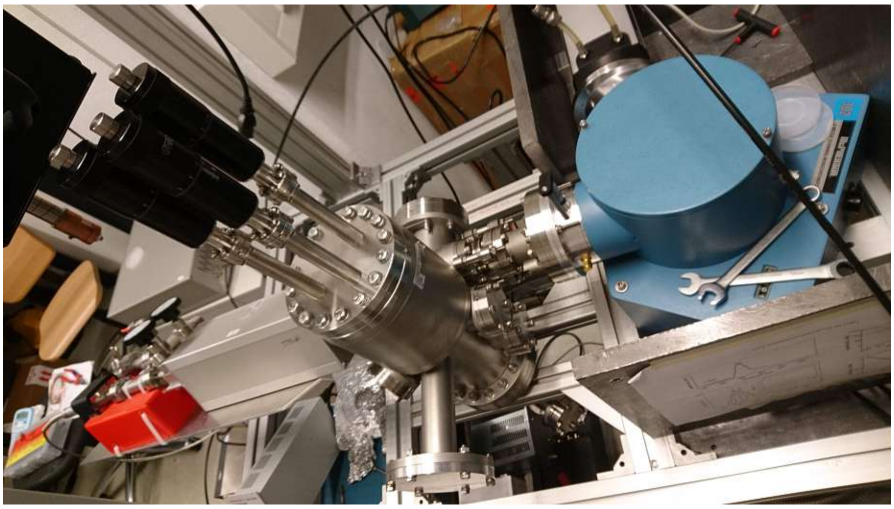

FIGURE 5.9: The total fluorescence excitation setup as built in the lab. The 3 micrometer screws can carefully change the alignment of the excitation mirror inside the system. The CCD camera needs water cooling to reach -100 °C. The system is encased in lead plates in order to reduce cosmic rays hitting the CCD chip.

optics. This chamber focuses the light of the lamp on the crystal (schematically shown in figure 5.7), and images the fluorescence onto a 234/302 McPherson spectrometer (schematically shown in figure 5.8). The spectrometer is connected to a CCD camera cooled to -100 °C in order to perform long integration measurements and minimize dark

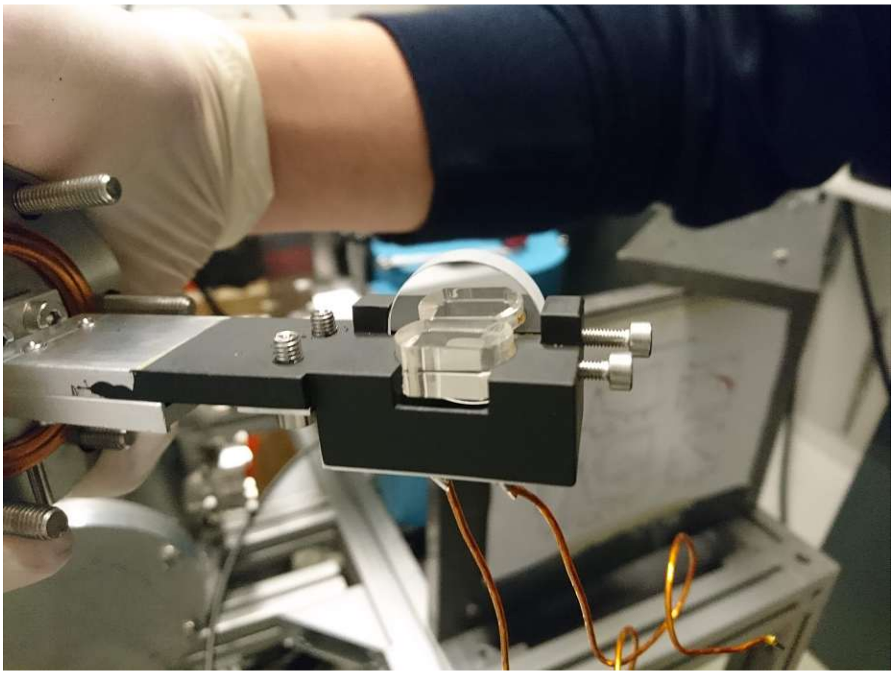

FIGURE 5.10: Holder for the ^{229}Th:CaF$_2$ crystal. The holder is painted with Aeroglaze Z306 in order to reduce scattering off the holder. Behind the crystal a 1 inch aluminum mirror is mounted to reflect more light into the spectrometer. Below the crystal, a VUV diode is mounted to improve ease of aligning the lamp onto the crystal. Both crystal and mirror are secured by set screws.

noise. The vacuum in the system was held better than 10^{-6} mbar.

The geometrical efficiency of the imaging system can be separated in three parts: Collection angle of the elliptical mirror (Ω_M), losses on the slit (η_1) and efficiency of the McPherson plus detector (η_2). Using the values in figure 5.7 the factors can be calculated. The collection angle Ω_M can be calculated using the distance to the mirror, the size of the mirror and its 45° angle to the crystal to be

$$\Omega_M = \frac{2\pi}{\sqrt{2}}\left(1 - \frac{80}{\sqrt{80^2+25^2}}\right) \approx 0.2\,\mathrm{sr}. \tag{5.10}$$

The factor η_1 can be calculated by knowing the size of the illuminated volume, its magnification due to the mirror and the size of the slit to be

$$\eta_1 = \frac{12\cdot 0.25}{5\cdot 7.8}\left(\frac{80}{225}\right)^2 \approx 0.01. \tag{5.11}$$

The factor η_2 can be taken from chapter 4.1.1 taking the CCD efficiency to be 26 % then $\eta_2 = 0.26\cdot 0.001 = 2.6\cdot 10^{-4}$ or 0.026 %. The total detection efficiency can then be estimated to be $0.2\,\mathrm{sr}\cdot 0.01\cdot 0.00026 = 5.2{\cdot}10^{-7}\,\mathrm{sr}$.

5.4 VUV Photon Irradiation Damaging Effects in CaF_2

VUV irradiation excites F and H center pairs which creates damage over time [47]. In this section the experimental results on damaging the Th:CaF_2 crystals with VUV irradiation is presented.

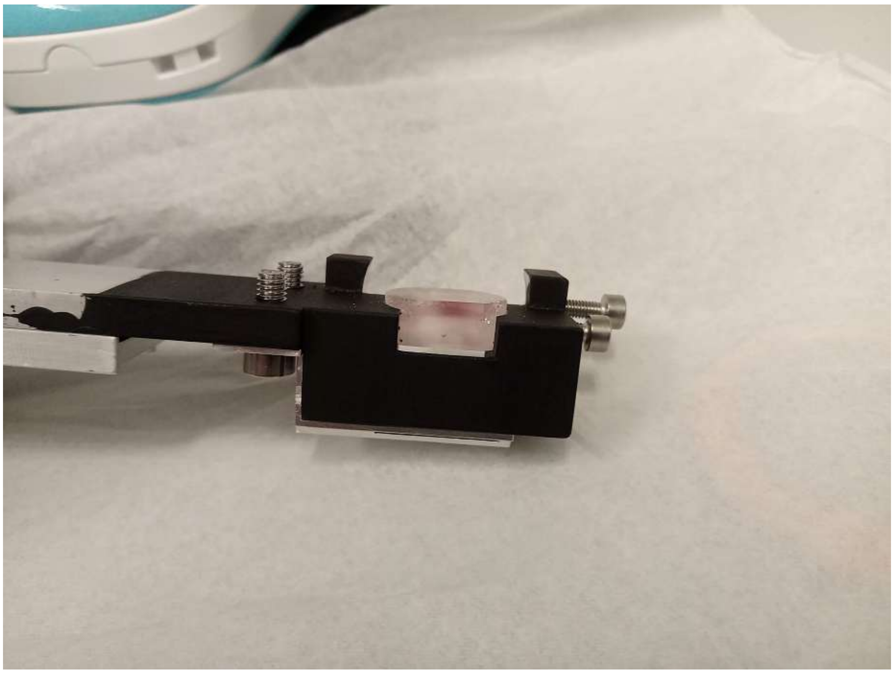

FIGURE 5.11: Highly doped ^{232}Th:CaF_2 crystal irradiated for 9 hours with the Excimer lamp filled with a Kr gas. This crystal had many defects due to rapid cooling at the end of the growth cycle, possibly increasing its susceptibility to damage. A purple/orange haze can be seen where the VUV lamp was focused. The haze probably consists of Ca metallic nanoparticles together with separate F/M/N centers. The Ca nanoparticles would give it a black/purple coloring and the F/M/N centers an orange coloring which in this crystal creates a color in between orange and purple giving it the characteristic color.

It has been observed that the damaged crystals gain a purple haze and glitter under intense VUV irradiation [211]. In the excitation setup described above a highly doped ^{232}Th:CaF_2 crystal was irradiated for 9 hours with the excimer lamp filled with a Kr gas. This produced a purple/orange haze, see figure 5.11. The same effect was observed in the fluoride annealed $^{229/232}$Th:CaF_2 crystal V057 in figure 4.55.

In more quantitative experiments a ^{232}Th:CaF_2 crystal was irradiated with a focused Hamamatsu L15094 VUV D_2 lamp for 24 hours and the spectral transmission was measured before and after irradiation. This was done in the cooling setup described in section 5.2, the crystal in its holder can be seen in figure 5.13. The results are shown in figure 5.12. It can be seen that the transmission has been significantly decreased, mostly for low wavelengths. The crystal obtains an orange colored layer on its surface at room temperature, which can be easily polished off. By polishing the crystal, transmission

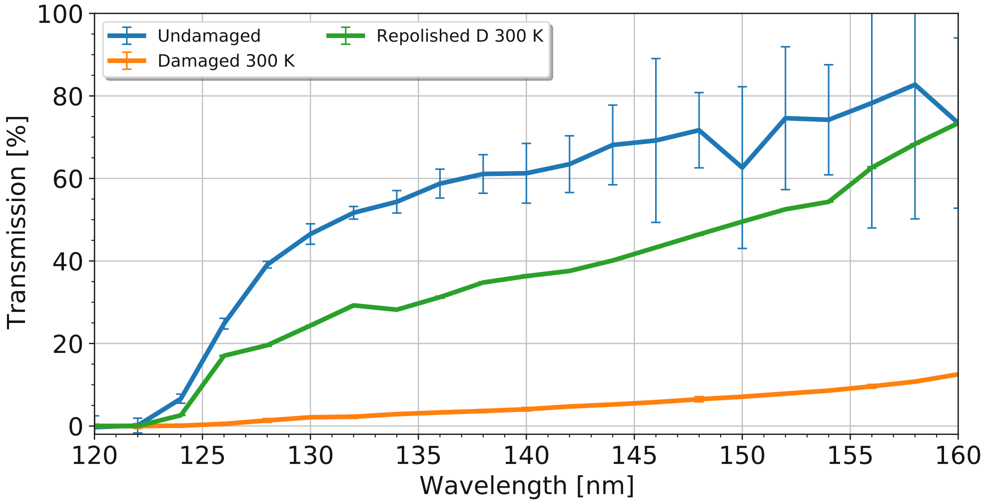

FIGURE 5.12: Low doped ^{232}Th:CaF$_2$ crystal (Cal3.1, $10^{17}\,\mathrm{cm}^{-3}$) irradiated for 24 hours with the a focused Hamamatsu L15094 VUV D$_2$ lamp. Damaging this crystal greatly reduced its transmission, especially at low wavelengths. Repolishing the crystal increases the transmission significantly, indicating the damage is mainly on the surface but penetrates deeper into the crystal.

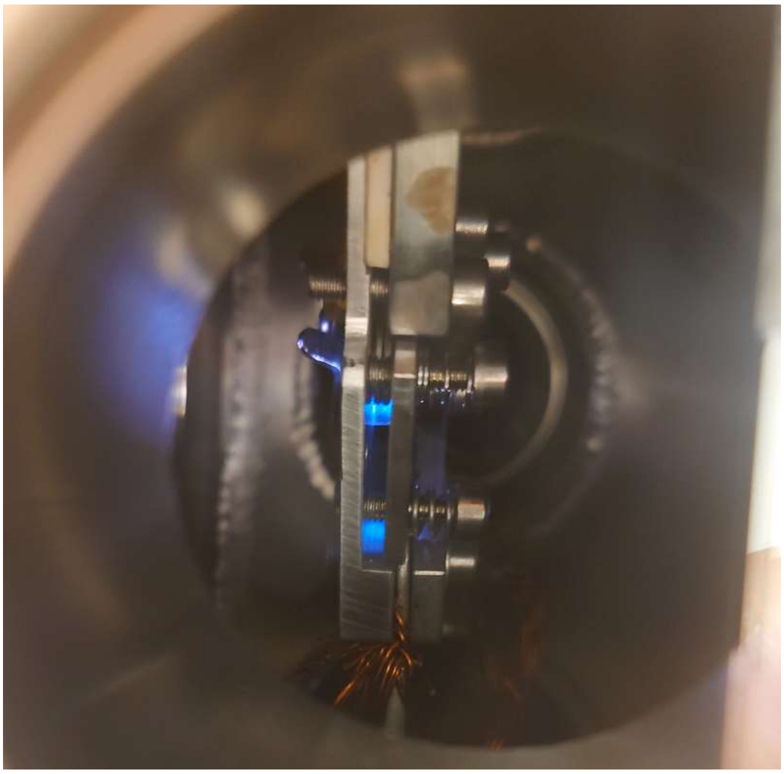

FIGURE 5.13: ^{232}Th:CaF$_2$ crystal in the cooled damaging setup while being irradiated with a Hamamatsu L15094 D$_2$ lamp. The attached cooling wires can be seen below, and the heater above. The STE fluoresces visibly blue due to the intense irradiation.

can be regained close to the original value, about 80 %. The increase in transmission shows that the surface contains a significant portion of the damage. The exact amount of transmission that can be regained needs to be studied further. These results can be

FIGURE 5.14: Crystal before and after damaging by VUV irradiation. An orange color is produced which is possibly due to F, M or N centers or due to deposition of cracked hydrocarbons that are leftover in the vacuum system.

used to assess the viability of the VUV irradiation experiments.

5.5 Prevention and Healing of VUV Irradiation Damage

Due to the expected long lifetime of the photon emission of isomeric ^{229}Th any experiment designed to excite the nucleus through VUV irradiation and subsequently detect photon emission will be irradiating and integrating for long periods of time. To reach the required amount of excited nuclei, irradiation times need to be long and to detect enough photons to see a signal above the noise, integration times need to be long.

VUV irradiation creates damage in the crystals which reduce both excitation efficiency and detection probability. To mitigate the effects of VUV irradiation damage it was attempted to prevent it by cooling and heal it by annealing. Annealing of crystals after damaging was done using the setup from 4.2.2. Cooling the crystals was done using the setup described in section 5.4. Possibly the annealing and cooling of Th:CaF_2 can also be used to mitigate neutron irradiation or x-ray irradiation damage.

By increasing or restricting the mobility of defects or fluorides in CaF_2, damage can be healed or prevented. Healing by annihilation of F and H centers through heating and damage prevention by annihilation upon creation through cooling are attempted. More details on the microscopic processes of annihilation can be found in section 2.2.

5.5.1 VUV Irradiation Damage Healing through Annealing

By irradiating the crystal, damage is created by formation of defects as described in section 2.2. If the crystal is annealed after damaging, the created F and H center pairs can be annihilated if they meet. Through heating, the mobility of these defects can be increased exponentially. This was tested by irradiating a ^{232}Th:CaF$_2$ with a focused L1835 Hamamatsu D$_2$ lamp (4.1.2) for 24 hours and annealing it. The transmission relative to the original transmission was measured for each temperature, after which the crystal was brought to a higher temperature with 2°Ć min^{-1} for 6 hours and then left to cool down with 2°Ć min^{-1}.

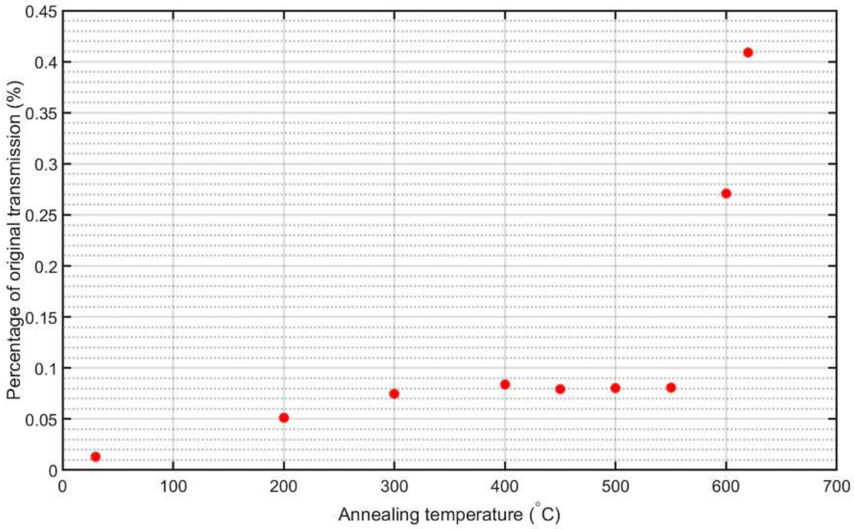

FIGURE 5.15: Transmission of annealed crystal as percentage of the original transmission versus annealed temperature. The setup described in section 4.2.2 was used to anneal the crystal and afterwards measure the transmission. Up until 400 °C the transmission increases slowly and reaches a plateau. After 600 °C the regained transmission increases strongly. Due to material constraints the temperature could not be increased further.

The results are shown in figure 5.15. It is observed that at 400 °C a first saturation is reached. After annealing at 600 °C the transmission increases rapidly. The crystal could not be heated to more than 620 °C in this setup due to material constraints. Still, only 0.4 % of the original transmission was recovered in this experiment. This indicates that longer annealing times/higher temperatures are needed or the damage is of a different nature then purely F and H centers. If the damaging process induces reactions of the crystal with oxygen, or amorphize the crystal, the damage cannot be recovered by annealing. Longer annealing times were not pursued, as this would take weeks which is impractical for experiments which reach these levels of damaging in hours.

In section 4.4.4, 600 °C was also found to make Th:CaF$_2$ the most transparent. The similar results indicate that at 600 °C an important step in the mobility of F and H centers or a larger defect centers is made. Sadly, annealing VUV irradiation damaged crystals after damaging does not bring back the original transmission.

5.5.2 VUV Irradiation Damage Prevention through Cooling

As was suggested in [47], cooling CaF_2 will possibly keep the F and H center pairs localized after creation and increase the probability of annihilation instead of separation. This would mean a radiative decay of the created pair instead of a non-radiative decay. An indication for the increase in annihilation and radiative decay can be found in [240] where the STE luminescence increases at colder temperatures. When more energy is lost through luminescence, less energy needs to go into the creation of defects and thus damage.

To test this theory, a ^{232}Th:CaF_2 crystal was irradiated by a focused L15094 D_2 lamp (4.1.2) in the setup described in section 5.2. The crystal was irradiated for 24 hours while being kept at 300 K, 183 K and 90 K using a cold finger. After this, the VUV transmission was measured in the setup described in section 4.2.1 and compared to its original transmission.

The results of this experiment are shown in figure 5.16. Here it can be seen that at 300 K, only 20-60 % of the original transmission remains after damaging. At 183 K no damage is observed above 145 nm and at 90 K no damage was observed whatsoever. Due to difficulties in the stability of the irradiation input, measurement differences in the transmission setup, and conditions in the vacuum, these results should only be taken as a qualitative proof. Improved experiments are ongoing.

In these experiments it was also observed that the orange spot in figure 5.14 was not present when damaging at low temperatures. The nature of the orange spot is either F/M/N centers or cracked hydrocarbons left over in the vacuum. To quantify the species present in the vacuum they were measured using a Pfeiffer quadrupole mass spectrometer as a function of cold finger temperature, as seen in figure 5.17. Only the largest signals on the mass spectrometer are shown here, the hydrocarbons were several orders of magnitude lower in signal.

As is expected, water is the strongest signal due to its low ionization energy as compared to nitrogen, and high abundance in air. It can be seen that compared to other gasses water at -100 ℃ decreases in signal by an order of magnitude. At this temperature water freezes in vacuum and is thus effectively removed from the background gas by the cold finger. The same happens for CO_2 at 130 K. Seeing water as the most likely cause of

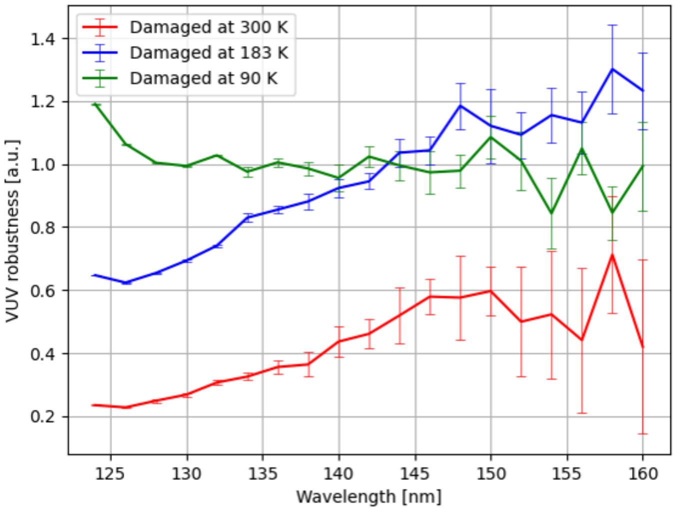

FIGURE 5.16: Spectral VUV robustness: Fraction of the transmission after damaging compared to before damaging, for damaging at three different temperatures. It can be seen at higher wavelengths that the measurements become unreliable. At 90 K no damage was observed. Coincidentally the damage is heavily reduced when the singlet STE luminescence exponentially increases, indicating more F and H center annihilation (see figure 2.23) .

the orange spot due to its abundance and sudden removal at lower temperatures it is conjectured that the VUV irradiation initiates the following photochemical reaction:

$$\mathrm{CaF_2} + \mathrm{H_2O} \xrightarrow{(VUV)} \mathrm{CaO} + 2\mathrm{HF}, \tag{5.12}$$

and thus incorporates oxygen in the lattice, increasing the absorption. This reaction is known to happen at high temperatures during crystal growing [188]. VUV irradiation could provide the energy to drive this reaction.

Other possibilities for the cause of the orange spot are the deposition of cracked hydrocarbons left over in the background gas or purely creating defects (such as F centers) in the crystal more effectively. The hydrocarbon deposition is often cited in literature [241] and F centers are known to produce orange coloring 2.5.3. Due to the fact that the largest reduction in damage from 180 K to 90 K coincides with the exponential increase in singlet STE luminescence (figure 2.23), the production of F and H pairs seems the most likely cause. A combination of all these effects together can also be the cause of this observation.

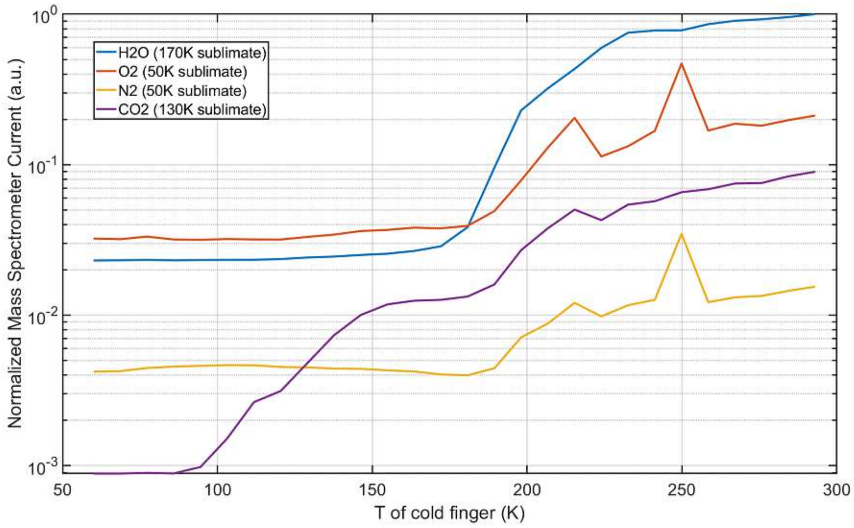

FIGURE 5.17: Normalized mass spectrometer current to cold finger temperature. The current was normalized to the H_2O current at room temperature. The N_2 and O_2 currents also decrease when the H_2O current decreases. This is due to the fact that the background current for each species decreases with decreasing vacuum. It can be clearly seen that both H_2O and CO_2 content decreases strongly at their respective sublimation temperatures.

5.6 Direct Excitation with VUV Photons

Using resonant VUV photons to directly excite the nucleus and measure the decay leads to building a nuclear optical clock. To work towards this goal, the setup described in section 5.3 was built to excite the ^{229}Th nuclei in the $^{229/232}$Th:CaF$_2$ crystal grown in [172] (V057) with a doping concentration of $4{\cdot}10^{15}/4{\cdot}10^{17}\,\text{cm}^{-3}$. This concentration is two orders of magnitude lower than the new crystals grown during this thesis and characterized in chapter 4. First the background was measured for crystal V057 using a measurement cycle of 9 hours of VUV irradiation excitation and subsequently 9 hours of integration with a CCD camera. This background characterization uncovered possible long lived color centers, see figure 5.18.

To further investigate the long lived color centers, the VUV induced luminescence was measured. To increase the signal intensity the crystal was continuously excited while recording a spectrum. Excitation and emission light was separated by a grating. The VUV induced luminescence uncovered that there is significant induced fluorescence in these crystals of which the origin is still unknown.

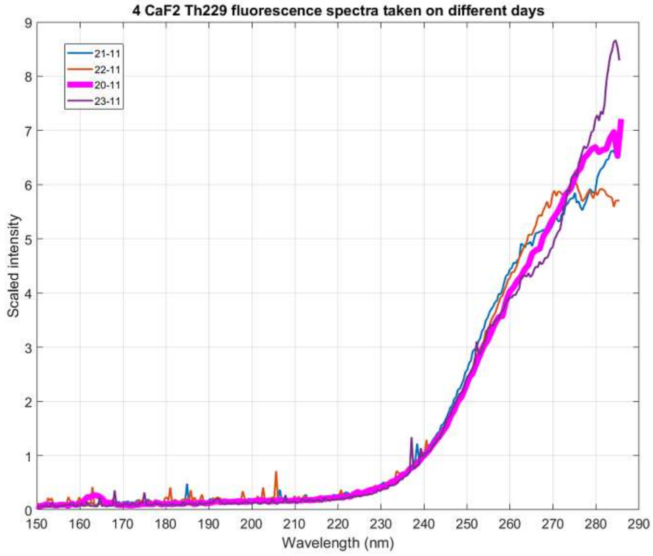

FIGURE 5.18: Afterglow spectrum of the V057 ^{229}Th:CaF$_2$ crystal grown in [172] after 9 hours of irradiation by a krypton filled excimer lamp (section 4.1.3) as measured in the direct excitation setup (section 5.3). This measurement was repeated several times on different days. At higher wavelengths the STE radioluminescence produced by this crystal as characterized in section 4.5.3 can be seen. For one measurement (21-11) a signal was observed above 160 nm which started the research into Th induced color centers. Possibly, this was no color center at all but a CCD chip burn-in signal (section 4.1.6).

5.6.1 Background VUV Induced Luminescence

Fluorescence in doped CaF$_2$ has long been studied and is still part of active research [51, 129]. To measure the fluorescence, the crystal to be studied is irradiated with excitation light. The crystal will absorb some of it and emit part of the absorbed light at characteristic wavelengths. Typically, the excitation happens at a higher energy (lower wavelength) than the emission. An excitation spectrum can thus be measured for a particular emission, and also an emission spectrum for a certain excitation. The excitation source used here is a broadband excitation from 123 nm to 180 nm. Only emissions lower in energy than the excitation light (higher in wavelength) will be observable. By studying the emitted light, the crystal and its dopants/contaminants can be studied.

Fluorescence in the VUV is often measured in synchrotrons due to lack of other high power VUV excitation light sources. Using the new excimer lamps we measured fluorescence in doped CaF$_2$ crystals that provides evidence towards the state of the dopant and possible defects. The analysis of these spectra is complex and not yet conclusive. Due to the many induced emissions, luminescence of CaF$_2$ itself and possible multiple contaminants, identification proves to be unreliable. Possibly by improving growing and detection methods better conclusions can be drawn using this method.

In figure 5.19 the fluorescence spectrum of undoped and $^{229/232}$Th crystals is shown. In this, a spectrum of the crystal is recorded while it is being irradiated by the krypton excimer light source (4.1.3) in the setup described in section 5.3. In this measurement an undoped crystal, ^{229}Th doped crystal and a low doped ^{232}Th crystal were investigated. The ^{229}Th doped crystal was measured twice, once with less background from the scattered lamp light. A large part of the signal (123 to 180 nm) is light directly from the lamp being scattered from particles in the crystal (the glitter 4.54), which can be compared to the spectrum in figure 4.11. From 200 to 280 nm the STE luminescence (figure 4.62) can be recognized.

Several peaks can be distinguished from 168 nm up until 250 nm. The peak around 168 nm is only found in the $^{229/232}$Th doped crystal. A broad peak around 187 nm, and narrow peaks around 219, 230, 238 and 250 nm are only detected in the $^{229/232}$Th doped crystal as well. The appearance of these peaks is possibly due to the radioactivity of the ^{229}Th in the crystal or the 100 times larger doping concentration as compared to the ^{232}Th doped crystal used here. A peak around 176 nm can be found in all crystals which we attribute to Pb^{2+} fluorescence leftover after growth [124]. The 219 nm peak was also observed in Pb doped CaF_2 [124].

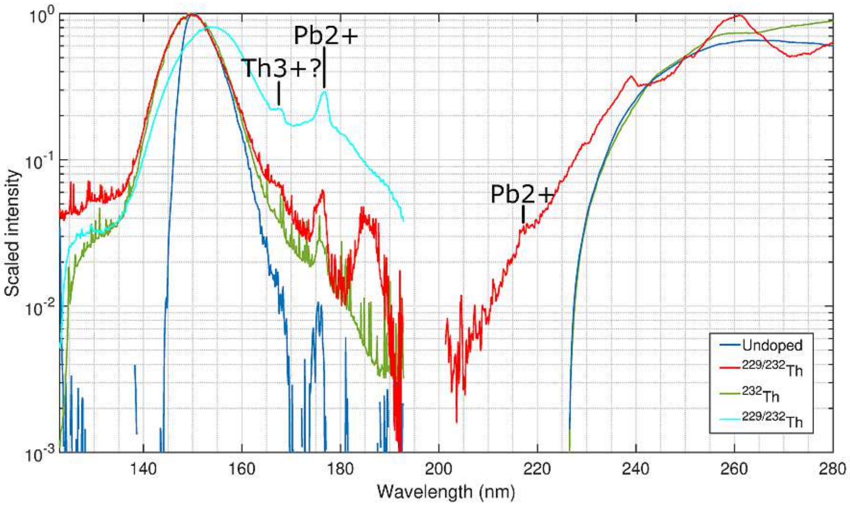

FIGURE 5.19: Fluorescence spectrum of four different crystals: Undoped, $^{229/232}$Th doped (10^{16} cm^{-3}/10^{18} cm^{-3}), low ^{232}Th doped (10^{16} cm^{-3}) and again the same $^{229/232}$Th doped. For the last spectra the system was realigned to reduce background of the excitation light. Because the grating only covers 90 nm two spectra were taken per crystal with a different center wavelength.

To further explore this behavior, known peaks of the free ions Th IV (3+) and Zr IV (3+) were compared to these peaks (see figure 5.20). These two species were the only dopants present with significant concentration. Normally the Th and Zr only take the 4+ oxidation state and should be optically inactive in the VUV. If their oxidation state changed in the crystal, even for a fraction of the total population, they might luminesce.

These ions are doped in a crystal thus the spectral peaks as opposed to the free ion lines, can shift and broaden, so few conclusions can actually be drawn. Possibly the peak around 168 nm is from Th^{3+}, the broad peak around 187 nm is from several Zr^{3+} lines and the peaks above 200 nm correspond to more Zr^{3+} lines.

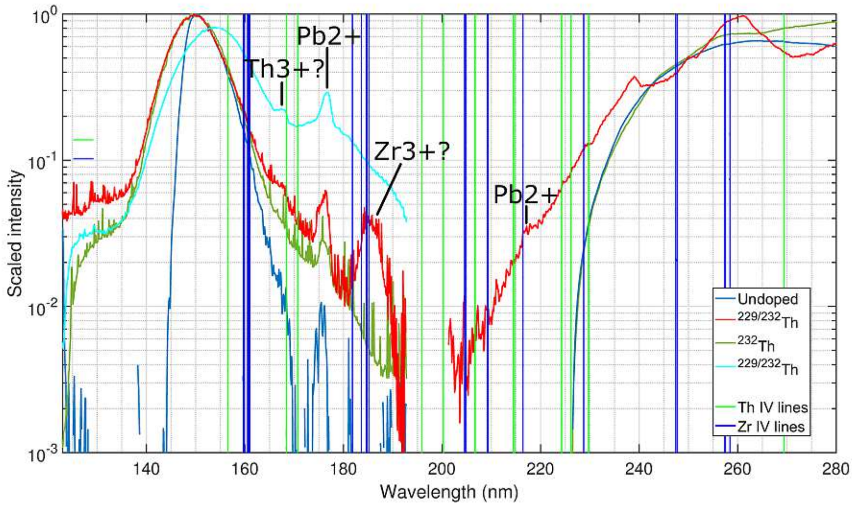

FIGURE 5.20: The same spectrum as in figure 5.19 but lines of the free ions Th IV and Zr IV are plotted. Few occasions can be seen where these coincide with peaks in the spectra. The peak at 168 nm possibly stems from Th and the peak at 187 nm from Zr.

It is not clear if the observed spectral peaks produced were due to ^{229}Th, Zr or simply not seen in a ^{232}Th doped crystal due to a too low doping concentration. Thus luminescence spectra were taken of a highly doped $^{232}Th:CaF_2$ crystal and a $Zr:CaF_2$ crystal. In the highly doped ^{232}Th doped crystal luminescence, the Pb^{2+} peaks at 176 nm and 219 nm become more apparent. Also a large fluorescence continuum from 160 nm to 200 nm is observed, possibly containing the 168 nm peak from before. The 168 nm and 187 nm peak is not found in $Zr:CaF_2$, indicating that no VUV peaks related to Zr are observed. Possibly in this crystal the oxidation state of the Zr is different because it's not a radioactive crystal. The peaks above 200 nm were observed for both Th and Zr doped crystal, indicating contaminants. Possibly Bi as a decay product of both Th and U contaminated the Zr doped crystal [125].

Finally the excitation light was blocked using a quartz window (7 % transmission at 146 nm) to decrease the energy of the excitation light. Effectively this studies the excitation spectrum of the observed emissions. If the absorption peak of a certain emission lies in the region truncated by the quartz window the emission should disappear. In figure 5.22 it can be seen that the fluorescence at 168 nm is not observed anymore. The 187 nm peak seems to be damped and the Pb peak at 176 nm seems unaffected. It is known that the excitation spectrum for the 176 nm peak is excited by absorption at

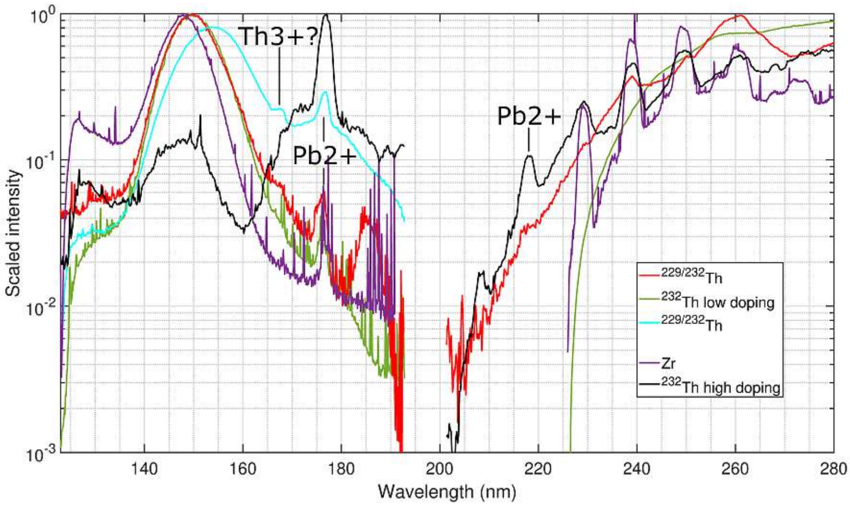

FIGURE 5.21: Fluorescence spectra of a Zr doped and a high ^{232}Th doped (10^{20} cm^{-3}) CaF$_2$ crystal are presented compared to spectra of $^{229/232}$Th of figure 5.19. The 176 nm peak of Pb^{2+} can now be seen more strongly. Peaks due to the same contamination can be seen in both crystals above 200 nm.

>150 nm, which should thus be unaffected by the quartz window [124]. It seems the 168 nm fluorescence is excited only by an absorption at a wavelength lower than 147 nm.

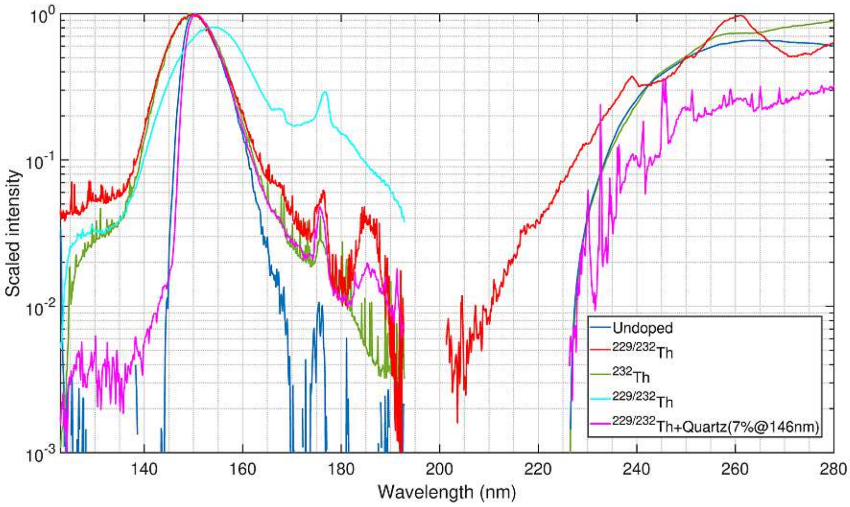

FIGURE 5.22: Fluorescence spectrum of the ^{229}Th:CaF$_2$ crystal while the excitation light is truncated at wavelengths below 147 nm by a quartz window. The intensities of the spectra are normalized their highest values. The spectrum is compared to those in figure 5.19.

The above spectra are very similar to Ho^{3+}:CaF$_2$ (and also to other lanthanides doped in CaF$_2$), which shows broad peaks around 168 nm and narrow peaks above 200 nm [134]. The lanthanides all show broad VUV peaks due to the interaction of the 5d electron with the surrounding lattice. These excitations are characterized as the 5d to 4f excitations. The narrow peaks are characterized in [134] as 4f to 4f transitions as the electrons in the $4f$ orbit do not interact as much with the lattice. This behavior in the lanthanides is probably also present in the actinides, where $6d$ to $5f$ excitations will produce VUV emission as can already be seen for uranium doped large bandgap crystals [242, 243]. A review on the very consistent emission behavior of lanthanides doped in crystals can be found in [244] and in particular data for CaF_2 [137].

To further study the fluorescence of Th:CaF_2 it is recommended to improve the used setup. Increasing Th doping concentration of the used crystals (≈0.01 %) and removing contaminants should produce a clearer, more intense spectrum. Using an intense tuneable narrowband excitation light source will make measurements of the excitation spectra of certain emissions possible. Using PMTs the lifetime of the emissions can be characterized. If the resolution is increased the bands can possibly be resolved in their components and further studied. Cooling the crystals to low temperatures will narrow the emission peaks and increase their intensity as well. Through this study possible defect centers and electronic transitions can be found.

5.7 Experimental Viability of the Resonant VUV Photon Method

The total photon rate on the camera can be estimated from section 5.1 and 5.3 to be $3{\cdot}10^3$ $\mathrm{sr^{-1}s^{-1}} \cdot 0.2\ \mathrm{sr} \cdot 0.01 \cdot 0.00026 = 1{\cdot}10^{-3}\,\mathrm{s^{-1}}$ or roughly 1 photon every 1 hour. The VUV irradiation damage can be mitigated by cooling the crystals to 80 K, the transmission is at maximum 45 % for C10. The VUV irradiation induced background after stopping irradiation is less than 1 count per 9 hours ($\approx 1 \cdot 10^{-5}$), which is insignificant. The total photon flux detected on the camera will then be $4.5{\cdot}10^{-4}\,\mathrm{s^{-1}}$.

Compared to the dark noise of a CCD camera ($31\,\mathrm{s^{-1}/cm^2}$ or $1\,\mathrm{s^{-1}}$ for the area of the signal) this signal is very small and would need an integration time of more than a 1000 hrs to have a signal to noise ratio of 1. This does not take into account the readout noise and the cosmic ray background producing noise. Due to this reason this setup was only used to take fluorescence measurements of the crystals.

In the future, a new setup will be used, produced by HP Spectroscopy, that mainly increases the collection angle of the mirror and the efficiency of the spectrometer by reducing the focal distance and increasing the size of the grating, increasing the system efficiency by two orders of magnitude. Also, the new highly doped (0 times increase in concentration) ^{229}Th:CaF_2 crystals will be used. In total this can increase the signal rate by more than three orders of magnitude, creating a photon signal on the order of the dark noise of a CCD camera. If now also an MCP is employed the signal can be tripled due to the higher efficiency and the dark noise reduced by two orders of magnitude. This would produce a signal to noise ratio after an integration of 1 second of around 100. The amount of photons falling on the detector would be 1.5 s^{-1} for a 3.2 mm diameter 1 mm long crystal.

Chapter 6

The Nuclear Excitation of ^{229}Th Through Nuclear Reactions

Using nuclear processes to excite the isomeric state of ^{229}Th seems to be the most logical approach, and is proven to work [8]. Processes like α, β^- or β^+/electron capture (EC) decay transmute from the parent isotope to ^{229}Th in a highly nuclear excited state. The highly excited ^{229}Th then de-excites through γ emission and might end up in the isomer state in this process. In this section we identify which nuclear reactions, and decays, create $^{229\text{m}}$Th in CaF_2. To see which isotope needs to be produced such that excited ^{229}Th is produced, one can take a look at the chart of nuclides 6.1.

We can identify 3 different spontaneous decays that lead to ^{229}Th: α-decay from ^{233}U, β^- decay from ^{229}Ac and electron capture or β^+ decay from ^{229}Pa. It is known that 2 % of all ^{233}U decays produce isomeric thorium [8] and it is predicted that >14 % of ^{229}Ac decays do [46], up to 93 %. For ^{229}Pa this population probability is >≈2.5 % [246]. In this study ^{229}Pa was produced through a (p,t) reaction with ^{231}Pa. Recently the cross section of ^{232}Th with low energy protons was measured to produce ^{229}Pa, another possible production method for isomeric thorium [247].

Other nuclear reactions that produce ^{229}Th are for example: light-ion fusion evaporation reaction ^{232}Th(p,p3n)$^{229\text{m}}$Th [248], neutron capture via ^{226}Ra [12] ^{228}Th(n,γ)$^{229\text{m}}$Th or a ^{230}Th(n,2n)$^{229\text{m}}$Th reaction. These approaches are left for the reader to study in future research, especially reactions with neutrons can be performed in a crystal using the right material and doping.

The production of these isotopes and their subsequent decay into the isomeric state of ^{229}Th are ways to produce isomeric thorium in the crystal environment. Only ^{233}U decay and ^{229}Ac decay are considered in this thesis.

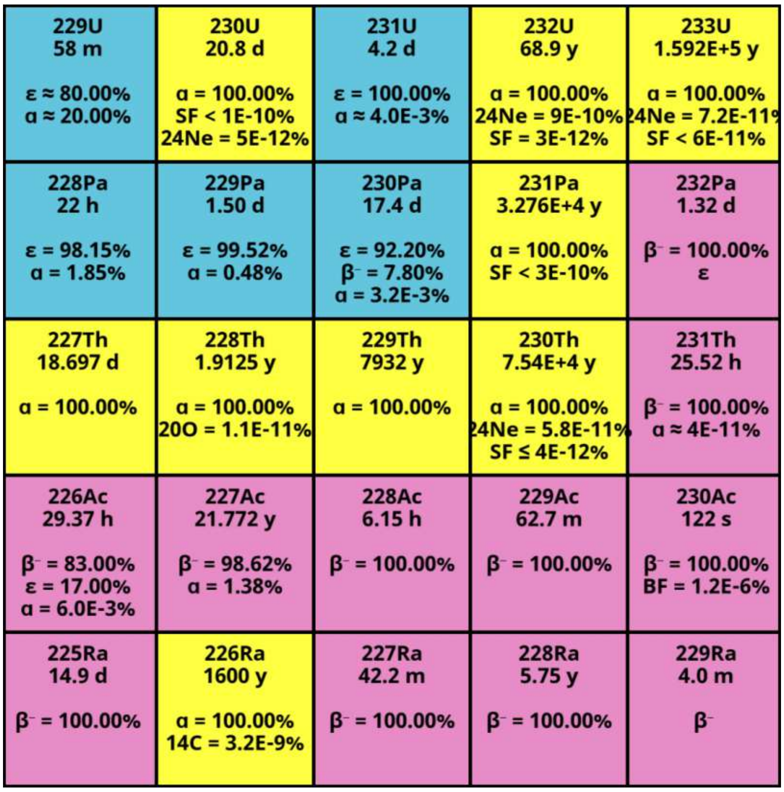

229U 58 m $\varepsilon \approx$ 80.00% $\alpha \approx$ 20.00%	230U 20.8 d α = 100.00% SF < 1E-10% 24Ne = 5E-12%	231U 4.2 d ε = 100.00% $\alpha \approx$ 4.0E-3%	232U 68.9 y α = 100.00% 24Ne = 9E-10% SF = 3E-12%	233U 1.592E+5 y α = 100.00% 24Ne = 7.2E-11% SF < 6E-11%
228Pa 22 h ε = 98.15% α = 1.85%	229Pa 1.50 d ε = 99.52% α = 0.48%	230Pa 17.4 d ε = 92.20% β^- = 7.80% α = 3.2E-3%	231Pa 3.276E+4 y α = 100.00% SF < 3E-10%	232Pa 1.32 d β^- = 100.00% ε
227Th 18.697 d α = 100.00%	228Th 1.9125 y α = 100.00% 20O = 1.1E-11%	229Th 7932 y α = 100.00%	230Th 7.54E+4 y α = 100.00% 24Ne = 5.8E-11% SF $\leq$ 4E-12%	231Th 25.52 h β^- = 100.00% $\alpha \approx$ 4E-11%
226Ac 29.37 h β^- = 83.00% ε = 17.00% α = 6.0E-3%	227Ac 21.772 y β^- = 98.62% α = 1.38%	228Ac 6.15 h β^- = 100.00%	229Ac 62.7 m β^- = 100.00%	230Ac 122 s β^- = 100.00% BF = 1.2E-6%
225Ra 14.9 d β^- = 100.00%	226Ra 1600 y α = 100.00% 14C = 3.2E-9%	227Ra 42.2 m β^- = 100.00%	228Ra 5.75 y β^- = 100.00%	229Ra 4.0 m β^-

FIGURE 6.1: Section of the nuclide chart of NuDat [245]. Relevant information such as half-life and decay mode with probability for each isotope is given. The decay paths for each isotope can therefore be easily recognized: Blue indicates electron capture or β^+-decay (decay product is one square diagonally down right), red indicates β^--decay (decay product is one square diagonally up left) and yellow indicates α-decay (decay product is two squares diagonally down left). The three decay paths to ^{229}Th can thus be conveniently identified: From ^{233}U α-decay, ^{229}Pa β^+-decay and ^{229}Ac β^--decay.

6.1 Viability of the Excitation of ^{229}Th through ^{233}U decay

The nuclear decay of ^{233}U was first used to estimate the energy of the thorium isomer [1]. By studying the γ spectra of this decay, the excited states of ^{229}Th can be identified. The isomer energy can then be indirectly calculated by subtracting the energies of different excited states [10]. Due to the long 159200 year half-life [249] of ^{233}U the decay rate is low, and large quantities are needed to produce significant amounts of $^{229\mathrm{m}}$Th.

Uranium-233, an artificial isotope, was produced in large quantities (about 2 tons) as part of the United States military and civilian nuclear program (of which 96 kg is unaccounted for). Probably this was lost in Uranium composite weapons testing[1]. ^{233}U can be produced by neutron or accelerator irradiation of ^{232}Th [165].

Through the radioactive decay of ^{233}U 2 % of the decayed nuclei end up populating the isomeric state of ^{229}Th [8]. In [45] we proposed using ^{233}U:CaF$_2$ to create $^{229\mathrm{m}}$Th in

---

[1] Private communication

CaF_2 and detect isomer photon emission using a spectrometer/detector setup. Using this method to create ^{229m}Th in CaF_2 has the advantage that ^{233}U is readily available, excitation rates are high and it is verified that ^{233}U decay produces ^{229m}Th. We call this the uranium experiment.

The most important challenge in this experiment is that the internal conversion decay channel has to be blocked in order to ensure isomer photon emission. When the ^{233}U decays it emits an α particle, with a Q value of 4.908 MeV [249]. This decay will have two effects: The α will cause damage and possibly create a locally amorphous crystal that will increase internal conversion. The recoil on the daughter ^{229}Th nucleus will displace it in the lattice, leaving it in an uncontrolled charge state, possibly allowing internal conversion in the process. The second effect is unknown and needs to be characterized in experiments if a photon signal can be measured. The first effect is estimated to be small, and can be elaborated on:

The α particle will have 4.824 MeV of kinetic energy and the daughter ^{229}Th will have 84.3 keV of kinetic energy if the momentum is distributed equally between the two. From figure 2.18 some indication is found on how CaF_2 responds to an extremely fast light ion (α particle) and a fast heavy ion (daughter nucleus). The α particle can maximally impart 57 % of its energy per collision (see section 2.4.1), so after 8 collisions, it has too little energy left to cause a displacement of a lattice ion. The α particle will mainly deposit its energy up to 10 μm [250] away from the decay site and cause damage.

The Th daughter will most likely deposit all its energy in the first collision, as it is much heavier than the surrounding ions, creating many defects in a localized region. It is unknown if this will move the Th into a Ca position, which would prohibit internal conversion the most. This is however most likely: impact of a Ca^{2+} moves mostly other Ca and creation of interstitials on the cationic lattice is unlikely [69, 110]. If no interstitials are created it is likely the Th takes up a substitutional position.

Since the recoiled daughter is most likely to be highly ionized, it can be assumed internal conversion does not take place during recoil. The neutralization in this insulator might happen quite slowly. It is known that neutralization of the ion plus decay of the thorium nucleus on a metal takes $\approx \mu$s. In an insulator with no electrons freely moving this will be most likely longer, much more than the recoil travel time ($\approx$ns). It is known from other fluorites that fast heavy ion damage creates a local anion (fluoride) deficiency [215]. The lack of fluorides might change the charge compensation of Th and promote internal conversion. More research is needed to investigate internal conversion probability during and after recoil.

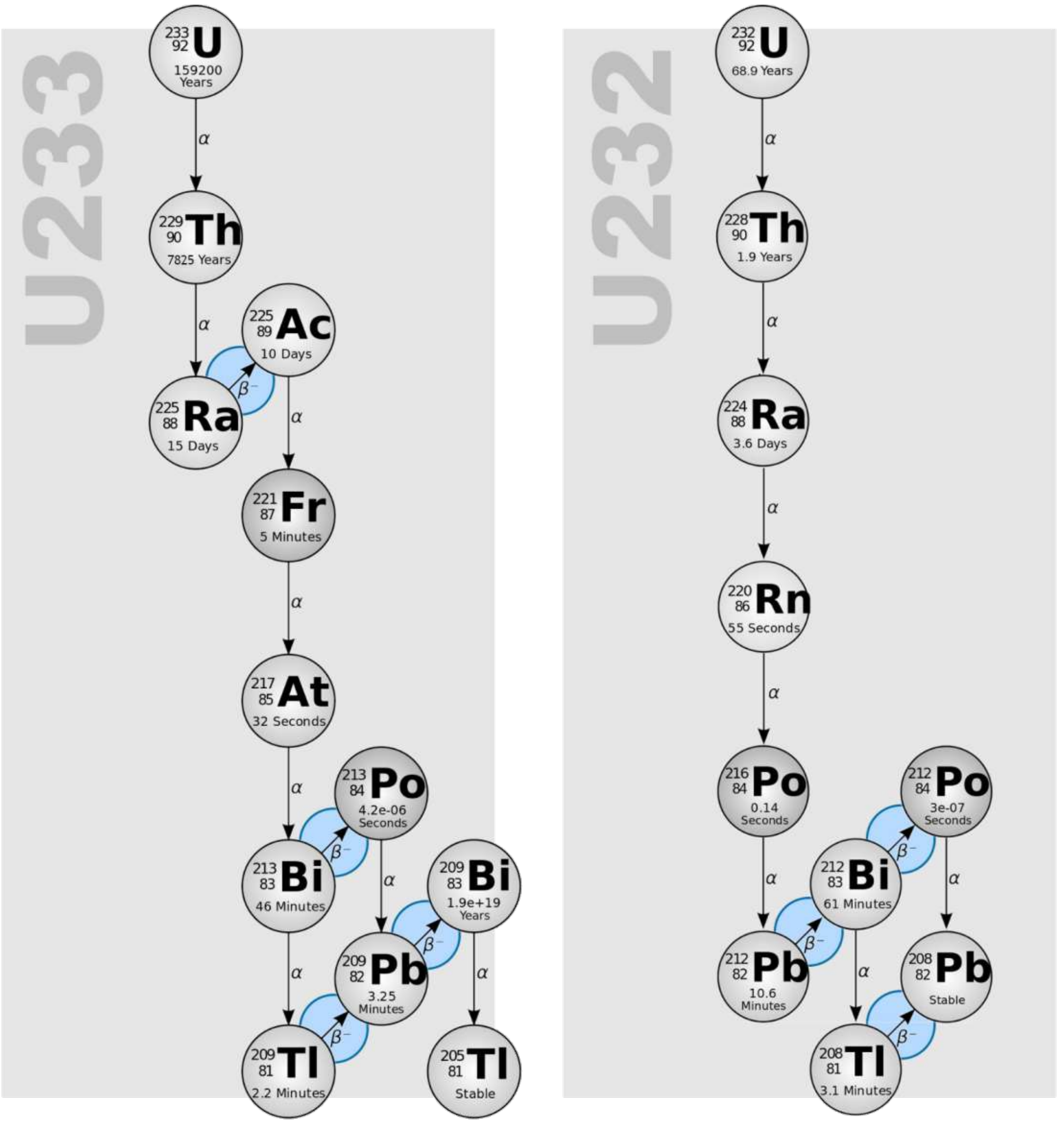

FIGURE 6.2: Decay chain of uranium-233 and uranium-232, both present in uranium compounds. ^{232}U is an unavoidable byproduct of the production of ^{233}U.

One can calculate the expected signal, background, and noise rate to estimate how viable the uranium experiment will be to detect photon emission from the isomer. In these calculations we use the experimental characteristics of the long integration setup from section 4.3 and we assume no internal conversion. The signal strength goes up with the activity of ^{233}U. The main background is Cherenkov radiation at 150 nm, produced by β^{-}-decays in the decay chain as is highlighted in figure 6.2, and STE light emission around 300 nm mainly produced by α-decays in the chain. Per α-decay almost 10^5 photons are created (see section 2.4.3), which are mostly filtered out by the grating and choice of solar blind PMT (see figure 4.3) in the long integration setup. We will now estimate the produced background Cherenkov photons.

6.1.1 Cherenkov Emission and Isomer Photon Emission Calculation

Not only does the Cherenkov emission produced by ^{233}U decay need to be taken into account. In almost any sample of ^{233}U there is a contamination of ^{232}U since it is a byproduct of its production in a (n,2n) reaction [165]. As can be seen in figure 2.20 even at a contamination level of 10 ppm the ^{232}U produces ten times more Cherenkov emission than the ^{233}U, drastically increasing background. Aside from this it emits higher energy α radiation, producing more STE emission and has a dangerous 2.6 MeV γ-ray in its decay chain. This contamination thus disturbs any experiment heavily.

To evaluate the viability of the experiment we calculate the total amount of photons emitted by the ^{229}Th nuclei per second, the nuclear photon emission flux. The flux can be easily calculated: $R_U = 2\,\%$ of all ^{233}U decays produce an isomeric thorium. Thus a crystal with volume V_c containing a concentration n_U of ^{233}U will produce a flux per steradian $\frac{\Phi_\gamma}{\Omega}$

$$\frac{\Phi_\gamma}{\Omega} = \frac{1}{4\pi}\lambda_{233}N_{233}R = \frac{0.02}{4\pi}\frac{\log(2)}{159200\text{ yrs}}V_c n_U \approx 2.2\cdot 10^{-16}\cdot V_c n_U \text{ sr}^{-1}\text{Hz} \tag{6.1}$$

where λ_{233} is the decay constant for ^{233}U and N_{233} the number of ^{233}U atoms assuming no internal conversion happens. One can quickly see that many nuclei are needed to produce any significant signal. From the binary phase diagram of UF$_4$ - CaF$_2$ we can see that UF$_4$ concentration density goes up to 42 wt % (weight ratio percentage) without changing the CaF$_2$ crystal structure or approximately 10^{21} U nuclei cm^{-3} [251]. If and how much this affects absorption is not known, in [45] it was found that the absorption was independent of doping at least up until $5\cdot10^{19}$ cm^{-3}.

By using the Frank-Tamm equations from section 2.4.3 for every β^--decay in the ^{233}U decay chain one can calculate the produced amount of Cherenkov photons, $\frac{dN_{ph}}{d\lambda}$. We calculate only those produced around 150 nm, where we expect the isomer energy to be. As one can see from equation 2.15, the intensity is proportional to $\frac{1}{\lambda}$ thus we expect higher intensities towards shorter wavelengths (or higher energies). In table 6.1 the Cherenkov photon fluxes have been calculated for all daughters of ^{233}U and ^{232}U. We assume in our estimations that Compton scattering and conversion electron processes have a minor effect as shown in [45].

The total Cherenkov photons are determined by the thorium decay because it takes very long (6 years for 232, and 24000 years for 233) for the U-Th system to be in equilibrium. So depending on the ingrowth time after chemical separation of uranium from its daughters, the amount of Cherenkov radiation will increase. The background will thus behave as

Cherenkov intensities			
β^--decay	Q_{β^-} (keV)	Occurence (%)	$\frac{dN_{ph}}{d\lambda}$ at 150 nm in 1 nm window per 100 Th decays
^{233}U decays			
^{225}Ra→^{225}Ac	356.0	31.2	0.03
^{225}Ra→^{225}Ac	316.0	68.80	0.03
^{213}Bi→^{213}Po	1423.0	64.80	39.7
^{213}Bi→^{213}Po	983.0	30.20	8.37
^{209}Pb→^{209}Bi	644.0	100.00	9.04
^{209}Tl→^{209}Pb	1827.0	2.04	2.11
^{232}U decays			
^{212}Bi→^{212}Po	2252.1	55.30	78.07
^{212}Bi→^{212}Po	1524.8	4.50	5.70
^{212}Bi→^{212}Po	739.4	1.44	0.19
^{212}Bi→^{212}Po	631.4	1.90	0.16
^{212}Bi→^{212}Po	569.9	13.30	0.73
^{212}Bi→^{212}Po	331.3	81.70	0.49
^{208}Tl→^{208}Pb	1801.3	17.70	17.05
^{208}Tl→^{208}Pb	1523.9	7.96	3.15
^{208}Tl→^{208}Pb	1290.5	8.71	4.43
^{208}Tl→^{208}Pb	1038.0	1.14	0.36

TABLE 6.1: Total cherenkov photons, $\frac{dN_{ph}}{d\lambda}$, produced per 100 ^{228}Th or ^{229}Th decay in a 1 nm window for all β^--decays in the $^{232/233}$U decay chains

$$\frac{\Phi_{cher}}{\Omega} = (0.59\cdot\lambda_{229} + 1.1\cdot\lambda_{228}\frac{\lambda_{232}}{\lambda_{233}}C_{232})\frac{\lambda_{233}V_c n_u}{4\pi}t \approx 3.22\cdot 10^{-24}V_c n_u t \ \mathrm{sr}^{-1}\mathrm{Hz} \qquad (6.2)$$

where t is the total time after last chemical separation of uranium from its daughters in seconds and C_{232} the ratio of ^{232}U to ^{233}U atoms. For the following approximation the ratio C_{232} was assumed to be 10 ppm [165]. The total signal-to-background ratio around 150 nm now becomes

$$\frac{\Phi_\gamma}{\Phi_{cher}} = \frac{R}{(0.59\cdot\lambda_{229} + 1.1\cdot\lambda_{228}\frac{\lambda_{232}}{\lambda_{233}}C_{232})t} \approx \frac{0.7}{t}\cdot 10^8. \qquad (6.3)$$

So after a day this ratio is 800, after a month 27, after a year 2.3 and after 5 years 0.5. This means that any of these experiments are done ideally within a year after chemical separation and crystal growth. Important to note here is that the Cherenkov background is broad and the nuclear photon emission is narrow. The amount of photons per wavelength of Cherenkov radiation decreases when a smaller wavelength bin size is taken, for the nuclear photon emission it stays constant. By increasing the resolution in a detection setup this can be exploited: By increasing the resolution the ratio of signal to Cherenkov background will increase.

Now the nuclear photon emission flux and background ratio have been calculated. By looking at experimental characterization done in chapter 4, a realistic estimate can be made for the viability of this experiment.

The main unknown in these calculations is internal conversion after the violent radioactive decay. The recoil on the ^{229}Th nucleus in the crystal can possibly open up avenues for internal conversion during motion. Alternatively, the position where the nucleus ends up can be not substitutional or not charge-compensated which could lead to internal conversion being the dominant decay path. We assume no internal conversion for these calculations.

Due to the low transmission at 150 nm for the ^{233}U crystal (figure 4.56) the viability of the experiment becomes low. From above calculations and the system efficiency from section 4.3 we can calculate an expected isomer photon flux rate to be 0.1 cps at 150 nm using a 1 mm slit assuming 10 % crystal transmission (^{233}U doped crystal). As can be seen from the Cherenkov radiation measurements (figure 6.17) signal rates of 0.25 Hz can be barely measured in the long integration setup (section 4.3).

Considering the expected signal rate of 0.1 cps, measuring nuclear photon emission is not expected. Cherenkov radiation should be 10 times stronger than isomer photon flux but was not measured. The ^{232}U doped crystal however is five times more transparent, which would mean 5 cps of Cherenkov photons which should be detectable.

This signal was detected, and presented in figure 4.60. The weak VUV signal in the ^{232}U:CaF$_2$, a factor of 0.06 weaker than expected, meant that probably no VUV Cherenkov radiation (≈0.06 cps) or isomer signal (≈0.006 cps) could be observable in the ^{233}U doped crystal. The Cherenkov light is produced regardless of internal conversion and should have ten times the signal strength as compared to the nuclear photon signal in these crystals (section 6.1).

Improving the crystal transmission and improving the doping concentration can make the experiment viable. The transmission however could be reduced by increasing doping concentration, this is part of active research. In [45] is is stated that doping concentrations at least up until $5{\cdot}10^{19}$ cm^{-3} do not affect VUV transmission. Other possibilities to reduce absorption in this region is to change the oxidation state of uranium. It is known that the oxidation state can be changed by changing the parameters during crystal growth [252] but verifying which oxidation state the uranium has (2+, 3+, 4+, 6+[79, 253], 5+[254]) and to which to change it is ongoing research.

Increasing the doping concentration by a factor of 10 (to 10^{20} cm^{-3}, and increasing transmission by a factor of 5 would create a signal of ≈0.3 cps which would be measurable with the current setup. The best approach seems to be improving the setup, such as the one suggested in section 5.7, which would increase the detection efficiency by two orders of magnitude. Increasing the concentration might be detrimental to the transparency. Although hard, the excitation of ^{229}Th through ^{233}U decay in CaF$_2$ seems to be feasible after improvements.

6.2 Viability of the Excitation of ^{229}Th through Activation of ^{228}Ra

From the nuclide chart (figure 6.1) we identified the possibility to produce isomeric thorium through actinium-229. The half-life of ^{229}Ac is 62.7 min [249] and decay via β^--decay with a Q value of 1.104 MeV. Due to its short half-life, this isotope needs to be produced and immediately used. To produce and use ^{229}Ac to populate the isomeric state has been attempted often [46, 255–261]. Production methods in these publications are ^{232}Th(γ,p2n)^{229}Ac reaction, ^{232}Th(p,α)^{229}Ac and ^{238}U spallation.

Actinium-229 beta decays into the isomer with an predicted efficiency between 14 % and 93 % [46]. This is much larger as compared to the ^{233}U decay. In combination with its much shorter half-life the production rate of isomeric thorium would be much higher, if an adequate amount of ^{229}Ac can be produced.

The approach of [46] is to produce ^{229}Ac online at the CERN ISOLDE facility and then implant the ^{229}Ac in pure CaF$_2$. This approach also uses the large bandgap of CaF$_2$ to prohibit internal conversion. The ^{229}Ac should decay to the isomer, and produce a photon emission signal.

The momentum kick from the β^--decay of ^{229}Ac is not expected to move the nucleus in the lattice, as opposed to excitation through ^{233}U decay, and the local electronic surrounding should thus not change. This is likely to prohibit internal conversion more effectively, making photon decay more probable and detectable [262]. The downsides of this experiment is the violent implantation of the nuclei, but has the benefit of a high production of ^{229}Ac through the ISOLDE facility (10^{10} nuclei/s implanted).

We follow the idea of doping ^{229}Ac into CaF$_2$, instead with a different production method of ^{229}Ac which is illustrated in figure 6.3. We call this the activation experiment. Through the neutron capture by ^{228}Ra and subsequent β^--decay of ^{229}Ra, ^{229}Ac is produced. The decay chain is then:

$$^{228}\mathrm{Ra} \xrightarrow{(n,\gamma)} {}^{229}\mathrm{Ra} \xrightarrow{\beta^-} {}^{229}\mathrm{Ac} \xrightarrow{\beta^-} {}^{229m}\mathrm{Th} \xrightarrow{\gamma} {}^{229}\mathrm{Th}. \tag{6.4}$$

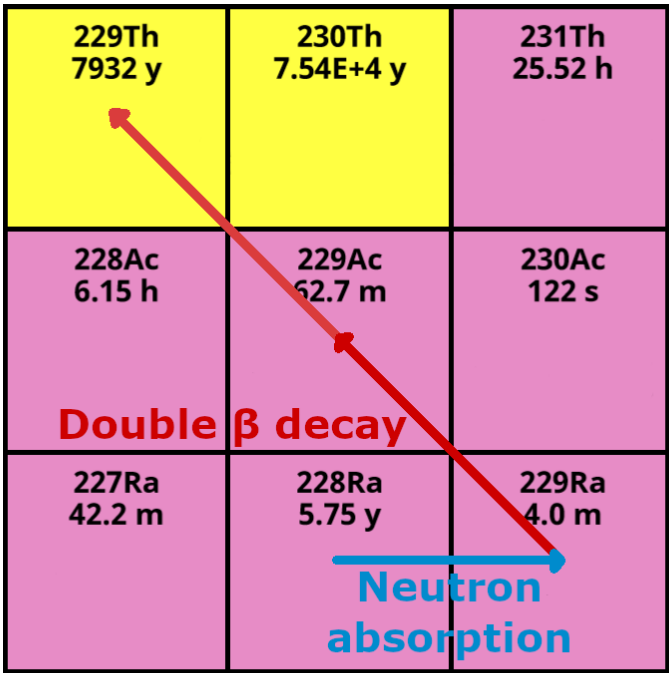

FIGURE 6.3: Production chain of $^{229\mathrm{m}}$Th through neutron capture of ^{228}Ra.

Benefits of this method is it uses only neutron activation, available to us through the TRIGA MARK II nuclear reaction (section 6.3) and the long half-life (5.75 years [263]) of ^{228}Ra allowing doping into crystals. After neutron activation the ^{229}Ra lives shortly (4 minutes [249]), producing many β^--decays (Q value 1.872 MeV) which contribute to background. After that, for several hours isomeric ^{229}Th is produced due to the 62.7 min half-life of ^{229}Ac. In this time the crystal could be transported from reactor to VUV spectrometer to see if photon emission from the nucleus can be measured.

We thus propose to grow ^{228}Ra:CaF$_2$ crystals, irradiate them in the neutron beam of the TRIGA MARK II nuclear reactor in Vienna and immediately measure these crystals in a spectrometer for isomer photons. The upside of this experiment is that the ^{228}Ra atoms will have a controlled crystal environment, as opposed to the implantation method, thus reducing possible internal conversion. The double β^--decay will ensure less distortion of the surrounding lattice as well, as opposed to ^{233}U α-decay.

The downside is that the crystals will be highly active due to the inherent radioactivity of ^{228}Ra. In order to produce a sufficient number of isomeric ^{229}Th the amount of ^{228}Ra needs to be high because the neutron absorption process is inefficient. Sufficient amounts of ^{228}Ra can be extracted from even larger amounts of old ^{232}Th. One kilogram of five year old ^{232}Th would have 500 kBq of ^{228}Ra. In practice, [12] managed to extract 1.5 MBq ^{228}Ra per kg ^{232}Th, which means it must have been older than 5 years. The radioactivity of the large amount of ^{228}Ra will produce a large gamma and Cherenkov photon background and damage the crystal (see section 2.4.2). Another downside is unwanted neutron activation of other species in the crystals, increasing the photon background and damage.

6.2.1 Cherenkov Emission and Isomer Photon Emission Calculation

To calculate the signal flux, we need to consider the total transmutation dynamics of the following nuclear reaction:

$$^{228}\mathrm{Ra} \xrightarrow{(n,\gamma)} {}^{229}\mathrm{Ra} \xrightarrow{\beta^-} {}^{229}\mathrm{Ac} \xrightarrow{\beta^-} {}^{229m}\mathrm{Th} \xrightarrow{\gamma} {}^{229}\mathrm{Th}. \tag{6.5}$$

For the calculations we will only consider activation through thermal neutrons since this is the dominant neutron flux in our reactor [264] and the process with the largest total cross section [12]. To calculate the time dependent activities $\frac{dN}{dt}$ of all species we need to consider 3 processes: Activation rate ($\Phi_{th}\sigma_{th}$), decay rate to daughter ($-\lambda N$) and production rate from mother ($+\lambda N$). For the three relevant processes then follows

$$A_{^{229}\mathrm{Ra}} = \Phi_{th}\sigma_{th}N_{^{228}\mathrm{Ra}} - \lambda_{^{229}\mathrm{Ra}}N_{^{229}\mathrm{Ra}} \tag{6.6}$$

$$A_{^{229}\mathrm{Ac}} = \lambda_{^{229}\mathrm{Ra}}N_{^{229}\mathrm{Ra}} - \lambda_{^{229}\mathrm{Ac}}N_{^{229}\mathrm{Ac}} \tag{6.7}$$

$$A_{^{229m}\mathrm{Th}} = R \cdot \lambda_{^{229}\mathrm{Ac}}N_{^{229}\mathrm{Ac}} - \Gamma_{^{229m}\mathrm{Th}}N_{^{229m}\mathrm{Th}}. \tag{6.8}$$

Here R_{Ac} is the amount of Ac decays that end up in the isomer state which is between 14 % and 93 % [46] and $\Gamma_{^{229m}\mathrm{Th}}$ the unknown ^{229}Th decay rate. The activity of the ^{229m}Th is now directly our photon flux, assuming no internal conversion. To calculate the abundances we assume to have 250 kBq of ^{228}Ra doped into CaF$_2$, which corresponds to a concentration of roughly 10^{15} cm^{-3} for a cylindrical crystal of 3.2 mm diameter and 1 cm length, as is explained in section 3.2. We consider 250 kBq of activity because we have handled these activities while growing ^{229}Th:CaF$_2$ crystals before, and above it was found that this amount is reasonably available. Crystals grown with this amount of ^{229}Th activity have shown up to 10 % transmission (crystal C13).

The TRIGA MARK II reactor in Vienna runs for 8 hours a day, producing a thermal neutron flux of approximately 10^{13} cm^{-2}s^{-1}. Our experimental cycle is characterized by activation, transport and detection. Since the lifetime of the isomer is not known, the best strategy is to maximize ^{229}Ac production. Even if the isomer lifetime is short, the isomer will be actively produced by ^{229}Ac decay during the measurement. If we assume the ^{229}Ra abundance to quickly reach saturation we can calculate the optimal

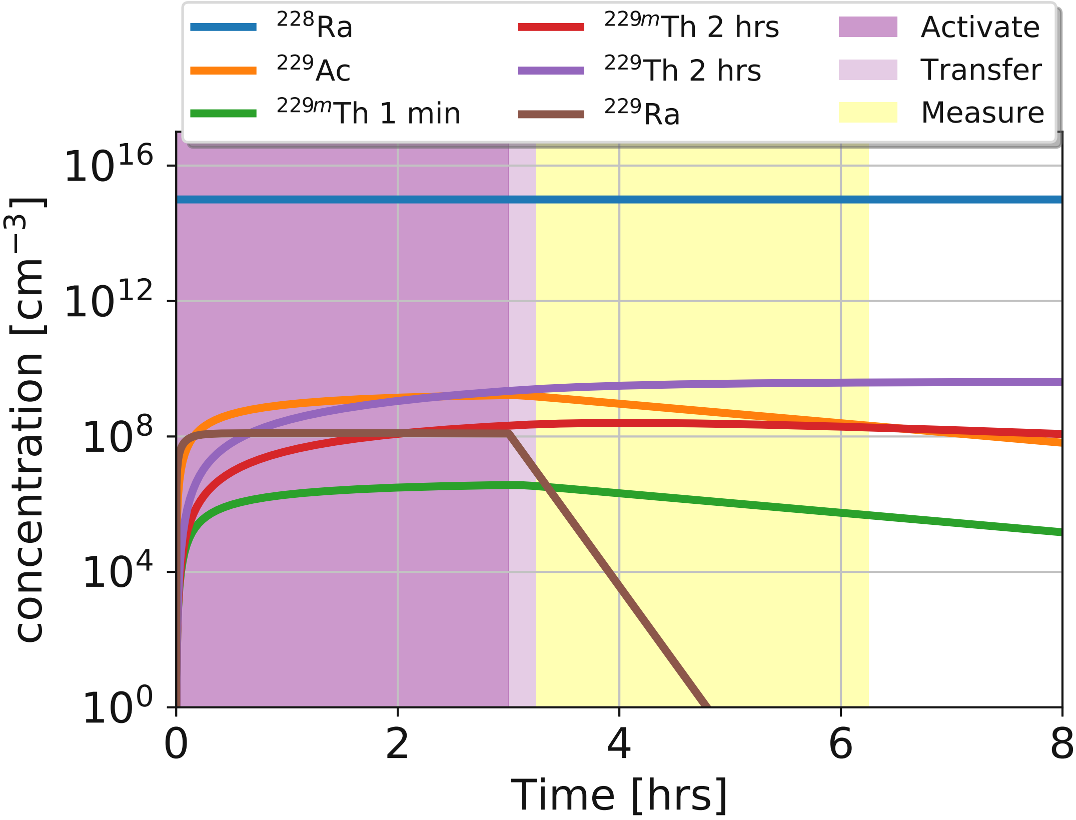

FIGURE 6.4: Concentration in the CaF$_2$ crystal over time during our experimental cycle. The three stages of the experiment are shown by the shaded areas: activation, transfer and measurement. The concentration of ^{228}Ra is barely affected by the activation process. The abundance curves are shown for 2 lifetimes of ^{229m}Th, 1 minute and 2 hours. It is conservatively assumed in this curve that 14 % of ^{229}Ac decays into the isomer. A different percentage would not change the time behavior of the curve, just the magnitude.

irradiation time. To reach 90 % of saturation activity of ^{229}Ac, which has a half-life of 62.7 minutes [249], the ^{228}Ra needs to be irradiated for 3.3 half-lifes of ^{229}Ac. We assume a transfer time of 15 minutes, in practice we have been able to move samples from reactor to measurement start in 10 minutes. Using these conditions, we can calculate the concentrations of all involved isotopes as seen in figure 6.4. Calculated β^--decay rate and isomer decay rate from ^{228}Ra abundance can be seen in figure 6.5.

We can see in figure 6.5 that the β^--decay rates are at most 100 times more than the isomer rates. However the maximum β^--decay energy of ^{228}Ra, 45.5 keV, is below the threshold of 158 keV for Cherenkov radiation in CaF$_2$. The daughter, ^{228}Ac, has a β^- that exceeds the energy threshold for Cherenkov radiation. For the dominant daughter, we can estimate our signal-to-background ratio. By using that (in a 1 nm bin) each β^--decay produces 0.1 photon at 150 nm (R_β) [45] and that the decay rate of ^{228}Ac is almost constant over our integration time of 10000 seconds we find for a cylindrical crystal of 1 cm length and 3.2 mm diameter that the

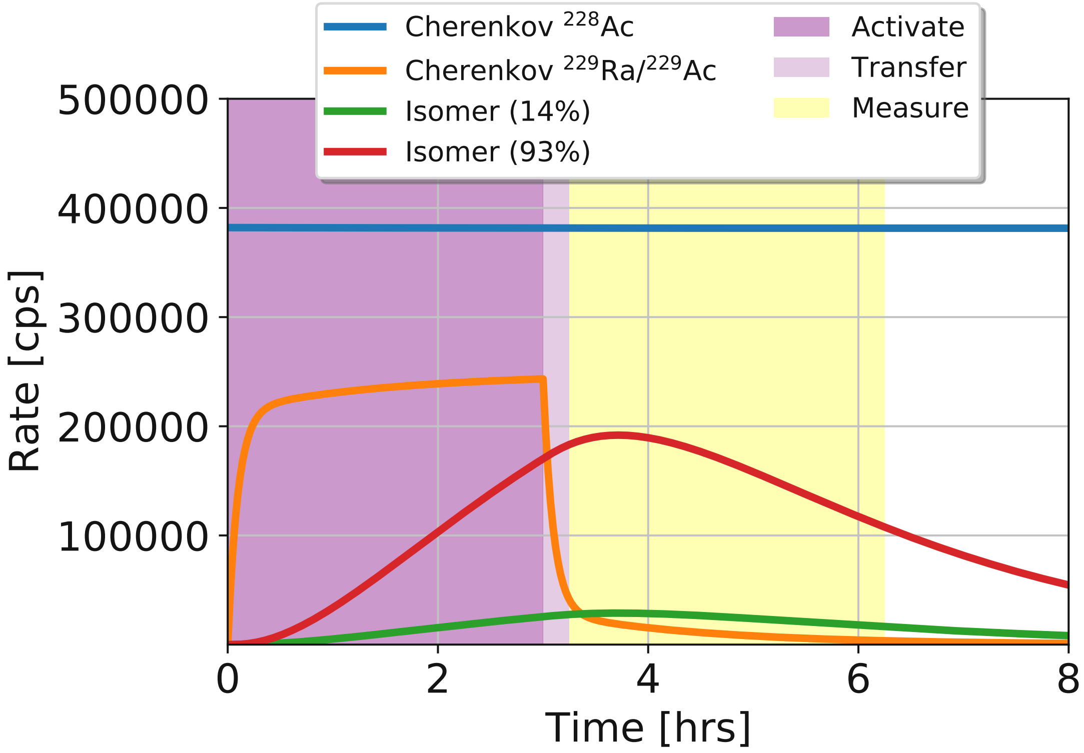

FIGURE 6.5: Photon rates of Cherenkov photons produced at 150 nm in a 1 nm bin by β^--decay and isomer photons. Here the isomer lifetime was set to 2 hours. A crystal volume of 1 cm^3 is assumed. The β^--decays will produce a Cherenkov background signal at the same wavelength as the isomer photon. We can see that the dominant Cherenkov signal is produced from ^{228}Ac. We can see also that in the both cases, isomer photons will dominate over the activation produced Cherenkov photons.

$$\mathrm{SNR} = \frac{\Phi_{isomer}}{\sqrt{\Phi_{isomer} + R_\beta \Phi_\beta}} * \sqrt{t} \approx 500. \tag{6.9}$$

Although the ^{228}Ac background dominates during the measurement, the amount of noise it produces scales only with the square root of this signal. By integrating for 3 hours, this background can be mitigated and a high signal-to-background ratio can be obtained for the isomer photon emission signal.

The SNR of 500 is a first indication that this experiment is promising, but other sources of background and detection efficiency need to be evaluated. Now we will present the simple detection system and its efficiency, measurements of the radioactive VUV background and crystal transmission reduction. Using these experimental characterizations we can evaluate the true viability of the proposed experiment.

6.3 Neutron Irradiation of CaF_2 with the TRIGA Mark-II Research Reactor

In Vienna at the Atominstitut of the TU Wien there is a TRIGA Mark-II research reactor built by General Atomic in the 1960s. The reactor is equipped with UZrH fuel elements to produce through fission chain reaction a maximum of 250 kW of power with a thermal neutron flux in the center (Zentrales Bestrahlungsrohr, ZBR) of 10^{13} neutrons/cm^2/s [265]. A schematic representation of the reactor can be seen in figures 6.6 and 6.7.

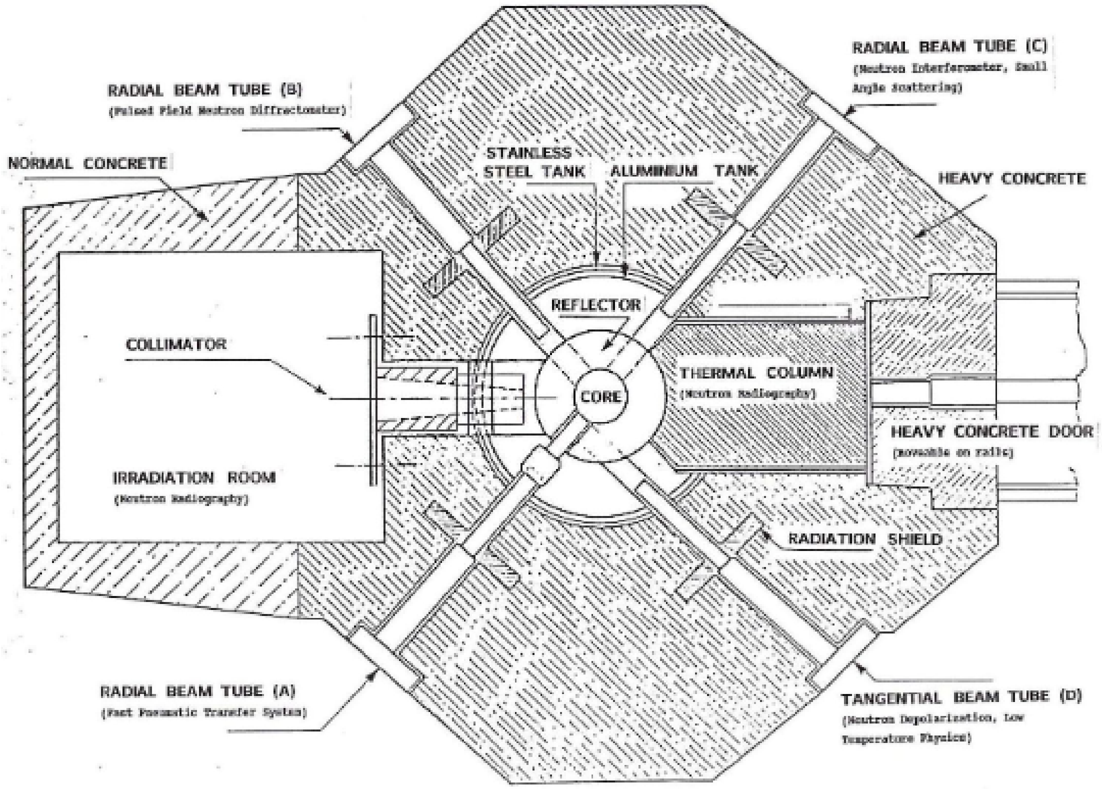

Figure 6.6: Top view of the TRIGA Mark-II research reactor, taken from [265].

By lowering a crystal into the ZBR with a string (see figure 6.8) it can be irradiated with neutrons. The nuclei in the crystal can absorb the neutrons and become activated. The neutron energy spectrum of the reactor contains in increasing energy order: thermal, epithermal, and fast neutrons. The thermal neutrons in general produce (n,γ) reactions where a single neutron is absorbed. Epithermal neutrons are more likely to produce other nuclear reactions, such as an (n,2n) reaction where one neutron is removed from the nucleus or an (n,p) reaction where a proton is replace by a neutron.

After a nuclear reaction the nucleus is often left excited or unstable and will possibly decay, emitting high energy γ photons. When measured on a γ spectrometer, the isotopes in the crystal can be identified by their characteristic γ emission, a so called neutron

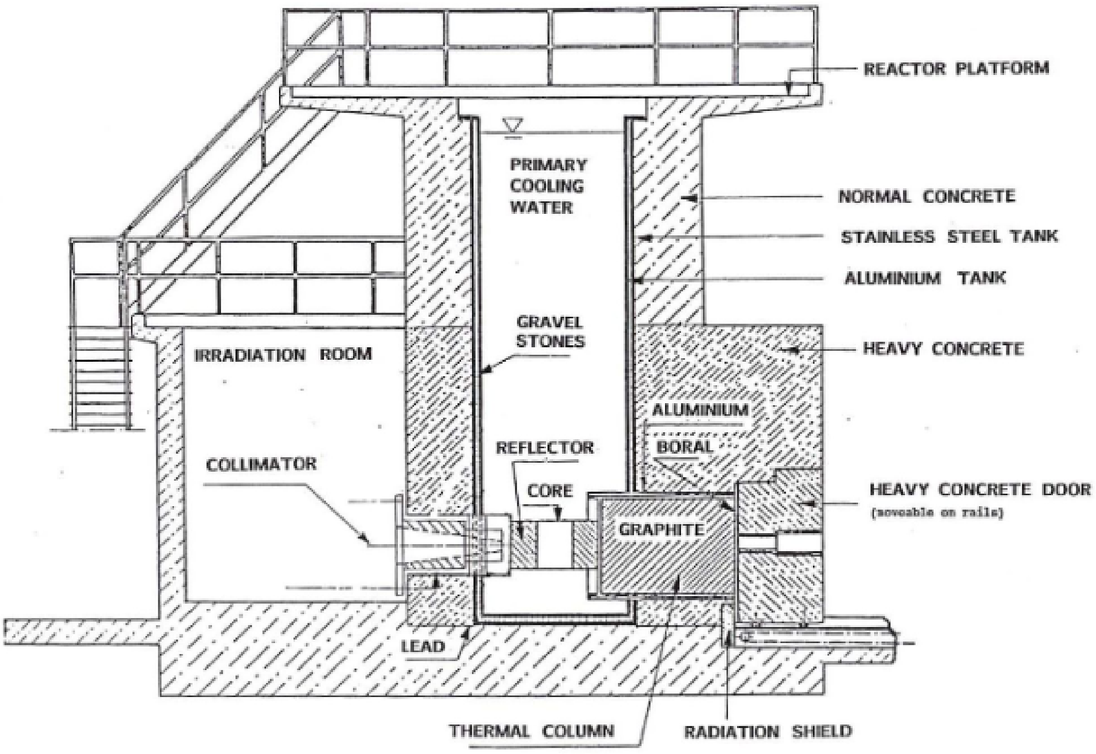

FIGURE 6.7: Side view of the TRIGA Mark-II research reactor, taken from [265].

activation analysis (NAA). The same process can be used to produce isomeric thorium-229 from radium-228 ($^{228}\text{Ra} \xrightarrow{(n,\gamma)} {}^{229}\text{Ra} \xrightarrow{\beta^-} {}^{229}\text{Ac} \xrightarrow{\beta^-} {}^{229\text{m}}\text{Th}$) as described above in section 6.2.

To safely transport the highly radioactive irradiated crystals and make sure measurement in the long integration setup can be quickly started, a special holder was designed. The holder is designed to fit in a KF40 vacuum tube that can quickly be mounted on the system. In this holder the crystal is secured by a set screw such that it only has to be handled in one of the appropriate radiochemistry labs. Using this setup the measurement of an irradiated crystal can start 8 minutes after the crystal is taken out of the neutron beam in the reactor. The holder can be seen in figure 6.9

This reactor was also used to produce ^{32}P for a calibration Cherenkov source and to activate undoped CaF_2 crystals for characterization to assess the viability of $^{228}\text{Ra:CaF}_2$ activation to produce isomeric ^{229}Th.

6.4 Production of a Calibration Cherenkov Source

Before characterizing the Cherenkov radiation emitted by a neutron irradiated crystal directly after irradiation, a dedicated Cherenkov calibration source was produced. The

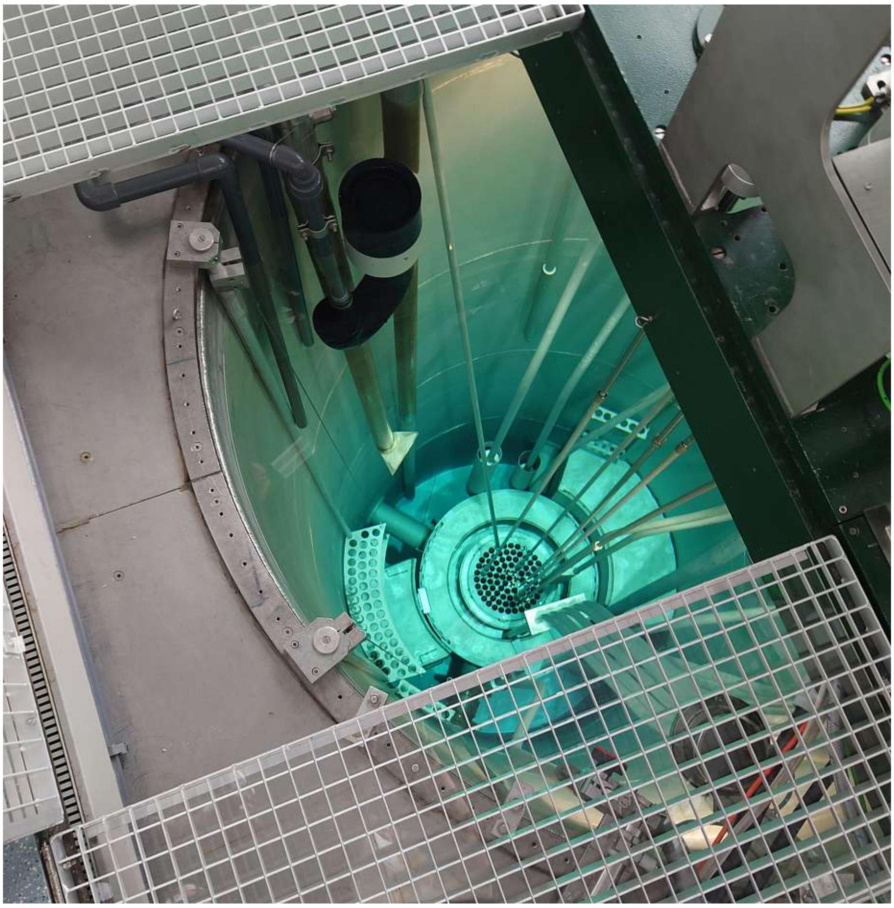

FIGURE 6.8: View on the pool of the reactor. The cylindrical fuel elements can be seen at the bottom of the pool. Some of the tubes are pneumatic transporters for samples. A crystal can be lowered in the center of the fuel elements to experience the highest neutron flux (ZBR).

goal was to characterize the spectrum emitted by a β^--decay in undoped CaF_2 with a longer-lived source as to have the integration time to measure the full spectrum. The choice was ^{32}P as source which decays to a stable element only by emitting β^- radiation, no γ radiation. The half-life of this isotope is 14.268(5) days [266], which gives enough time to record a full VUV Cherenkov spectrum.

To build the Cherenkov source, ^{32}P was produced through an (n,p) reaction of ^{32}S in an epithermal neutron beam. The phosphorus was dried in the 2 mm diameter 4 mm deep drill hole in the 3.2 mm diameter 12 mm height cylindrical CaF_2 seed crystal (figure 3.6) and sealed with torrseal onto a screw and vacuum flange. The high energy β^--decay of ^{32}P would then cause Cherenkov radiation being produced inside the CaF_2. The other side of the crystal was cleaved to produce optimal optical transparency. The end result can be seen in figure 6.10.

In order to produce ^{32}P, the $^{32}\mathrm{S} \xrightarrow{(n,p)} {}^{32}\mathrm{P}$ nuclear reaction was used using epithermal neutrons from the Atominstitut reactor. For the production, 256.66 mg of finely ground

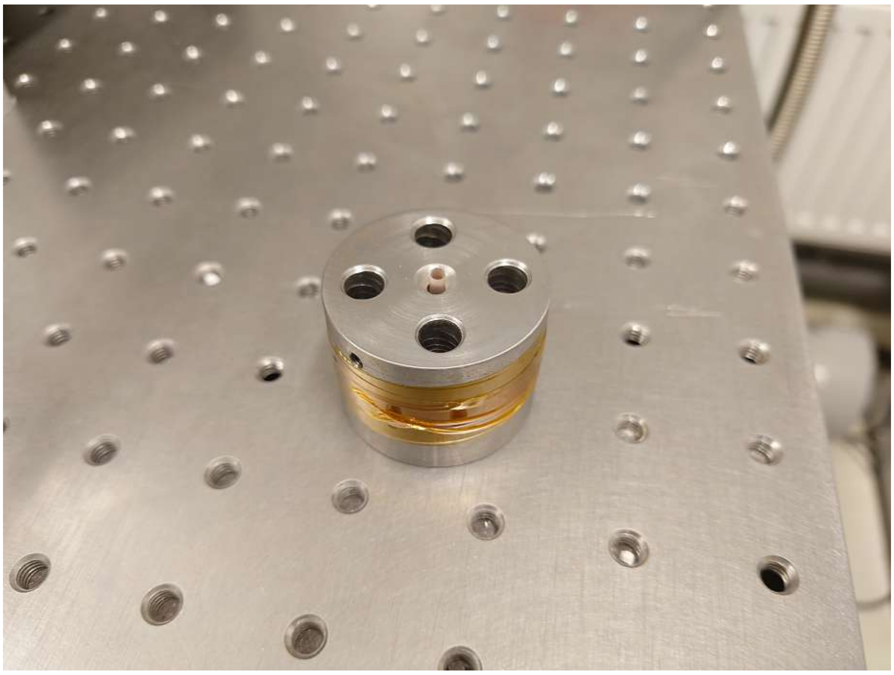

FIGURE 6.9: Neutron irradiated crystal in the holder for the long integration setup.

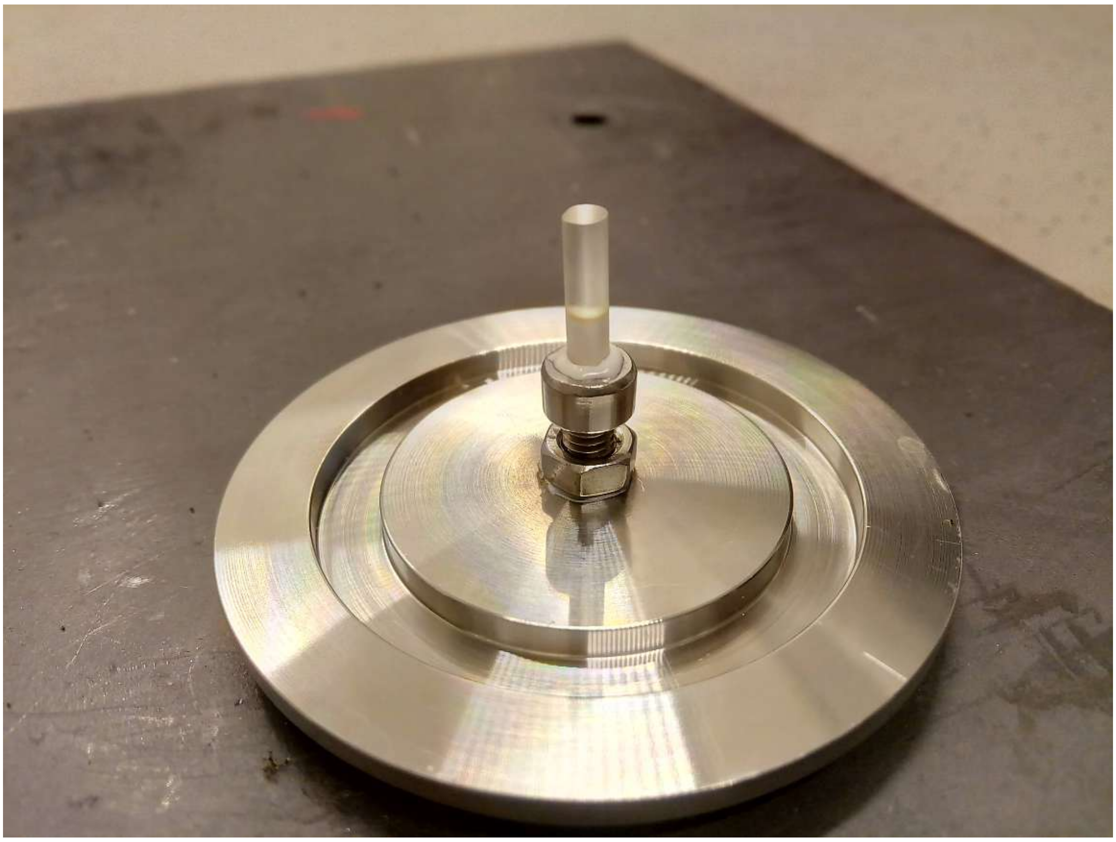

FIGURE 6.10: Vacuum solution for mounting the Cherenkov source. The screw can be removed and easily inserted in any setup. The crystal pocket filled with torrseal is clearly visible, the ^{32}P containing solid is invisible due to its small amount. The top of the crystal is cleaved to provide 70 % optical transmission at 150 nm.

sulfur (Johnson Matthey "Spectrographically Standardised Substance") was transferred into a polyethylene sample tube (Emerald plastics) using a plastic spatula and closed. The capsule was irradiated in dry irradiation position R3 for 8 hours at 250 kW ($1.8{\cdot}10^{12}$ thermal neutrons/cm^2/s; 10^{11} fast neutrons/cm^2/s). After the irradiation the produced phosphorus is expected to form a complex with the sulfur (e.g. P_4S_{10}). The irradiated sulfur was transferred to a 35 mL "Eppendorf" sample vial and 25 mL (21.52557 g) of toluene was added (Merck "zur analyze"). The vial was closed with a magnetic stirrer and was stirred in a 60 °C water bath until all solids had dissolved yielding a clear near colorless (slightly yellow) solution. The solution is allowed to cool to room temperature.

To determine the contents of the solution, liquid scintillation counting (LSC) was used. In this process, a fluorescent dye is added to the solution that fluoresces due to the radioactive decays in the material. Depending on the energy released by the decay a proportional amount of photons will be emitted by the dye. By measuring the amount of photons produced per decay an energy spectrum of the solution can be recorded. A 50 μL aliquot of the toluene solution is taken in an LSC vial and 10 mL PE UltimaGold scintillation cocktail is added to measure the fluorescence of the sulfur contamination. The fluorescence can be seen in figure 6.11. Here it can be seen that mostly ^{35}S (Q_β = 167 keV) is present in this phase because of the lower energy β^--decay, some of the higher energy ^{32}P β^--decay (Q_β = 1710 keV) can be seen. The ^{35}S isotope is produced much more than the ^{32}P and thus needs to be chemically separated.

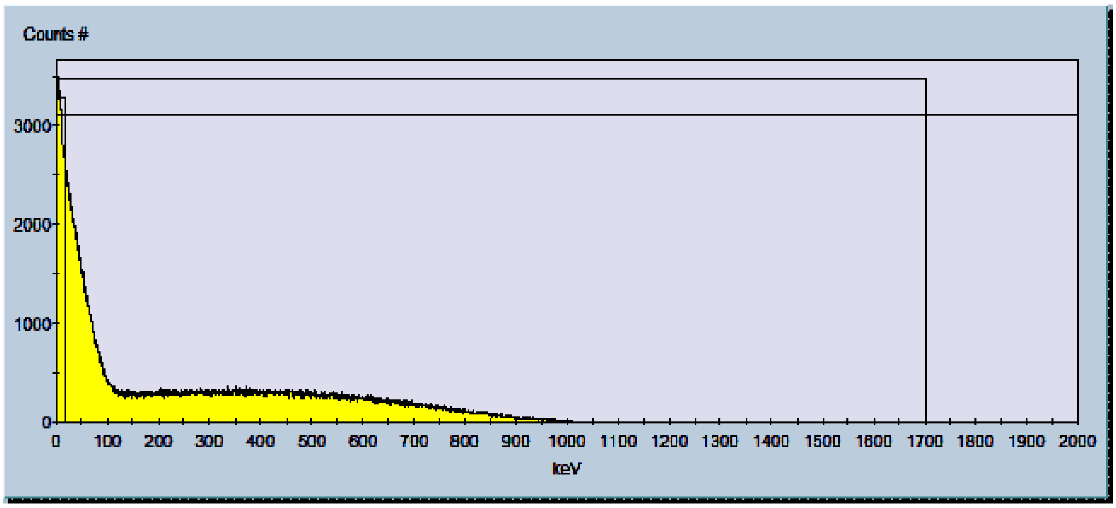

FIGURE 6.11: Fluorescence spectrum of the aliquot of the toluene solution before chemical separation. The PE UltimaGold scintillation cocktail emits photons proportional to the energy of the β^--decay. Due to this we can see the low energy β^- spectrum of ^{35}S as well as small amounts of the high energy ^{32}P spectrum.

To chemically separate the ^{35}S, HCl (1.0 M, 500 μL, 0.45335 g) dissolved in water is added and the vial is again heated to 60 °C and stirred for 60 minutes at 300 rpm. The HCl will react with the P_3S_8 and water to oxidize the phosphorus to different phosphates and phosphides (PO_4^{3-}, PO_3^{2-}, PH_3, HPO_2^{1-}, $H_2PO_4^-$, H_3PO_4) which will dissolve in the water. After letting the vial settle and cool for 20 minutes the aqueous layer of the HCl solution sits on the top. With a syringe the layer is collected (less than 5 mL) and transferred to a new vial (35 mL Eppendorf). Care was taken not to take any of the toluene solution and thus some of the layer remained in the vial.

The ^{32}P solution was measured on a medical activity meter and registered 391 kBq. An aliquot was taken of this solution (50 μL) and 10 mL PE UltimaGold scintillation cocktail is added to measure the fluorescence, the result can be seen in figure 6.12. No fluorescence peak correlated to the low energy β^--decay can be seen indicating a successful separation of sulfur and phosphorus. Another aliquot was taken of the remaining toluene solution (50 μL) and 10 mL PE UltimaGold scintillation cocktail is added to measure the fluorescence, the result can be seen in figure 6.13. Here it can be seen that approximately all the sulfur from before the separation is in the remaining toluene solution. The next step is to dry the ^{32}P solution in a crystal.

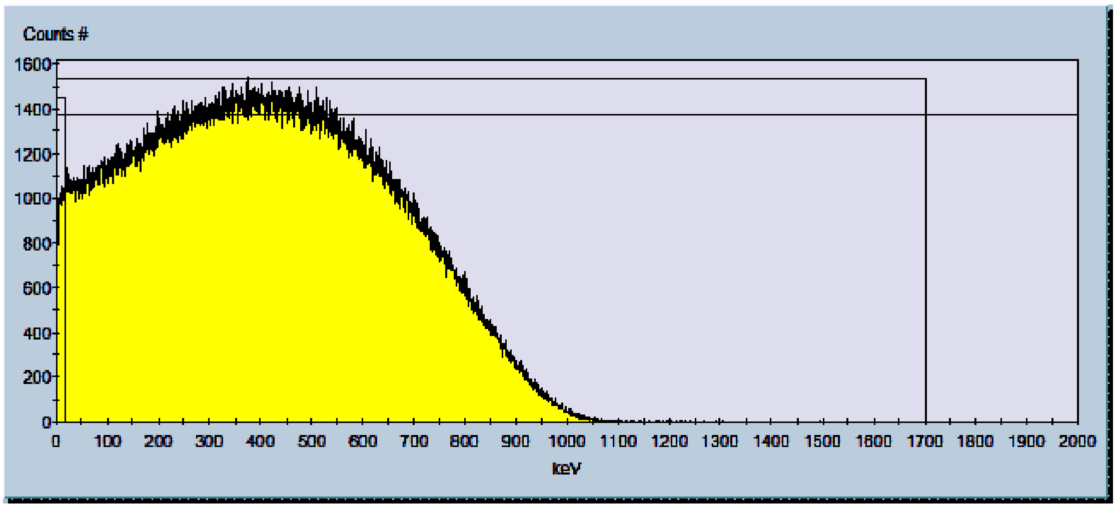

FIGURE 6.12: Fluorescence spectrum of the aliquot of the water ^{32}P solution. The PE UltimaGold scintillation cocktail emits photons proportional to the energy of the β^--decay. As opposed to the other spectra in figures 6.11 and 6.13 we do not significantly detect ^{35}S. This proves that the separation was successful.

To dry the ^{32}P, the crystal was put into a metal piece with the pocket upwards onto a hot plate set to 80 °C. With a pipette the ^{32}P solution is carefully dripped into the drill hole. After the water has boiled away the process is repeated. After many repetitions approximately 90 % the ^{32}P is transferred to the crystal. The rest of the drill hole is filled with torrseal and a screw is attached to the end.

These crystals were produced several times to record its emission as discussed in section 6.5.2.

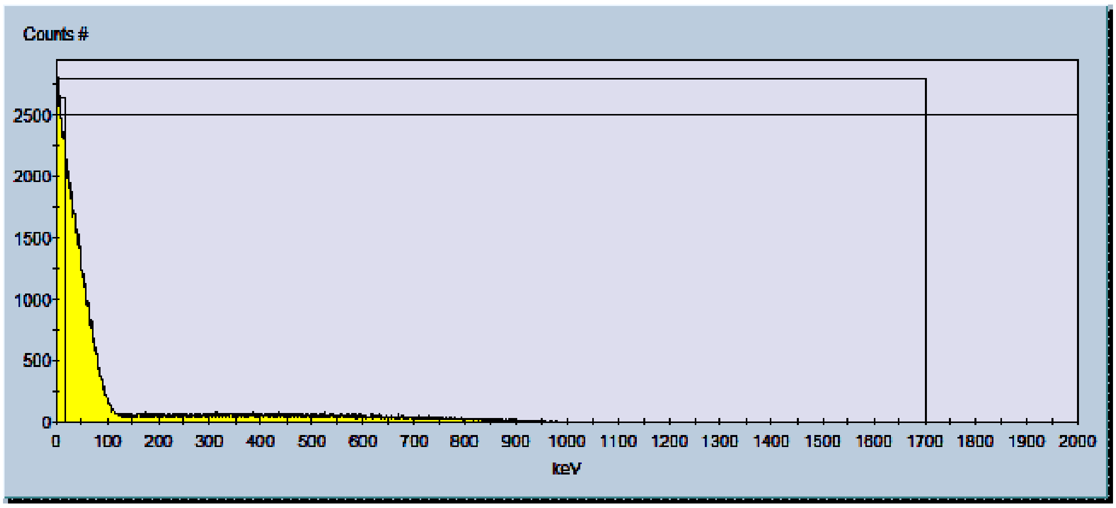

FIGURE 6.13: Fluorescence spectrum of the aliquot of the toluene solution after chemical separation. The PE UltimaGold scintillation cocktail emits photons proportional to the energy of the β^--decay. Due to this we can see the low energy β^- spectrum of ^{35}S as well as small amounts of the high energy ^{32}P spectrum. It can be seen that the total counts in the ^{35}S spectrum have remained approximately constant before and after separation. Also the ratio of P to S fluorescence has decreased, indicating phosphor was removed. This shows that the two substances were separated to a high degree.

6.5 Neutron Activation Characterization Measurements

In order to estimate the viability of the ^{228}Ra activation experiment, the experimental procedure had to be further characterized. Firstly the transmission of ^{228}Ra:CaF$_2$ crystals and their neutron irradiation needs to be evaluated. The damage of neutron irradiation on VUV transmission is characterized in section 6.5.1. Since no ^{228}Ra:CaF$_2$ crystals have been grown so far, we need to infer the VUV transparency of these crystals from the characteristics of radium and of other doped crystals that were grown.

Radium is an alkaline earth metal just as calcium and thus has similar properties. It has the same preferred oxidation state (2+) and forms a cubic lattice just as CaF$_2$ [267]. The ionic radius is larger, 148 pm for Ra^{2+} instead of 112 pm for Ca^{2+} for a coordination number of 8 [58, 268]. Grown CaF$_2$ crystals routinely contain Sr and Ba contamination. It was found that all alkaline-earth metals (Mg,Sr,Ba) are retained in the lattice of CaF$_2$, but the larger the ionic radius difference, the stronger the segregation [269]. It is thus expected that CaF$_2$ crystals would retain some Ra in their lattice. We could not find any previous experimental studies of the transmission or growth of single crystal RaF$_2$, probably due to the radioactivity of such a crystal.

Theoretical work on the transmission shows that RaF$_2$ has a significantly different lattice constant and a smaller bandgap than CaF$_2$, possibly affecting the transmission of the crystal [270]. The theoretical bandgap of RaF$_2$ of roughly 10 eV would still be large enough to prevent internal conversion of the isomer. Due to the low doping concentrations needed for this experiment (10^{15} cm^{-3}) significant effects are not expected. Doping can reduce transmission as is seen in figure 4.45 for thorium doped crystals grown in our group. Naturally, thorium perturbs the lattice more due to its 4+ oxidation state which needs charge compensation and thus might produce more absorption than radium doping. Characterizing the VUV transmission of a Ra:CaF$_2$ single crystal is thus needed to assess the viability of the Activation experiment. The VUV transmission of an neutron irradiated undoped CaF$_2$ crystal was done to approximate this characterization in the following section.

The next aspect to characterize is the Cherenkov radiation produced by the ^{228}Ra doping and the neutron irradiation of the crystal. The Cherenkov spectrum of β^--decay in CaF$_2$ is characterized in section 6.5.2 by using the developed Cherenkov source (section 6.4). This source consisting of undoped CaF$_2$ and ^{32}P. The information gained here can be used to characterize the quickly decaying Cherenkov radiation produced through the neutron irradiation of an undoped CaF$_2$ crystal.

In the last section the VUV background created due to irradiation of CaF$_2$ is characterized. Because of the time sensitivity of these experiments, as explained in section 6.2, the time behavior of this VUV background is crucial. To perform the measurements fast enough with the setup detailed in section 4.3, only four wavelengths are sampled. The rest can be inferred from the Cherenkov spectrum of the calibration Cherenkov source. Finally in section 6.6, these characterizations are taken into account to predict the viability of the experiment.

6.5.1 Neutron Irradiation Damaging Effects in CaF$_2$

Isomeric ^{229}Th can thus be produced by irradiating ^{228}Ra doped in a CaF$_2$. If the ^{229m}Th decays through photon emission the next critical question is if the crystal environment is transparent to this photon. Irradiating a crystal with neutrons in a nuclear reactor creates damage in CaF$_2$. The damage is created by the α, β, x-ray and γ radiation that is absorbed by the crystal [271–273].

We irradiated undoped Excimer grade CaF$_2$ crystals for different time durations in the TRIGA mark II reactor described in section 6.3, and measured their VUV and UV (405 nm) transmission. After the irradiation, the crystals take on an orange coloring (see figure 6.14). The color of the damage looks very similar to the highly doped ^{229}Th:CaF$_2$ (see figure 3.21), indicating a similar origin. The orange color can be attributed to F, M, and N centers that absorb around 400 nm and emit at 600 nm in the orange (see table 2.5.3).

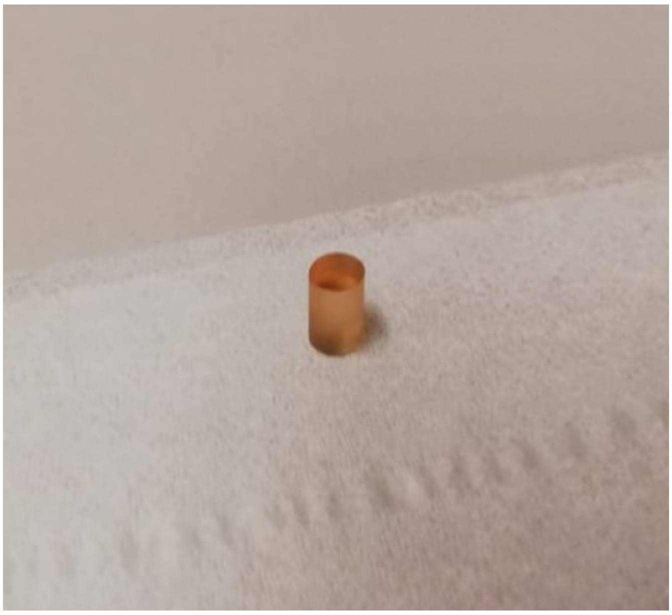

FIGURE 6.14: Undoped CaF_2 crystal that was irradiated by neutrons in the TRIGA mark II reactor for 3 hours. The orange coloring is indicative of many highly localized defect centers in the form of F, M and N centers. Any larger agglomerations of defects would color the crystals purple as is seen in heavily damaged CaF_2 with higher concentrations of F centers [111]. This indicates this crystal has a low F center concentration which are not agglomerated.

As can be seen in figure 6.15 the VUV transmission does not decrease drastically after reactor irradiation, at most by a factor of 0.2. The decrease of transmission seems to be mostly a surface effect; after repolishing the surfaces the original transmission was completely regained. The surface absorption is probably due to radioactive self sputtering [106]. In this processes the violent decay process deteriorate the surface and create dust particles with a diameter in the 100s of nm. The exact self sputtering process is not yet understood.

To test the hypothesis that the orange coloring is due to F, M and N centers created through the movement of F centers the transparency around the broad F center absorption (400 nm, see table 2.5.3) was measured. If the crystal absorbs in this region it indicates that the broadband absorption of these defect centers is present. The results are displayed in table 6.2.

The transmission of a 405 nm laser was measured using a UV Thorlabs photodiode. The UV transparency of undoped CaF_2 was measured to be 93 %, thus the neutron irradiation heavily decreased the UV absorption. A correlation in length can be seen, which indicates a volume absorption. A correlation in irradiation time can also be seen, which indicates that the process is not saturated yet. More experiments are underway to quantify this effect.

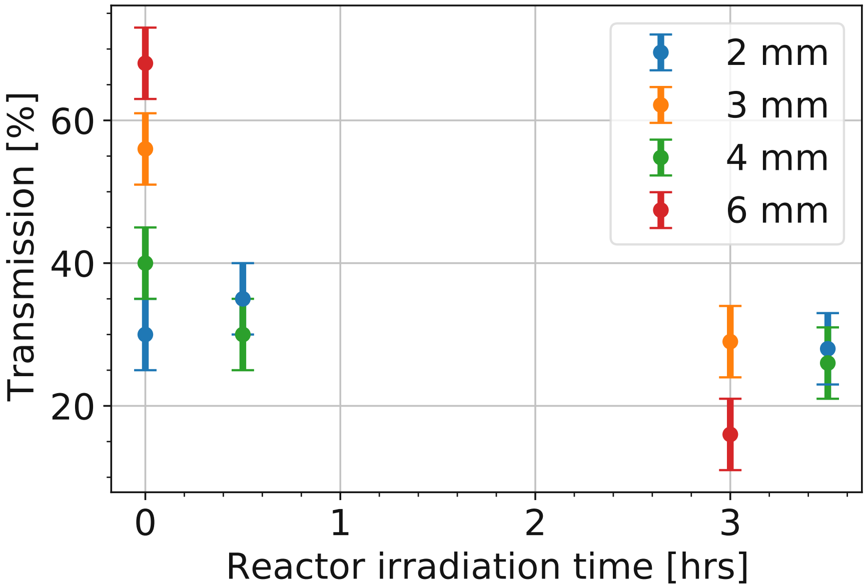

FIGURE 6.15: Transmission at 150 nm for four undoped CaF$_2$ crystals with different lengths. The surface quality affects transmission significantly, as can be seen in the scattering of values before irradiation (irradiation time 0). Polishing quality and surface water absorbant were not kept constant in these measurements. Before any irradiation, mechanical abrasion due to handling and quality of polishing affects the transmission greatly. After 3 hours of irradiation we see only a small reduction in transmission, only the longest crystal has a significant reduction in transmission. Probably for this crystal both bulk and surface absorption are affected.

TABLE 6.2: Transmission of a 405 nm laser measured for neutron irradiated crystals of different height. The 3 and 6 mm crystals were irradiated for 3 hours and the 2 and 4 mm crystals were irradiated for 3.5 hours which explains the difference in transmission.

Crystal length [mm]	Transmission [%]	Irradiation time (hrs)
2	35	3.5
3	40	3
4	7	3.5
6	11	3

To further investigate the transmission of the neutron irradiated crystals the spectral transmission was measured with the setup described in section 4.2.1. After the crystal was annealed at 550 °C for 1 hour and repolished, the transmission was remeasured. The results are shown in figure 6.16. Firstly it was observed that the orange coloring of the crystal can be removed by annealing. Secondly it seems the original transmission cannot be completely recovered, even after annealing. Possibly longer 600 °C annealing as found in section 5.5.1 needs to be used.

Another explanation for not regaining the original transmission is that the transmuted Ca (to K, Sc or Ti) and F (to Ne) creates absorption centers. A second option is that the crystal became more non-stoichiometric due to unequal transmutation of Ca and F due to their different thermal neutron capture cross sections ($\sigma_{Ca} > \sigma_F$).

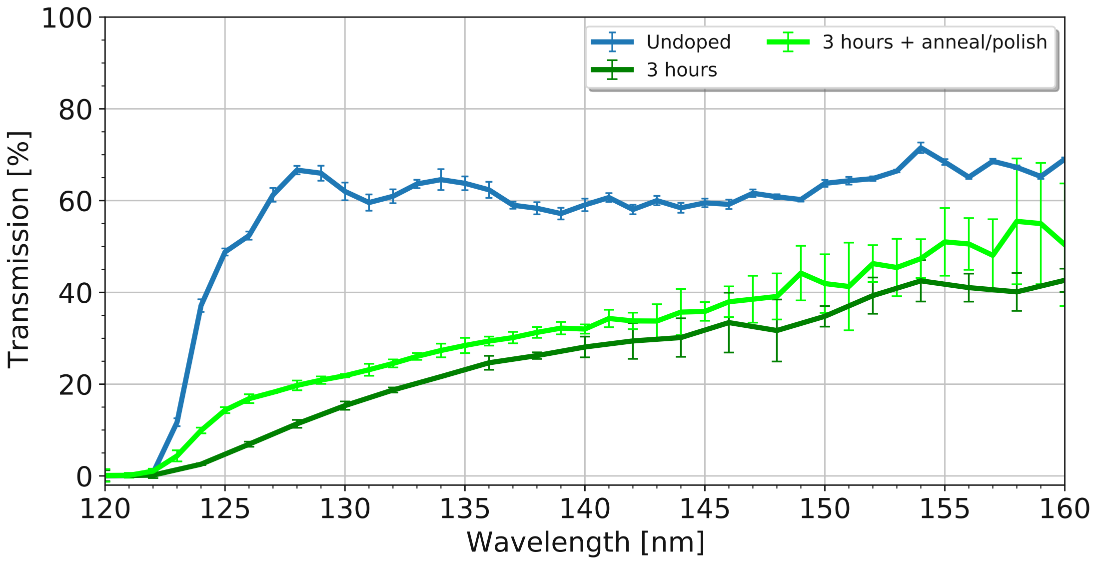

FIGURE 6.16: Spectral transmission for the 3 hours irradiated crystal, Korth RAMAN/Excimer CaF_2 window is shown for reference. Transmissions of the Korth crystal and neutron irradiated crystals were measured with different light sources, D_2 lamp for the undoped CaF_2 window and argon excimer lamp for the neutron irradiated crystal. It can be seen that annealing mainly improves the low wavelength transmission and less at higher wavelengths.

The study of neutron irradiation on undoped crystals cannot be assumed to generate the same result as for ^{228}Ra:CaF_2. For example, it is reported that additional absorption due to neutron irradiation is only created around 180 nm for undoped CaF_2 [272]. The absorption at 150 nm for ^{232}Th:CaF_2 (see figure 4.47) indicates that doping can shift the center of this absorption. Any doped crystal might thus be affected differently by the neutron irradiation than pure CaF_2.

If the production of isomeric ^{229}Th through ^{228}Ra neutron irradiation is attempted, as described in section 6.2, then the ^{228}Ra doping will increase the absorbed amount of neutrons. The larger neutron absorption cross section of ^{228}Ra will induce more radioactivity and thus more damage. Further experiments are needed to characterize the damage of doped crystals. Other isotopes can be used to study this: Such as ^{228}Th and ^{226}Ra because they have similar half-life and neutron absorption cross-section. Also ^{133}Ba can be considered because it is a chemical proxy to ^{228}Ra and again has similar half-life and neutron absorption cross-section.

6.5.2 (V)UV Spectrum of the Cherenkov Calibration Source

The Cherenkov source described in section 6.4 was produced to characterize the Cherenkov radiation of undoped CaF_2. This information is used to compare it to the Cherenkov radiation produced by radioactively doped CaF_2 crystals and neutron irradiated crystals.

The shape of the Cherenkov spectrum of the calibration source was used to choose which wavelengths to measure while characterizing the neutron activation induced VUV luminescence. In this manner a time dependent Cherenkov spectrum can be reconstructed by measuring the VUV emission at single wavelengths for neutron activated crystals. Also its UV spectrum was characterized to determine the produced background by STE emission.

The VUV luminescence of the Cherenkov calibration source described in section 6.4 was measured. The produced spectrum of the undoped CaF_2 with 300 kBq of ^{32}P, a pure beta emitter, inserted can be seen in figure 6.17. The ^{32}P β^--decay in CaF_2 produces a background of 2 cps as measured by the detector around 150 nm. It can be calculated that the ^{32}P decay produces 0.06 150 nm photon per decay. Considering 300 kBq of ^{32}P and 0.05 % efficiency of the detection system one would expect 9 cps. The phosphorous is not homogeneously distributed but on one side of the crystal. Because of this at most half of all β^--decays will penetrate the crystal. Most of their energy will be lost not in the crystal but in the phosphorous itself, thereby reducing the photon count to less than the calculated 9 cps.

The Cherenkov spectrum can be calculated numerically as well [45], and scaled to the spectrum which matches well with the measured values. The shape of the spectrum is mainly dominated by the transmission cutoff of CaF_2 at 122 nm, the increase in Cherenkov radiation towards lower wavelengths (see section 2.4.3) and the reduction in efficiency of the grating and PMT towards higher wavelengths (see figure 4.3).

The UV emission of the Cherenkov calibration source was also measured. The β^--decay produces significant STE luminescence, as only a small fraction of the total energy of the β^--decay (1 % to 5 %) goes into producing Cherenkov radiation.

Finally, the VUV background to a possible isomer photon emission can be characterized of a neutron irradiated undoped CaF_2 crystal with the knowledge gained on the spectral shape of the Cherenkov emission and STE luminescence.

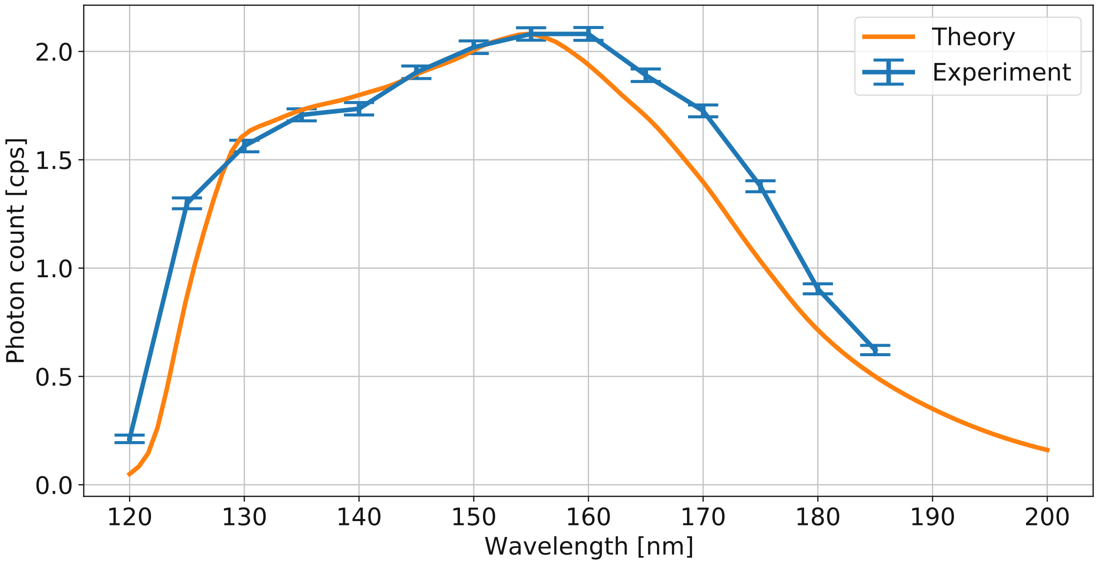

FIGURE 6.17: The detected VUV spectrum of the Cherenkov source described in section 6.4 compared to a scaled theoretically computed Cherenkov spectrum that takes into account the spectral efficiency of the system. The maximum cps was 2 cps. The transmission cutoff of CaF_2 below 122 nm can be seen, as well as loss in efficiency of the PMT and grating for higher wavelengths. A 1 mm slit size was used. The theoretical prediction matches well to the measured values, only a broadening is observed which is most likely due to the slit size used.

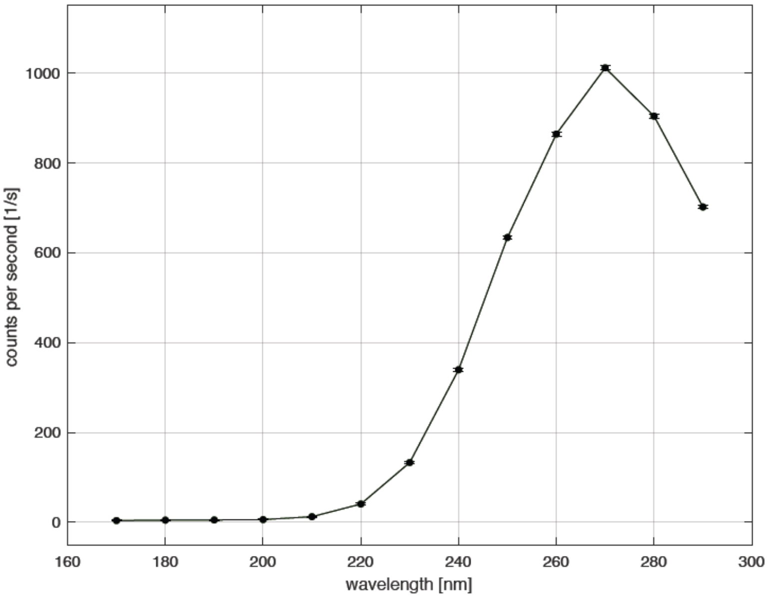

FIGURE 6.18: Radioactivity induced STE luminescence in a ^{32}P irradiated undoped CaF_2 crystal. After 200 nm the intensity of the STE luminescence start increasing. The Cherenkov radiation at lower wavelengths is almost invisible on these scales. The typical peaks can not be distinguished due to the loss in efficiency of the PMT at higher wavelengths and the low resolution with which the measurement was taken (1 mm slit).

6.5.3 Characterization of Neutron Absorption Induced VUV Background

The shape of the VUV Cherenkov background, induced mainly by β^-decay [45], was characterized as described above. We can see in figure 6.17 that this produces a background of 2 cps as measured by the detector around 150 nm using the same setup as envisioned for the ^{228}Ra activation experiment. By knowing the shape of this spectrum we can select four wavelengths to measure in this time sensitive experiment: 120 nm is chosen to measure the noise background, 150 and 170 nm to measure the Cherenkov background and 300 nm to measure the STE background.

Pure CaF_2 crystals were irradiated with a thermal neutron flux of 10^{13} neutrons cm^{-2} s^{-1} for 30 min, 60 min and 180 min, after which the VUV background was measured. The crystals needed to be transferred from the nuclear reactor core to the VUV spectrometer. The transfer took a certain time (≈10 min) during which the VUV emission could not be measured. After a first attempt at measuring the VUV background, lead shielding was added to the detector due to a high background of gamma radiation, directly striking the PMT. The shielding reduced the background by two orders of magnitude.

With a shutter, light and dark measurements were taken in quick succession: 0.5 s of dark and 1.5 s of light measurements. The average difference is plotted in figure 6.19 for a 3 hour activation. One can see the Cherenkov light emitted at 150 nm and 170 nm, and the STE light at 300 nm [51]. The radioactive background produced on average 200 cps in the first 3 hours after a 3 hour neutron irradiation as measured by the detector around 150 nm. It can be seen that the fitted single exponentials of 150 and 170 nm do not match well to the initial points, indicating that the tail of the short lived ^{49}Ca β^--decay dominates the Cherenkov radiation here. It is hard to see if the 300 nm STE fluorescence also deviates in the first minutes from the fitted exponential, as it was not measured there. From the approximately 1 hour half-life of the fitted exponentials it can be deduced that the decay product of ^{49}Ca, ^{49}Sc, produces most of the background.

In figure 6.20 the fluorescence of a 30 minutes neutron irradiated CaF_2 crystal is shown. The radioactive background produced on average 30 cps in the first 3 hours after a 30 minutes neutron irradiation as measured by the detector around 150 nm (figure 6.19). The activity in the first 5 minutes (not visible in the figure) was much higher than during the rest of the measurement. This is due to the production and subsequent decay of ^{49}Ca, which has a lifetime of 9 minutes [274]. The transfer time in this activation was 3 minutes shorter than the above measurement which caused the decay of ^{49}Ca to be strongly visible. The increased background due to ^{49}Ca decay disappears after several minutes and will produce a negligible background as compared to the expected isomer decay time of >1 min [8].

From the data we can conclude that increasing the neutron irradiation time by a factor of 6 increased the radioluminescence by a factor of 50. The long term background F and H center recombination that produces STE light only increased by a factor of 5. For 3 hours of activation, the Cherenkov radiation reduces to almost background after approximately 2 hours and the STE luminescence after approximately 3.5 hours.

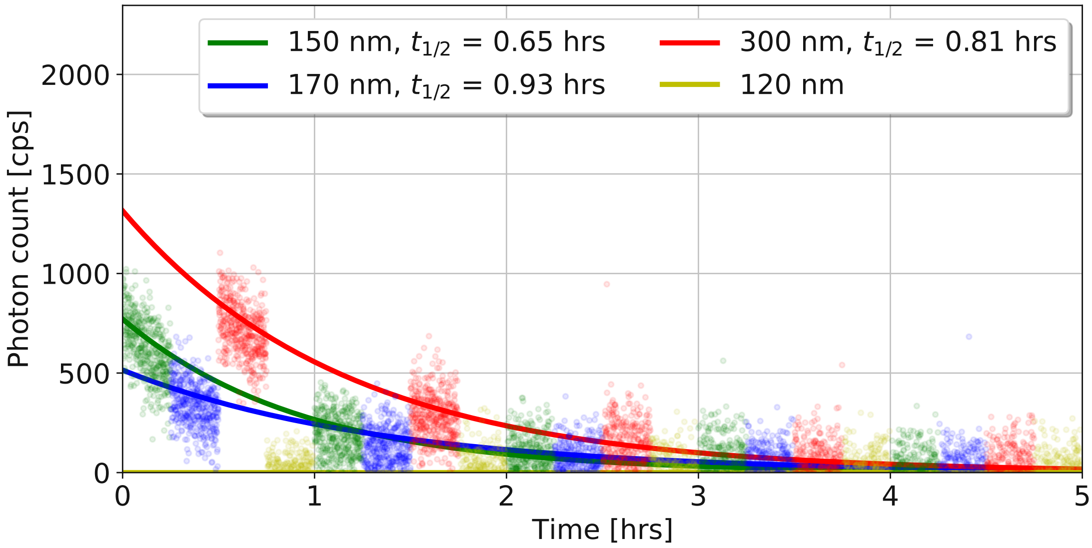

FIGURE 6.19: Radioluminescence of a 1 cm long 3.2 mm diameter pure CaF_2 crystal after 3 hours of neutron irradiation in the TRIGA MARK II reactor. Due to the nature of the setup (4.3), only one wavelength could be measured at a time. Slit size was 2 mm, thus 8 nm wide spectra are measured around each wavelength. Measurement started 11 minutes after activation end in the reactor. The original data points are shown on top of single exponentials fitted to the data. The 120 nm background was subtracted in this plot which was 66 cps.

6.6 Experimental viability of the Activation of ^{228}Ra

When measuring isomer photons, the Cherenkov VUV radiation is the dominant background. It can be calculated from figures 6.20 and 6.19 that the irradiation of the crystal produces on average respectively 80 cps and 25 cps as measured by our detection system after the first hour at 150 nm for a slit size of 2 mm. During the first hour after neutron irradiation the background can be larger due to the decay of the shorter lived ^{49}Ca. The ^{228}Ra contributes ≈5 cps for 300 kBq (or 10^{15} cm^{-3} in a 3.2 mm diameter 1 cm long crystal), taking the detection system efficiency into account while using the Cherenkov photon rates in figure 6.5 and a slit size of 1 mm. This value is ≈2.5 times larger than the measured number for ^{32}P which has similar activity and β^--decay energy. The ^{32}P

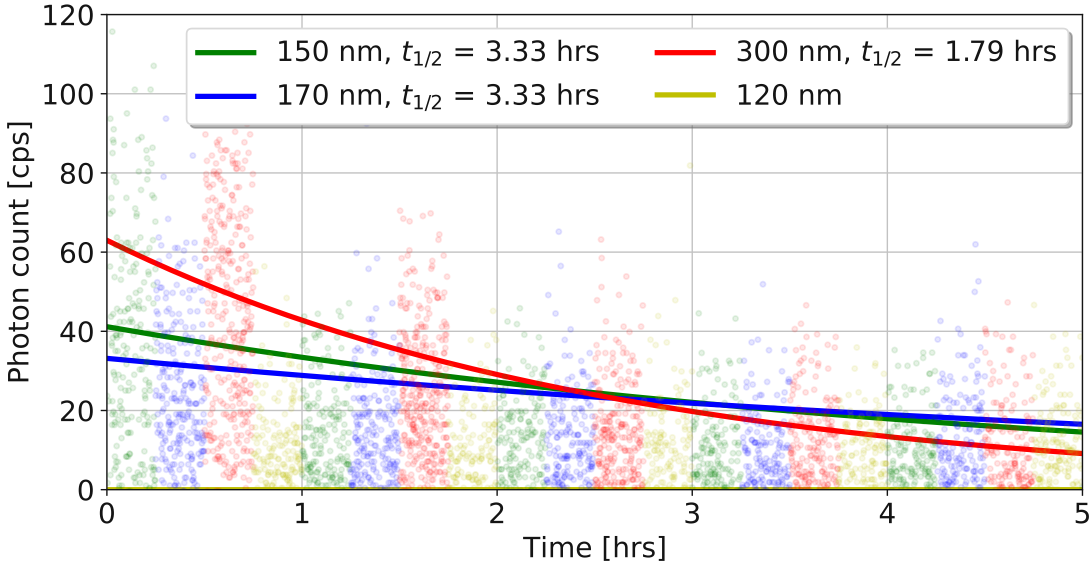

FIGURE 6.20: Radioluminescence of a 1 cm long 3.2 mm diameter pure CaF_2 crystal after 30 minutes of neutron irradiation in the TRIGA MARK II reactor. Due to the nature of the setup, only one wavelength could be measured at a time. Measurement started 8 minutes after activation end in the reactor. Slit size was 2 mm, thus 8 nm wide spectra are measured around each wavelength. The original data points are shown on top of single exponentials fitted to the data. Due to the short transfer time, remaining luminescence from the ^{49}Ca decay was observed in the first minutes. The 120 nm background was subtracted in this plot which was 11 cps

source is not directly in the crystal and some of the energy of the β^--decay will be lost in the source itself, which results in less Cherenkov radiation produced in the crystal.

We can see that if 300 kBq of ^{228}Ra is used, it produces slightly lower background as compared to the average background produced by 3 hours of neutron irradiation of the undoped crystal. For a slit size of 1 mm the background due to activation of the undoped crystal would amount to 40 cps, as compared to 5 cps due to the Cherenkov produced by ^{228}Ra. The transmission of the crystal is not significantly affected by these low doping concentrations, especially compared to the transmission loss through neutron irradiation (figure 6.15). Assuming 30 % transmission at 150 nm, 300 kBq of ^{228}Ra and the measurement cycle proposed in section 6.2.1 we can calculate the signal to noise ratio for different isomer lifetimes and population efficiencies (figure 6.21).

Here we see that in the worst case scenario; 14 % population efficiency instead of 93 % (see 6.2.1), and an isomer lifetime of 1 min, we obtain an SNR of more than 17. Important is to calculate the minimum photon flux, to assure we can measure it on our detector. The result of the calculation is shown in figure 6.22, where the minimum photon flux is equal to what was detected in the ^{32}P experiment.

It seems in figure 6.21 that the ideal lifetime of the isomer is that of the ^{229}Ac half-life. The decay of ^{229}Ac constantly produces ^{229m}Th nuclei during the measurement process

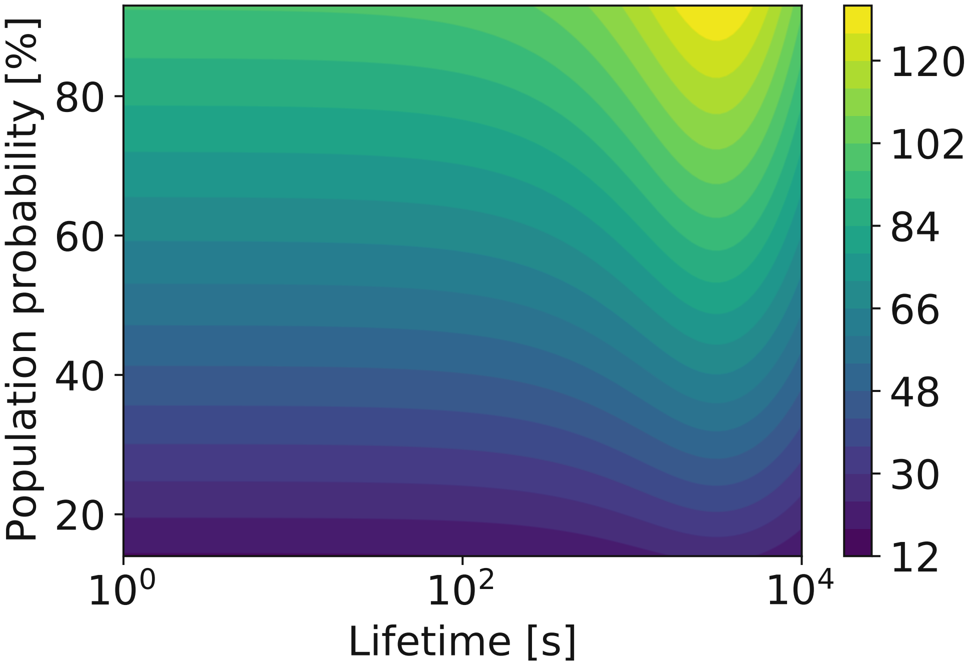

FIGURE 6.21: Signal to noise ratio calculated for the activation experiment for different isomer lifetimes and population probability from the ^{229}Ac decay. In this calculation, the experimentally characterized background, system detection efficiency with a slit size of 1 mm and signal strength were used. One can calculate that in all reasonable cases the SNR will be above 17.5. If the isomer lifetime is as estimated in [16] to be 5000 s, the SNR will be above 20.

and thus is the dominant time scale of the experiment. If the half-life of the isomer is shorter than the ^{229}Ac half-life, the isomer nuclei produced during activation will not contribute to signal. If the isomer half-life is longer than ^{229}Ac it will fall outside our measurement period and not contribute to signal. If the half-life is that of ^{229}Ac it will fall in our measurement period and the isomer nuclei produced during activation will contribute to signal. These calculations and measurements show that if a ^{228}Ra:CaF$_2$ crystal is grown with sufficient doping and transparency, the experiment is viable using the current experimental setup and can measure a wide range of possible half-lifes and wavelengths of the ^{229}Th isomeric decay with high SNR.

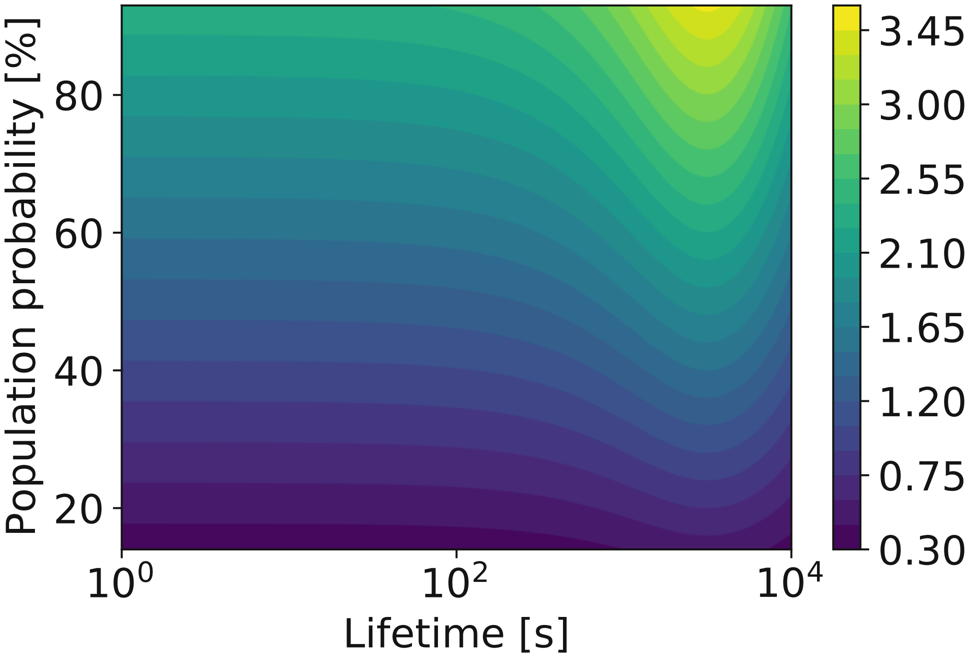

FIGURE 6.22: Average isomer photon flux (in cps) detected in our system, calculated for the proposed experiment for different isomer lifetimes and population probability from the ^{229}Ac decay. In this calculation the experimentally characterized background, system detection efficiency with a slit size of 1 mm and signal strength were taken into account. The lowest photon flux shown here, 0.35 cps, was measured in figure 6.17

Chapter 7

The Nuclear Excitation of ^{229}Th with X-ray Photons

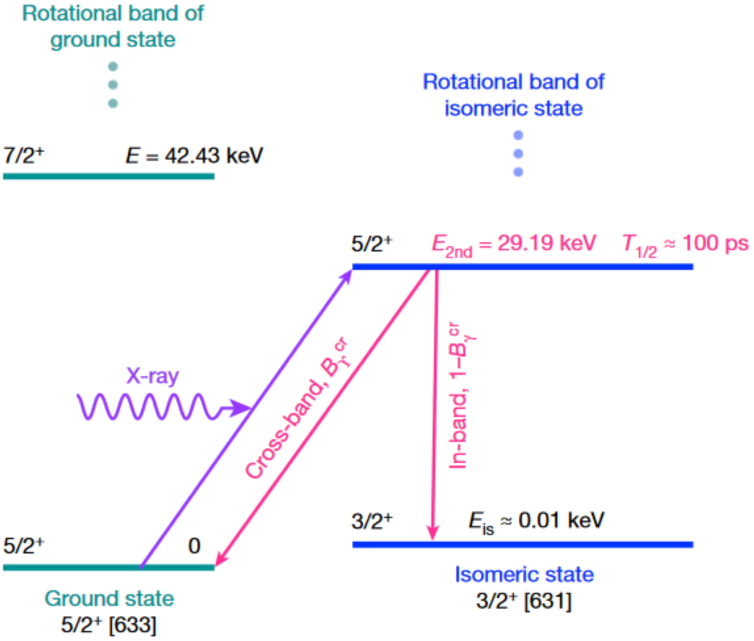

Figure 7.1: Simple nuclear level structure of the ^{229}Th nucleus including only the lowest four states which are in two rotational bands: collections of nuclear states which emerge for non-spherical nuclei. The Nilsson model for deformed nuclei describes these by the Nilsson quantum numbers, which are the same within a band. The NRS process is indicated which excites the ^{229}Th nucleus from ground to second excited state. Taken from [43]

Excitation of the ^{229}Th nucleus with x-rays is achieved through a process known as nuclear resonant Scattering (NRS). In this process, narrowband x-ray photons irradiate a metal ^{229}Th target. The nuclei can absorb the photon and get excited to the second excited state at 29 keV. This excitation process is depicted in figure 7.1 for ^{229}Th. In the case of ^{229}Th [43], several tens of picoseconds later ($t_{1/2} = 82.2 \pm 4.0\,\mathrm{ps}$) the nucleus excited to 29 keV will re-emit the energy in the form of a photon or will undergo internal conversion and emit an electron. The internal conversion dominates this decay. The delayed re-emission of energy by the nucleus is what is measured in NRS. By confirming this process we know that we have excited ^{229}Th to the second excited state, which we call the x-ray Experiment.

In this chapter the viability of this approach will be tested. First (section 7.1) a theoretical calculation is presented where the nuclear photon emission rate is calculated in order to assess where experimental characterization is needed. In section 7.2 the experimental setup is shown: From undulator to the photon detection at the crystal. Two photon detection setups were used: One which maximized the detection efficiency around 150 nm in an attempt to measure a signal (section 7.2.3) and one that characterized the spectral features of the crystal radioluminescence and x-ray induced luminescence (section 7.2.4). Finally the experimental viability of this method is assessed using the experimental characterizations.

7.1 Viability of the Excitation of ^{229}Th with X-rays

The nucleus in the second excited state will mostly decay to the first excited state due to selection rules: The cross-band de-excitation is semi-forbidden because it is a transition between same parity states. The decay of second to first excited state happens both by photon emission and by internal conversion. The benefit of using this method is that it is proven, a downside is that it still needs highly doped crystals, the high intensity of x-rays will definitely damage the crystal and possibly change the oxidation state of the dopant [70] which might promote internal conversion.

The excitation rate of the 2nd excited state of ^{229}Th can be calculated through the cross section of the NRS process which is described by the Breit-Wigner equation [275]

$$\sigma_{NRS}(E) = g_{sp}\frac{\lambda_{2nd}^2}{\pi}\left[\frac{\Gamma_\gamma^{cr}\Gamma_t/4}{(E-E_{2nd})^2+(\Gamma_t/2)^2}\right]. \tag{7.1}$$

Here λ_{2nd} is the wavelength of the second nuclear excitation, Γ_γ^{cr} is the width of only the cross band excitation to the second nuclear excited state, Γ_t the width of the total excitation, E the energy of the excitation light, E_{2nd} the energy of the second nuclear excitation and g_{sp} the spin multiplicity factor which is given by

$$g_{sp} = \frac{2I_e+1}{2(2I_g+1)} = \frac{1}{2}, \tag{7.2}$$

where I_e=5/2 and I_g=1/2 are the nuclear spins of ground and second excited state of the nucleus. By using the cross section σ_{NRS} we can calculate the excitation rate for the second excited state W_{2nd}:

$$W_{2nd} = \int \sigma_{NRS}(E)\frac{d\Phi}{dE}, \tag{7.3}$$

where $\frac{d\Phi}{dE}$ is the beam intensity per unit energy. The distribution of beam intensity per unit energy is heavily dependent on the source. For example one could use radioactive decay, x-ray tubes or synchrotrons to produce these types of x-rays. The most ideal for these type of experiments is a synchrotron, which gives energy tuneability and high intensities. This intensity per energy distribution is in synchrotron experiments [43] well described by a Gaussian distribution

$$\frac{d\Phi}{dE} = \Phi_0 \frac{1}{\sqrt{2\pi}\sigma_{Xray}} \exp\left[-\frac{(E-E_0)^2}{2\sigma_{Xray}^2}\right], \tag{7.4}$$

where σ_{Xray} is the linewidth of the beam, Φ_0 the amplitude and E_0 the center energy of the beam. By combining the above equations this leads to

$$W_{2nd} = \frac{\lambda_{2nd}^2}{4s_beam}\frac{\Gamma_\gamma^{cr}}{\sqrt{2\pi}\sigma_{Xray}}\Phi_0. \tag{7.5}$$

To calculate the excitation rate for the isomer through NRS (W_{NRS}) we need to take into account that part of it decays to the ground state and part to the isomer state, named the branching ratio $B_{\gamma+ic}^{in}$. We will in this case sum over internal conversion decay and radiative decay since both contribute to production of isomer nuclei. We assume that the second excited state decays instantly (82.2 ps) such that we can calculate this using the parameters of [43]

$$W_{NRS} = B_{\gamma+ic}^{in} W_{2nd} = \frac{\Gamma_\gamma^{in} + \Gamma_{ic}^{in}}{\Gamma_t} W_{2nd} = 0.58 W_{2nd} \approx 10^{-13} \text{ Hz per nucleus} \tag{7.6}$$

where Γ_γ^{in} and Γ_{ic}^{in} are the in-band linewidths for radiative and internal conversion decay. We can now continue to calculate the $N_{eq,NRS}$ for NRS and the signal rate using the values of [43] ($\Phi_0 = 80{\cdot}10^{12}$ Hz, $\Gamma_\gamma^{cr} = 1.70$ neV, $\lambda_{2nd} = 0.04247$ nm, $\sigma_{Xray} = 1.4$ eV). We also need the crystal characteristics (1x1x10 mm crystal) and isomer characteristics: The isomer decay rate is estimated to be $\Gamma_m = 2.8{\cdot}10^{-4}$ Hz [16], $\lambda = 152.1$ nm, $n(152.1)$ = 1.575 [56], $\mathrm{s_{beam}} = 1\,\mathrm{mm}^2$ and $\mathrm{N_{Th}} = 10^{16}$ ($\approx 10^{18}\,\mathrm{cm}^{-3}$ doping in 1x1x10 mm crystal).

$$N_{eq,NRS} = N_{Th}\frac{W_{NRS}}{\Gamma_m n^3} \approx 9 \cdot 10^7 \tag{7.7}$$

$$\frac{\Phi_\gamma}{\Omega} = \frac{n^3\Gamma_m N_{eq,NRS}}{4\pi} \approx 7 \cdot 10^3 \text{ sr}^{-1}\text{s}^{-1}. \tag{7.8}$$

These values are comparable to the excitation rate through resonant VUV photon excitation (see section 5.1.1). The NRS excitation of the isomer state therefore gives high excitation rates and the nuclei are confirmed to be excited. Using the x-ray excitation, the crystal induced background can be very effectively separated due to the narrow excitation to the second level: If the x-ray energy is tuned slightly away from the nuclear resonance (≈100 meV), the crystal will still absorb the x-rays similarly, but the nucleus will be not excited. These on- and off-resonance excitations can be subtracted from one another to remove the background to a high degree.

The damage the x-ray beam induces in the crystal (transparency reduction) needs to be characterized to assess the viability of this experiment. The change in oxidation state of the ^{229}Th nucleus through x-ray irradiation [67] was not characterized, but should be in the future. The x-ray induced luminescence was also characterized. If the intensity is too high the induced luminescence can still lead to large errors in the on- and off nuclear resonance detection scheme.

7.2 SPring-8 BL19LXU X-ray Source

The SPring-8 (an acronym of Super Photon ring - 8 GeV) storage ring in Hyogo, Japan, stores 8 GeV electrons in its ring. These electrons are used in the long 25 m SLUS-1 undulator [276] of beam line BL19LXU to produce high intensity x-ray beams from 7 to 70 keV. These x-rays are used for resonant nuclear excitation experiments, such as NRS as described in the previous section. The bandwidth of this beam is reduced by using two monochromators which consist of 2 silicon single crystals that diffract the x-rays into different orders. In this system the 14.41 keV line of ^{57}Fe was characterized through NRS with an energy resolution of 2.6 meV using the [11 5 3] crystal plane of silicon [277].

The NRS process can also be applied to the second excited level of ^{229}Th at 29 keV, as demonstrated in [43]. After being excited a fraction of the nuclei will decay to the ground state, and if this decay is detected one can learn more about the isomer state. Here, the second excited state of ^{229}Th was excited and detected with an energy resolution of 100 meV. A fraction (≈60 %) of the second excited state of ^{229}Th then decays to the first excited state, or isomer state. Effectively, with this method ^{229}Th nuclei can be pumped from ground state to isomer state. In order to measure the isomer decay and reduce internal conversion (IC) of the nucleus, the thorium nuclei are doped in a CaF_2 crystal inhibiting IC as described in section 2.1. This will ensure that the nucleus emits as many isomer photons as possible. The photons can then be measured in a spectrometer detector setup. In this section the undulator and x-ray optics are described that make the NRS process possible together with its calibration which is important to specifically excite the ^{229}Th nuclei. The setups used to measure VUV photons produced by the x-ray irradiated crystal are detailed as well.

7.2.1 Undulator and X-ray Optics

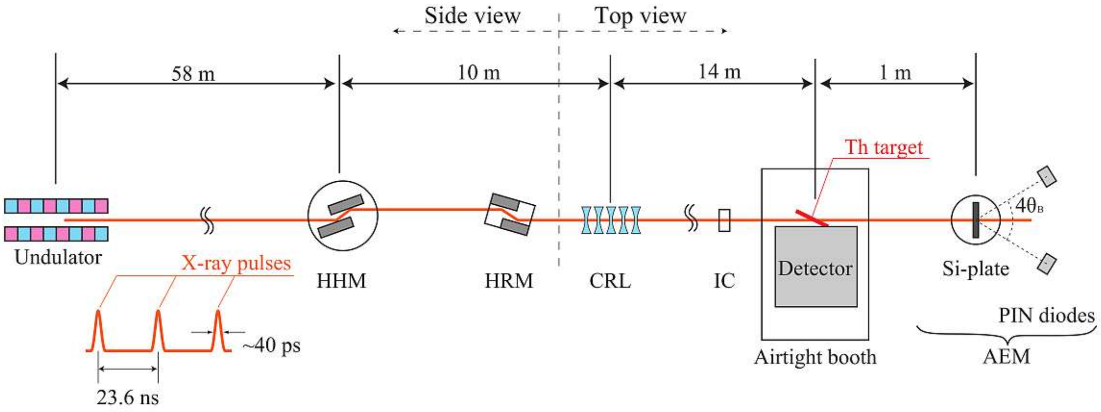

FIGURE 7.2: Schematic overview of the used beamline BL19LXU. The bunches of 8 GeV electrons produce pulses of x-rays which travel through two monochromators that decrease the bandwidth of the x-rays. After these the beam is focused down on the target by a compound refractive lens. At the target the NRS is detected. After the NRS setup a silicon plate is used for an absolute calibration of the x-ray beam as detailed in the next section. Taken from [43].

To produce the 29 keV x-rays that excite the ^{229}Th nucleus, an undulator is used. The undulator works by applying 0.59 T magnetic fields, using a series of permanent magnets, which constantly flip, with a period of 32 mm, along the traveling direction of the electron beam (see figure 7.2). The oscillating magnetic field perceived by the electrons will cause them to move transversely from their trajectory, effectively wiggling them. The resulting wiggling of the electrons and thus transverse acceleration will produce photons in the traveling direction of the electrons. By using a very regularly oscillating magnetic field, an undulator, a spectrally narrow distribution of photons will be produced [276].

The undulator has 780 periods making its total length 25 m. The SPring-8 storage ring is filled with electron bunches by an injector. Every bunch will produce a pulse of synchrotron light which is kept very regular. The time information of the electron bunches can be used to perform time-sensitive measurements. The electron bunches are

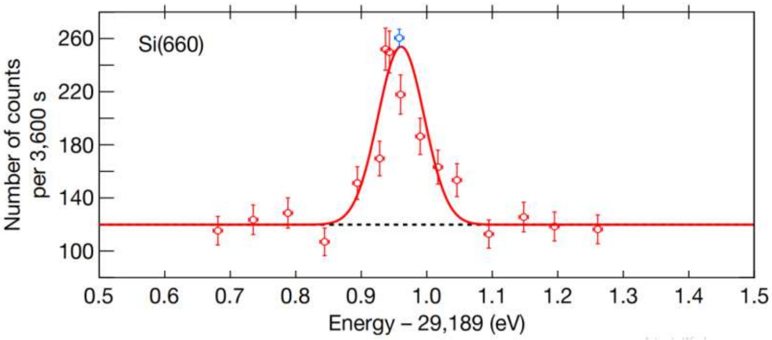

FIGURE 7.3: Resonance curve of the second nuclear excited state of ^{229}Th. The vertical axis is the number of confirmed NRS events per 3600 s. The horizontal axis is the energy of x-ray photons used, offset by 29189 eV. The Si single crystal monochromator was used using the 660 crystal plane. The blue point indicates a longer integration time of 21600 s. The red fit is a gaussian curve through the measured points. Figure taken from [43]

diverted from the undulator after x-ray production to circle around once again. In this fashion a pure x-ray pulse remains that can be used for experiments.

The x-rays pulses are passed through a cryogenically cooled High Heat load Monochromator (HHM). This device is a silicon single crystal that uses the diffraction on its crystal planes to disperse the incoming x-rays. By using a slit the bandwidth of the spectrum can then be effectively reduced by cutting out other wavelengths. Due to the high incoming intensity this monochromator needs to be cooled to not be affected by heat-induced changes in lattice constant. The beam is then passed through a High Resolution Monochromator (HRM) which narrows down the beam spectrum even more. After that the beam is passed through a Compound Refractive Lens (CRL) to focus it down from a spot size of 1.5 by 0.8 mm to a spot size of 0.15 by 0.065 mm. An ionization chamber (IC) is used to monitor the intensity of the beam.

After the IC the ^{229}Th:CaF$_2$ crystal with VUV photon detection chamber is placed to use the x-ray beam to pump to the isomeric state. Downstream of the crystal, there is another ^{229}Th target. The target is a ThN$_3$ solution dried on a metal plate and is fitted with a detector nearby consisting of avalanche photodiodes to detect the NRS process. This second target is used to calibrate the energy of the x-ray beam during experiments to ensure it is on-resonance with the second excited state of ^{229}Th by validating the presence of NRS. A scan of the resonance of the second excited state can be seen in figure 7.3. Validating NRS is not possible in the crystal due to the lower densities as compared to a pure ^{229}Th compound.

The center energy of the beam drifts during the experiments due to temperature changes in the silicon single crystals and need to be adjusted during long runs. By scanning the monochromators, changing the center energy of the beam, the NRS resonance peak can be identified using this target. The absolute energy of the beam is then measured by a Bond diffractometer which is positioned at the end of the beamline. This consists of a silicon plate with two detectors. We need to know the exact energy of the x-ray beam because during the experimental cycle to measure the isomer decay of ^{229}Th the energy is changed from on resonance to off resonance. In the following sections, the calibration process and the VUV detection setup with the experimental cycle is described.

7.2.2 Calibration of an X-ray Beam

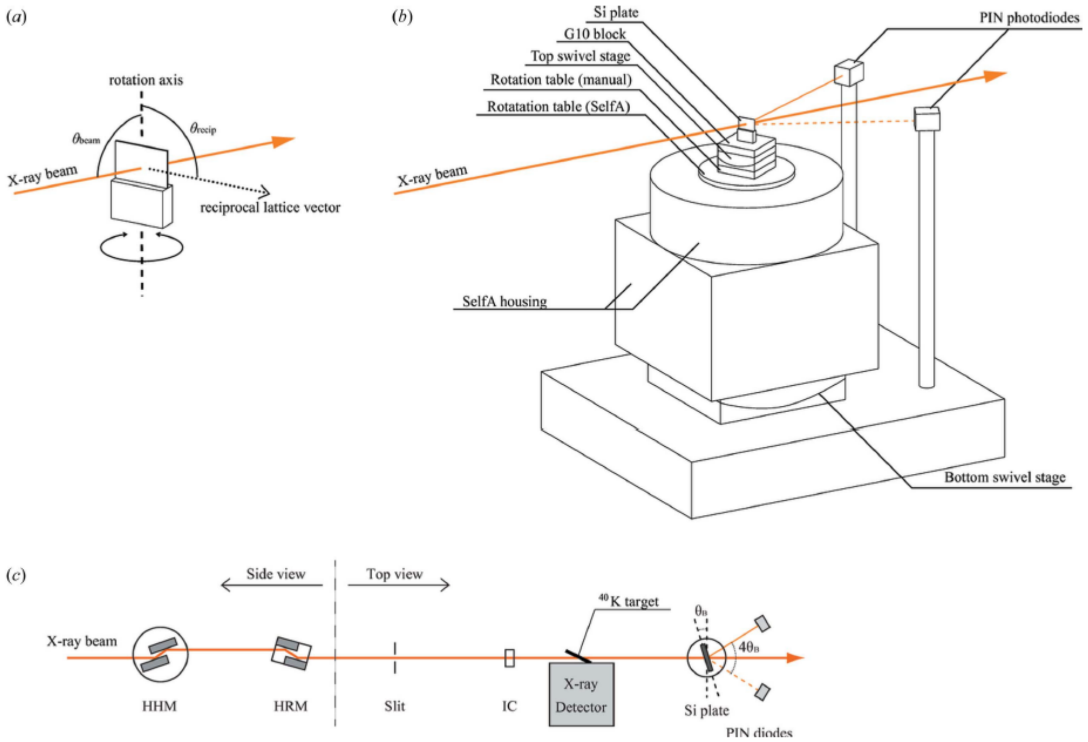

FIGURE 7.4: Schematic image of (a) the Si single crystal used for x-ray diffraction with the relevant angles, (b) the Bond diffractometer in the beamline and (c) the x-ray beamline. Beamline is the same as in figure 7.2. Taken from [278].

To measure the absolute energy of x-ray photons a Bond diffractometer is used, essentially another monochromator. This device was first conceived to accurately measure the lattice constant of a single crystal using narrowband Cu Kα_1 x-rays [279]. Here it is used with the opposite purpose: By using a crystal with a known lattice constant the wavelength of the incoming x-rays can be measured. The crystal used is a silicon single crystal ($d_{220} = 192.01559 \pm 0.00002$ pm) characterized by using combined x-ray (Laue diffraction) and optical interferometry [280]. The setup is schematically detailed in figure 7.4, and the lab view is seen in figure 7.5.

The Bond diffractometer works by rotating the silicon plate such that the angle of the silicon plate with the beam equals the Bragg angle and hits the first PIN diode. Now

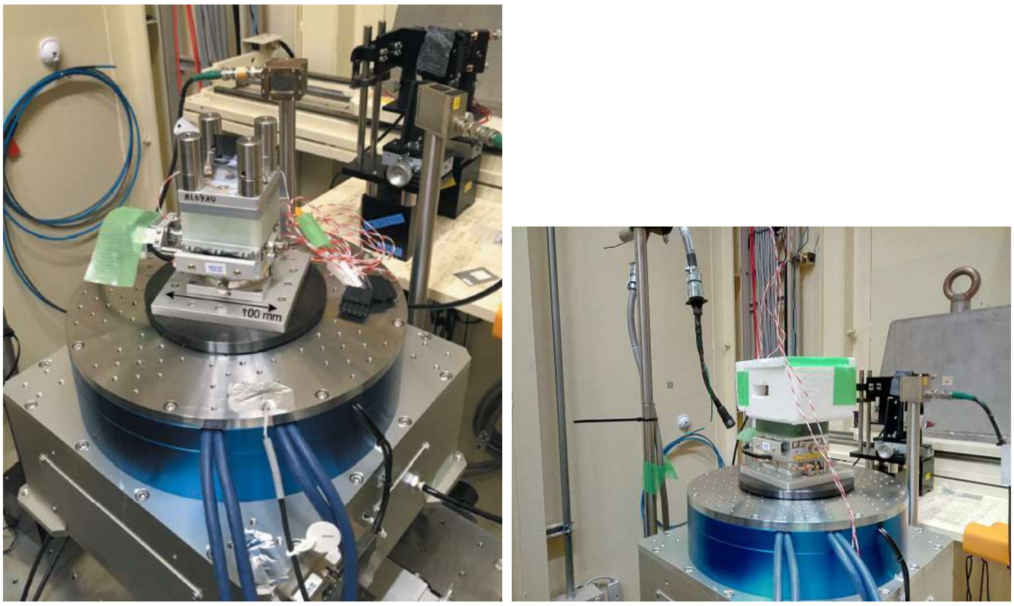

Figure 7.5: Bond diffractometer setup in the beamline. The cables to the platform are removed when the 360° SelfA calibration is performed to avoid tangling. The crystal (black, center) is housed in a styrofoam casing in order to provide more isolation and thus temperature stability of the crystal.

the plate is rotated in the other direction until the Bragg reflection hits the other PIN diode. Now the difference between these two angles will be a rotation of the plate of twice the Bragg angle. The angle between the two PIN diodes now equals four times the Bragg angle because the diffracted beam has an angle of twice the Bragg angle with the beam on both sides (see figure 7.4). The two diodes were put at a 45° angle with the beam. As can be seen in figure 7.4 the two other space angles ($\theta_{beam}, \theta_{recip}$) of the beam with the crystal also determine the direction of diffraction. By using the swivel stages, these angles are set to 90° only approximately: every deviation from 90° mildly affect the outcome of the measurement.

The angle between the silicon crystal and the x-ray beam is accurately measured by a rotary encoder controlled by SelfA. SelfA is an advanced grating based absolute rotation angle detection setup. SelfA performs the absolute calibration on itself by using the equal division averaged method and the fact that a full rotation is 360°. If uncalibrated, when performing a full rotation, it will thus detect an angle deviation from 360°. It measures this deviation by measuring when grating lines of the rotating disc pass by optical reading heads that are positioned equally spaced around the disc. This measures the deviation from an ideal 360° signal. By using this calibration and measuring the grating lines passing by the optical reading heads it gives an accurate absolute measurement of the rotation angle. The system shows a reproducibility of $\frac{\Delta E}{E} = 2\,\text{ppm}$. By measuring the Bragg angle, the energy of the x-ray beam can now be calculated by

$$E_{Xray} = \frac{1.239841857(\mathrm{keV}\cdot\mathrm{nm})}{2d(P,T)\sin\theta_B \sin\theta_{beam}\sin\theta_{recip}} \tag{7.9}$$

$$d(P,T) = \frac{d_{220}}{2}\left(1 - \frac{PC_{comp}}{3}\right)(1 + [T - 22.5\ (^\circ\mathrm{C})]C_{temp}) \tag{7.10}$$

with P the pressure in Pa, C_{comp} the compressibility, T the temperature in °C and C_{temp} the thermal expansion coefficient. In these equations it is assumed the [4 4 0] plane of the crystal is used, therefore the factor $\frac{1}{2}$ was added to d_{220}. Using this system, the x-ray energy could be calibrated accurately and the second excited state of ^{229}Th could be accurately excited. If the ^{229}Th doped in a CaF$_2$ crystal could be excited in the SPring-8 setup and if no internal conversion takes place, the photons produced by the isomer decay should be measured.

7.2.3 Photon Detection at 150 nm

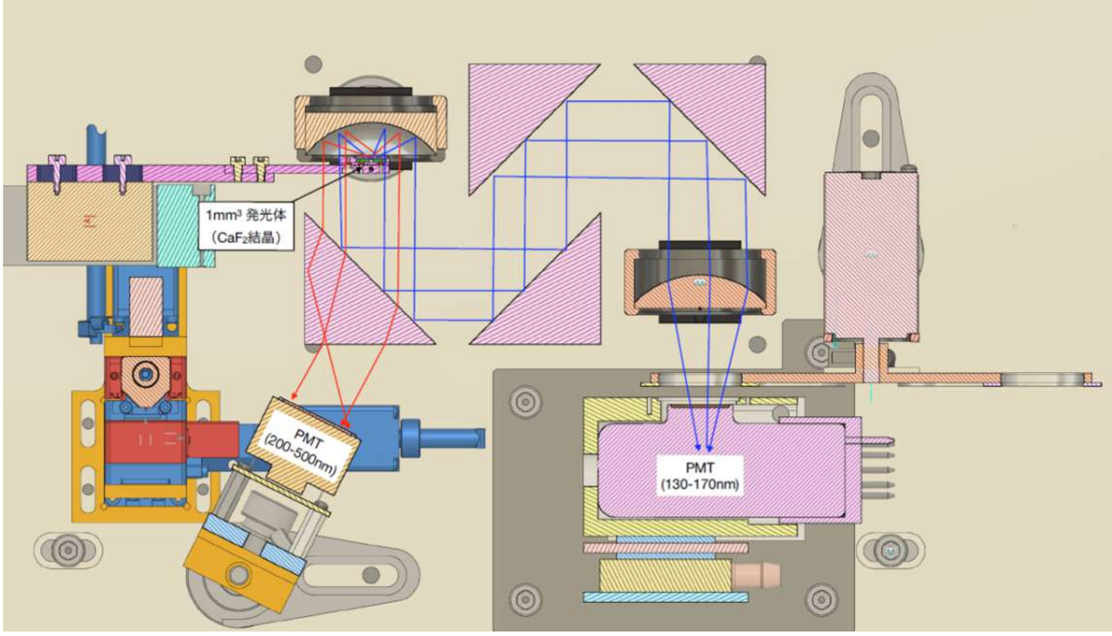

Figure 7.6: Schematic image of the 150 nm photon detection system. The holder of the crystal on the left is mounted on a 3D translation stage to align the crystal. The crystal is mounted on the holder by strapping the crystal in a cross pattern to the holder using two wires. This thus blocks out a small part of the crystal in a cross shaped pattern.

To efficiently measure photons at 150 nm, a setup was developed that would capture as many photons from the irradiated crystal as possible and filter out all wavelengths except a broadband region around 150 nm. This would ensure the highest efficiency of the system to detect the low intensity photon flux produced by the isomer decay after excitation. A schematic representation can be seen in figure 7.6 where more details on

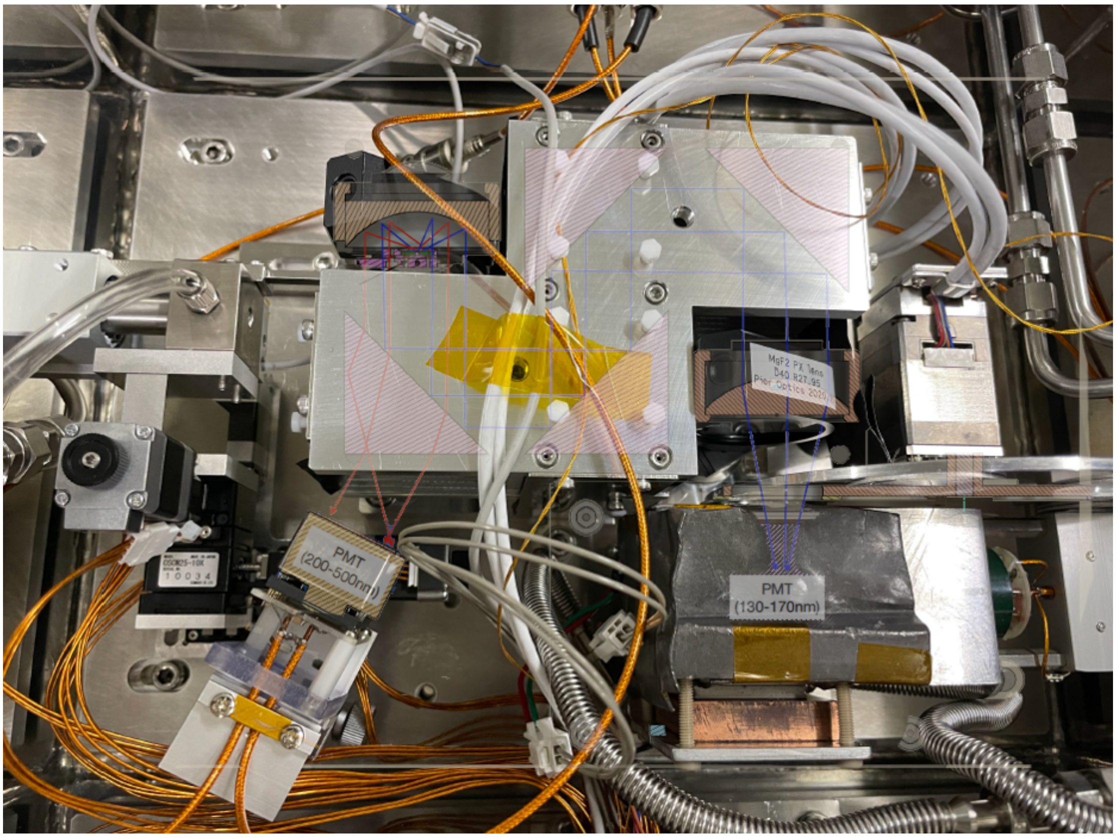

FIGURE 7.7: Picture of the 150 nm photon detection setup in the lab, with figure 7.6 overlaid. Note the pneumatic tube on the left to move the crystal from the x-ray irradiation chamber to the detection chamber. Separating these decreased background significantly. Also see the PMT cooling mechanism using water tubes and a Peltier element as in the long integration photon detection.

the setup can be found. In the lab the setup looks as in figure 7.7, note the lead shielding around the VUV PMT against the large amount of background x-ray radiation. The vacuum in the system was held better than 10^{-6} mbar.

In this experiment the crystal was irradiated by nuclear on resonant x-ray photons for 30 minutes, thereby exciting the ^{229}Th to the second excited state. Irradiation time was chosen to be 30 minutes as it was a round number close to the expected thorium nuclear isomer lifetime. The crystal is moved after excitation from irradiation chamber to detection chamber and then the VUV signal was measured. The nucleus would then quickly decay to the isomeric first excited state from which it is assumed to decay slowly.

In figure 7.6, the VUV signal exiting the crystal is depicted by blue lines. Aside from a nuclear VUV signal, STE emission induced by the radioactivity (red lines) is emitted. The light emitted in one semi sphere of the crystal is made parallel using a parabolic aluminum mirror and directed towards reflecting prisms. Four quartz prisms, coated with a dielectric coating (by OptoSigma), transmit 200 nm and above but reflect light in a broadband region around 150 nm (see figure 7.8). By using several prisms, the ratio

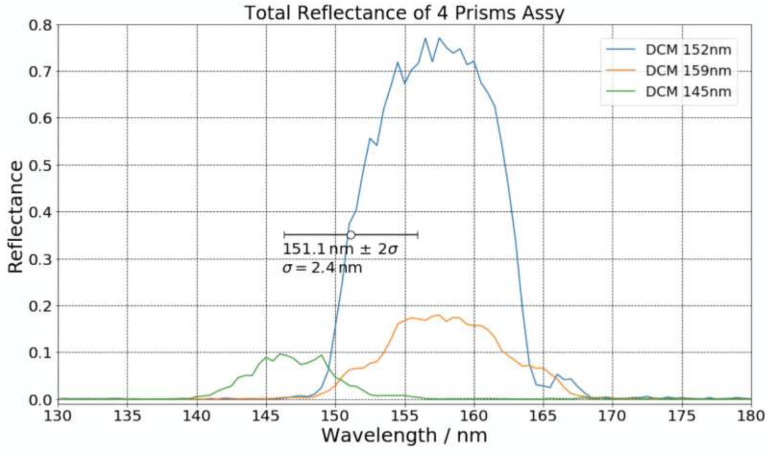

FIGURE 7.8: Total reflection of the 4 prism array set in a S/P/S/P polarization arrangement to reduce polarization related reflection effects. Three different sets of coated prisms are shown with differently designed central reflected wavelength. The reliability of this center wavelength is unsure: The center of the first 145 nm prism set was far from the design wavelength. The expected range of the nuclear isomer energy is shown.

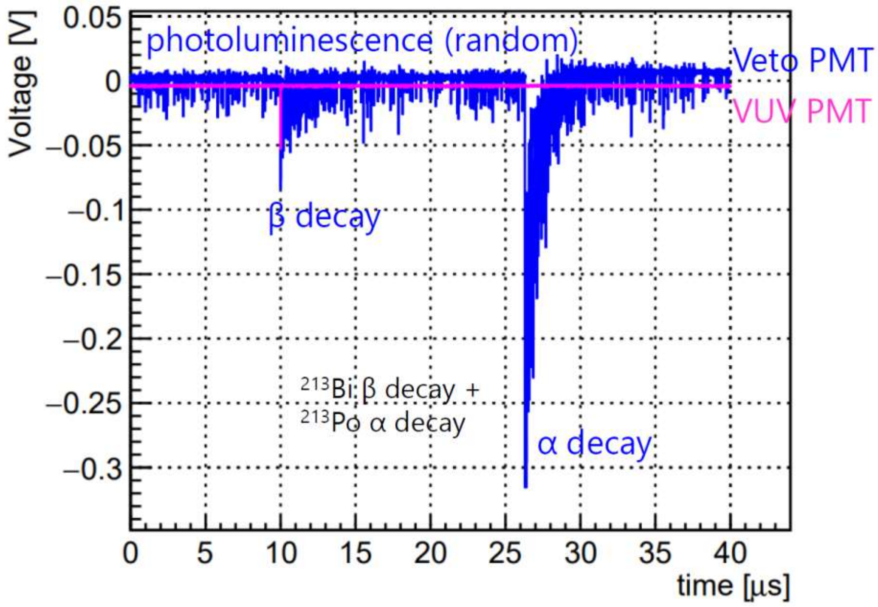

FIGURE 7.9: Electronic PMT signal as seen by the UV veto PMT and the VUV detection PMT. The ^{229}Th daughter, ^{213}Bi decays through a β^--decay which is quickly followed by a ^{213}Po α-decay (Half-life 3.72 μs). The β^--decay produces defects in the crystal and thus STE luminescence, but also produces Cherenkov radiation which can be detected on the VUV PMT. This way it can be distinguished from the α-decay which produces no Cherenkov radiation and thus mainly STE luminescence. As a UV background, single F and H defect pairs produced by decays and x-ray irradiation slowly annihilate depending on crystal temperature.

between reflected signal to background is increased. Finally the light is focused onto a R10454 CsI PMT using a MgF_2 lens. In between these two elements is a revolver that is able to block the light, or put an extra narrowband 150 nm filter in the light path.

A second PMT is used to detect the radioluminescence to reject the photon background produced by the violent radioactive decay. Each α and β^--decay produces a different type of signal and can be recognized on this PMT, see figure 7.9. All signal waveforms are stored which in post-processing can be distinguished easily from a nuclear signal, which would only produce a single VUV signal. To save the waveforms a National Instruments PXIe-5162 oscilloscope is used. The oscilloscopes uses different waveforms to trigger the VUV PMT and the UV PMT signal.

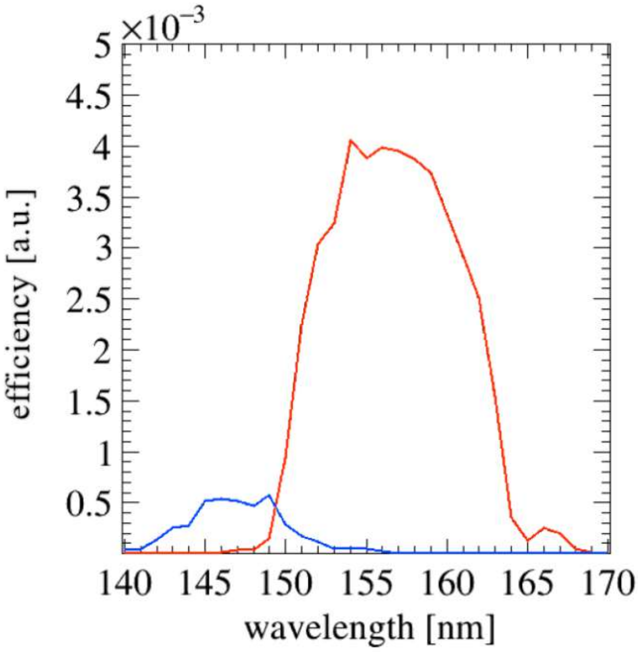

FIGURE 7.10: Total wavelength dependent efficiency of the 150 nm detection system. The efficiency is dominated by the reflectivity of the prisms as in figure 7.8. Indicated is the efficiency as fraction of photons being detected by the system, blue for the 145 nm prisms and red for the 152 nm prisms. Due to the lower reflectivity of the low wavelength prisms the efficiency is poor in the lower wavelength region.

The total efficiency of this system was calculated using raytracing in OpTaliX, the measured transmission of the ^{229}Th:CaF$_2$ crystals, the prisms reflectivity and the PMT efficiency. Combining all these factors leads to the wavelength dependent efficiency as shown in figure 7.10.

7.2.4 Spectrally Resolved Photon Detection

If a signal around 150 nm would be detected with enough intensity the exact wavelength can be determined using a spectrometer. Before that, the (V)UV background created by the crystal needs to be characterized. In this experiment, a Czerny-Turner spectrometer from Princeton instruments (Acton VM504 monochromator) with a PIXIS-XO CCD camera was chosen. The setup was used to characterize the x-ray luminescence and radioluminescence of the ^{229}Th:CaF$_2$ crystals.

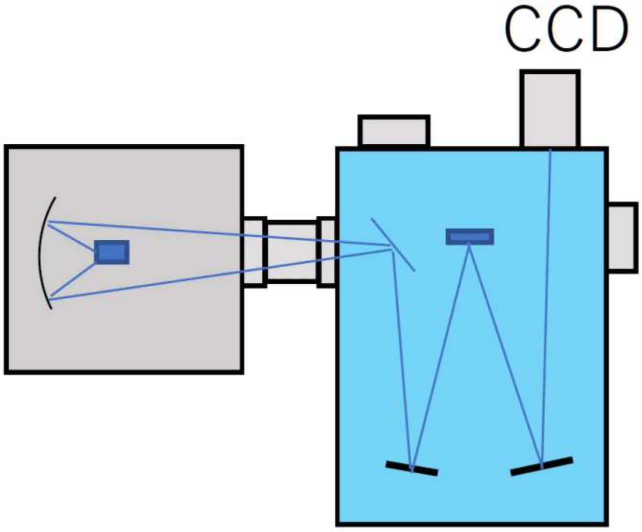

FIGURE 7.11: Schematic representation of the spectrally resolving system. On the left the crystal with an elliptical focusing mirror can be seen in the x-ray irradiation chamber. The elliptical mirror is on a motorized stage to focus the system without breaking vacuum. On the right the VM504 monochromator with CCD is displayed.

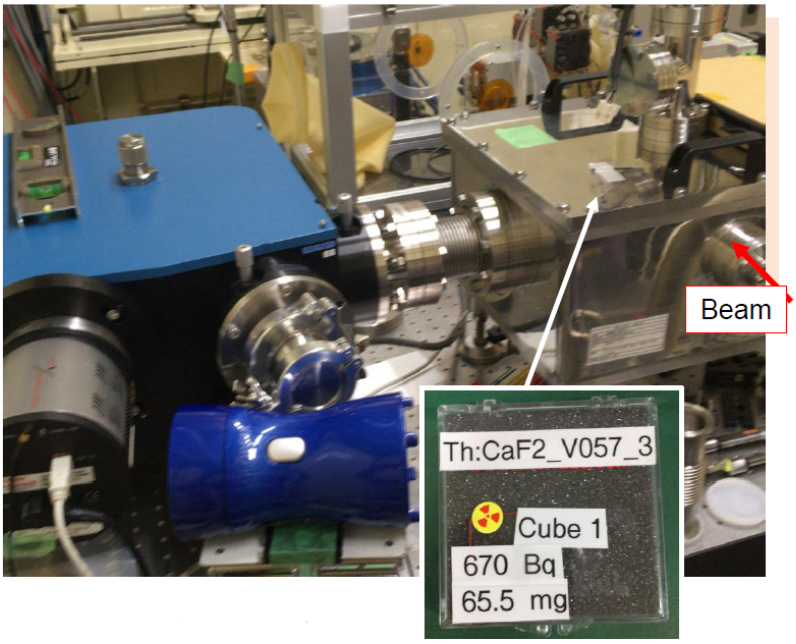

FIGURE 7.12: Spectrally resolving system in the lab. On the right the irradiation chamber can be seen and on the left the monochromator and CCD camera. The cut V057 2x2x2 mm ^{229}Th:CaF$_2$ crystal is placed in the irradiation chamber. The bellows in between the chambers is to overcome aligning differences between the chambers. The focusing point is aligned using the elliptical mirror onto the entrance slit of the spectrometer.

The monochromator and irradiation chamber setup is drawn in figure 7.11 and a picture from the lab in figure 7.12. The vacuum in the system was held better than 10^{-6} mbar. On the left (right for figure 7.12) the crystal is irradiated by x-rays, and the fluorescence can be detected while the crystal is being irradiated. This is not possible when using PMTs, they were found to be creating high levels of noise due to the background x-rays. The CCD, further away from the chamber than the PMT, seems to be less sensitive to the background x-rays than the PMTs.

The VM504 monochromator uses two focusing mirrors (black) and one grating (blue) to image the spectrum that enters its entrance slit onto the CCD camera. The efficiency of this system is drastically decreased as compared to the 150 nm setup, more than 3 orders of magnitude. No VUV signal was measured using this method, but the STE UV luminescence could be characterized. The radioluminescence was identified offline.

7.3 X-ray Pumping of the Isomer at SPring-8

At the SPring-8 storage ring a 29 keV x-ray beam was produced to induce NRS in a ^{229}Th:CaF$_2$ crystal (C10.1). The induced NRS would excite the ^{229}Th nuclei to their second excited state, after which a fraction would decay to the isomer state. In a crystal, these would then decay under emission of a photon, which would be detected with the setup described in section 7.2.4.

FIGURE 7.13: Fluorescence of the ^{229}Th:CaF$_2$ crystal in the SPring-8 x-ray beam as seen through a color webcam. Many lower energy blue photons of the STE annihilation are emitted.

During 6 beam times at SPring-8 the setup was gradually improve to increase the signal to noise ratio. Due to the large x-ray induced luminescence background, filters for the x-ray induced STE luminescence had to be installed. A picture of the 1 mm^3 crystal in the x-ray beam is shown in figure 7.13 to indicate the intensity of the produced defects in the crystal.

7.3.1 X-ray Irradiation Damaging Effects in CaF_2

The effect of x-rays on undoped CaF_2 have been extensively studied in literature as described in section 2.4. Using the SPring-8 x-ray source with 29 keV photons described in section 7.2, undoped and doped crystals were irradiated. The x-ray photon flux was $\Phi_0 = 80{\cdot}10^{12}$ Hz and the spot size 1.5 by 0.8 mm, resulting in an irradiation of $8.3{\cdot}10^{15}$ Hz cm^{-2}. The photon attenuation coefficient of CaF_2 at these energies $\approx$ 31.8 cm^{-1} (see figure 2.22), and thus for a 1 mm thick crystal $e^{-31.8*0.1} \approx 4\,\%$ of the irradiation is absorbed. The absorbed x-ray flux is then $3.5{\cdot}10^{14}$ Hz cm^{-2}.

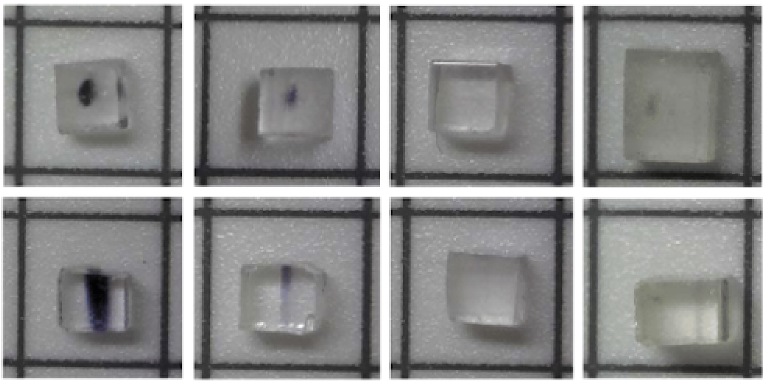

FIGURE 7.14: CaF_2 crystals damaged for 3 hours by the SPring-8 x-ray beam, side and top view. From left to right: Korth produced crystal, undoped CaF_2 grown in Vienna, ^{232}Th:CaF_2 crystal, ^{229}Th:CaF_2 crystal.

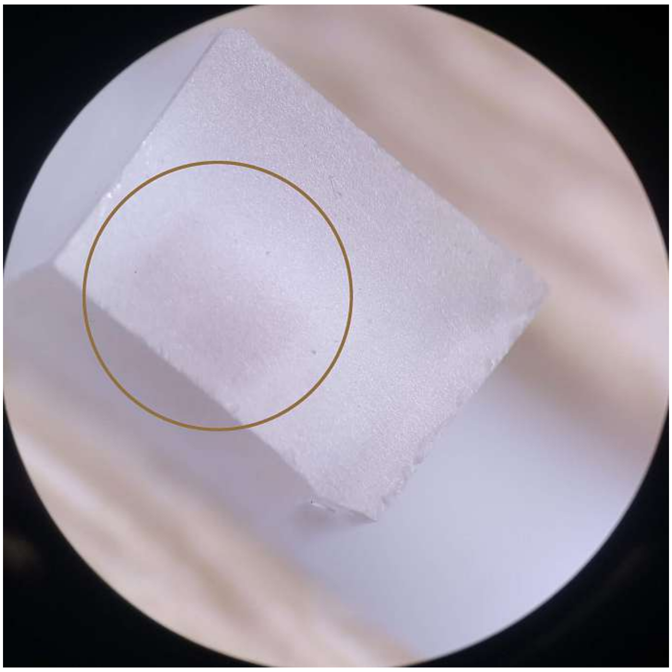

FIGURE 7.15: Zoom of ^{229}Th:CaF_2 crystal damaged by the SPring-8 x-ray beam using a microscope. Note the small dim almost invisible area of orange discoloration in the left corner in the drawn circle.

In figure 7.14 undoped and doped crystals irradiated by x-rays are shown. When an undoped crystal is irradiated, a dark purple haze is formed in the crystal indicative of large Ca nanoparticles. When Th doped crystals are irradiated, the visible damage is much lower and more orange in color, see the zoom in figure 7.15. This could be an indication that the Th atoms pin down the F centers, as was derived from detecting dislocation loops in the TEM images 4.3. This process would prevent F centers to conglomerate to larger centers and prevent the purple haze.

The x-ray irradiation of (Th:)CaF$_2$ crystals produces fluorescence, such as STEs (see figure 7.13), and ultimately also crystal damage. The $^{229/232}$Th:CaF$_2$ crystals produced VUV photons after x-ray irradiation: For ^{229}Th doped crystals by β^--decay induced Cherenkov radiation (section 2.4.3) and for ^{232}Th doped crystals by the excitation of color centers by x-rays. Emitted VUV photons by irradiated crystals were monitored during x-ray irradiation by using the setup described in section 7.2.4 to study the damaging effects of these x-rays.

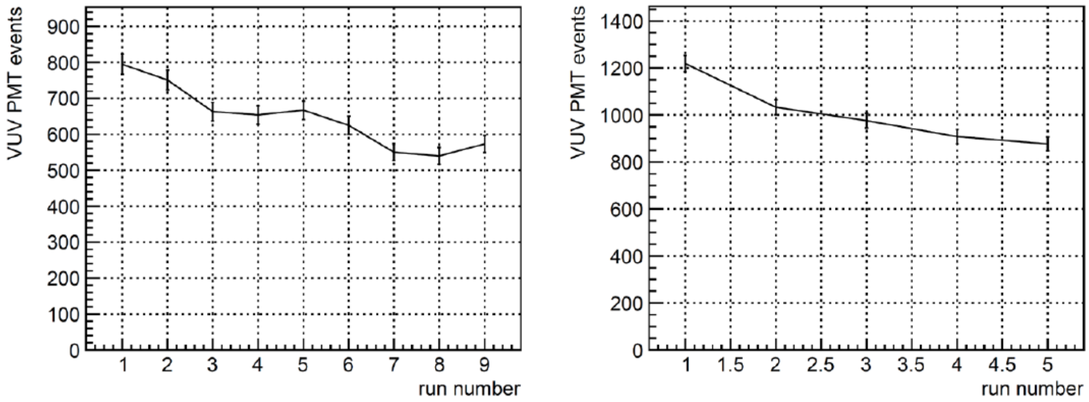

FIGURE 7.16: VUV emission of 2 crystals monitored over several experimental cycles of 30 min x-ray irradiation. Left: Cherenkov radiation was monitored for ^{229}Th: Considering radioactive background (200 counts) and electronic background (80 counts) about 40 % of the original transmission (45 %) was lost (total transmission after irradiation = 0.45*0.6 = 0.27). Right: VUV fluorescence was monitored for ^{232}Th. Considering electronic background about 30 % of the original transmission (40 %) was lost (total transmission after irradiation = 0.4*0.7 = 0.28).

The emission of VUV photons was monitored for both a ^{232}Th:CaF$_2$ and a ^{229}Th:CaF$_2$ crystal during x-ray irradiation measurements as seen in figure 7.16. This experiment shows the reduction in VUV transmission during the experiment. No saturation was observed yet, and both crystals reduced in transmission significantly. Over longer irradiation times, three hours, a saturation in damage is observed for ^{232}Th doped crystals, as is shown in figure 7.17. From the pictures and measured transmission reductions it can be concluded that in the presence of Th in CaF$_2$, saturation in damage is reached

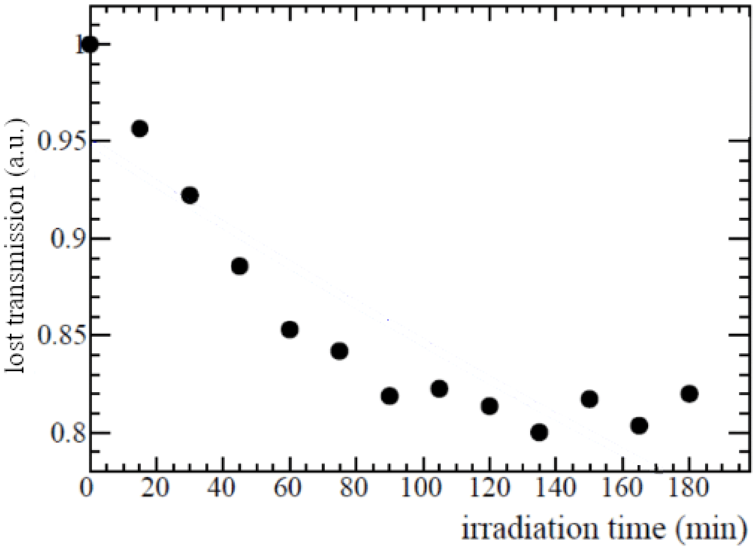

FIGURE 7.17: Fractional transmission loss measured for a ^{232}Th:CaF$_2$ crystal as a function of x-ray irradiation time. The ratio between transmission before and after irradiation was taken. After two hours of x-ray irradiation damage saturation was observed. The average damage from 140 to 170 nm is plotted.

earlier than for undoped crystals, which turn purple. The damage is however more localized in the bulk of the crystal and can thus only be repaired by annealing, not by polishing.

7.3.2 Background X-ray Induced Fluorescence

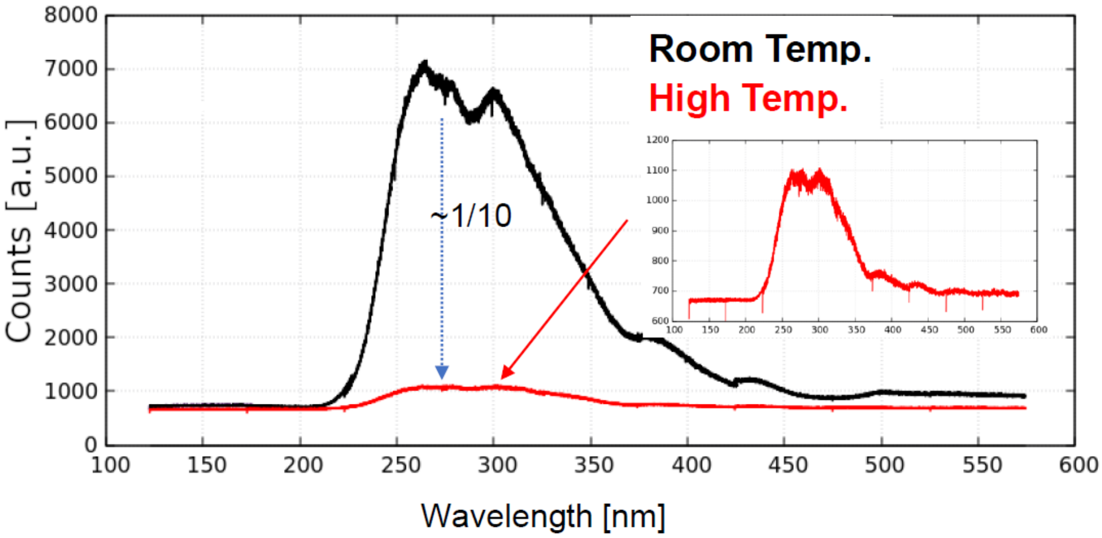

FIGURE 7.18: UV luminescence of the ^{229}Th:CaF$_2$ crystal during irradiation by the SPring-8 x-ray beam for room temperature and 150 °C. At high temperatures the photoluminescence is decreased by a factor of ten.

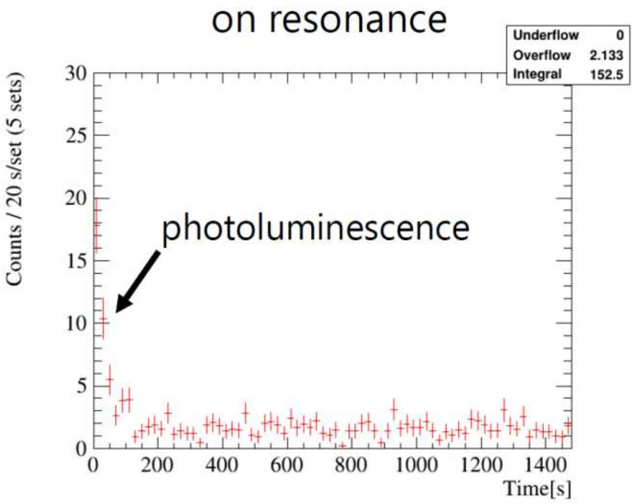

Figure 7.19: VUV luminescence of the ^{229}Th:CaF$_2$ crystal after irradiation by the SPring-8 x-ray beam. Lifetime is around 1 minute.

In these experiments the x-ray induced UV luminescence was characterized as a function of temperature, see figure 7.18. The spectrum is very similar to the radioluminescence of ^{229}Th decay in CaF$_2$, see figure 4.62. At high temperatures the STE decays non-radiatively and produces less luminescence.

As stated in the previous section, VUV luminescence was observed in x-ray irradiated ^{229}Th:CaF$_2$ crystals. The decay of this signal can be seen in figure 7.19. The wavelength of this signal has not been measured. Taking the system efficiency into account (7.10) the wavelength needs to be between 140 and 170 nm. The possible luminescence measured in Cherenkov measurements in figure 4.59 around 170 nm, the fluorescence in figure 5.19 at 168 nm and this fluorescence might be caused by the same defect.

7.4 Experimental Viability of the X-ray Method

As calculated in section 7.1, an isomer photon flux of $7 \cdot 10^3$ sr^{-1}s^{-1} was expected for a 3.2 mm diameter 1 cm long crystal. Using the calculations and parameters from section 7.1 while changing the size of the crystal to 1 mm^3, the system efficiency of section 7.2.3 (figure 7.10), the observed reduction in transmission from section 7.3.1 and VUV background (figure 7.19), the isomer photon signal rate should have been 1.5 to 10 cps at equilibrium population of excited nuclei. The background noise level of the system in section 7.2.3 is 0.1 cps and the VUV background disappears entirely after 1 min, which would allow detection of this signal assuming 100 % of the nuclei undergo decay through photon emission (no internal conversion).

Sadly, x-ray pumping of the ^{229}Th nucleus in CaF$_2$ crystals at SPring-8 did not produce a nuclear photon signal until now. The last experimental cycle was performed with ^{229}Th:CaF$_2$ crystals with a doping concentration of $4{\cdot}10^{17}$ cm^{-3}.

The only remaining background after excitation was an x-ray induced VUV luminescence with a lifetime of around one minute and an intensity of 1 cps (see figure 7.19). Even with this background a signal should have been measured. Excitation of the nucleus is constantly confirmed through NRS measurements of another ^{229}Th sample (section 7.2.1). The population of excited nuclei might be overestimated. The NRS resonance is possibly shifted in the crystal resulting in the nucleus not exciting or the nucleus does not preferentially decay to the isomer state in the crystal.

Another possibility is that the isomer energy is released through some other process. Possible explanations are: The nucleus decays while not emitting a nuclear photon, decays much faster than expected, or the crystal becomes nontransparent/amorphizes through x-ray damage. The last explanation was evaluated through transmission measurements and seems unlikely, only reducing signal strength by 20 to 40 %.

The most likely explanation is the decay of the nucleus without emission of a nuclear photon. This can happen through either internal conversion or an electron bridge process. Both processes can be evaluated:

Internal conversion would mean that the crystal environment is imperfect and allows for significant electronic excitation below its bandgap. Possibly in combination with thermal excitation, the nucleus could excite an STE or other nearby defects. During x-ray irradiation many excited states are present in the crystal such as STEs, self trapped holes, F centers, electrons in the conduction band, excited impurities and more. If the wave function of any of these overlap with the nucleus, the energy of the nuclear excited state could be used to excite an electron into the conduction band, or into a higher excited state of the conduction band. If the Charge Transfer State (CTS see section 5.1.2) of the Th doping is excited in this process, the electron that moves from the fluoride to the thorium could be promoted to the conduction band as well.

Assuming the oxidation state of thorium is 4+ it could decay through EB to the CTS instead of emitting its own photon. The probability for this process happening is low if the energy of the two states is not exactly the same. If the CTS predicted in [42] has an energy lower than the isomer energy, the nucleus can use this state to spontaneously decay with a low probability.

If the oxidation state of thorium is any different, other EB processes could cause the nucleus to decay without emitting a photon. The oxidation state can change through x-ray irradiation [67], electron emission through internal conversion of the second excited state, or non-stoichiometry in the crystal (see section 4.4). The lower oxidation states have lower lying electronically excited states [216, 281] which could quench the nucleus through EB. If the x-ray irradiation completely neutralizes the atom, the thorium atom can possibly undergo internal conversion using its bound electrons.

Any of these processes could quench the nuclear state, although the probability is low. The probability of these processes is correlated to the overlap of the wavefunction of the nucleus and the other excited state. Only atomic s orbits have a significant overlap with the nucleus. Excitation of the crystal usually creates displaced mixed states and thus should have extremely low overlap with the nucleus. This means that the probability of any of these processes happening is small so we focus on processes happening on the thorium atom.

Quenching through CTS promotion to the conduction band, through EB of an electron in an s orbit of $\mathrm{Th}^{3+/2+/1+}$ or complete neutralization of the thorium atom through x-ray irradiation seem the most probable processes. The electron involved in the CTS is most likely to end up in a mixed d and f state thus will have low overlap with the nucleus. Thus EB excitation of a $\mathrm{Th}^{3+/2+/1+}$ s orbit electron or complete neutralization seem to be the most probable causes.

Chapter 8

Conclusion and Outlook

8.1 Conclusion

In this thesis, highly doped ^{229}Th:CaF$_2$ crystals were grown (chapter 3), characterized (chapter 4) and excitation of the thorium nucleus was attempted (chapters 5, 6 and 7). No excitation effort yielded a detection of a nuclear photon. Many of the observations made in this thesis need further investigation to increase understanding. A much deeper qualitative understanding was gained on crystal growth, crystal characteristics and nuclear excitation. Concluding remarks are in order to finalize the research.

8.1.1 Growth of single crystalline Th:CaF$_2$

In the growth of Th:CaF$_2$ several conclusions can be made: Doped small single crystals of 3.2 mm diameter and 1 cm length can be grown using the VGF method (3.3). Doping concentrations of ^{232}Th up to $2.6{\cdot}10^{20}$ cm^{-3} can be grown and give reasonable (5 %) transmission at 150 nm, whereas a concentration of up until $1.2{\cdot}10^{18}$ cm^{-3} was achieved for ^{229}Th with 10 % transmission at 150 nm (4.4.1).

Through characterization of the doped crystals it is suggested that the growth of (doped) CaF$_2$ inherently produces fluoride deficient crystals (4.4.2), as seen in other publications [252]. Using high activities during the growing process amplifies the fluoride loss and creates fluoride deficient crystals, possibly through the nuclear-chemical process described in equation 4.11. This process also drains fluorides from non-molten superionic parts of the crystal, as described in figure 4.52.

8.1.2 Th Color Center and Oxidation State

Through characterization of these crystals it was learned that the crystals grown with ^{232}Th displayed a strong absorption around 124 nm as opposed to crystals grown with ^{229}Th (4.4.1). Using higher radioactivity during growth caused increased broadband absorption in the VUV, possibly caused by the fluoride deficiency or non-stoichiometry of the crystal. By annealing the fluoride deficient crystal with a pure CaF_2 crystal fluoride was transferred to the deficient crystal as predicted (4.2.2). This decreased the broadband VUV absorption and increased the absorption around 124 nm which was not seen before in this crystal.

The appearance and disappearance of the absorption around 124 nm shows that in stoichiometric crystals the oxidation state of thorium is probably 4+ as was predicted [57] and measured (4.6) for the case of crystals grown with ^{232}Th. The absorption at 124 nm is then most probably the predicted CTS [29]. When the crystal is fluoride deficient either the Th changes oxidation state or the Th is neutralized and absorbed in a Ca metallic nanoparticle making this CTS disappear, and with it the absorption at 124 nm. When growing with ^{229}Th, the thorium thus changes oxidation state. Most likely this thorium will be in the 3+ state as was seen in other non-stoichiometric compounds [59]. In self irradiation studies of the actinides the dopants only changed their oxidation state by one, indicating that Th^{3+} is more likely [49]. It is not excluded that other oxidation states would be possible. The neutralization of Th in metal Ca is unlikely, as VUV induced luminescence was observed which is characteristic for lanthanides and actinides doped in CaF_2 [134, 137, 243]. A DFT calculation on Th^{3+} doped in CaF_2 should be performed to study the possible electronic excited states of this system. The DFT calculation of Th^{3+}:CaF_2 is underway in Vienna.

8.1.3 Damage Studies of Th:CaF_2

In the study of damaging Th:CaF_2 different processes were characterized. Neutron irradiation (6.5.1) seemed to increase absorption in the VUV region less than in the UV region. An absorption akin to fluoride deficiency was observed as annealing and polishing did not significantly increase transmission in these crystals. Most of the damage was thus bulk damage which annealing could not heal.

VUV irradiation (5.4) could heavily damage the crystal, but cooling the crystal to cryogenic temperatures (80 K) reduces mobility of the created defects and forces the annihilation of these. The cryogenic cooling of any CaF_2 completely protects the crystal from VUV irradiation damage (5.5.2). The VUV damage was mostly contained on the surface and was heavily dependent on the remaining water content in the vacuum system, indicating a photochemical reaction. Annealing the crystal to more than 600 °C heals the crystal (5.5.1), but not to its original value due to the photochemical reactions. Possibly, the cooling to 80 K of crystals applied here can be used to prevent damage in the other methods of irradiation.

X-ray damaging studies (7.3.1) showed that doped crystals are more robust (only 40 % transmission loss) to x-ray damage than undoped crystals (complete transparency loss). Together with TEM images made of the doped crystals (4.6) and previous publications [52], it can be concluded that the thorium dopant pins down the motion of F centers and prevents agglomeration which is the main cause of absorption in the VUV region (Ca metallic nanoparticles). If the F centers remain separate, only absorption in the UV increases 2.5.3.

The radioactive decay of the dopant damaged the crystals by creating F centers but little increase in VUV absorption was measured (4.4.5).

8.1.4 Excitation of ^{229}Th and VUV Color Center Luminescence

Three different methods of isomer excitation were tested in this thesis: Excitation through α-decay of ^{233}U, direct excitation with VUV photons and x-ray excitation via the second excited state. For every method hurdles have been identified and insights were gained.

Excitation through α-decay of ^{233}U (6.1.1) needs improvements such as increase of doping concentration and increase of crystal transmission. Possibly through control of the uranium oxidation state absorption in the relevant VUV region can be decreased.

VUV excitation of the ^{229}Th nucleus was unsuccessful (5.5). Higher doped crystals were grown to increase viability of these experiments. Using an improved spectrometer, the detection of the nuclear excitation should become viable in the near future (5.7). In the VUV excitation experiments, luminescence of the ^{229}Th:CaF$_2$ crystals was observed. Most notably was a peak around 168 nm which can possibly be assigned to Th or its CTS.

X-ray excitation of the isomer was successful, but no VUV photon signal was detected, whereas it should have been detected (7.4). Possibly the irradiation with x-rays itself forces the nucleus to decay through a non-radiative path. VUV luminescence around 170 nm was observed in this experiment after x-ray irradiation for both ^{229}Th and ^{232}Th.

In the VUV irradiation luminescence (5.5.1), in the X-ray excitation experiments (7.3.2) and in the characterization of the Cherenkov emission of ^{229}Th:CaF$_2$ crystals (4.5.1), a luminescence around 168 nm was detected that cannot be attributed to an obvious contaminant. Since most abundant, the most likely candidate is a color center associated to Th. Since Th^{4+} has a radon like electronic configuration it is not likely to produce excited states in the VUV. The only known absorption is the CTS created when Th^{4+} is doped in the crystal. Either the oxidation state of Th is changed to Th^{3+} (through self irradiation or fluoride deficiency compensation) which has localized electronic excited states in the VUV [216], which is observed in all lanthanides and actinides [134, 137, 243], or the CTS absorbs around 124 nm and emits around 168 nm. The latter is less likely since the ^{229}Th doped crystals which did not show an absorption around 124 nm were the ones that showed luminescence around 168 nm.

Through all these observations a final preliminary conclusion is made. The oxidation state of Th can be changed from 4+ to 3+ in CaF_2, possibly through addition or subtraction of fluoride. Both states are present in any crystal, however the ratio changes. This produces two distinct scenarios which calls for different approaches of exciting the nucleus in CaF_2 which are depicted in figure 8.1.

In low-radioactivity and stoichiometric crystals, the Th is mostly in the 4+ state as measured in RBS/C and EPR experiments (4.6). In this case, there are defect states around 124 nm. To use these defect states an argon excimer lamp in combination with an 800 nm laser could be used to excite the nucleus through a charge transfer state electron bridge process. In this configuration quenching of the isomer state through these defect states is not possible since the defect states are higher in energy.

In high radioactivity and non-stoichiometric crystals the Th is mostly in the 3+ state, with an electron configuration of $[\mathrm{Rn}]5f$. In this state there is a luminescence around 168 nm which most likely can also absorb photons. Using this defect state possibly a new unstudied electron bridge excitation can be used to excite the thorium nucleus. In this case a 170 nm xenon excimer lamp and a 1700 nm laser could create the two photon electron bridge excitation. Possibly, the nucleus is quenched by the 170 nm defect state using 2-photon quenching. This would explain the null result in the x-ray excitation experiments. If stoichiometric high radioactivity crystals would be created it can be studied what drives the oxidation state change, self irradiation or fluoride deficiency.

8.2 Outlook

With the observations made in this thesis and the preliminary conclusions drawn many new directions of research and experimental recommendations can be given. Still many

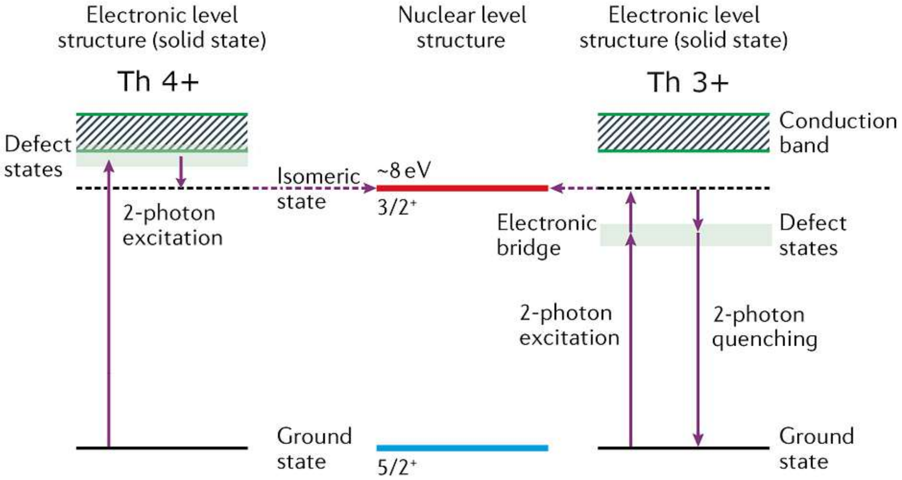

FIGURE 8.1: Schematic energy level scheme of two possible configurations of ^{229}Th in CaF_2. On the left, the bandgap of CaF_2 with the defect states around 124 nm of the 4+ oxidation close to the bandgap at 122 nm is displayed. In the middle the energy of the ^{229}Th nuclear isomer is displayed. On the right, the bandgap of CaF_2 with the defect states around 168 nm of the 3+ oxidation is shown. In the case of the 3+ oxidation, both excitation and quenching of the nucleus is possible via the defect states as opposed to the 4+ oxidation where only excitation is possible. The physical nature of the defect states is possibly very different, but depicted the same. Image adapted from [22].

avenues of characterization have not been performed extensively on all crystals. Examples are neutron scattering, nuclear quadrupole resonance, electron paramagnetic resonance, x-ray diffraction and electron microscopy. Using these solid state characterization methods, more can be learned about the microscopic surroundings of the Th nucleus and with it a higher probability of succeeding in exciting the nuclear excited state in the crystal. Using the methods already developed, the following research directions can be pursued.

Firstly, in any future experiment involving irradiation of ^{229}Th:CaF_2, it is recommended to cool the crystal to cryogenic temperatures. This will reduce the damage caused and possibly also reduces quenching of the nucleus through crystal defect states. Since the surface of CaF_2 is more easily damaged it is recommended to research the damaging processes. Possibly the water that is absorbed on the surface during storage [93] contributes heavily to damage processes by incorporating oxygen into the lattice.

Second of all, the fluorination of CaF_2 should be studied. Annealing in an F_2 gas or electrochemical insertion of F or removal of Ca as done for Li in [59] can decrease non-stoichiometry. Decreasing fluoride deficiency can possibly remove the broadband VUV absorption of for example crystal X2 and the ^{233}U doped crystal. If the highly doped ^{229}Th or ^{233}U doped crystals can be fluorinated, the x-ray irradiation and the radioactive excitation experiments should be repeated. Possibly, overfluorinating the crystal can protect it from damage by restricting fluoride motion. Controlling the fluoride content might also make it possible to change the oxidation state of any dopant in the crystal which opens up both paths in figure 8.1 for any crystal. Also changing the oxidation state of the uranium [79] might reduce VUV absorptions. This method can also be valuable for other fields of research by changing oxidation states in lanthanides which influences scintillator and laser crystal efficiencies [282]. Using techniques such as x-ray photoelectron spectroscopy, x-ray absorption fine structure, mass spectrometry or a SQUID the oxidation state of any dopant in the material can be uncovered. Using NMR, neutron activation analysis or or electron energy loss spectroscopy one can accurately determine the amount of fluoride in the system and prove that it is fluoride deficient.

Thirdly the preliminary evidences found towards color centers around 124 nm and 168 nm need to be confirmed. Direct excitation and lifetime measurements should be done to characterize these levels. Using the argon-filled excimer lamp, the 124 nm can be selectively excited, and the 168 nm level can be excited with a xenon-filled excimer lamp. By measuring their characteristics it can be checked, whether these levels are due to Th. For example, temperature dependent lifetime, concentration dependent intensity and possibly zero phonon line can be measured. Studying the intensity dependency on stoichiometry could help identify the ratio between oxidation states and identify which ones are present. Using a synchrotron for the necessary excitation intensity and detection efficiency can be crucial. The P66 beamline of Petra III is ideal for this [283]. Setting up an experiment that sets out to excite the ^{229}Th nucleus through these defect states can be done after or simultaneous with these characterizations.

Fourth point is that after the characterization measurements in this thesis, the radioactive excitation of ^{229}Th through activation of ^{228}Ra seems very viable (6.5). The biggest hurdle is growing VUV transparent CaF_2 doped with ^{228}Ra. Possibly loss of fluoride will be large here thus growth under a fluorinating atmosphere is recommended. Using a CF_4 gas [177], more PbF_2 or mixing the powder with Teflon might provide a higher local partial pressure of F_2. If this hurdle is passed, the neutron activation in the TRIGA mark II reactor and the detection of its luminescence should be performed. Upgrading the setup described in section 4.3 with a CCD or MCP detector will greatly reduce integration time because the grating does not have to be moved and thus will increase viability of the experiment. Having the possibility of measuring more wavelengths simultaneously opens up the possibility of studying also the time behavior of each spectral component.

Gaining understanding of the microscopic surrounding of the ^{229}Th nucleus will be key for a future nuclear clock. Firstly for nuclear excitation and subsequently for detection of a nuclear photon. Hopefully by following above research directions, more understanding is gained and a solid state nuclear optical clock can be built in a reasonable time frame.

Bibliography

[1] LA Kroger and CW Reich. Features of the low-energy level scheme of ^{229}th as observed in the α-decay of ^{233}u. *Nuclear Physics A*, 259(1):29–60, 1976.

[2] DG Burke, PE Garrett, Tao Qu, and RA Naumann. Additional evidence for the proposed excited state at 5 ev in th-229. *Physical Review C*, 42(2):R499, 1990.

[3] R. G. Helmer and C. W. Reich. An excited state of Th-229 at 3.5 eV. *Physical Review C*, 49(4):1845–1858, 1994. ISSN 05562813. doi: 10.1103/PhysRevC.49.1845.

[4] EV Tkalya, VO Varlamov, VV Lomonosov, and SA Nikulin. Processes of the nuclear isomer ^{229m}th (3/2+, 3.5±1.0 ev) resonant excitation by optical photons. *Physica Scripta*, 53(3):296, 1996.

[5] ZO Guimarães-Filho, O Helene, and PR Pascholati. Level and gamma-ray energies of ^{229}th. In *AIP Conference Proceedings*, volume 769, pages 257–260. American Institute of Physics, 2005.

[6] B. R. Beck, J. A. Becker, P. Beiersdorfer, G. V. Brown, K. J. Moody, J. B. Wilhelmy, F. S. Porter, C. A. Kilbourne, and R. L. Kelley. Energy splitting of the ground-state doublet in the nucleus ^{229}Th. *Phys. Rev. Lett.*, 98:142501, Apr 2007. doi: 10.1103/PhysRevLett.98.142501. URL `https://link.aps.org/doi/10.1103/PhysRevLett.98.142501`.

[7] BR Beck, C Wu, P Beiersdorfer, GV Brown, JA Becker, KJ Moody, JB Wilhelmy, FS Porter, CA Kilbourne, and RL Kelley. Improved value for the energy splitting of the ground-state doublet in the nucleus ^{229m}th. 2009. LLNL-PROC-415170.

[8] Lars von der Wense, Benedict Seiferle, Mustapha Laatiaoui, Jürgen B. Neumayr, Hans-Jörg Maier, Hans-Friedrich Wirth, Christoph Mokry, Jörg Runke, Klaus Eberhardt, Christoph E. Düllmann, Norbert G. Trautmann, and Peter G. Thirolf. Direct detection of the ^{229}Th nuclear clock transition. *Nature*, 533(7601):47–51, may 2016. ISSN 0028-0836. doi: 10.1038/nature17669. URL `http://www.nature.com/articles/nature17669`.

[9] Benedict Seiferle, Lars von der Wense, Pavlo V. Bilous, Ines Amersdorffer, Christoph Lemell, Florian Libisch, Simon Stellmer, Thorsten Schumm, Christoph E. Düllmann, Adriana Pálffy, and Peter G. Thirolf. Energy of the ^{229}th nuclear clock transition. *Nature*, 573(7773):243–246, 2019. ISSN 1476-4687. doi: 10.1038/s41586-019-1533-4. URL `https://doi.org/10.1038/s41586-019-1533-4`.

[10] Tomas Sikorsky, Jeschua Geist, Daniel Hengstler, Sebastian Kempf, Loredana Gastaldo, Christian Enss, Christoph Mokry, Jörg Runke, Christoph E Düllmann, Peter Wobrauschek, et al. Measurement of the th-229 isomer energy with a magnetic microcalorimeter. *Physical Review Letters*, 125(14):142503, 2020.

[11] Richard M Essex, Jacqueline L Mann, Ronald Collé, Lizbeth Laureano-Perez, Megan E Bennett, Heather Dion, Ryan Fitzgerald, Amy M Gaffney, Alkiviadis Gourgiotis, Amélie Hubert, et al. New determination of the ^{229}th half-life. *Journal of radioanalytical and nuclear chemistry*, 318(1):515–525, 2018.

[12] Susan Hogle, Rose Ann Boll, Karen Murphy, David Denton, Allison Owens, Tamara J. Haverlock, Marc Garland, and Saed Mirzadeh. Reactor production of thorium-229. *Applied Radiation and Isotopes*, 114:19–27, 2016. ISSN 0969-8043. doi: https://doi.org/10.1016/j.apradiso.2016.05.002. URL `https://www.sciencedirect.com/science/article/pii/S0969804316301622`.

[13] S.K. Roy, Rajendra Prasad, Sambhu N. Datta, and P. Chandra. Electron correlation and relativistic effects in atomic structure calculations of th$^+$, th$^+$ ions. *Chemical Physics Letters*, 550:25–32, 2012. ISSN 0009-2614. doi: https://doi.org/10.1016/j.cplett.2012.08.048. URL `https://www.sciencedirect.com/science/article/pii/S0009261412009827`.

[14] E Browne and JK Tuli. Nuclear data sheets for a= 239. *Nuclear Data Sheets*, 122: 293–376, 2014.

[15] E. Peik and Chr Tamm. Nuclear laser spectroscopy of the 3.5 eV transition in Th-229. *Europhysics Letters*, 61(2):181, 2003. ISSN 02955075. doi: 10.1209/epl/i2003-00210-x.

[16] Y Shigekawa, A Yamaguchi, K Suzuki, H Haba, T Hiraki, H Kikunaga, T Masuda, S Nishimura, N Sasao, A Yoshimi, et al. Estimation of radiative half-life of th-229 m by half-life measurement of other nuclear excited states in th-229. *Physical Review C*, 104(2):024306, 2021.

[17] Ernest Rutherford and EN da C Andrade. Xciv. the wave-length of the soft γ rays from radium b. *The London, Edinburgh, and Dublin Philosophical Magazine and Journal of Science*, 27(161):854–868, 1914.

[18] YA Ellis and MR Schmorak. Survey of nuclear structure systematics for a 229. *Nuclear Data Sheets*, 8(4):345–387, 1972.

[19] Sven Gösta Nilsson. Binding states of individual nucleons in strongly deformed nuclei. *Dan. Mat. Fys. Medd.*, 29(CERN-55-30):1–69, 1955.

[20] SB Utter, P Beiersdorfer, A Barnes, RW Lougheed, JR Crespo López-Urrutia, JA Becker, and MS Weiss. Reexamination of the optical gamma ray decay in th-229. *Physical review letters*, 82(3):505, 1999.

[21] Johannes Thielking, Maxim V. Okhapkin, Przemyslaw Glowacki, David M. Meier, Lars von der Wense, Benedict Seiferle, Christoph E. Düllmann, Peter G. Thirolf, and Ekkehard Peik. Laser spectroscopic characterization of the nuclear-clock isomer ^{229m}th. *Nature*, 556(7701):321–325, 2018. ISSN 1476-4687. doi: 10.1038/s41586-018-0011-8. URL `https://doi.org/10.1038/s41586-018-0011-8`.

[22] Kjeld Beeks, Tomas Sikorsky, Thorsten Schumm, Johannes Thielking, Maxim V Okhapkin, and Ekkehard Peik. The thorium-229 low-energy isomer and the nuclear clock. *Nature Reviews Physics*, pages 1–11, 2021.

[23] Andrew D Ludlow, Martin M Boyd, Jun Ye, Ekkehard Peik, and Piet O Schmidt. Optical atomic clocks. *Reviews of Modern Physics*, 87(2):637, 2015.

[24] TL Nicholson, SL Campbell, RB Hutson, GE Marti, BJ Bloom, RL McNally, Wei Zhang, MD Barrett, MS Safronova, GF Strouse, et al. Systematic evaluation of an atomic clock at $2{\cdot}10^{-18}$ total uncertainty. *Nature communications*, 6(1):1–8, 2015.

[25] Giuseppe Marra, Cecilia Clivati, Luckett Richard, Anna Tampellini, Jochen Kronjäger, Louise Wright, Alberto Mura, Filippo Levi, Stephen Robinson, André Xuereb, et al. Ultra-stable laser interferometry for earthquake detection with terrestrial and submarine optical cables. 2021.

[26] Jozsef Seres, Enikoe Seres, C Serrat, EC Young, JS Speck, and T Schumm. All-solid-state vuv frequency comb at 160 nm using high-harmonic generation in nonlinear femtosecond enhancement cavity. *Optics express*, 27(5):6618–6628, 2019.

[27] James Jespersen and Jane Fitz-Randolph. *From sundials to atomic clocks: understanding time and frequency*. Courier Corporation, 1999.

[28] G A Kazakov, A N Litvinov, V I Romanenko, L P Yatsenko, A V Romanenko, M Schreitl, G Winkler, and T Schumm. Performance of a^{229}thorium solid-state nuclear clock. *New Journal of Physics*, 14(8):083019, aug 2012. doi: 10.1088/1367-2630/14/8/083019. URL `https://doi.org/10.1088/1367-2630/14/8/083019`.

[29] Brenden S Nickerson, Martin Pimon, Pavlo V Bilous, Johannes Gugler, Georgy A Kazakov, Tomas Sikorsky, Kjeld Beeks, Andreas Grüneis, Thorsten Schumm, and Adriana Pálffy. Driven electronic bridge processes via defect states in th-229-doped crystals. *Physical Review A*, 103(5):053120, 2021.

[30] G. A. Kazakov, A. N. Litvinov, V. I. Romanenko, L. P. Yatsenko, A. V. Romanenko, M. Schreitl, G. Winkler, and T. Schumm. Performance of a ^{229}Thorium solid-state nuclear clock. *New Journal of Physics*, 2012. ISSN 13672630. doi: 10.1088/1367-2630/14/8/083019.

[31] Ekkehard Peik and Maxim Okhapkin. Nuclear clocks based on resonant excitation of γ-transitions. *Comptes Rendus Physique*, 16(5):516–523, 2015. ISSN 16310705. doi: 10.1016/j.crhy.2015.02.007.

[32] E Peik, T Schumm, M S Safronova, A Pálffy, J Weitenberg, and P G Thirolf. Nuclear clocks for testing fundamental physics. *Quantum Science and Technology*, 6(3):034002, apr 2021. doi: 10.1088/2058-9565/abe9c2. URL `https://doi.org/10.1088/2058-9565/abe9c2`.

[33] E. V. Tkalya, Christian Schneider, Justin Jeet, and Eric R. Hudson. Radiative lifetime and energy of the low-energy isomeric level in ^{229}th. *Phys. Rev. C*, 92:054324, Nov 2015. doi: 10.1103/PhysRevC.92.054324. URL `https://link.aps.org/doi/10.1103/PhysRevC.92.054324`.

[34] D.-M. Meier, J. Thielking, P. Głowacki, M. V. Okhapkin, R. A. Müller, A. Surzhykov, and E. Peik. Electronic level structure of th^{+} in the range of the ^{229m}Th isomer energy. *Phys. Rev. A*, 99:052514, May 2019. doi: 10.1103/PhysRevA.99.052514. URL `https://link.aps.org/doi/10.1103/PhysRevA.99.052514`.

[35] C. J. Campbell, A. G. Radnaev, and A. Kuzmich. Wigner crystals of ^{229}Th for optical excitation of the nuclear isomer. *Phys. Rev. Lett.*, 106:223001, Jun 2011. doi: 10.1103/PhysRevLett.106.223001. URL `https://link.aps.org/doi/10.1103/PhysRevLett.106.223001`.

[36] Karin Groot-Berning, Felix Stopp, Georg Jacob, Dmitry Budker, Raphael Haas, Dennis Renisch, Jörg Runke, Petra Thörle-Pospiech, Christoph E. Düllmann, and

Ferdinand Schmidt-Kaler. Trapping and sympathetic cooling of single thorium ions for spectroscopy. *Phys. Rev. A*, 99:023420, Feb 2019. doi: 10.1103/PhysRevA.99.023420. URL `https://link.aps.org/doi/10.1103/PhysRevA.99.023420`.

[37] Simon Stellmer, Georgy Kazakov, Matthias Schreitl, Hendrik Kaser, Michael Kolbe, and Thorsten Schumm. Attempt to optically excite the nuclear isomer in ^{229}Th. *Phys. Rev. A*, 97:062506, Jun 2018. doi: 10.1103/PhysRevA.97.062506. URL `https://link.aps.org/doi/10.1103/PhysRevA.97.062506`.

[38] Justin Jeet, Christian Schneider, Scott T. Sullivan, Wade G. Rellergert, Saed Mirzadeh, A. Cassanho, H. P. Jenssen, Eugene V. Tkalya, and Eric R. Hudson. Results of a direct search using synchrotron radiation for the low-energy ^{229}Th nuclear isomeric transition. *Phys. Rev. Lett.*, 114:253001, Jun 2015. doi: 10.1103/PhysRevLett.114.253001. URL `https://link.aps.org/doi/10.1103/PhysRevLett.114.253001`.

[39] G. W. Rubloff. Far-ultraviolet reflectance spectra and the electronic structure of ionic crystals. *Phys. Rev. B*, 5:662–684, Jan 1972. doi: 10.1103/PhysRevB.5.662. URL `https://link.aps.org/doi/10.1103/PhysRevB.5.662`.

[40] M. Letz, A. Gottwald, M. Richter, and L. Parthier. Temperature-dependent urbach tail measurements of caf$_2$ single crystals. *Phys. Rev. B*, 79:195112, May 2009. doi: 10.1103/PhysRevB.79.195112. URL `https://link.aps.org/doi/10.1103/PhysRevB.79.195112`.

[41] P Dessovic, P Mohn, RA Jackson, G Winkler, M Schreitl, G Kazakov, and T Schumm. ^{229}thorium-doped calcium fluoride for nuclear laser spectroscopy. *Journal of Physics: Condensed Matter*, 26(10):105402, 2014.

[42] Brenden S. Nickerson, Martin Pimon, Pavlo V. Bilous, Johannes Gugler, Kjeld Beeks, Tomas Sikorsky, Peter Mohn, Thorsten Schumm, and Adriana Pálffy. Nuclear excitation of the ^{229}Th isomer via defect states in doped crystals. *Phys. Rev. Lett.*, 125:032501, Jul 2020. doi: 10.1103/PhysRevLett.125.032501. URL `https://link.aps.org/doi/10.1103/PhysRevLett.125.032501`.

[43] Takahiko Masuda, Akihiro Yoshimi, Akira Fujieda, Hiroyuki Fujimoto, Hiromitsu Haba, Hideaki Hara, Takahiro Hiraki, Hiroyuki Kaino, Yoshitaka Kasamatsu, Shinji Kitao, Kenji Konashi, Yuki Miyamoto, Koichi Okai, Sho Okubo, Noboru Sasao, Makoto Seto, Thorsten Schumm, Yudai Shigekawa, Kenta Suzuki, Simon Stellmer, Kenji Tamasaku, Satoshi Uetake, Makoto Watanabe, Tsukasa Watanabe, Yuki Yasuda, Atsushi Yamaguchi, Yoshitaka Yoda, Takuya Yokokita, Motohiko Yoshimura, and Koji Yoshimura. X-ray pumping of the ^{229}Th nuclear

clock isomer. *Nature*, 573(7773):238–242, 2019. ISSN 1476-4687. doi: 10.1038/s41586-019-1542-3. URL `https://doi.org/10.1038/s41586-019-1542-3`.

[44] Justin Jeet, Christian Schneider, Scott T. Sullivan, Wade G. Rellergert, Saed Mirzadeh, A. Cassanho, H. P. Jenssen, Eugene V. Tkalya, and Eric R. Hudson. Results of a direct search using synchrotron radiation for the low-energy ^{229}Th nuclear isomeric transition. *Phys. Rev. Lett.*, 114:253001, Jun 2015. doi: 10.1103/PhysRevLett.114.253001. URL `https://link.aps.org/doi/10.1103/PhysRevLett.114.253001`.

[45] Simon Stellmer, Matthias Schreitl, Georgy A. Kazakov, Johannes H. Sterba, and Thorsten Schumm. Feasibility study of measuring the ^{229}Th nuclear isomer transition with ^{233}U-doped crystals. *Phys. Rev. C*, 94:014302, Jul 2016. doi: 10.1103/PhysRevC.94.014302. URL `https://link.aps.org/doi/10.1103/PhysRevC.94.014302`.

[46] M. Verlinde, S. Kraemer, J. Moens, K. Chrysalidis, J. G. Correia, S. Cottenier, H. De Witte, D. V. Fedorov, V. N. Fedosseev, R. Ferrer, L. M. Fraile, S. Geldhof, C. A. Granados, M. Laatiaoui, T. A. L. Lima, P.-C. Lin, V. Manea, B. A. Marsh, I. Moore, L. M. C. Pereira, S. Raeder, P. Van den Bergh, P. Van Duppen, A. Vantomme, E. Verstraelen, U. Wahl, and S. G. Wilkins. Alternative approach to populate and study the ^{229}Th nuclear clock isomer. *Phys. Rev. C*, 100:024315, Aug 2019. doi: 10.1103/PhysRevC.100.024315. URL `https://link.aps.org/doi/10.1103/PhysRevC.100.024315`.

[47] Stephan Rix Doktor Der Naturwissenschaften. *Radiation-induced Defects in Calcium Fluoride and Their Influence on Material Properties under 193 nm Laser Irradiation*. PhD thesis, 2011.

[48] Ruslan Assylbayev, Abdirash Akilbekov, Alma Dauletbekova, Aleksandr Lushchik, evgeni Shablonin, and evgeni Vasil'chenko. Radiation damage caused by swift heavy ions in caf$_2$ single crystals. *Radiation Measurements*, 90:18–22, 2016. ISSN 1350-4487. doi: https://doi.org/10.1016/j.radmeas.2015.12.034. URL `https://www.sciencedirect.com/science/article/pii/S135044871530113X`. Proceedings of the 9th International Conference on Luminescent Detectors and Transformers of Ionizing Radiation (LUMDETR 2015).

[49] JJ Stacy, N Edelstein, and RD McLaughlin. Effects of gamma irradiation on actinide ions in calcium fluoride. *The Journal of Chemical Physics*, 57(11):4980–4988, 1972.

[50] VN Makhov, S Kh Batygov, LN Dmitruk, M Kirm, S Vielhauer, and G Stryganyuk. Vuv 5 d-4 f luminescence of gd 3+ and lu 3+ ions in the caf$_2$ host. *Physics of the Solid State*, 50(9):1625–1630, 2008.

[51] Piotr A Rodnyi. *Physical processes in inorganic scintillators*, volume 14. CRC press, 1997.

[52] V Teodorescu, LC Nistor, and SV Nistor. Electron microscopy study of pure and doped synthetically grown caf$_2$ crystals. *physica status solidi (a)*, 52(2):711–717, 1979.

[53] John J Fontanella and Mary C Wintersgill. Electrical relaxation in calcium fluoride doped with thorium and zirconium. Technical report, NAVAL ACADEMY ANNAPOLIS MD DEPT OF PHYSICS, 1986.

[54] LC Nistor, SV Nistor, and V Teodorescu. The effect of impurities on the ordering of irradiation defect aggregates in caf$_2$ crystals. *physica status solidi (a)*, 58(2): 675–678, 1980.

[55] HG Dill and B Weber. Accessory minerals of fluorite and their implication regarding the environment of formation (nabburg–wölsendorf fluorite district, se germany), with special reference to fetid fluorite (“stinkspat”). *Ore Geology Reviews*, 37(2):65–86, 2010.

[56] Masahiko Daimon and Akira Masumura. High-accuracy measurements of the refractive index and its temperature coefficient of calcium fluoride in a wide wavelength range from 138 to 2326 nm. *Applied optics*, 41(25):5275–5281, 2002.

[57] Philipp Dessovic. *Ab-initio calculations for thorium doped calcium fluoride (CaF$_2$)*. PhD thesis, Wien, 2016.

[58] RD T Shannon and C Tfc Prewitt. Effective ionic radii in oxides and fluorides. *Acta Crystallographica Section B: Structural Crystallography and Crystal Chemistry*, 25 (5):925–946, 1969.

[59] Marc Dubois, Belto Dieudonne, Adel Mesbah, Pierre Bonnet, Malika El-Ghozzi, Guillaume Renaudin, and Daniel Avignant. Stabilization of th$^+$ ions into mixed-valence thorium fluoride. *Journal of Solid State Chemistry*, 184(1):220–226, 2011.

[60] Robert D Shannon. Revised effective ionic radii and systematic studies of interatomic distances in halides and chalcogenides. *Acta crystallographica section A: crystal physics, diffraction, theoretical and general crystallography*, 32(5):751–767, 1976.

[61] Gauthier J-P Deblonde, Mavrik Zavarin, and Annie B Kersting. The coordination properties and ionic radius of actinium: A 120-year-old enigma. *Coordination Chemistry Reviews*, 446:214130, 2021.

[62] Pierre Hohenberg and Walter Kohn. Inhomogeneous electron gas. *Physical review*, 136(3B):B864, 1964.

[63] Walter Kohn and Lu Jeu Sham. Self-consistent equations including exchange and correlation effects. *Physical review*, 140(4A):A1133, 1965.

[64] Nathan Argaman and Guy Makov. Density functional theory: An introduction. *American Journal of Physics*, 68(1):69–79, 2000.

[65] Peter E Blöchl. Theory and practice of density-functional theory. *arXiv preprint arXiv:1108.1104*, 2011.

[66] Kieron Burke et al. The abc of dft. *Department of Chemistry, University of California*, 40, 2007. URL `https://dft.uci.edu/doc/g1.pdf`.

[67] William Hayes. *Crystals with the fluorite structure*. Clarendon Press, 1974.

[68] Richard JD Tilley. *Defects in solids*, volume 4. John Wiley & Sons, 2008.

[69] William Hayes and Arthur Marshall Stoneham. *Defects and defect processes in nonmetallic solids*. Courier Corporation, 2012.

[70] W Hayes. Point defects in alkaline earth fluorides. *Radiation Effects*, 4(2):239–246, 1970.

[71] R Rauch. Photoluminescence of color centers in alkaline earth fluoride crystals. In *Luminescence of Crystals, Molecules, and Solutions*, pages 502–507. Springer, 1973.

[72] VM Reiterov, LN Safonova, and LP Shishatskaya. Effect of heat-treatment on transmission of fluorite crystal windows in the vacuum ultraviolet spectral region. *SOVIET JOURNAL OF OPTICAL TECHNOLOGY*, 43(7):431–433, 1976.

[73] Alexandr I Ryskin, Pavel P Fedorov, Aleksandr Lushchik, Michail E Generalov, Aleksandr E Angervaks, Maksim V Stolyarchuk, evgeni Vasilchenko, and Irina Kudryavtseva. Absorption spectrum of dark purple fluorite, kent deposit, kazakhstan. *Journal of Fluorine Chemistry*, 240:109654, 2020.

[74] DL Staebler and ZJ Kiss. Photo-reversible charge transfer in rare-earth-doped-caf$_2$. *Applied Physics Letters*, 14(3):93–94, 1969.

[75] Liangbi Su, Jun Xu, Yongjun Dong, Weiqiao Yang, Guoqing Zhou, and Guangjun Zhao. Characteristics and optical spectra of u: Caf$_2$ crystal grown by tgt. *Journal of crystal growth*, 261(4):496–501, 2004.

[76] R Rauch and G Schwotzer. Disturbed colour centres in oxygen-and alkali-doped alkaline earth fluoride crystals after x-ray irradiation at 77 and 295 k. *physica status solidi (a)*, 74(1):123–132, 1982.

[77] JMG Tijero and F Jaque. Thermal and optical properties of the f_A and $(f^{2+})_A$ centers in na-doped caf$_2$ crystals. *Physical Review B*, 41(6):3832, 1990.

[78] Liangbi Su, Jun Xu, Weiqiao Yang, Xiong Jiang, Zhiwei Zhao, Guoqing Zhou, Hongjun Li, and Jiliang Si. Effect of gamma irradiation on undoped and uranium doped calcium fluoride crystals. *Solid State Communications*, 132(11):757–760, 2004. ISSN 0038-1098. doi: https://doi.org/10.1016/j.ssc.2004.09.038. URL `https://www.sciencedirect.com/science/article/pii/S0038109804008178`.

[79] Liangbi Su, Weiqiao Yang, Jun Xu, Yongjun Dong, and Guoqing Zhou. Optical absorption properties and valence states of uranium in caf$_2$ crystals grown by tgt. *Journal of Crystal Growth*, 270(1):150–155, 2004. ISSN 0022-0248. doi: https://doi.org/10.1016/j.jcrysgro.2004.06.013. URL `https://www.sciencedirect.com/science/article/pii/S0022024804007286`.

[80] AE Hughes and SC Jain. Metal colloids in ionic crystals. *Advances in Physics*, 28 (6):717–828, 1979.

[81] Gustav Mie. Beitrage zur optik truber medien, speziell kolloidaler metallosungen. *Annalen der physik*, 330(3):377–445, 1908.

[82] W. Heitmann and E. Ritter. Production and properties of vacuum evaporated films of thorium fluoride. *Appl. Opt.*, 7(2):307–309, Feb 1968. doi: 10.1364/AO.7.000307. URL `http://opg.optica.org/ao/abstract.cfm?URI=ao-7-2-307`.

[83] T Balaji, G Lifante, E Daran, R Legros, and G Lacoste. Growth by molecular beam epitaxy and characterization of caf2: Pr3+ planar waveguides. *Thin Solid Films*, 339(1-2):187–193, 1999.

[84] Aleksandr E. Angervaks, Andrei V. Veniaminov, Maksim V. Stolyarchuk, Vyacheslav E. Vasilev, Irina Kudryavtseva, Pavel P. Fedorov, and Aleksandr I. Ryskin. Optical study of calcium precipitates in additively colored caf$_2$ crystals. *J. Opt. Soc. Am. B*, 35(6):1288–1294, Jun 2018. doi: 10.1364/JOSAB.35.001288. URL `http://josab.osa.org/abstract.cfm?URI=josab-35-6-1288`.

[85] VM Orera and E Alcalá. Optical properties of cation colloidal particles in caf$_2$ and srf$_2$. *physica status solidi (a)*, 44(2):717–723, 1977.

[86] JH Beaumont, William Hayes, DL Kirk, and GP Summers. An investigation of trapped holes and trapped excitons in alkaline earth fluorides. *Proceedings of the Royal Society of London. A. Mathematical and Physical Sciences*, 315(1520):69–97, 1970.

[87] KS Song and Richard T Williams. Self-trapped excitons. 2013.

[88] Simon Stellmer, Matthias Schreitl, and Thorsten Schumm. Radioluminescence and photoluminescence of th:caf$_2$ crystals. *Scientific reports*, 5(1):1–10, 2015.

[89] M Adair, CH Leung, and KS Song. Equilibrium configuration of the self-trapped exciton in caf$_2$ and srf$_2$. *Journal of Physics C: Solid State Physics*, 18(28):L909, 1985.

[90] CRA Catlow, KM Diller, and LW Hobbs. Irradiation-induced defects in alkali halide crystals. *Philosophical Magazine A*, 42(2):123–150, 1980.

[91] Ch. Görling, U. Leinhos, and K. Mann. Surface and bulk absorption in caf$_2$ at 193 and 157 nm. *Optics Communications*, 249(1):319–328, 2005. ISSN 0030-4018. doi: https://doi.org/10.1016/j.optcom.2005.01.027. URL `https://www.sciencedirect.com/science/article/pii/S0030401805000490`.

[92] Klaus-Werner Benz and Wolfgang Neumann. *Introduction to crystal growth and characterization*. John Wiley & Sons, 2014.

[93] V Denks, T Savikhina, and V Nagirnyi. Dependence of luminescence processes and transmission in vacuum-ultraviolet region on surface condition in caf$_2$ single crystals. *Applied Surface Science*, 158(3):301–309, 2000. ISSN 0169-4332. doi: https://doi.org/10.1016/S0169-4332(00)00009-X. URL `https://www.sciencedirect.com/science/article/pii/S016943320000009X`.

[94] É Ya Goz, RS Sokolova, and A Ya Kuznetsov. Thickness and index of refraction of a water film adsorbed on crystals. *Opt.-Mekh. Promyshl*, (12):69, 1969.

[95] VM Reiterov, LM Trofimova, and LP Shishatskaya. Influence of adsorbed films on the change in the spectral transmission of fluoride crystal windows in the vacuum ultraviolet (vuv). *SOV. J. OPT. TECH.*, 47(5):284–287, 1980.

[96] S. Gogoll, E. Stenzel, M. Reichling, H. Johansen, and E. Matthias. Laser damage of caf$_2$(111) surfaces at 248 nm. *Applied Surface Science*, 96-98:332–340, 1996. ISSN 0169-4332. doi: https://doi.org/10.1016/0169-4332(95)00440-8. URL `https://www.sciencedirect.com/science/article/pii/0169433295004408`.

[97] Jue Wang, Steven VanKerkhove, and Horst Schreiber. Evaluation of coated and uncoated caf$_2$ optics by variable angle spectroscopic ellipsometry. *Thin Solid Films*, 519(9):2881–2884, 2011.

[98] M Batzill and KJ Snowdon. Shape transition of calcium islands formed by electron-stimulated desorption of fluorine from a caf$_2$ (111) surface. *Applied Physics Letters*, 77(13):1955–1957, 2000.

[99] R Souda, T Suzuki, E Asari, and H Kawanowa. Effects of potential energy on sputtering of f+ from the caf$_2$ (111) surface by noble-gas ion bombardment. *Physical Review B*, 60(19):13854, 1999.

[100] R Bennewitz, D Smith, and M Reichling. Bulk and surface processes in low-energy-electron-induced decomposition of caf$_2$. *Physical Review B*, 59(12):8237, 1999.

[101] Jürgen Hafner. Ab-initio simulations of materials using vasp: Density-functional theory and beyond. *Journal of computational chemistry*, 29(13):2044–2078, 2008.

[102] Luis Seijo. personal communication.

[103] L van Pieterson, M Heeroma, E de Heer, and A Meijerink. Charge transfer luminescence of yb3+. *Journal of Luminescence*, 91(3):177–193, 2000. ISSN 0022-2313. doi: https://doi.org/10.1016/S0022-2313(00)00214-3. URL `https://www.sciencedirect.com/science/article/pii/S0022231300002143`.

[104] Yu Pan, Wenjun Wang, Liqun Zhou, Haibing Xu, Qinghua Xia, Li Liu, Xiaoguang Liu, and Ling Li. Feu3+ charge transfer energy and local crystal environment in eu3+ doped calcium fluoride. *Ceramics International*, 43(16):13089–13093, 2017. ISSN 0272-8842. doi: https://doi.org/10.1016/j.ceramint.2017.06.197. URL `https://www.sciencedirect.com/science/article/pii/S0272884217314098`.

[105] Zsolt Varga, Adrian Nicholl, and Klaus Mayer. Determination of the th-229 half-life. *Physical Review C*, 89(6):064310, 2014.

[106] V Baryakhtar, V Gonchar, A Zhidkov, and V Zhydkov. Radiation damages and self-sputtering of high-radioactive dielectrics: spontaneous emission of submicronic dust particles. *Condensed Matter Physics*, 2002.

[107] James Joseph Stacy. Optical studies of lanthanide and actinide ions in calcium fluoride. 1971.

[108] P Gary Eller and RA Penneman. Stabilization of actinides and lanthanides in unusually high oxidation states. Technical report, Los Alamos National Lab., nm (USA), 1986.

[109] Young-Seung Kim and Martin W Brechbiel. An overview of targeted alpha therapy. *Tumor biology*, 33(3):573–590, 2012.

[110] J. Morris, B.J. Cowen, S. Teysseyre, and A.A. Hecht. Molecular dynamics investigation of threshold displacement energies in caf$_2$. *Computational Materials Science*, 172:109293, 2020. ISSN 0927-0256. doi: https://doi.org/10.1016/j.commatsci.2019.109293. URL `https://www.sciencedirect.com/science/article/pii/S0927025619305920`.

[111] H. Amekura, R. Li, N. Okubo, N. Ishikawa, and F. Chen. Swift heavy ion irradiation to non-amorphizable caf$_2$ and amorphizable y$_3$al$_5$o$_{12}$ (yag) crystals. *Nuclear Instruments and Methods in Physics Research Section B: Beam Interactions with Materials and Atoms*, 474:78–82, 2020. ISSN 0168-583X. doi: https://doi.org/10.1016/j.nimb.2020.04.023. URL `https://www.sciencedirect.com/science/article/pii/S0168583X20302007`.

[112] V Denks, A Kotlov, V Nagirnyi, T Savikhina, and GD Jones. Impurity-related excitonic processes in caf$_2$: Sr. *physica status solidi (a)*, 191(2):628–632, 2002.

[113] ZJ Kiss and DL Staebler. Dynamics of oxidation-reduction processes in rare-earth-doped caf$_2$. *Physical Review Letters*, 14(17):691, 1965.

[114] Benjamin Welber. Direct charge transfer by x irradiation in the system caf$_2$: Eu, tm. *Journal of Applied Physics*, 36(9):2744–2745, 1965.

[115] Pieter Dorenbos. Systematic behaviour in trivalent lanthanide charge transfer energies. *Journal of Physics: Condensed Matter*, 15(49):8417, 2003.

[116] VB Mikhailik, H Kraus, J Imber, and D Wahl. Scintillation properties of pure caf$_2$. *Nuclear instruments and methods in physics research section A: accelerators, spectrometers, detectors and associated equipment*, 566(2):522–525, 2006.

[117] Yuki Shimizu, Makoto Minowa, Wataru Suganuma, and Yoshizumi Inoue. Dark matter search experiment with caf$_2$ (eu) scintillator at kamioka observatory. *Physics Letters B*, 633(2-3):195–200, 2006.

[118] Cristina Plettner, Guntram Pausch, Falko Scherwinski, CM Herbach, Ralf Lentering, Yong Kong, Katja Roemer, M Grodzicka, T Szcześniak, J Iwanowska, et al. Caf$_2$ (eu): an“old”scintillator revisited. *Journal of Instrumentation*, 8(06):P06010, 2013.

[119] Simon Stellmer, Matthias Schreitl, Georgy Kazakov, Koji Yoshimura, and Thorsten Schumm. Towards a measurement of the nuclear clock transition in

^{229}th. In *Journal of Physics: Conference Series*, volume 723, page 012059. IOP Publishing, 2016.

[120] IE Tamm and IM Frank. Coherent radiation of fast electrons in a medium. In *Dokl. Akad. Nauk SSSR*, volume 14, pages 107–112, 1937.

[121] Martin J Berger. Estar, pstar, and astar: Computer programs for calculating stopping-power and range tables for electrons, protons, and helium ions. *Unknow*, 1992.

[122] John H Hubbell and Stephen M Seltzer. Tables of x-ray mass attenuation coefficients and mass energy-absorption coefficients 1 kev to 20 mev for elements z= 1 to 92 and 48 additional substances of dosimetric interest. Technical report, National Inst. of Standards and Technology-PL, Gaithersburg, MD (United . . . , 1995.

[123] Janis Sils. Defektenspektroskopie im hochreinen und dotierten caf$_2$ für optische anwendungen im duv. 2009.

[124] Vladimir Babin, Koert D. Oskam, Peter Vergeer, and Andries Meijerink. The role of pb^{2+} as a sensitizer for gd^{3+}–eu^{3+} downconversion couple in fluorides. *Radiation Measurements*, 38(4):767–770, 2004. ISSN 1350-4487. doi: https://doi.org/10.1016/j.radmeas.2003.12.015. URL `https://www.sciencedirect.com/science/article/pii/S1350448703003524`. Proceedings of the 5th European Conference on Luminescent Detectors and Transformers of Ionizing Radiation (LUMDETR 2003).

[125] KP Oboth, FJ Lohmeier, and F Fischer. Vuv and uv spectroscopy of pb^{2+} and bi3+ centres in alkaline-earth fluorides. *physica status solidi (b)*, 154(2):789–803, 1989.

[126] SB Mirov, A Yu Dergachev, WA Sibley, L Esterowitz, TT Basiev, VB Sigachev, and AG Papashvili. Photoluminescence studies in sc: Caf$_2$ and sc, ce: Caf$_2$ crystals. *Journal of luminescence*, 69(1):35–40, 1996.

[127] M. Yamaga, S. Yabashi, Y. Masui, M. Honda, H. Takahashi, M. Sakai, N. Sarukura, J.-P.R. Wells, and G.D. Jones. Optical, infrared and epr spectroscopy of caf$_2$:ce3+ crystals co-doped with li+ or na+. *Journal of Luminescence*, 108(1):307–311, 2004. ISSN 0022-2313. doi: https://doi.org/10.1016/j.jlumin.2004.01.065. URL `https://www.sciencedirect.com/science/article/pii/S002223130400078X`. Proceedings of the Fourteenth International Conference on Dynamical Processes in Excited States of Solids.

[128] K.D Oskam, A.J Houtepen, and A Meijerink. Site selective 4f5d spectroscopy of caf$_2$:pr3+. *Journal of Luminescence*, 97(2):107–114, 2002. ISSN 0022-2313. doi: https://doi.org/10.1016/S0022-2313(01)00242-3. URL `https://www.sciencedirect.com/science/article/pii/S0022231301002423`.

[129] Noriaki Kawaguchi, Hiromi Kimura, Masaki Akatsuka, Go Okada, Naoki Kawano, Kentaro Fukuda, and Takayuki Yanagida. Scintillation characteristics of pr: Caf$_2$ crystals for charged-particle detection. *Sensors and Materials*, 30(7):1585–1590, 2018.

[130] Hidehiko Tanaka, Noriaki Kawaguchi, Naoto Abe, Yuki Furuya, Yuui Yokota, Takayuki Yanagida, Jan Pejchal, Martin Nikl, Yoshiyuki Kawazoe, and Akira Yoshikawa. Crystal growth and scintillation properties of nd:caf$_2$. *Optical Materials*, 33(3):284–287, 2011. ISSN 0925-3467. doi: https://doi.org/10.1016/j.optmat.2010.08.031. URL `https://www.sciencedirect.com/science/article/pii/S0925346710004076`.

[131] Fumiya Nakamura, Takumi Kato, Go Okada, Noriaki Kawaguchi, Kentaro Fukuda, and Takayuki Yanagida. Scintillation and dosimeter properties of caf$_2$ transparent ceramics doped with nd^{3+} produced by sps. *Journal of the European Ceramic Society*, 37(15):4919–4924, 2017. ISSN 0955-2219. doi: https://doi.org/10.1016/j.jeurceramsoc.2017.06.010. URL `https://www.sciencedirect.com/science/article/pii/S0955221917304338`.

[132] PP Feofilov. Absorption and luminescence of bivalent ions of rare-earth elements in natural and synthetic fluorite crystals. *Opt. Spektrosk*, 1:992–999, 1956.

[133] W Kaiser, CGB Garrett, and DL Wood. Fluorescence and optical maser effects in caf$_2$:sm^{++}. *Physical Review*, 123(3):766, 1961.

[134] E Radzhabov, V Nagirnyi, M Kirm, and E Prosekina. 5d-4f emission of nd^{3+}, sm^{3+}, ho^{3+}, er^{3+}, tm^{3+} ions in alkaline earth fluorides. *IEEE Transactions on Nuclear Science*, 59(5):2074–2078, 2012.

[135] IV Stepanov and PP Feofilov. Two types of luminescence spectra for the rare earths in synthetic crystals of fluorite. In *Dokl. Akad. Nauk SSSR*, volume 108, pages 615–618, 1956.

[136] JR O'connor and HA Bostick. Radiation effects in caf$_2$:sm. *Journal of Applied Physics*, 33(5):1868–1870, 1962.

[137] A Meijerink and RT Wegh. Vuv spectroscopy of lanthanides: extending the horizon. In *Materials Science Forum*, volume 315, pages 11–26. Trans Tech Publ, 1999.

[138] PP Feofilov. The nature of the primary luminescence of europium (iii) in calcium fluoride. In *Dokl. Akad. Nauk SSSR*, volume 99, pages 975–978, 1954.

[139] PP Feofilov. The orientation of europium ions in the calcium fluoride crystal lattice. In *dokl. Akad. Nauk sssr*, volume 99, pages 731–733, 1954.

[140] PP Feofilov. The spectra and the kinetics of luminescence of caf$_2$-tb monocrystals. *Opt. Spektrosk*, 10:142–144, 1961.

[141] Lin Sun, Enzhou Liu, Jun Fan, Xiaoyun Hu, Jun Wan, Juan Li, Hua Li, and Yang Hu. Fabrication and luminescence properties of tb^{3+} and tb^{3+}/ag-doped caf$_2$ microcubes. *Journal of Luminescence*, 166:361–365, 2015. ISSN 0022-2313. doi: https://doi.org/10.1016/j.jlumin.2015.04.048. URL `https://www.sciencedirect.com/science/article/pii/S002223131500246X`.

[142] Zoltan J Kiss. Energy levels of dy^{2+} in the cubic hosts of caf$_2$, srf$_2$, and baf$_2$. *Physical Review*, 137(6A):A1749, 1965.

[143] A. Sivaram, H. Jagannath, D.Ramachandra Rao, and Putcha Venkateswarlu. Steady state and transient fluorescence studies of caf$_2$:dy^{3+} single crystals. *Journal of Physics and Chemistry of Solids*, 40(12):1007–1018, 1979. ISSN 0022-3697. doi: https://doi.org/10.1016/0022-3697(79)90132-X. URL `https://www.sciencedirect.com/science/article/pii/002236977990132X`.

[144] Ya E Kariss and PP Feofilov. Absorption and emission of divalent holmium and erbium ions in fluorite-type crystals. *Opt. Spectry.(USSR)(English Transl.)*, 15, 1963.

[145] T Szczurek and M Schlesinger. $4f \rightarrow 5d$ transition studies of ho^{3+} in calcium fluoride. *Physical Review B*, 9(9):3938, 1974.

[146] MB Seelbinder and JC Wright. Site-selective spectroscopy of caf$_2$:ho^{3+}. *Physical Review B*, 20(10):4308, 1979.

[147] S Ray Bullock, BR Reddy, P Venkateswarlu, and SK Nash-Stevenson. Site-selective energy upconversion in caf$_2$: Ho 3+. *JOSA B*, 14(3):553–559, 1997.

[148] L Van Pieterson, MF Reid, and A Meijerink. Reappearance of fine structure as a probe of lifetime broadening mechanisms in the 4 f n→ 4 f n- 1 5 d excitation spectra of tb 3+, er 3+, and tm 3+ in caf$_2$ and liyf 4. *Physical review letters*, 88 (6):067405, 2002.

[149] SA Pollack. Multistage radiative transitions in caf$_2$: Er3+. *The Journal of Chemical Physics*, 38(10):2521–2529, 1963.

[150] Zoltan J Kiss. Energy levels of divalent thulium in caf$_2$. *Physical Review*, 127(3): 718, 1962.

[151] T. Szczurek and M. Schlesinger. Spectroscopic studies of excited tm^{3+} ions in caf$_2$ crystals. *Phys. Rev. B*, 34:6109–6111, Nov 1986. doi: 10.1103/PhysRevB.34.6109. URL `https://link.aps.org/doi/10.1103/PhysRevB.34.6109`.

[152] Noriaki Kawaguchi, Takayuki Yanagida, Yoshisuke Futami, Yutaka Fujimoto, Kentaro Fukuda, Shinji Kajimoto, Hiroshi Fukumura, Shunsuke Kurosawa, Yuui Yokota, and Akira Yoshikawa. Doping concentration dependence on vuv luminescence of tm:caf$_2$. *Optical Materials*, 35(11):1898–1901, 2013. ISSN 0925-3467. doi: https://doi.org/10.1016/j.optmat.2013.01.026. URL `https://www.sciencedirect.com/science/article/pii/S0925346713000797`. Photoluminescence in Rare Earths: Photonic Materials and Devices - Selected papers from PRE'12 Conference.

[153] S. Renard, P. Camy, Alain Braud, J.L. Doualan, and R. Moncorgé. Caf$_2$ doped with tm^{3+}: A cluster model. *Journal of Alloys and Compounds*, 451(1):71–73, 2008. ISSN 0925-8388. doi: https://doi.org/10.1016/j.jallcom.2007.04.132. URL `https://www.sciencedirect.com/science/article/pii/S0925838807009681`. The 6th International Conference on f-Elements (ICFE-6).

[154] Naoki Kawano, Daisuke Nakauchi, Kentaro Fukuda, Go Okada, Noriaki Kawaguchi, and Takayuki Yanagida. Comparative study of scintillation and dosimetric properties between tm-doped caf$_2$ translucent ceramic and single crystal. *Japanese Journal of Applied Physics*, 57(10):102401, 2018.

[155] Sławomir M Kaczmarek, Taiju Tsuboi, Masahiko Ito, Georges Boulon, and Grzegorz Leniec. Optical study of yb^{3+}/yb^{2+} conversion in caf$_2$ crystals. *Journal of Physics: Condensed Matter*, 17(25):3771, 2005.

[156] Eugene Loh. Ultraviolet absorption spectra of photochromic centers in caf$_2$ crystals. *Physical Review B*, 4(6):2002, 1971.

[157] A Natarajan, SD Wang, and JO Artman. Observation and analysis of the optical absorption and fluorescence spectra of green-colored np:caf$_2$. *The Journal of Chemical Physics*, 62(7):2707–2719, 1975.

[158] R McLaughlin, R White, N Edelstein, and John G Conway. Optical spectra of pu in caf$_2$. *The Journal of Chemical Physics*, 48(3):967–969, 1968.

[159] N. Edelstein, D. Hendrie, and M. Michel. Nuclear chemistry division annual report, 1969. 1 1970. doi: 10.2172/4081875. URL `https://www.osti.gov/biblio/4081875`.

[160] Manfred Deicher. Radioactive isotopes in solid state physics. *europhysics news*, 33(3):81–85, 2002.

[161] Philip J Potts. *A handbook of silicate rock analysis*. Springer Science & Business Media, 2012.

[162] JO Artman. Optical spectroscopy of ^{237} np in caf$_2$. progress report, may 1, 1972–april 30, 1973. Technical report, Carnegie-Mellon University, Pittsburgh, Pennsylvania, 1973.

[163] B.E. Burakov, Ya.V. Domracheva, M.V. Zamoryanskaya, M.A. Petrova, V.M. Garbuzov, A.A. Kitsay, and V.A. Zirlin. Development and synthesis of durable self-glowing crystals doped with plutonium. *Journal of Nuclear Materials*, 385 (1):134–136, 2009. ISSN 0022-3115. doi: https://doi.org/10.1016/j.jnucmat.2008.09.040. URL `https://www.sciencedirect.com/science/article/pii/S0022311508006272`. Plutonium Futures - The Science 2008.

[164] Jörn Schmedt auf der Günne, Martin Mangstl, and Florian Kraus. Occurrence of difluorine f$_2$ in nature—in situ proof and quantification by nmr spectroscopy. *Angewandte Chemie International Edition*, 51(31):7847–7849, 2012.

[165] Robert Alvarez. Managing the uranium-233 stockpile of the united states. *Science & Global Security*, 21(1):53–69, 2013.

[166] CW Forsberg and LC Lewis. Uses for uranium-233: What should be kept for future needs? *ORNL*, 6952(7), 1999.

[167] Wade G Rellergert, Scott T Sullivan, D DeMille, R R Greco, M P Hehlen, R A Jackson, J R Torgerson, and Eric R Hudson. Progress towards fabrication of^{229}th-doped high energy band-gap crystals for use as a solid-state optical frequency reference. *IOP Conference Series: Materials Science and Engineering*, 15:012005, nov 2010. doi: 10.1088/1757-899x/15/1/012005. URL `https://doi.org/10.1088/1757-899x/15/1/012005`.

[168] Bradley D Patton and Sharon M Robinson. Minor actinide production at oak ridge national laboratory. Technical report, Oak Ridge National Lab.(ORNL), Oak Ridge, TN (United States), 2019.

[169] Tero Pilvi, Kai Arstila, Markku Leskelä, and Mikko Ritala. Novel ald process for depositing caf$_2$ thin films. *Chemistry of materials*, 19(14):3387–3392, 2007.

[170] C Pandurangappa, BN Lakshminarasappa, and BM Nagabhushana. Synthesis and characterization of caf$_2$ nanocrystals. *Journal of alloys and compounds*, 489(2): 592–595, 2010.

[171] Y Hatanaka, H Yanagi, T Nawata, Y Inui, T Mabuchi, K Yasumura, E Nishijima, and T Fukuda. Properties of ultra-large caf$_2$ crystals for the high na optics. In *Optical Microlithography XVIII*, volume 5754, pages 1279–1284. International Society for Optics and Photonics, 2005.

[172] Matthias Schreitl. *Growth and characterization of (doped) calcium fluoride crystals for the nuclear spectroscopy of Th-229*. PhD thesis, Wien, 2016.

[173] R. Leckebusch and K. Recker. Perfektion von caf$_2$-einkristallen in abhängigkeit von der zuchttechnik. *Journal of Crystal Growth*, 13-14:276–281, 1972. ISSN 0022-0248. doi: https://doi.org/10.1016/0022-0248(72)90169-8. URL `https://www.sciencedirect.com/science/article/pii/0022024872901698`. Third International Conference on Crystal Growth.

[174] Jan Czochralski. Ein neues verfahren zur messung der kristallisationsgeschwindigkeit der metalle. *Zeitschrift für physikalische Chemie*, 92(1):219–221, 1918.

[175] RC Newman. Oxygen diffusion and precipitation in czochralski silicon. *Journal of Physics: Condensed Matter*, 12(25):R335, 2000.

[176] Akira Yoshikawa and Valery Chani. Growth of optical crystals by the micro-pulling-down method. *MRS bulletin*, 34(4):266–270, 2009.

[177] K Shimamura, Hiroki Sato, A Bensalah, V Sudesh, H Machida, N Sarukura, and T Fukuda. Crystal growth of fluorides for optical applications. *Crystal Research and Technology: Journal of Experimental and Industrial Crystallography*, 36(8-10):801–813, 2001.

[178] Tsuguo Fukuda and Valery I Chani. *Shaped crystals: growth by micro-pulling-down technique*, volume 8. Springer Science & Business Media, 2007.

[179] P. W. Bridgman. Certain physical properties of single crystals of tungsten, antimony, bismuth, tellurium, cadmium, zinc, and tin. *Proceedings of the American Academy of Arts and Sciences*, 60(6):305–383, 1925. ISSN 01999818. URL `http://www.jstor.org/stable/25130058`.

[180] M Chase. *NIST-JANAF Thermochemical Tables, 4th Edition*. American Institute of Physics, -1, 1998-08-01 1998. URL `https://janaf.nist.gov/`.

[181] F. Stöber. Xvii. künstliche darstellung großer, fehlerfreier kristalle. *Zeitschrift für Kristallographie - Crystalline Materials*, 61(1-6):299–314, 1924. doi: doi:10.1524/zkri.1924.61.1.299. URL `https://doi.org/10.1524/zkri.1924.61.1.299`.

[182] E Capelli, O Benes, PE Raison, M Beilmann, C Kunzel, and RJM Konings. Thermodynamic investigation of the caf$_2$–thf$_4$ and the lif–caf$_2$–thf$_4$ systems. *Journal of Chemical & Engineering Data*, 60(11):3166–3174, 2015.

[183] CRA Catlow and W Hayes. The nature of disorder in the superionic state of fluorites. *Journal of Physics C: Solid State Physics*, 15(3):L9, 1982.

[184] Adam Dent, Paul A Madden, and Mark Wilson. Simulation of caf$_2$ in the superionic state: comparison of an empirical and realistic potential. *Solid State Ionics*, 167(1-2):73–81, 2004.

[185] John Peterson, Margaret MacDonell, Lynne Haroun, Fred Monette, R Douglas Hildebrand, and Anibal Taboas. Radiological and chemical fact sheets to support health risk analyses for contaminated areas. *Argonne National Laboratory Environmental Science Division*, 133:40–41, 2007.

[186] C Apostolidis, R Molinet, G Rasmussen, and A Morgenstern. Production of ac-225 from th-229 for targeted α therapy. *Analytical chemistry*, 77(19):6288–6291, 2005.

[187] Masafumi Mizuguchi, Hideo Hosono, Hiroshi Kawazoe, and Tohru Ogawa. Generation of optical absorption bands in caf$_2$ single crystals by arf excimer laser irradiation: Effect of yttrium impurity. *Journal of Vacuum Science & Technology A: Vacuum, Surfaces, and Films*, 16(5):3052–3057, 1998.

[188] JM Ko, S Tozawa, A Yoshikawa, K Inaba, T Shishido, T Oba, Y Oyama, T Kuwabara, and T Fukuda. Czochralski growth of uv-grade caf$_2$ single crystals using znf$_2$ additive as scavenger. *Journal of crystal growth*, 222(1-2):243–248, 2001.

[189] A Molchanov, J Friedrich, G Wehrhan, and G Müller. Study of the oxygen incorporation during growth of large caf$_2$-crystals. *Journal of crystal growth*, 273(3-4):629–637, 2005.

[190] John H Bruning. Optical lithography: 40 years and holding. In *Optical Microlithography XX*, volume 6520, page 652004. International Society for Optics and Photonics, 2007.

[191] C Kunz and J Voss. Scientific progress and improvement of optics in the vuv range. *Review of scientific instruments*, 66(2):2021–2029, 1995.

[192] T Feigl, J Heber, A Gatto, and N Kaiser. Optics developments in the vuv—soft x-ray spectral region. *Nuclear Instruments and Methods in Physics Research Section A: Accelerators, Spectrometers, Detectors and Associated Equipment*, 483(1-2):351–356, 2002.

[193] Geoffrey V Marr. *Handbook on Synchrotron Radiation: Vacuum Ultraviolet and Soft X-ray Processes*, volume 2. Elsevier, 2013.

[194] T Namioka. Theory of the concave grating. iii. seya-namioka monochromator. *JOSA*, 49(10):951–961, 1959.

[195] Jerome Loicq, Christian Kintziger, Alexandra Mazzoli, Tim Miller, Cathy Chou, Harald U Frey, Thomas J Immel, and Stephen B Mende. Optical design and optical properties of a vuv spectrographic imager for icon mission. In *Space Telescopes and Instrumentation 2016: Ultraviolet to Gamma Ray*, volume 9905, page 990507. International Society for Optics and Photonics, 2016.

[196] Christopher Palmer and Erwin G Loewen. Diffraction grating handbook. 2005.

[197] Armon McPherson, Ned Rouze, WB Westerveld, and John S Risley. Calibration of a vuv spectrometer–detector system using synchrotron radiation. *Applied optics*, 25(2):298–310, 1986.

[198] MJ Persky. Review of black surfaces for space-borne infrared systems. *Review of Scientific Instruments*, 70(5):2193–2217, 1999.

[199] James A Samson and David L Ederer. *Vacuum ultraviolet spectroscopy*, volume 32. Academic press, 2000.

[200] Hamamatsu Photonics K.K. Deuterium Lamps. `https://www.hamamatsu.com/resources/pdf/etd/D2lamps_TLS1017E.pdf`, 2021. [Online; accessed 20-October-2021].

[201] H Abgrall, E Roueff, Xianming Liu, DE Shemansky, and GK James. High-resolution far ultraviolet emission spectra of electron-excited molecular deuterium. *Journal of Physics B: Atomic, Molecular and Optical Physics*, 32(15):3813, 1999.

[202] Robert S Freund, James A Schiavone, and Henry Milton Crosswhite. The electronic spectrum and energy levels of the deuterium molecule. *Journal of physical and chemical reference data*, 14(1):235–383, 1985.

[203] J Wieser, DE Murnick, A Ulrich, HA Huggins, A Liddle, and WL Brown. Vacuum ultraviolet rare gas excimer light source. *Review of Scientific Instruments*, 68(3):1360–1364, 1997.

[204] A Ulrich, T Heindl, R Krücken, A Morozov, C Skrobol, and J Wieser. Electron beam induced light emission. *The European Physical Journal Applied Physics*, 47(2):22815, 2009.

[205] PJ Key and RC Preston. Magnesium fluoride windowed deuterium lamps as radiance transfer standards between 115 and 370 nm. *Journal of Physics E: Scientific Instruments*, 13(8):866, 1980.

[206] Bayarto K Lubsandorzhiev. On the history of photomultiplier tube invention. *Nuclear Instruments and Methods in Physics Research Section A: Accelerators, Spectrometers, Detectors and Associated Equipment*, 567(1):236–238, 2006.

[207] Hamamatsu Photonics K.K. Photomultiplier Tubes - Basics and Applications. `https://www.hamamatsu.com/resources/pdf/etd/PMT_handbook_v4E.pdf`, 2021. [Online; accessed 9-November-2021].

[208] HO Meyer. Dark rate of a photomultiplier at cryogenic temperatures. *arXiv preprint arXiv:0805.0771*, 2008.

[209] Flora M Li, Arokia Nathan, et al. Degradation behavior and damage mechanisms of ccd image sensor with deep-uv laser radiation. *IEEE Transactions on Electron Devices*, 51(12):2229–2236, 2004.

[210] GW Fraser, JF Pearson, and JE Lees. Dark noise in microchannel plate x-ray detectors. *Nuclear Instruments and Methods in Physics Research Section A: Accelerators, Spectrometers, Detectors and Associated Equipment*, 254(2):447–462, 1987.

[211] Stephan Rix, Ute Natura, Felix Loske, Martin Letz, Claudia Felser, and Michael Reichling. Formation of metallic colloids in caf$_2$ by intense ultraviolet light. *Applied Physics Letters*, 99(26):261909, 2011.

[212] VA Dmitrievskii and AI Migachev. Dissociation of uf6 by uranium fission fragments. *Journal of Nuclear Energy. Part A. Reactor Science*, 12(4):185–190, 1960.

[213] Kathleen M. Cirillo and John C. Wright. Fluorine oxidation of rare earth dopant ions in caf$_2$ single crystals. *Journal of Crystal Growth*, 85(3):453–460, 1987. ISSN 0022-0248. doi: https://doi.org/10.1016/0022-0248(87)90476-3. URL `https://www.sciencedirect.com/science/article/pii/0022024887904763`.

[214] Kathleen M Cirillo and John C Wright. Fluorine oxidation of rare earth dopant ions in caf$_2$ single crystals. *Journal of crystal growth*, 85(3):453–460, 1987.

[215] William F Cureton, Cameron L Tracy, and Maik Lang. Review of swift heavy ion irradiation effects in ceo2. *Quantum Beam Science*, 5(2):19, 2021.

[216] PFA Klinkenberg. Spectral structure of trebly ionized thorium, th iv. *Physica B+C*, 151(3):552–567, 1988.

[217] VS Teodorescu, Liviu Nistor, and J Van Landuyt. High resolution tem observation of in situ colloid formation in caf$_2$ crystals. In *Materials Science Forum*, volume 239, pages 671–674. Trans Tech Publ, 1997.

[218] JT Mouchovski, IV Haltakov, and VL Lyutskanov. Growth of ultra-violet grade caf$_2$ crystals and their application for excimer laser optics. *Journal of crystal growth*, 162(1-2):79–82, 1996.

[219] Nikolay Minkov and Adriana Pálffy. Theoretical predictions for the magnetic dipole moment of th-229m. *Physical Review Letters*, 122(16):162502, 2019.

[220] Nikolay Minkov and Adriana Pálffy. Th-229m isomer from a nuclear model perspective. *Physical Review C*, 103(1):014313, 2021.

[221] Akira Ozawa and Yohei Kobayashi. Vuv frequency-comb spectroscopy of atomic xenon. *Physical Review A*, 87(2):022507, 2013.

[222] NG Basov, VA Danilychev, Yu M Popov, and DD Khodkevich. Laser operating in the vacuum region of the spectrum by excitation of liquid xenon with an electron beam. *JETP lett*, 12(10):329–331, 1970.

[223] V Losev, S Alekseev, N Ivanov, B Kovalchuk, L Mikheev, G Mesyats, Yu Panchenko, A Puchikin, N Ratakhin, and A Yastremsky. Development of hybrid (solid/gas state) ultra-high power femtosecond laser system on the basis of xef (ca) amplifier. *Opt. Precision Eng*, 19(2):252–259, 2011.

[224] A. Ulrich, A. Adonin, J. Jacoby, V. Turtikov, D. Fernengel, A. Fertman, A. Golubev, D. H. H. Hoffmann, A. Hug, R. Krücken, M. Kulish, J. Menzel, A. Morozov, P. Ni, D. N. Nikolaev, N. S. Shilkin, V. Ya. Ternovoi, S. Udrea, D. Varentsov, and J. Wieser. Excimer laser pumped by an intense, high-energy heavy-ion beam. *Phys. Rev. Lett.*, 97:153901, Oct 2006. doi: 10.1103/PhysRevLett.97.153901. URL `https://link.aps.org/doi/10.1103/PhysRevLett.97.153901`.

[225] S.N. Bagaev. Beginning of the laser era in the ussr. 2010. URL `http://62.44.99.18/photonics/Lasers/Beginning-of-the-Laser-Era-in-the-USSR.pdf#page=140`.

[226] James Wishart. Tools for radiolysis studies. In *Radiation Chemistry*, pages 17–34. EDP Sciences, 2020.

[227] Tomoharu Nakazato, Isao Ito, Yohei Kobayashi, Xiaoyang Wang, Chuangtian Chen, and Shuntaro Watanabe. Phase-matched frequency conversion below 150 nm in kbe2bo3f$_2$. *Opt. Express*, 24(15):17149–17158, Jul 2016. doi: 10.

1364/OE.24.017149. URL `http://www.osapublishing.org/oe/abstract.cfm?URI=oe-24-15-17149`.

[228] Qin-Jun Peng, Nan Zong, Shen-Jin Zhang, Zhi-Min Wang, Feng Yang, Feng-Feng Zhang, Zu-Yan Xu, and Xing-Jiang Zhou. Duv/vuv all-solid-state lasers: twenty years of progress and the future. *IEEE Journal of Selected Topics in Quantum Electronics*, 24(5):1–12, 2018.

[229] Philippe Wernet, Jérôme Gaudin, Kai Godehusen, Olaf Schwarzkopf, and Wolfgang Eberhardt. Femtosecond time-resolved photoelectron spectroscopy with a vacuum-ultraviolet photon source based on laser high-order harmonic generation. *Review of Scientific Instruments*, 82(6):063114, 2011.

[230] A Heinrich, W Kornelis, MP Anscombe, CP Hauri, P Schlup, J Biegert, and U Keller. Enhanced vuv-assisted high harmonic generation. *Journal of Physics B: Atomic, Molecular and Optical Physics*, 39(13):S275, 2006.

[231] Shirly Espinoza, Fabio Samparisi, Fabio Frassetto, Steffen Richter, Mateusz Rebarz, Ondrej Finke, Martin Albrecht, Matej Jurkovic, Ondrej Hort, Nicola Fabris, et al. Characterization of the high harmonics source for the vuv ellipsometer at eli beamlines. *Journal of Vacuum Science & Technology B, Nanotechnology and Microelectronics: Materials, Processing, Measurement, and Phenomena*, 38 (2):024005, 2020.

[232] Jozsef Seres, Enikoe Seres, C Serrat, and Thorsten Schumm. Non-perturbative generation of duv/vuv harmonics from crystal surfaces at 108 mhz repetition rate. *Optics express*, 26(17):21900–21909, 2018.

[233] S. G. Porsev and V. V. Flambaum. Electronic bridge process in $^{229}\mathrm{Th}^{+}$. *Phys. Rev. A*, 81:042516, Apr 2010. doi: 10.1103/PhysRevA.81.042516. URL `https://link.aps.org/doi/10.1103/PhysRevA.81.042516`.

[234] S. G. Porsev and V. V. Flambaum. Effect of atomic electrons on the 7.6-ev nuclear transition in $^{229}\mathrm{Th}^{3+}$. *Phys. Rev. A*, 81:032504, Mar 2010. doi: 10.1103/PhysRevA.81.032504. URL `https://link.aps.org/doi/10.1103/PhysRevA.81.032504`.

[235] PV Borisyuk, NN Kolachevsky, AV Taichenachev, EV Tkalya, I Yu Tolstikhina, and VI Yudin. Excitation of the low-energy th-229 m isomer in the electron bridge process via the continuum. *Physical Review C*, 100(4):044306, 2019.

[236] A Ya Dzyublik. Excitation of th-229 m in the electron bridge via continuum, as a scattering process. *Physical Review C*, 102(2):024604, 2020.

[237] EV Tkalya. Excitation of th-229 m at inelastic scattering of low energy electrons. *Physical Review Letters*, 124(24):242501, 2020.

[238] GA Kazakov, M Schreitl, G Winkler, JH Sterba, G Steinhauser, and T Schumm. Atomic clock with nuclear transition: current status in tu wien. *arXiv preprint arXiv:1110.0741*, 2011.

[239] Alexander Neumeier, T Dandl, T Heindl, A Himpsl, L Oberauer, W Potzel, S Roth, S Schönert, Jochen Wieser, and Andreas Ulrich. Intense vacuum ultraviolet and infrared scintillation of liquid ar-xe mixtures. *EPL (Europhysics Letters)*, 109(1): 12001, 2015.

[240] K Chakrabarti, VK Mathur, RJ Abbundi, N Kristianpoller, and WF Hornyak. Study of low temperature luminescence and thermoluminescence in calcium fluoride crystals. *Journal of luminescence*, 48:828–832, 1991.

[241] BR Müller, J Feldhaus, F Schäfers, and F Eggenstein. Cleaning of carbon contaminated vacuum ultraviolet-optics: Influence on surface roughness and reflectivity. *Review of scientific instruments*, 63(1):1428–1431, 1992.

[242] VN Makhov, N Yu Kirikova, JC Krupa, M Kirm, E Negodin, G Zimmerer, and JY Gesland. $6d5f$–$5f_2$ luminescence of u^{4+} doped into liyf$_4$ crystal.

[243] N.Yu. Kirikova, M. Kirm, J.C. Krupa, V.N. Makhov, G. Zimmerer, and J.Y. Gesland. 6d5f configuration of u^{4+} doped into liyf4 crystal. *Journal of Luminescence*, 97(3):174–179, 2002. ISSN 0022-2313. doi: https://doi.org/10.1016/S0022-2313(02)00221-1. URL `https://www.sciencedirect.com/science/article/pii/S0022231302002211`.

[244] Pieter Dorenbos. A review on how lanthanide impurity levels change with chemistry and structure of inorganic compounds. *ECS Journal of Solid State Science and Technology*, 2(2):R3001, 2012.

[245] RR Kinsey, CL Dunford, JK Tuli, and TW Burrows. The nudat/pcnudat program for nuclear data. Technical report, Brookhaven National Lab., Upton, NY (United States), 1996.

[246] I Ahmad, JE Gindler, RR Betts, RR Chasman, and AM Friedman. Possible ground-state octupole deformation in pa-229. *Physical Review Letters*, 49(24): 1758, 1982.

[247] CU Jost, Justin R Griswold, Stephanie H Bruffey, S Mirzadeh, DW Stracener, and CL Williams. Measurement of cross sections for the 232 th (p, 4 n) 229 pa

reaction at low proton energies. In *AIP conference proceedings*, volume 1525, pages 520–524. American Institute of Physics, 2013.

[248] V Sonnenschein, ID Moore, S Raeder, A Hakimi, A Popov, and K Wendt. The search for the existence of ^{229m}th at igisol. In *Three decades of research using IGISOL technique at the University of Jyväskylä*, pages 311–325. Springer, 2012.

[249] E Browne and JK Tuli. Nuclear data sheets for a=229. *Nuclear Data Sheets*, 109 (11):2657–2724, 2008.

[250] Dan Sporea, Laura Mihai, Adelina Sporea, and Ion Vâţã. Optical and thz investigations of mid-ir materials exposed to alpha particle irradiation. *Scientific reports*, 7(1):1–7, 2017.

[251] NP Nekrasova, EN Oblomeev, VN Golovanova, and AV Beznosikova. Investigation of the system uf 4-caf$_2$. *Soviet Atomic Energy*, 22(4):367–371, 1967.

[252] K. Recker and R. Leckebusch. Zur züchtung von caf$_2$ und caf$_2$:u-einkristallen aus der dampfphase. *Journal of Crystal Growth*, 9:274–280, 1971. ISSN 0022-0248. doi: https://doi.org/10.1016/0022-0248(71)90242-9. URL `https://www.sciencedirect.com/science/article/pii/0022024871902429`.

[253] R McLaughlin, U Abed, John G Conway, N Edelstein, and EH Huffman. Oxidation states and site symmetries of caf$_2$:u crystals. *The Journal of Chemical Physics*, 53 (5):2031–2034, 1970.

[254] V Lupei, A Lupei, and I Ursu. Pentavalent uranium in caf$_2$. *Journal of Physics C: Solid State Physics*, 10(22):4587, 1977.

[255] T Mitsugashira, M Hara, T Ohtsuki, H Yuki, K Takamiya, Y Kasamatsu, A Shinohara, H Kikunaga, and T Nakanishi. Alpha-decay from the 3.5 ev isomer of ^{229}th. *Journal of radioanalytical and nuclear chemistry*, 255(1):63–66, 2003.

[256] H Kikunaga, Y Kasamatsu, and K Takamiya. Production of th-229m in nuclear reaction and its identification by alpha-spectrometry. 2004.

[257] Hidetoshi Kikunaga, Yoshitaka Kasamatsu, Koichi Takamiya, Toshiaki Mitsugashira, Mitsuo Hara, Tsutomu Ohtsuki, Hideyuki Yuki, Atsushi Shinohara, Seiichi Shibata, Norikazu Kinoshita, et al. Search for α-decay of ^{229m}th produced from ^{229}ac β-decay following ^{232}th (γ, p2n) reaction. *Radiochimica Acta*, 93(9-10):507–510, 2005.

[258] E Ruchowska, WA Płóciennik, J Żylicz, H Mach, J Kvasil, Alejandro Algora, N Amzal, Torbjörn Bäck, MG Borge, Rafik Boutami, et al. Nuclear structure of th-229. *Physical Review C*, 73(4):044326, 2006.

[259] A. Yamaguchi, H. Muramatsu, T. Hayashi, N. Yuasa, K. Nakamura, M. Takimoto, H. Haba, K. Konashi, M. Watanabe, H. Kikunaga, K. Maehata, N. Y. Yamasaki, and K. Mitsuda. Energy of the ^{229}Th nuclear clock isomer determined by absolute γ-ray energy difference. *Phys. Rev. Lett.*, 123:222501, Nov 2019. doi: 10.1103/PhysRevLett.123.222501. URL `https://link.aps.org/doi/10.1103/PhysRevLett.123.222501`.

[260] Y Shigekawa, Y Kasamatsu, E Watanabe, H Ninomiya, S Hayami, N Kondo, Y Yasuda, H Haba, and A Shinohara. Observation of internal-conversion electrons emitted from th-229m produced by β decay of ac-229. *Physical Review C*, 100(4): 044304, 2019.

[261] A. Yamaguchi, H. Muramatsu, T. Hayashi, N. Yuasa, K. Nakamura, M. Takimoto, H. Haba, K. Konashi, M. Watanabe, H. Kikunaga, K. Maehata, N. Y. Yamasaki, and K. Mitsuda. Energy of the Th-229 Nuclear Clock Isomer Determined by Absolute γ -ray Energy Difference. *Physical Review Letters*, 2019. ISSN 10797114. doi: 10.1103/PhysRevLett.123.222501.

[262] Sandro Kraemer, Kjeld Beeks, Michael Block, Thomas Cocolios, Guilherme Correia, Stefaan Cottenier, Hilde De Witte, Kristof Dockx, Rafael Ferrer, Sarina Geldhof, Ulli Köster, Mustapha Laatiaoui, Razvan Lica, Pin Lin, Vladimir Manea, Janni Moens, Iain Moore, Lino Pereira, Sebastian Raeder, Mikael Reponen, Sebastian Rothe, Thorsten Schumm, Benedict Seiferle, Simon Sels, Peter Thirolf, Paul Van Den Bergh, Piet Van Duppen, André Vantomme, Matthias Verlinde, Elise Verstraelen, and Ulrich Wahl. Study of the radiative decay of the low-energy isomer in ^{229}Th. Technical report, CERN, Geneva, May 2020. URL `http://cds.cern.ch/record/2717784`.

[263] Khalifeh Abusaleem. Nuclear data sheets for a = 228. *Nuclear Data Sheets*, 116: 163–262, 2014.

[264] M Cagnazzo, C Raith, M Villa, and H Böck. Measurements of the in-core neutron flux distribution and energy spectrum at the triga mark ii reactor of the vienna university of technology/atominstitut. In *Proceedings of the International Conference Nuclear Energy for New Europe (NENE), Portorož, Slovenia*, 2014.

[265] Rustam Khan. *Neutronics analysis of the TRIGA Mark II reactor core and its experimental facilities*. PhD thesis, 2010.

[266] Christian Ouellet and Balraj Singh. Nuclear data sheets for a= 32. *Nuclear Data Sheets*, 112(9):2199–2355, 2011.

[267] Richard C Ropp. *Encyclopedia of the alkaline earth compounds*. Newnes, 2012.

[268] RD t Shannon and CT Prewitt. Revised values of effective ionic radii. *Acta Crystallographica Section B: Structural Crystallography and Crystal Chemistry*, 26(7):1046–1048, 1970.

[269] Tetsuo Yonezawa, Kentaro Matsuo, Jun Nakayama, and Yoji Kawamoto. Behaviors of metal-oxide impurities in caf$_2$ and baf$_2$ single-crystals grown with pbf$_2$ scavenger by stockbarger's method. *Journal of Crystal Growth*, 258(3):385–393, 2003. ISSN 0022-0248. doi: https://doi.org/10.1016/S0022-0248(03)01567-7. URL `https://www.sciencedirect.com/science/article/pii/S0022024803015677`.

[270] M. Jibran, G. Murtaza, M.A. Khan, R. Khenata, S. Muhmmad, and Roshan Ali. First principle study of mf$_2$ (m=mg, ca, sr, ba, ra) compounds. *Computational Materials Science*, 81:575–581, 2014. ISSN 0927-0256. doi: https://doi.org/10.1016/j.commatsci.2013.09.010. URL `https://www.sciencedirect.com/science/article/pii/S092702561300534X`.

[271] AT Davidson, AG Kozakiewicz, JD Comins, TE Derry, K Schwartz, and C Trautmann. The colouration of caf$_2$ crystals by kev and gev ions. *Radiation effects and defects in solids*, 157(6-12):637–641, 2002.

[272] T. Aoki, L.A.J. Garvie, and P. Rez. Observation of color center peaks in calcium fluoride. *Ultramicroscopy*, 153:40–44, 2015. ISSN 0304-3991. doi: https://doi.org/10.1016/j.ultramic.2015.02.007. URL `https://www.sciencedirect.com/science/article/pii/S0304399115000224`.

[273] Martin Nikl, Hiroki Sato, eva Mihokova, Toshiro Mabuchi, Teruhiko Nawata, A. Yoshikawa, Jan Pejchal, Naoriaki Kawaguchi, Sumito Ishizu, Kentaro Fukuda, and Toshihisa Suyama. Factors affecting the transmission and stability in complex fluorides in VUV spectral region. In Libor Juha, Saša Bajt, and Ryszard Sobierajski, editors, *Damage to VUV, EUV, and X-Ray Optics II*, volume 7361, pages 196 – 205. International Society for Optics and Photonics, SPIE, 2009. URL `https://doi.org/10.1117/12.822558`.

[274] TW Burrows. Nuclear data sheets for a= 49. *Nuclear Data Sheets*, 109(8):1879–2032, 2008.

[275] Masaharu Tanabashi, K Hagiwara, K Hikasa, Katsumasa Nakamura, Y Sumino, F Takahashi, J Tanaka, K Agashe, G Aielli, Claude Amsler, et al. Review of particle physics. *Physical Review D*, 98(3):030001, 2018.

[276] H Kitamura, T Bizen, T Hara, X Marechal, T Seike, and T Tanaka. Recent developments of insertion devices at spring-8. *Nuclear Instruments and Methods in*

Physics Research Section A: Accelerators, Spectrometers, Detectors and Associated Equipment, 467:110–113, 2001.

[277] M Yabashi, T Mochizuki, H Yamazaki, S Goto, H Ohashi, K Takeshita, T Ohata, T Matsushita, K Tamasaku, Yoshihito Tanaka, et al. Design of a beamline for the spring-8 long undulator source 1. *Nuclear Instruments and Methods in Physics Research Section A: Accelerators, Spectrometers, Detectors and Associated Equipment*, 467:678–681, 2001.

[278] Takahiko Masuda, Tsukasa Watanabe, Kjeld Beeks, Hiroyuki Fujimoto, Takahiro Hiraki, Hiroyuki Kaino, Shinji Kitao, Yuki Miyamoto, Koichi Okai, Noboru Sasao, et al. Absolute x-ray energy measurement using a high-accuracy angle encoder. *Journal of Synchrotron Radiation*, 28(1), 2021.

[279] W_ L Bond. Precision lattice constant determination. *Acta Crystallographica*, 13 (10):814–818, 1960.

[280] G Cavagnero, H Fujimoto, Giovanni Mana, Enrico Massa, K Nakayama, and G Zosi. Measurement repetitions of the si (220) lattice spacing. *Metrologia*, 41(1): 56, 2003.

[281] D.-M. Meier, J. Thielking, P. Głowacki, M. V. Okhapkin, R. A. Müller, A. Surzhykov, and E. Peik. Electronic level structure of th$^+$ in the range of the ^{229m}Th isomer energy. *Phys. Rev. A*, 99:052514, May 2019. doi: 10.1103/PhysRevA.99.052514. URL `https://link.aps.org/doi/10.1103/PhysRevA.99.052514`.

[282] MI Danilkin, AP Belousov, SO Klimonskii, VD Kuznetsov, AL Lust, VN Nikiforov, LN Paama, I Kh Pammo, and VO Seeman. Formation of eu^{2+} and eu^{3+} centers in synthesis of caf$_2$: Eu luminophores. *Journal of Applied Spectroscopy*, 74(6): 858–865, 2007.

[283] W Drube, M Bieler, WA Caliebe, H Schulte-Schrepping, J Spengler, M Tischer, and R Wanzenberg. The petra iii extension. In *AIP Conference Proceedings*, volume 1741, page 020035. AIP Publishing LLC, 2016.